Swansea University
Prifysgol Abertawe

Active Control Methods in Nonlinear Aeroelasticity

by

James Daniel Ellis

Doctor of Philosophy

at

Swansea University

April 2025

Declarations

This work has not previously been accepted in substance for any degree and is not being concurrently submitted in candidature for any degree.

Signed..[redacted].....

Date.....24/04/2025.....

This thesis is the result of my own investigations, except where otherwise stated. Other sources are acknowledged by footnotes giving explicit references. A bibliography is appended.

Signed. [redacted].....

Date.....24/04/2025.....

I hereby give consent for my thesis, if accepted, to be available for electronic sharing

Signed [redacted].....

Date.....15/08/2024.....

The University's ethical procedures have been followed and, where appropriate, that ethical approval has been granted.

Signed. [redacted].....

Date.....24/04/2025.....

Abstract

Aeroelasticity is the study of how aerodynamic, elastic, and inertial forces interact with each other and influence the static and dynamic response of structures. By utilising computer simulation and wind tunnel testing, the dynamic responses of an aeroelastic system can be determined for a range of airspeeds and combinations of system parameters, for both structurally linear and nonlinear configurations. The inclusion of one or more control surfaces enables the exploration of a variety of control methods that may be tailored to achieve a desired outcome, and could also potentially introduce additional dynamic phenomena arising from the control surface. The application of linear and nonlinear active control methods to mitigate vibrations is explored, both in the presence of gusts and to extend the flutter speed for a given system. The effects of gusts, both uncontrolled and controlled, on the dynamic behaviour of the system are also investigated. The approach used in meeting the above aims includes simulating aeroelastic response of a numerical model of various configurations of a flexible fixed-wing rig equipped with two control surfaces (suitable for wind tunnel mounting and testing), already available for use. The model in question is then used to investigate the Receptance Method for gust response alleviation, with numerical results showing a significant reduction in wing deflection due to gusts, with oscillations returning to rest within 3 seconds following a gust encounter. Then, the design of an updated version of the available wing that is better suited to the Swansea University test conditions is used to again employ the Receptance Method, but with the aim of extending the flutter speed. Numerical results show that a 22% increase to the flutter speed could be achieved using this method. Experimental tests demonstrated the importance of the position of natural frequencies for different modes as coupled motion prevents the acquisition of receptance data. Numerically, a nonlinearity is designed and implemented, and feedback linearisation is carried out on the system, with results showing reduction in vibration by counteracting flutter following perturbation due to gusts, resulting in a stable system. Finally, a new wing model capable of using a fixed, passive folding, and active folding wing tips is used in the wind tunnel to analyse the wing root bending moment in the presence of gusts. The active control law used is PD control, which results in up to a 29.3% reduction in bending moment due to gusts for some experimental cases. The outcome is that this project investigated some novel methods for active control of aeroelastic systems, which are also effective in situations where gust inputs are significant. Such an increase in the ability to control the dynamics of aeroelastic systems in the presence of nonlinearities and gust inputs – both of which are very real phenomena in the real world – could translate to practical

benefits such as longevity of aircraft, increased passenger comfort, not requiring overly conservative safety factors in the design process etc, ultimately resulting in significant cost savings and greener engineering. The control methods used in this work have shown promise and should be used for environmentally friendly future aircraft designs.

Acknowledgements

I would like to express my utmost gratitude to my supervisors Dr. Shakir Jiffri, Prof. Mike Friswell and Prof. Hamed Haddad Khodaparast for their invaluable support during my studies. Thanks to them, I have continued to learn and grow over the course of my project and their hard work and characters are inspiring.

I would also like to thank Dr. Sebastiano Fichera for his collaboration and support on some of the work documented here.

This project was able to proceed with financial backing from the EPSRC Doctoral Training Partnerships and the Swansea University Faculty of Science and Engineering

I am grateful to my colleagues Davide, Pushpa and Nidhal for their friendship and support during my project.

I am thankful for my friends, particularly Ilias, Leo and Henry whom I could not live without, and especially Lucas who has been, and will be forever, a brother to me. I love you all.

Finally, my biggest gratitude to my family for their constant love, support and belief in me. This work is dedicated to my Mum and Dad, Granny, and Jean. Thank you for everything.

CONTENTS

Title **Page No.**

LIST OF FIGURES

Title **Page No.**

LIST OF TABLES

Title **Page No.**

ABBREVIATIONS

AFS	Active Flutter Suppression
AIC	Aerodynamic Influence Coefficient
AOA	Angle of Attack
AR	Aspect Ratio
ATAG	Air Transport Action Group
ATI	Aerospace Technology Institute
CFD	Computational Fluid Dynamics
CO_2	Carbon Dioxide
DoF	Degree-of-Freedom
EFTA	European Free Trade Association
FEA	Finite Element Analysis
FOSMC	Fractional-Order Sliding Mode Control
FRF	Frequency Response Function
HALE	High-Altitude Long Endurance
IATA	International Air Transport Association
I& I	Immersion and Invariance
LCC	Low-Cost Carrier
LCO	Limit Cycle Oscillation
LE	Leading Edge
LQR	Linear Quadratic Regulator
MIMO	Multiple-Input Multiple-Output
PDE	Partial Differential Equation
PD	Proportional-Derivative
PID	Proportional-Integral-Derivative
RFA	Rational Fraction Approximation
RFP	Rational Fraction Polynomial
RHDoF	Root-Heave Degree-of-Freedom
RMS	Root Mean Square
SAF	Sustainable Aviation Fuel
SFC	Specific Fuel Consumption
SIMO	Single-Input Multiple-Output

SISO	Single-Input Single-Output
SMC	Sliding Mode Control
TE	Trailing Edge
WRBM	Wing Root Bending Moment
2DoF	Two Degree-of-Freedom
3DoF	Three Degree-of-Freedom

NOMENCLATURE

$\mathbf{A}$	Inertia Matrix
AR	Aspect Ratio
a_W	Lift Curve Slope
$\mathbf{B}$	Aerodynamic Damping Matrix
c	Chord Length
$\mathbf{C}$	Aerodynamic Stiffness Matrix for an aeroelastic system
C_D	Drag Coefficient
C_{D_i}	Induced Drag Coefficient
C_L	Lift Coefficient
C_{l_β}	Trailing Edge Control Surface Lift Coefficient
C_{l_γ}	Leading Edge Control Surface Lift Coefficient
C_M	Moment Coefficient
$C_{m_{\beta-eff}}, C_{m_{\gamma-eff}}$	Control Surface Effective Moment Derivatives
$\mathbf{D}$	Structural Damping Matrix
e	Elastic Axis Position Constant
$\mathbf{E}$	Structural Stiffness Matrix
EI	Flexural Rigidity
$\mathbf{f}$	Vector of Control Gains
$\mathbf{F}$	Matrix of Control Gains
$\mathbf{F_{nl}}$	Vector of Nonlinear Terms
f_n	Natural Frequency (Hz)
g	Acceleration due to Gravity
GJ	Torsional Rigidity
$\mathbf{g}$	Control Distribution Vector, Vector of Control Gains
$\mathbf{G}$	Control Distribution Matrix, Matrix of Control Gains
$\mathbf{h}$	Gust Force Distribution Vector
$\mathbf{H}$	Matrix of Measured Receptance
$\hat{\mathbf{H}}$	Matrix of Measured Closed Loop Receptance
K_d	Derivative Gain
K_p	Proportional Gain
m	Total Mass

$M_{\dot{\theta}}$	Oscillatory Aerodynamic Derivative
$\mathbf{q}$	State Vector of Assumed Modes Coordinates
$\mathbf{Q}_{Aero}$	Generalised Aerodynamic Force Vector
$\mathbf{Q}_{RFA}$	Rational Fraction Approximation in Modal Space
$\mathbf{R}$	Matrix of Receptance due to Controller Input
R_{AC}	Aircraft Range
s	Wing Span
SFC	Specific Fuel Capacity
t	Time
$\mathbf{T}$	Transform Matrix from Degrees of Freedom to Assumed Modes
$\mathbf{T}_{\boldsymbol{\Phi}}$	Transform Matrix from Assumed Modes to Linearised Coordintaes
U	Airspeed
$\mathbf{u}$	Vector of Control Inputs
v	Artificial Input
w_g	Gust Velocity
x_f	Position of Flexural Axis
$x_{h_{LE,TE}}$	Control Surface Hinge Axis
$\mathbf{y}$	Output Vector
y_h	Wing Span to Tip Hinge (Leading Edge)
y_t	Wing Tip Span (Leading Edge)
z	Root-Heave Displacement
β	Trailing Edge Surface Deflection
γ	Leading Edge Surface Deflection
ζ	Damping Ratio
θ	Torsion Angle
θ_t	Wing Tip Deflection Angle
Λ_f	Wing Tip Flare Angle
$\mathbf{\Lambda}_f$	Diagonal Matrix of Maximum Expected Velocities
λ_g	Gust Wavelength
$\mathbf{\Lambda}_g$	Diagonal Matrix of Maximum Expected Displacements
ξ	Bending Displacement
ρ	Air Density
$\boldsymbol{\Phi}$	State Vector of Linearised Coordinates
ω_n	Natural Frequency (rad/s)

Superscripts

$\dot{()}$	Differentiation with respect to time
$\tilde{()}$	State Space
$()'$	Transpose

Chapter 1

INTRODUCTION

1.1 Motivation

Since the historic flight by the Wright brothers in 1903, the aerospace industries have continuously expanded and modernized. Over the past century, significant advancements in aircraft design and flight operations have ushered in a transportation revolution, greatly enhancing the ability to transport people and goods. Among all transportation sectors, the aviation industry stands out for its rapid growth and is considered to have the fastest growth of any method of transport [11]. Prior to the COVID-19 pandemic, global aviation passenger numbers were projected to double by 2037 [12], leading to a surge in air traffic and consequently higher pollution levels. The number of scheduled passengers on commercial flights between 2009 and 2018 grew from 2.5 billion to 4.3 billion [13], and is predicted to increase to 10 billion by 2040 [14].

Carbon dioxide (CO_2) emissions from aircraft engines during operations represent the primary pollutant. From 1990 to 2016, CO_2 emissions from all flights departing from the European Union (EU28) and the European Free Trade Association (EFTA) increased significantly, rising from 88 to 171 million tonnes (+95%). Despite efforts to improve efficiency between 2005 and 2014, the gains were overshadowed by the growth in flight numbers, aircraft size, and distance travelled, resulting in a net increase in CO_2 emissions.

Projections suggest that future CO_2 emissions, based on both base traffic forecasts and advanced technology scenarios, are expected to continue rising [15]. This underscores the urgent need for the development of more efficient and sustainable aircraft to mitigate the environmental impact. To meet the increasing demands in air travel, there is a need to produce a considerable number of new aircraft, for example Airbus has announced the increase in A350 production from 6 to 12 per month by 2028 [16]. This is essential not only to expand the global aircraft fleet, but also to replace older planes that are no longer cost-effective to operate. However, despite these efforts, the aviation industry faces significant challenges in terms of its long-term sustainability. With increasing awareness of the irreversible consequences of climate change, there is mounting pressure on the industry to develop a new generation of aircraft that have a lesser impact on the environment. For example, the International Air Transport Association (IATA) has set ambitious goals to cut CO_2 emissions from aircraft by 50% compared to 2005 levels by 2050 [1], namely by introducing ultra-high aspect ratio winged aircraft by the late 2020s, and more advanced configurations being tested before 2035 (see Figure 1.1).

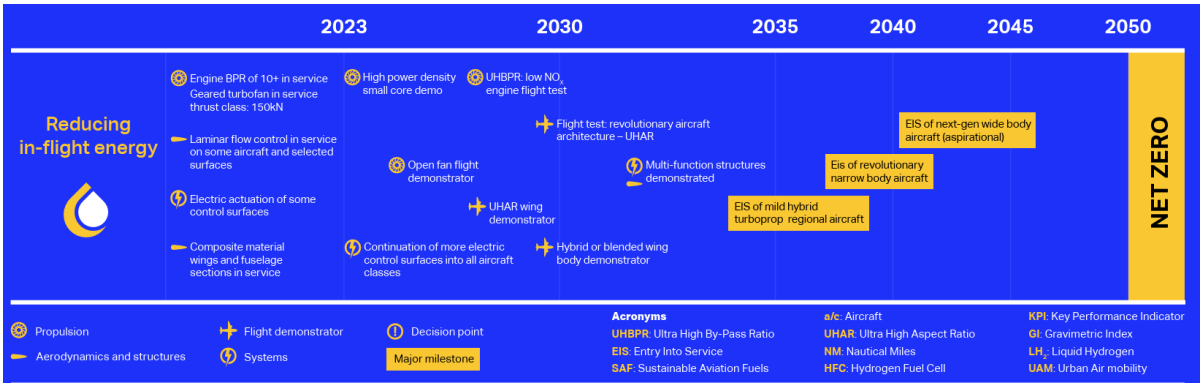

FIGURE 1.1: IATA Net Zero Roadmap for Aircraft Technology 2022. *(Adapted from [1])*

Similarly, the Aerospace Technology Institute (ATI) produced several road maps for zero carbon emission and ultra efficient aircraft technologies, with the aim of introducing folding wing tips, flutter suppression and load alleviation technologies in the 2020s, an advanced highly flexible wing in the 2030s, and targetting the use of dry wing technology required for hydrogen powered aircraft [2]. These road maps are shown in Figures 1.2 and 1.3.

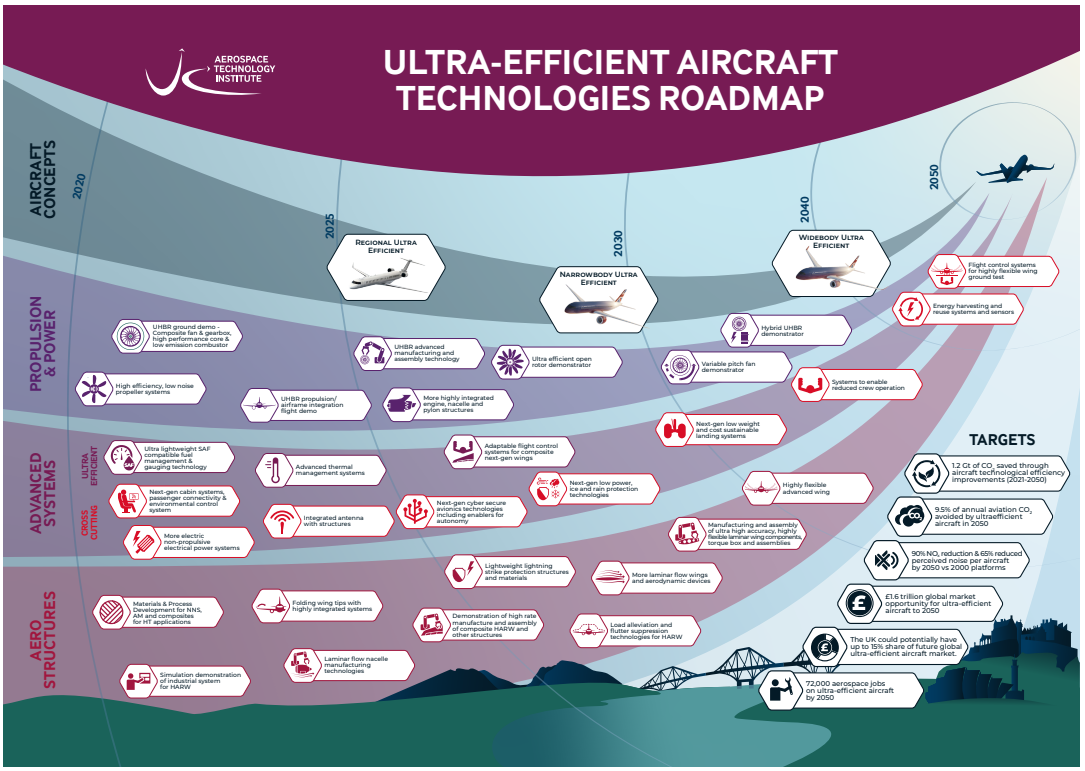

FIGURE 1.2: ATI Ultra-Efficient Aircraft Technologies Road Map. *(Adapted from [2])*

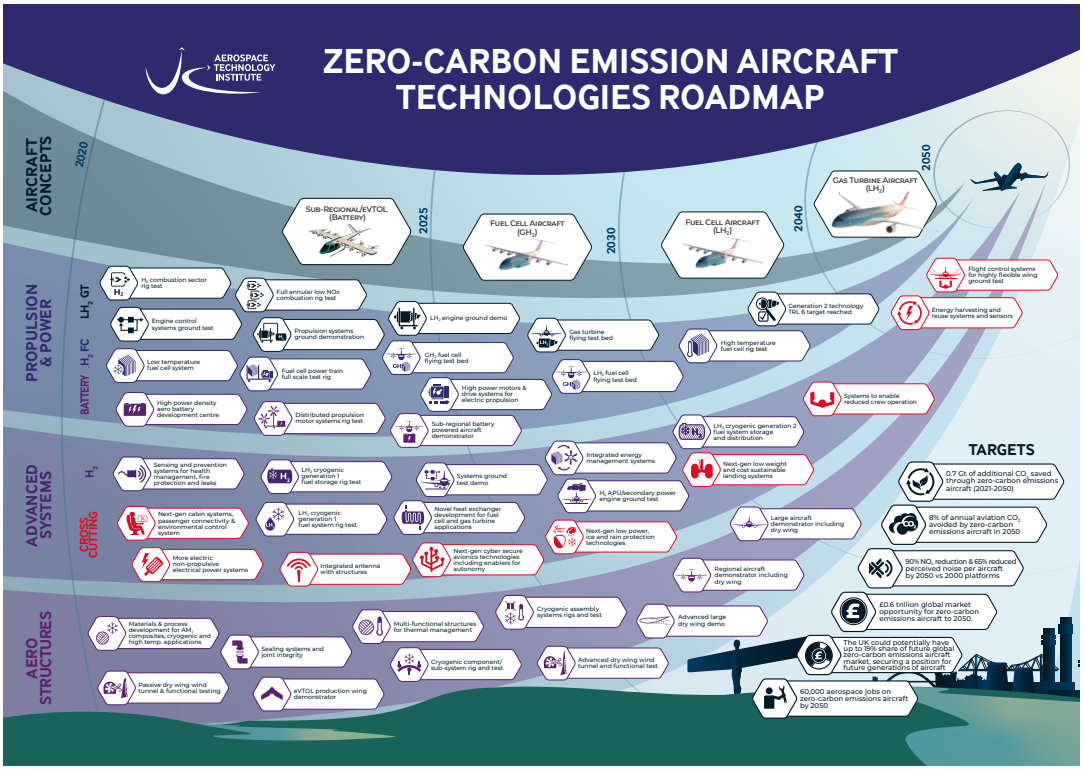

FIGURE 1.3: ATI Zero Carbon Emission Technologies Aircraft Technologies Road Map. *(Adapted from [2])*

The European Union has also established a clear plan for Climate Neutral Aviation by 2050 (Figure 1.4) through the Clean Aviation research project by introducing low-carbon alternatives before progressing to climate neutral options.

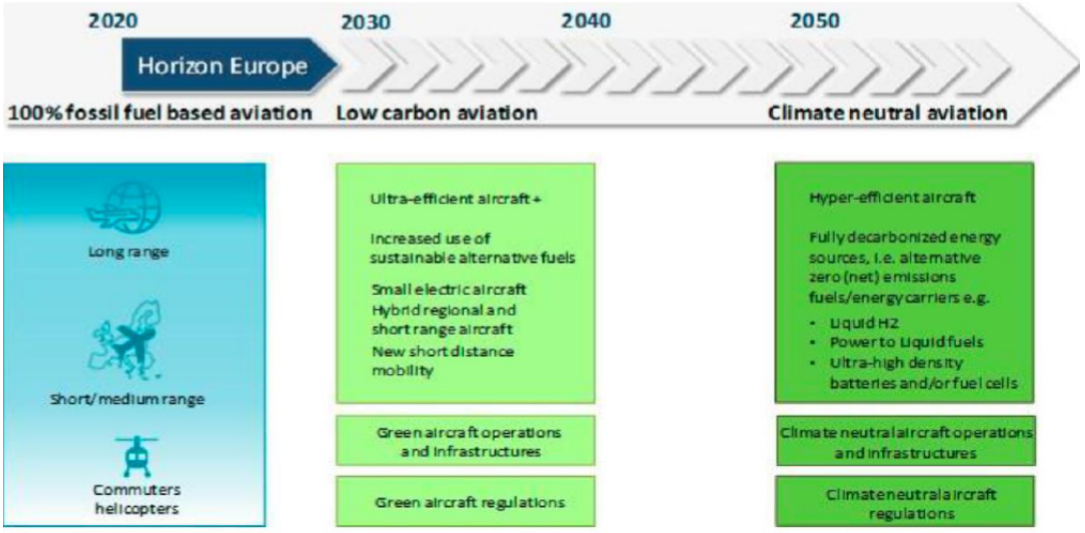

FIGURE 1.4: Clean Aviation Trajectory Towards Net Zero Aviation. *(Adapted from [3])*

Enhancing sustainability within the aviation sector presents a complex challenge. Firstly, it demands significant advancements in research and development across various engineering disciplines, a process that requires considerable financial investment and resource allocation. Secondly, even with the discovery of new technologies, stringent regulations can hinder their swift implementation into existing aircraft fleets, resulting in a considerable gap between cutting-edge innovations and practical adoption. Lastly, any improvements must offer economic advantages to airlines, especially considering the prevalent trend of low-cost carrier (LCC) models in the industry [17]. Airlines prioritise operational efficiency and cost reduction to remain competitive in this evolving landscape. The impact on the future aviation market is detailed in Figure 1.5 by the ATI [2], calculating the required reduction in carbon emissions by: lowering tailpipe emissions through more efficient aircraft designs and engines, minimising fuel consumption throughout the lifecycle with improved air traffic management, and offsetting remaining emissions by utilising sustainable aviation fuels (SAF) or hydrogen.

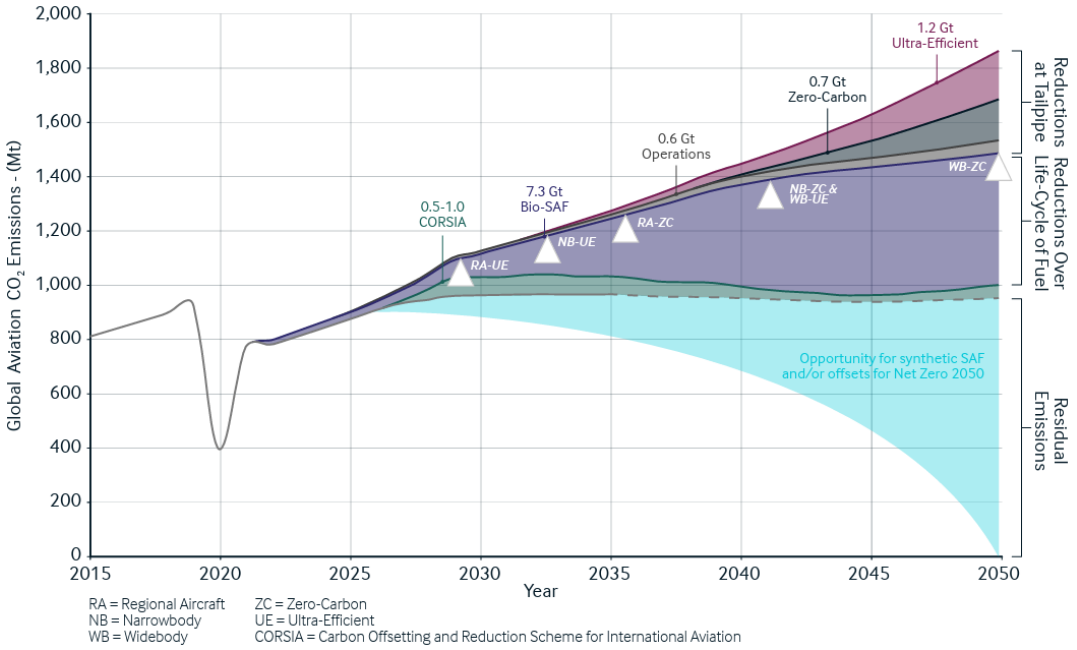

FIGURE 1.5: ATI Impact of Future Aviation Market on CO_2 Emissions. *(Adapted from [2])*

The Air Transport Action Group (ATAG) also outlined previous charts for achieving net zero using three different charts [4]. Figure 1.6 shows their three scenarios for achieving net zero: (a) by pushing for technology and operational changes, (b) an aggressive deployment of sustainable fuels, and (c) a perspective on aspirational and aggressive technology.

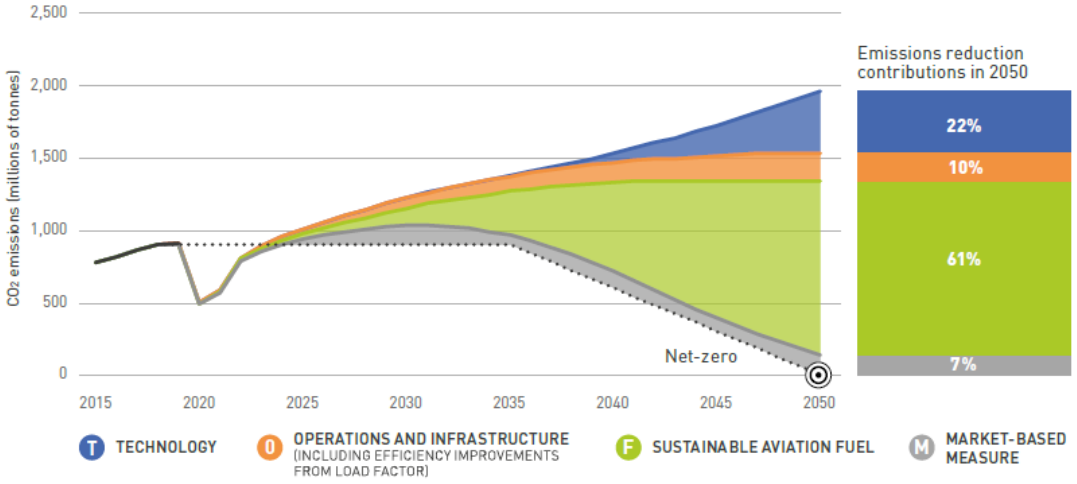

(a)

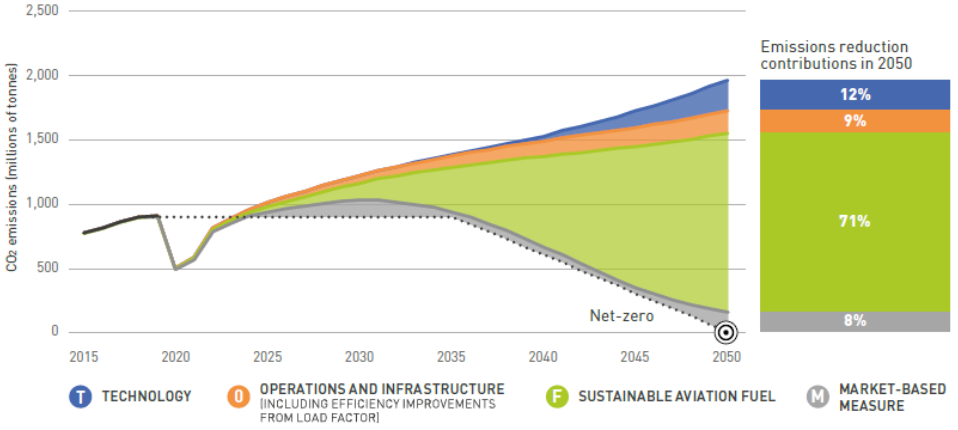

(b)

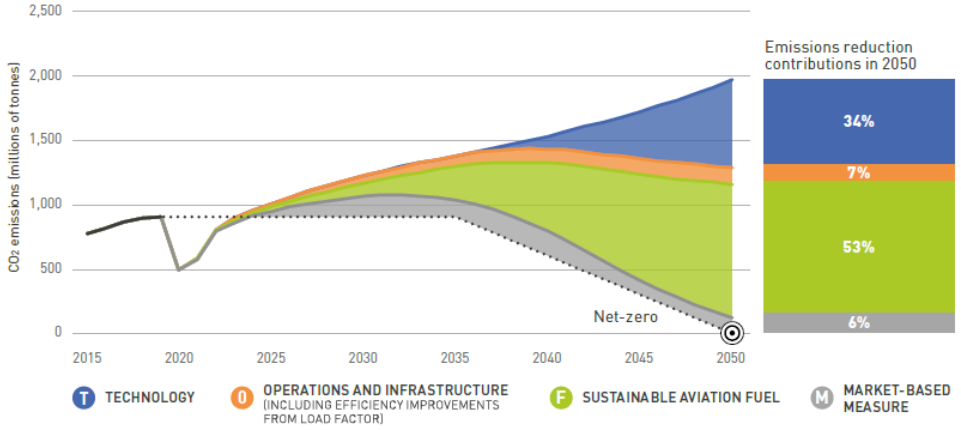

(c)

FIGURE 1.6: ATAG Goals and Change Drivers. *(Adapted from [4])*

The first scenario, shown in Figure 1.6a, aims to prioritise technology improvements, with the use of unconventional airframes and a transition towards hybrid or fully electric aircraft. The second scenario (Figure 1.6b) is based on current powerplant technology

and prioritises investment in sustainable fuels as opposed to hybrid/electric power. Finally, the third scenario (Figure 1.6c) provides multiple options for aircraft depending on their size, with fully electric for aircraft with up to 100 passengers, zero-emissions hydrogen aircraft for 100-200 seat aircraft, and hybrid powered aircraft for larger vessels [4].

The performance of an aircraft is expressed by the Breguet formula in terms of the aircraft's achievable range as a function of the engine, aerodynamic and structural design parameters as:

$$R_{AC} = \frac{V_f}{g} \frac{1}{SFC} \frac{C_L}{C_D} \ln \frac{W_i}{W_f} \tag{1.1}$$

where the flight speed is given as V_f, g is acceleration due to gravity, SFC is the specific fuel consumption which is the rate of fuel consumption divided by the power produced. The lift and drag coefficients are represented by C_L and C_D respectively and the aircraft initial and final weights are given by W_i and W_f. Given this relation, aircraft designers should consider a few things to improve the aircraft range. Maximising cruise speed and engine efficiency are clearly important, especially as greater engine efficiency allows for a slower fuel burn rate. Improving the aerodynamic efficiency can be achieved by maximising the lift/drag ratio, and the structural weight can be minimised to reduce the final aircraft weight.

Reduction in structural weight and improvements to the aerodynamics must be made in tandem to achieve significant improvements to the overall aircraft performance. Around 30%-40% of the overall drag is lift-induced. This can be estimated for a planar wing with elliptical lift distribution as:

$$C_{D_i} = \frac{C_L^2}{\pi e AR}, \quad \text{where} \quad AR = \frac{b^2}{S} \tag{1.2}$$

where e is the wing span efficiency, b is the wing span, S is the surface area and the aspect ratio is AR. It is clear that a larger aspect ratio reduces the induced drag, and the easiest way to achieve this is to increase the wing span. The AR of commercial aircraft has been steadily increasing since the 1960s, as shown in Figure 1.7:

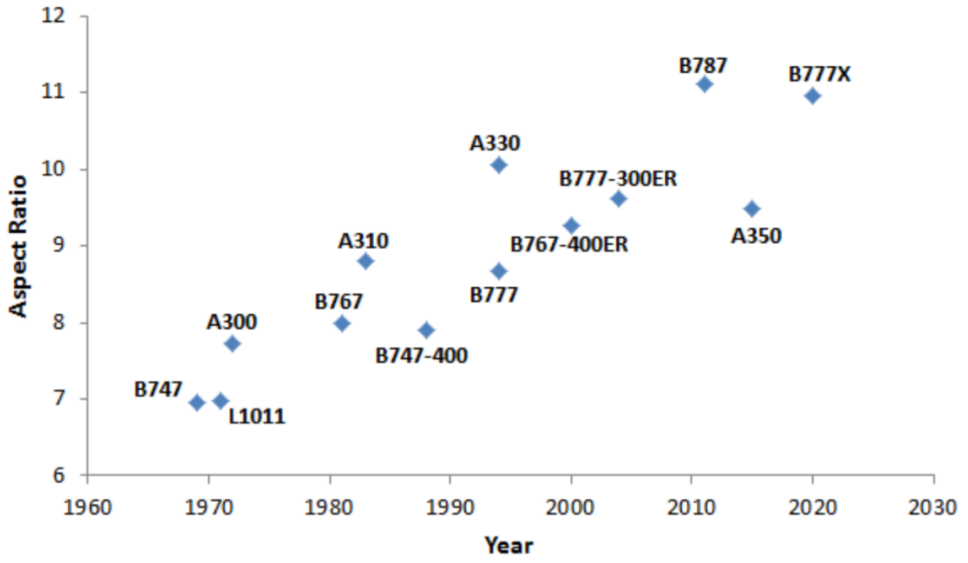

FIGURE 1.7: Aircraft Aspect Ratios Since 1960s. *(Adapted from [5])*

With an increased wing span comes more supporting structure which of course increases the weight, or if the weight is to be kept the same then the structure will have a lower stiffness which results in increased bending. This highlights the importance of Load Loops in preliminary aircraft design [7, 18, 19]. Accurate aerodynamic load estimations must be made as these loads can lead to large deformations that can be catastrophic. The load estimations then lead to material selection, which in turn defines the structural weight, which is a limiting factor to range as shown in Eq. 1.1, thus the aim is to reduce the structural weight of the aircraft. By simply reducing the structural weight by removing material from the support structure, which results in reduced stiffness of an aircraft's aerodynamic surfaces, this can introduce risks to the structure in the form of larger gust induced oscillations and loads and a reduction in flutter speed. This thesis aims to investigate the use of active control to alleviate the wing response and loads due to gusts and also extend the flutter speed of the wing. By reducing the loads on the wing in this way, this leads to a reduction in the required stiffness of the wing, which in turn results in reducing the structural material and reducing weight. Additionally, an increased AR would create aircraft that cannot fit into airport gates, so part of this thesis investigates applying active control via a folding wing tip to address this.

1.2 Linear and Nonlinear Aircraft Aeroelasticity and Loads

Aeroelasticity is defined by Wright and Cooper as the subject that describes the interaction of aerodynamic, inertia and elastic forces for a flexible structure and the phenomena that can result [7]. When control surfaces are involved, with their own aerodynamic forces contributing to the system, this is known as aeroservoelasticity. The definition of aeroelasticity comes from the Collar Triangle, which describes the relationship between these forces and their contribution to flutter, buffeting, and combined loading amongst other phenomena [6].

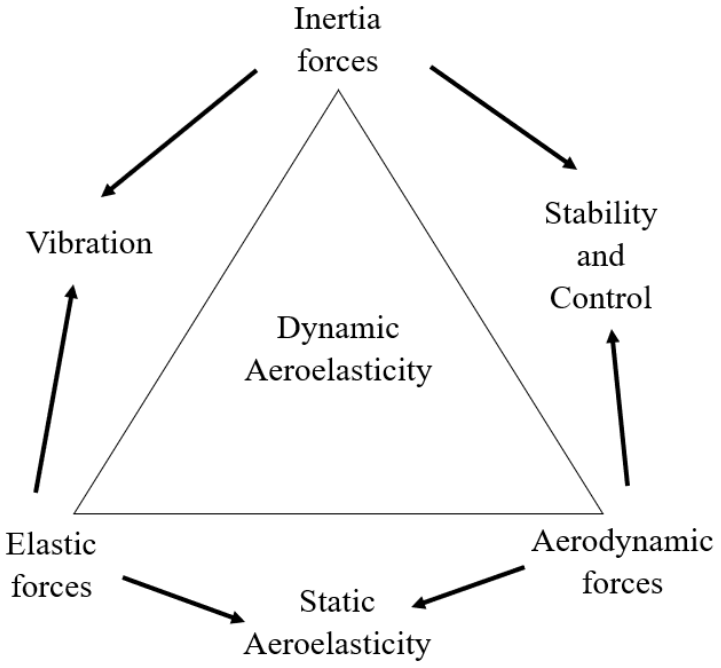

FIGURE 1.8: Collar's Aeroelastic Triangle. *(Adapted from [6])*

Bisplinghoff et al. define dynamic and static aeroelastic phenomena, depending on which forces are interacting to cause the phenomena [20, 21]. The forces described by Collar and their resulting phenomena have a significant and potentially disastrous effect on aerodynamic surfaces. This literature review will attempt to summarise the key aspects and phenomena that are relevant to the work shown in this thesis.

1.2.1 Aeroelastic Modelling

Many methods have been developed and used for modelling aeroelastic systems. Each has their benefits depending on what a researcher hopes to achieve with their model. One thing remains constant with any modelling approach, which is that aeroelastic systems are comprised of the structure, the aerodynamics, and any actuators if present. Some classical models are the 2DoF (Two Degree-of-Freedom) aerofoil, the cantilever flexible wing, and the full aircraft model. Each has their advantages and limits, and may require different computational methods to model accurately [22].

1.2.1.1 Structural Modelling

First of all, the structural part of the aeroelastic system should be modelled. This relates the displacement of the structure at one or more points to any externally applied forces or moments. This relationship can be derived from basic principles by independently modelling each component of the structure. This process involves formulating a partial differential equation (PDE) for each part, such as a beam or plate, and then integrating them into a single, combined model. However, this method is impractical because of its complexity. Instead, structural dynamics are typically approximated using discretisation techniques via mathematical models using algebraic models, differential equation models, state-space models, or transfer function models. These techniques simplify the system by breaking it down into a limited number of masses, each associated with a degree of freedom. These degrees of freedom are then interconnected using a series of spring and damping elements.

For a linear system, the form of the general discretised structural state-space model is:

$$\mathbf{M}\ddot{\mathbf{q}} + \mathbf{C}\dot{\mathbf{q}} + \mathbf{K}\mathbf{q} = \mathbf{f} \tag{1.3}$$

where $\mathbf{M}$ is the mass matrix, $\mathbf{C}$ is the damping matrix, and $\mathbf{K}$ is the stiffness matrix. The Degrees-of-Freedom (DoF) vector $\mathbf{q}$ is associated to the discrete masses, and $\mathbf{f}$ is the vector of generalised forces. The main considerations for structural modelling are to determine the necessary number of degrees of freedom and to find suitable mass, stiffness and damping matrices.

The number of DoFs selected for an aeroelastic model should be a balance between model accuracy and computation time. A common aeroelastic model is the pitch-plunge aerofoil, which is only a 2DoF system unless control surfaces are also modelled. The

advantage of this kind of model is the simplicity of testing the effectiveness of control on responses to external forces, or flutter prevention, amongst other things. However, in reality aerodynamic surfaces are flexible and not rigid. For an aircraft wing structure, a flexible cantilever wing is more advantageous if accuracy is the primary concern. For a flexible wing model, there are infinite mode shapes that can be considered, which of course requires additional computational effort with each mode shape included in the model. Model reduction is necessary for flexible wing models so that the structural modes in the frequency range of interest are considered to increase the model accuracy, without requiring more computational power than necessary. If higher modes are sufficiently spaced and damped for a given frequency range, they can be omitted from the reduced order model. Even if high degrees of accuracy are not required, it has always been common to approximate an aircraft wing using a binary aeroelastic model, where generally the first bending and torsion modes of the wing are modelled. This allows for simple eigenvalue analyses thanks to the low order of the model, as well as being easily constructed using Newton's laws. One key downside to the binary aeroelastic model is that the two modes must be the modes that couple to cause flutter. Other modes could occur with natural frequencies in the region of the coupling flutter modes which would have to be neglected for the binary flutter model, reducing the model accuracy.

For simple systems, the mass, stiffness and damping matrices are directly obtainable through Lagrangian mechanics [7]. The Lagrangian Function can be used to derive the equations of motion of a system:

$$L = T - V \tag{1.4}$$

where T is the kinetic energy of the system and V is the potential energy of the system. The Euler-Lagrange equation is then used to derive the equations of motion:

$$\frac{d}{dt}\left(\frac{\partial L}{\partial \dot{q}_i}\right) - \left(\frac{\partial L}{\partial q_i}\right) = 0 \tag{1.5}$$

where q_i are the generalised coordinates of the system, $\dot{q}_i$ are the generalised velocities, and $\frac{\partial L}{\partial q_i}$ are the generalised forces. The resulting derivation gives the necessary structural and inertial terms for a second order equation of motion:

$$\mathbf{A}\ddot{\mathbf{q}} + \mathbf{D}\dot{\mathbf{q}} + \mathbf{E}\mathbf{q} = \mathbf{f} \tag{1.6}$$

where $\mathbf{A}$ is the inertial matrix, $\mathbf{D}$ is the structural damping matrix, and $\mathbf{E}$ is the structural stiffness matrix. The Lagrangian Function is also used to find the aerodynamic damping and stiffness matrices, $\mathbf{B}$ and $\mathbf{C}$ respectively.

Computational methods are available for structural modelling, such as Multibody Dynamics (MBD), Machine Learning models, and Finite Element Analysis (FEA). MBD is used to model interconnected rigid or flexible bodies, but is less suited for highly flexible bodies [23]. Machine learning methods are best used for regression models and structural health monitoring. FEA is commonly used in the modern day due to the advancement of computation and the complexity of modern aircraft. Due to the high fidelity and detail of FEA, it is the industry standard [24]. No matter the method used, it is necessary to obtain accurate parameters for mass, stiffness and damping from manufacturing data sheets, historical information, and tests. In FEA, discretisation is the process of dividing a continuous domain (such as a structure, fluid, or thermal field) into a finite number of smaller, simpler elements. This transformation allows the complex physical problem to be approximated using numerical methods. Material properties must be included in the FEA model, such as Young's Modulus, Poisson's Ratio, and Shear Modulus. The effects on the material density, elasticity and plasticity due to temperature should also be modelled for temperatures that are likely to be experienced by the physical model. Boundary conditions are essential in FEA as they define how a structure interacts with its environment, ensuring a well-posed mathematical model. They restrict degrees of freedom and influence how the system responds to loads.

1.2.1.2 Aerodynamic Modelling

Following the structural model creation, it is then possible to model the aerodynamics, with the aim of coupling the aerodynamics and structural model by relating the force on the structure to the displacements, velocities and accelerations at the reduced DoFs. There are a range of aerodynamic models that can be aeroelastic and aeroservoelastic applications, with the key differences lying in the assumptions made on the flow. The simplest aerodynamic model is the steady flow model, where aerodynamic forces are assumed to be time-invariant, i.e. the aerodynamic forces are a function of the instantaneous positions for each DoF. This is simple to implement, but significantly lacks detail and accuracy when compared to real life. The neglecting of unsteady aerodynamics means that the accuracy of the aerodynamic force and moment estimates on the system are insufficient for most applications.

In order to overcome these limitations, one could use a quasi-steady model. Again, the aerodynamics forces are not written directly as a function of time, but do now include instantaneous displacements and velocities of the aeroelastic system being modelled. It is assumed that there are no frequency dependent effects, but that the behaviour of the aeroelastic system at any time is equivalent to the same system with instantaneous

displacements and velocities [7]. In the quasi-steady model, a term representing the unsteady aerodynamics appears in the aerodynamic damping matrix **B**. The example is given below for a binary model:

$$\mathbf{B} = \begin{bmatrix} \frac{s}{10} c a_w & 0 \\ \frac{-c^2 s}{8} e a_w & \frac{-c^3 s}{24} M_{\dot{\theta}} \end{bmatrix} \tag{1.7}$$

The term $M_{\dot{\theta}}$ is an Oscillatory Aerodynamic Derivative for the moment about the elastic axis, and is used to create a simplified unsteady aerodynamic model. It is defined as:

$$M_{\dot{\theta}} = \frac{\partial C_M}{\partial \left(\dot{\theta}_c / U \right)} \tag{1.8}$$

The use of an unsteady aerodynamic model is necessary for analysis of the system in flutter and gust response as the behaviour of the model during dynamic motion is required.

Finally, there are unsteady aerodynamic models. For models with a large degree of unsteadiness, it is best to use models that fully interpret the unsteadiness, such as the Theordorsen model [25]. In the Theodorsen model, the approach is to use a potential flow to model unsteady aerodynamic forces acting on a thin, symmetric aerofoil, which was originally developed for binary aeroelastic system. Despite capturing the unsteady aerodynamic effects, the Theodorsen method is still limited by restrictive assumptions. Firstly, inviscid flow is assumed and therefore boundary layers are neglected. Next, it is known that flow is rotational, however the Theodorsen model assumes an irrotational flow. Finally, it is assumed that density variations can be ignored as the flow is deemed to be incompressible. If frequency domain analysis is being applied to the system model, it is important to include the effects of reduced frequency dependent aerodynamics in the frequency region of interest [7]. For 3D strip theory, Aerodynamic Influence Coefficient (AIC) functions are needed, and can be found through experimental measurements at a set of reduced frequencies, or approximated in model space via Rational Fraction Approximation (RFA), as detailed by Eversman and Tewari [26]. The AIC matrix relates the lift on each wing element to the dynamic pressure and the angle of incidence, and is detailed by Wright and Cooper [7]. First, the classical aeroelastic model is considered but with the aerodynamic terms moved to the right hand side of the equation.

$$\mathbf{A}\ddot{\mathbf{q}} + \mathbf{D}\dot{\mathbf{q}} + \mathbf{E}\mathbf{q} = \mathbf{Q}_{Aero}(t) \tag{1.9}$$

where $\mathbf{Q}_{Aero}$ is the generalised aerodynamic force vector, $\mathbf{A}$ is the inertial matrix, $\mathbf{D}$ is the structural damping matrix, and $\mathbf{E}$ is the structural stiffness matrix. Equation 1.6 above is represented in the Laplace domain as

$$\left(\mathbf{A}s^2 + \mathbf{D}s + \mathbf{E}\right)\mathbf{q}(s) = \frac{\rho U^2}{2}\mathbf{Q}_{RFA}(s)\mathbf{q}(s) \tag{1.10}$$

where $\mathbf{Q}_{RFA}(s)$ is the RFA to the AIC expressed in modal space. The air density is given as ρ, with speed U. Then, $\mathbf{Q}_{RFA}(s)$ is expanded via a RFA in terms of their Laplace variable $s = j\omega$ (where $j = \sqrt{-1}$), to give

$$\mathbf{Q}_{RFA}(s) = \mathbf{A}_0 + \mathbf{A}_1\frac{sb}{U} + \mathbf{A}_2\left(\frac{sb}{U}\right)^2 + \frac{U}{b}\sum_{n=1}^{N}\frac{\mathbf{A}_{n+2}}{(s + \frac{U}{b}p_n)} \tag{1.11}$$

where $\mathbf{A}_i,\ i = 0, 1, \ldots N+2$ are unknown matrices to be found, b is the semi-span of the wing and p_n are the N_L poles (lag parameters). The RFA approach allows for nonlinear effects to be examined in the state-space time domain using a 3D aerodynamic panel approach, however nonlinearities do not have to be present for this method to work. An example of reduced order aerodynamic modelling is given by Tang et al. [27], with results accurately predicting the dynamic behaviour of the wing.

As in structural modelling, the use of modern technology allows aerodynamic modelling to be carried out using computational methodology such as Computation Fluid Dynamics (CFD), with the aim of extracting aerodynamic coefficients to determine loading on the structure. A significant drawback of CFD is from a control viewpoint, as while the model physics are better understood, model reduction is often necessary for control implementation. If a simpler model is used from the beginning, then it eliminates the additional required step of model reduction, however the level of accuracy and usability is a balance that the user needs to determine for their own model. An example of CFD is Vio et al. coupled with FEA for the structural analysis to model a three-dimensional wing [28].

Wright and Cooper give an overview of the hierarchy of aerodynamic modelling [7]. A range of methods are available depending on the required accuracy and application of the method. First of all, simple formulas can be used for a low accuracy representation of the aerodynamics during the preliminary design phase. Air-worthiness regulations require the use of either 2D unsteady strip theory or 3D unsteady panel methods for the analysis of gusts and flutter, with the panel method being more widely used as it is more accurate. However, both of these methods do not accurately represent transonic behaviour. Euler

equations can be used in the transonic and supersonic regimes as the method captures compressibility effects for an inviscid flow, but is limited due to the neglection of viscous effects, boundary layer phenomena, and heat transfer. Various categories of Navier-Stokes equations can also be used, namely Reynolds-Averaged Navier-Stokes (RANS), Large Eddy Simulation (LES), and Direct Numerical Simulation (DNS). Each has their benefits and all are used in high fidelity simulations in design and research, but while highly accurate there is also a very high computational cost.

1.2.1.3 Actuator Modelling

Modelling actuators can introduce additional complexity into the numerical model. The purpose of an actuator model is relating the desired control input dynamics to those of the observed control input. An actuator is generally comprised of many electrical and mechanical subsystems, and control surfaces often have hydraulics and mechanical connections, each with their own dynamics to be modelled. The simplest way to model control surfaces, as is carried out in the work throughout this thesis, is to only model them as force inputs to the system as this does not require additionally measured states. Of course, in reality there is a delay between demanding control and the control surface movement, however if the control surface has a sufficiently quick response to a demanded input, these errors can be small and therefore do not warrant the added detail of an actuator model. An example of such a case is the model used by Ko et al.[29], where the controller reaches the desired input within 0.1s. Alternatively, Edwards et al. model the control surface dynamics as no control is applied to the system, and their focus is on the effects of unsteady flow on all degrees of freedom of the system [30].

1.2.1.4 Model Coupling

All three models must be combined to complete the full aeroservoelastic numerical model. Commonly, this is done by including each sub-model into state-space form which then couple for a single state-space model. The details of state-space modelling are discussed in Chapter 2.

1.2.2 Flutter

Flutter is a phenomenon that can occur in linear systems, where the coupling of two or more modes can cause violent unstable oscillation due to their associated aerodynamic forces, which leads to structural failure. The flutter boundary is the group of points in

the flight envelope at which the aeroelastic system is neutrally stable [31]. Should the system encounter a disturbance in this region of airspeed and air density (or altitude), it would result in a simple harmonic oscillation. The danger of flutter is that it is self-excited, making it an unstable oscillation as the structure acquires more energy from the airflow than it can dissipate [32]. Because of this, large structural deflections can occur, which could lead to fatigue or even complete structural failure.

Wright and Cooper detail the differences between Soft and Hard flutter [7]. As shown in Figure 1.9, Soft flutter occurs when the critical damping ratio trend is approaching the critical speed with a low gradient. The flutter develops gradually, and increases in severity over time, which allows time for corrective actions before catastrophic failure. In contrast, Hard flutter occurs following a sudden drop in damping ratio, and results in a sudden and violent flutter occurance which can quickly result in structural failure.

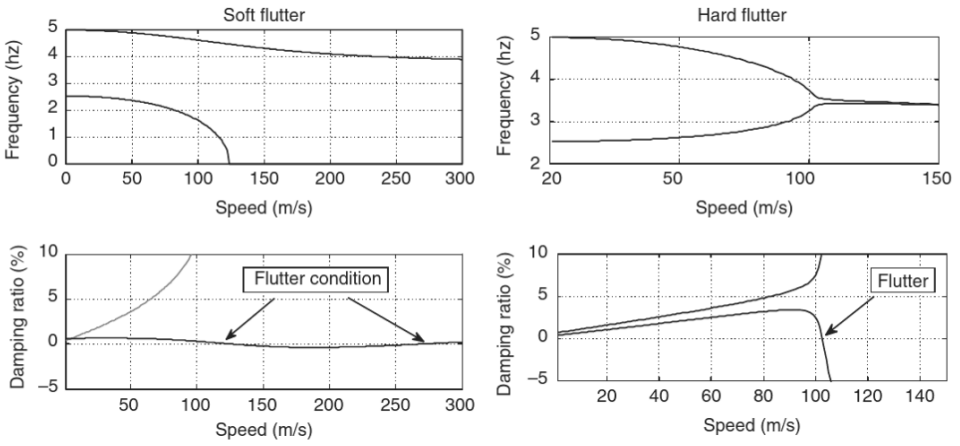

FIGURE 1.9: Illustration of Soft and Hard Flutter. *(Adapted from [7])*

For a binary flutter model, flutter can be easily predicted using simple eigenvalue analysis and is characterised by the convergence of the natural frequencies of the modes associated with the two degrees of freedom, and the negative value of one of the damping ratios. With this is mind, it is simple to design a controller for flutter suppression. Details of Active Flutter Suppression (AFS) can be found in Chapter 4. Flutter can occur in linear systems, however in nonlinear systems Limit Cycle Oscillations (LCO) can occur beyond the linear flutter speed. The main difference between flutter and LCO is that flutter is an unbounded, growing instability that will lead to failure, whereas LCO will grow up to a point and be bound due to the nonlinear stiffness. An example of this can be seen in Figure 1.10:

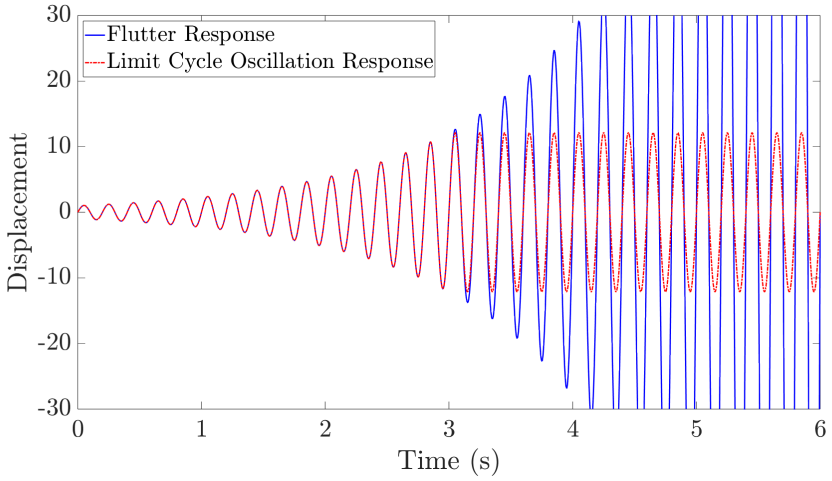

FIGURE 1.10: Example of Flutter vs LCO Responses

Dowell et al. investigate LCO for aerofoils with stiffness nonlinearities, high aspect ratio wings, and nonlinear structural damping [33]. It was detailed how a benign nonlinearity will produce a stable LCO when the flutter speed is exceeded, which will generally increase in amplitude as the airspeed is increased above the flutter boundary. Tang and Dowell provide a detailed account of experimental models for flutter and LCO measurement [34]. The same authors investigated the gust response for a delta wing with control surface freeplay [35, 36].

LCO behaviour can be further defined by subcritical or supercritical LCO [7, 8, 33, 37], as shown by Figure 1.11. A Supercritical LCO has stable limit cycles and occurs when the present nonlinearity has a hardening effect. These oscillations will only occur above the linear flutter speed and tend to grow as the airspeed is increased, and this behaviour is reversible in that the amplitude of the oscillations will decrease along the same path should the airspeed be decreased. In contrast, a Subcritical LCO occurs when the present nonlinearities are softening, which results in a limit cycle that can be unstable (denoted by the dotted line in Figure 1.11), when occurring below the linear flutter speed, or will jump to the large amplitude (but stable) oscillations above the flutter speed.

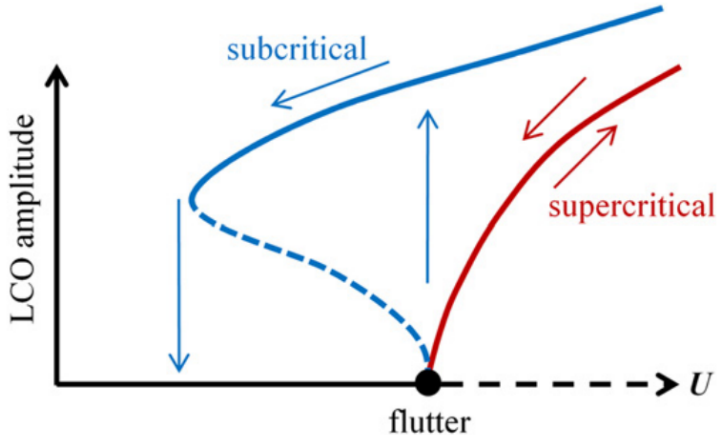

FIGURE 1.11: Illustration of Subcritical and Supercritical LCO. *(Adapted from [8])*

Dimitriadis and Cooper investigate the effects of control surface nonlinearities in an aeroservoelastic system on flutter and LCO [38]. It was determined that LCO behaviour is more stable than flutter, however high-amplitude LCO can negatively affect structural rigidity and even low-amplitude LCO will increase fatigue on the mechanical parts of the control system.

1.2.3 Nonlinearity

The study of nonlinearities in aeroelasticity has been ongoing for decades [39–41]. Nonlinearities can occur structurally through nonlinear stiffness or damping profiles, or aerodynamically due to changes in local flow conditions [37]. Breitbach details the physical sources of structural nonlinearities in aircraft structures [42]. They state that structural nonlinearities can be generally subdivided into distributed and concentrated nonlinearities. Distributed nonlinearities are continuously effective throughout the whole structure by the structure's deformation, whereas concentrated nonlinearities act locally, for example in a control mechanism linkage or connecting parts. Worden and Tomlinson give details of common nonlinearities [43], such as cubic stiffness where the stiffness either hardens or softens with a cubic polynomial profile, piecewise linear stiffness where multiple linear regions exist with sharp crossover points between the regions, and nonlinear damping, the most common of which is a quadratic polynomial damping.

Dowell et al. define nonlinearities as either static or dynamic [33, 44–46], and a linear system must be both statically and dynamically linear in its response (wholly linear), or one that has a statically linear response and a linear dynamic response. For a wholly linear structure, the deformation to the static or dynamic forces is linearly proportional to the forces applied. If a structure is statically nonlinear, but dynamically linear, the static

deformations are sufficiently large that the static response is no longer proportionally to the applied static force. Some common nonlinearities are explored in these works, such as control surface freeplay, nonlinear effects due to tension from large amounts of bending, and aerodynamic nonlinearities occurring due to shock at airspeeds that are transonic or higher.

An example of aerodynamic nonlinearity study is Volterra theory, which is used by Silva to numerically and experimentally analyse nonlinear aeroelastic phenomena using flutter data [47]. An oscillating turntable experimental setup is used to measure unsteady pressure and loads on both rigid and flexible wing models to identify flow phenomena associated with flutter, LCO, shock, and other nonlinear unsteady flow dynamics. Geometric nonlinearity can occur due to a large structural deformation, which then alters the local aerodynamic flow conditions, for example a high AR wing undergoing large bending deflections [48], as is present on HALE aircraft. This change in aerodynamic flow can lead to a change in load distribution on the structure. Additionally, the large deflections can cause a hardening effect on the wing, leading to an increase in natural frequency in the bending mode, which could lead to mode coupling and instability. Dynamic Stall can occur due to nonlinearities in Unsteady Flow [37, 49]. Nonlinear pressure distribution can occur during shock, leading to a nonlinear relationship between the resulting aerodynamic forces and the structure [33, 37].

When attempting to understand nonlinear behaviour, it is important to understand equilibrium points, their stability, and the stability of periodic oscillations about these points [50]. Khalil describes a number of nonlinear behaviours that cannot be modelled using linear methods. For example, Limit Cycle Oscillation (LCO) where a nonlinear system will oscillate at a fixed amplitude and frequency, irrespective of the initial state [51]. O'Neil et al. investigated the behaviour of a rigid wing with smooth nonlinear stiffness by setting a freestream velocity and initial displacements [52, 53]. Flutter was determined by monitoring the frequency and damping of the measured motion as well as observation of the system response.

Thompson and Strganac analyse the dynamics of store-induced LCO by using the Method of Variation of Parameters to analyse the equations of motion [54, 55]. While this method does not directly draw conclusions, it was found that it is possible to identify the system parameters that can be used to determine if the system is near resonance.

Connor et al. numerically analyse the LCO occurrence for a 3DoF aerofoil system with piecewise nonlinearity in the control surface [56, 57]. They detail the importance of identifying the switching point between linear regions and accurately achieve this via Henon

integration [58]. Similarly, Al-Mashhadani et al. numerically and experimentally explore the LCO occurrence due to freeplay nonlinearity in the tab hinge [59]. Theodorsen theory was used for modelling unsteady airflow, with good accuracy found between the numerical model and experiments.

For other nonlinear systems, Chaos can be observed [60]. During Chaos, a nonlinear system can exhibit more complicated steady state behaviour that is not equilibrium, periodic, or almost periodic oscillation, and in fact seems to exhibit random oscillation despite the motion being determined by the system. The effects of chaos and bifurcation are detailed by Lee et al. [37], who detailed the effects various structural nonlinearities such as cubic nonlinearity, freeplay and hysteresis for a pitch-plunge aerofoil model. The assumption of structural linearity is often made for simplicity and so standard computational methods can be used for determining flutter characteristics of aeroelastic models. However, aircraft structures are often nonlinear and affect wing motion and flutter characteristics. Many aircraft have experienced flutter-induced LCO due to control surface freeplay, where there is a region of control surface deflection where there is no stiffness and the control surface is able to move freely. This effect was investigated by Verstraelen et al. [61], where equivalent linearisation is used to determine the conditions of LCO to predict their amplitudes and frequencies.

1.2.4 Gust Loads

In aircraft design, it is imperative to understand the effects of gusts and the loads they induce within the system, particularly with the industry change towards high aspect ratio wings. Continuously loading and unloading on a wing structure, due to gusts or other means, can slowly lead to fatigue, particularly for wings with lower stiffness that experience large deformations. Additionally, if the flight speed is sufficiently high and close to flutter, an external perturbation such as gusts could cause instability in the wing system. If the effects of gust loads, and in particular the worst cases, are understood then preparations can be made to combat these effects in the structure of the wing or through active control. Airworthiness regulations discuss the importance of 1-cosine gusts and random turbulence [62, 63], this thesis concentrates on 1-cosine gusts to reflect the desires of the regulations.

A number of 1-cosine gusts can be used to determine a critical 'tuned discrete gust' [64], which aid in determining limit loads in aircraft design [65]. Haddad Khodaparast et al. explore the prediction of worst case loads produced by a 1-cosine gust for models that encompass the entire flight envelope and different fuel loads using relatively fewer test points [66]. This work uses an assumed modes, free-free aircraft model with five

"interesting quantities," such as load factors and shear stresses. It is demonstrated that accurate predictions can be found of the worst case gusts with far fewer gust response calculations than in conventional approaches. Haddad Khodaparast and Cooper then investigate reducing the computational effort required for determining the worst case gust loads for an aircraft [67]. For both a simple wing and full-scale aircraft models, they were able to reduce the amount of computation needed for gust responses by 56%, and by 50% for modal reanalysis. The ability to quickly calculate and predict worst case loads is beneficial not only for the aircraft design process, but also during flight as quick gust load prediction can help with control implementation to reduce the loads if an incoming gust can be detected. A number of 1-cosine gusts can be used to determine a critical 'tuned discrete gust' [64], which aid in determining limit loads in aircraft design [65].

Scott et al. investigated Gust Load Alleviation using a semispan flying wing SensorCraft [68, 69]. In this work, the aeroelastic model was first implemented with a fixed root to assess the effects of gusts and alleviate gust loads using active control. The system was then implemented with a two degree of freedom (2DoF) sidewall mount, allowing for pitch and heave motion. The advantage of a sidewall mount such as this is that if actuation is used, the additional degrees of freedom can be used to model aircraft dynamics in a hybrid testing setup.

Gust loads must be included in the preliminary aircraft design process so that loads such as bending moments, shear forces and torques along the entire wing can be accounted for in the structural design. Larger loads generally require larger, stiffer structures to prevent excessive deformation or failure. With increased structure comes increased weight, reducing the efficiency of the aircraft. This introduces the possibility of using control methods to actively reduce loads caused by gust encounters, which also reduces the required supporting structure. Thus, weight can be reduced, resulting in more efficient aircraft.

1.3 Active Control Aims and Methods

After the observation and understanding of aeroelastic phenomena, the next natural step is to attempt to control these phenomena. This section will discuss various means of controlling both linear and nonlinear systems. While the control methods discussed

in this section are applicable to dynamic systems in general, the focus of this section will be placed on controlling aeroelastic systems.

1.3.1 Linear Control

Many linear control methods exist with their own advantages to be selected at the discretion of a controller designer. One example of a linear control method is a Linear Quadratic Regulator (LQR). LQR can be applied when the system dynamics are described by a set of linear differential equations and is a form of optimal control. For the linear system in question, the cost of controlling the system is described using a quadratic function. A simple and common cost function for an LQR controller is as follows:

$$J = \int_0^\infty \left(\mathbf{x}^T\mathbf{Q}\mathbf{x} + \mathbf{u}^T\mathbf{R}\mathbf{u}\right)\, dt \tag{1.12}$$

where J is the cost, $\mathbf{x}$ is the vector of states we wish to control, $\mathbf{u}$ is the vector of control inputs, and $\mathbf{Q}$ and $\mathbf{R}$ are weighting matrices to balance the performance and effort of the controller. This is applicable for any given amount of states and inputs. The benefit of LQR is that the weighting factors can be tuned to produce optimal control gains, where the control aim is achieved for minimal cost of actuation power. Brown et al. implement a full-state feedback controller, then tuned using LQR, to control a 3DoF (Three Degree-of-Freedom) aerofoil system before LCO onset [70], however it was observed to be ineffective after the onset of LCO. Bueno et al. propose the use of a LQR controller for active flutter suppression of a 3DoF aerofoil [71], with the aim of increasing the damping of the system to eliminate flutter.

A common linear control method is Pole Placement, where the closed loop poles are changed according to the desired natural frequencies and damping ratios of the system [72]. This has conventionally been carried out passively using a state-space approach, using the mass, damping and stiffness matrices of the system [73, 74]. Ram and Mottershead pioneered the Receptance Method [75], where the receptance of the system to the controller is measured and can then be used for Pole Placement. This method only accounts for a single actuator in the system, so could introduce a limit to changing the poles depending on the system and how much control authority is available. Later work by the same authors introduces the capability of using multiple inputs. The basis of the Receptance Method is as follows:

$$\mathbf{y_x} = \mathbf{R}(s).\beta \tag{1.13}$$

$$\mathbf{R}(s) = \mathbf{H}(s).\mathbf{b} = \begin{bmatrix} \frac{N_1(s)}{D(s)} \\ \frac{N_2(s)}{D(s)} \end{bmatrix} \tag{1.14}$$

where $\mathbf{R}(s)$ is a $n \times 1$ vector, $\mathbf{y_x}$ is the output vector of the system and $\mathbf{H}(s)$ is the receptance matrix, which may be be determined in practice from the matrix of measured receptances $\mathbf{H}(i\omega)$ at the coordinates of the sensors used. In the general case, $\mathbf{H}(s)$ is defined as:

$$\mathbf{H}(s) = \left[\mathbf{M}s^2 + \mathbf{C}s + \mathbf{K}\right]^{-1} \tag{1.15}$$

where $\mathbf{M}$, $\mathbf{C}$ and $\mathbf{K}$ are the mass, damping and stiffness matrices of the system. A key attribute of the Receptance Method is that it is a purely experimental method and does not require a numerical model of the system, whereas other control methods described in this Chapter do have this requirement.

Mottershead et al. also demonstrated that the Receptance Method can not only assign closed loop poles to the system, but also assign the sensitivities of the poles [76]. This approach can be applied for vibration absorption to avoid resonance and is desirable from the view of robust dynamical performance.

The Receptance Method has been adapted to allow for Partial Pole Placement by Ghandchi et al. [77, 78], where the aim is to change only the troublesome poles of the system while leaving more stable poles untouched. It is shown experimentally that the chosen poles are assigned to predetermined values without affecting the position of other poles of interest.

Further adaptation was then made to the Receptance Method by Ram and Mottershead for multiple inputs to be used for active control [79]. The benefit of this is that shifting the poles of a system, particularly the natural frequencies, requires a large amount of control authority, so having multiple actuators available allows for greater manipulation of the closed loop poles.

Singh et al. implement the Receptance Method on an aeroelastic system [80, 81]. The aim of this work was to numerically implement the Receptance Method to a wing with multiple control surfaces in order to extend the flutter boundary of the system. Similar work is carried out numerically and experimentally to the MODFLEX wing designed at the University of Liverpool [82]. Mokrani et al. aimed to assign the natural frequencies and damping ratios of the first two vibration modes in order to increase the flutter margin of the wing [83], generating an increase in the flutter speed of 22%. This work was then

built on by Adamson et al. who used an iterative approach to extend the flutter speed [84–86]. The Receptance Method is applied in this work over a range of airspeeds, where the closed loop system for the first airspeed (i.e. the first iteration) becomes the open loop system for the next, higher airspeed, where receptance measurements are taken again and the process repeats. This process finds the globally optimum pole placement using the Differential Evolution genetic algorithm presented by Storn and Price [87].

There are several advantages of using the Receptance Method for an aeroelastic system. First of all, it captures the true interaction between the wing structure and the aerodynamic loads. The direct receptance measurement from experiments also avoids approximation errors due to reduced order modelling as there is no model required. While most work regarding the Receptance Method was for linear systems, it is also applicable to a class of nonlinear systems that can be characterised using describing functions, as applied by Ghandchi et al. [88], where an iterative Sherman-Morrison receptance formula is used to account for changes in the open loop system as a result of feedback control. Only numerical results are given in this work, but it demonstrated that the complexity of applying control to nonlinear systems is generally increased when compared to controlling linear systems.

1.3.2 Nonlinear Control

Many forms of nonlinear control exist, such as Feedback Linearisation, Sliding Mode Control, and various Adaptive Control methods [89]. Perruquetti and Barbot provide an extensive account of Sliding Mode Control (SMC) [90]. It is designed to force the system to "slide" along a predetermined surface, called the "sliding surface" or "sliding manifold," in the state space. This control strategy is particularly valued for its ability to handle system uncertainties and external disturbances. The sliding surface is a predefined condition that the system's state variables should satisfy. When the system's state reaches this surface, it "slides" along it towards the desired equilibrium point. The sliding surface is usually designed based on the system's dynamics and control objectives. A discontinuous control law is generally used so that the system in its initial state is first driven towards the sliding surface, then along the surface to the equilibrium point. While SMC is robust against uncertainties and disturbances, a significant practical challenge in SMC is chattering, which is a high-frequency oscillation caused by the rapid switching of the control input near the sliding surface and can lead to fatigue in mechanical systems.

Cao et al. use fractional-order sliding mode control (FOSMC) based on LQR and input/output Feedback Linearisation [91]. The FOSMC is design to reject system uncertainties and reduce the magnitude of control chattering. Lyapunov stability theory is

then used to prove the convergence of the closed loop system. The simulations presented suggest excellent performance from the proposed control scheme.

For many linear and nonlinear control systems, state feedback is essential for implementing control to a system. Recursive control design allows for backstepping, where a stable subsystem is known and controlled, then the designer can "back out" new controllers to progressively stabilise each outer subsystem [92]. The process ends when the final external control is reached. This approach is applied in Feedback Linearisation, where a set of stable "zero dynamics" are known and then feedback from the system is used to control the unstable dynamics.

Extensive work into Feedback Linearisation has been carried out, where in order to apply Pole Placement, a nonlinear system is first linearised through feedback. Ko et al. carried out feedback linearisation experimentally on a pitch-plunge aerofoil system using one and two control surfaces [29]. A polynomial hardening nonlinearity is present in the pitch degree of freedom. It was found that a single control surface used in pitch primary partial feedback linearisation would obtain a locally stable response. With the addition of a second control surface, global stability was achieved as full feedback linearisation was carried out now that the number of control surfaces matches the number of modes.

The same authors extended this research using the same system but implementing plunge primary control [93]. It was found that the response was again locally asymptotically stable, with the exception of certain locations of the elastic axis and some airspeeds where the feedback strategy exhibits bifurcation phenomena due to one or more unstable equilibrium points, depending on the combination of elastic axis position and airspeed tested. Global stability was then again achieved as a second control surface is introduced into the system.

Block and Strganac continued work on the same system [94]. In this work, an unsteady aerodynamic model is developed to approximate the flutter velocity and frequency of the pitch-plunge aerofoil system. Coulomb damping and hardening of the pitch stiffness are implemented into the model and the control is tested numerically and experimentally with results proving the nonlinear system can be controlled, with flutter suppression occurring within 2 seconds.

Da Ronch et al. investigate active control for flutter and LCO for a pitch-plunge aerofoil model in wind tunnel experiments [95]. An unsteady aerodynamic model is used with good correlation between simulation and partial feedback linearisation experiments. For

comparison, a linear controller based on pole placement is also applied for the nonlinear system and experiences LCO above the linear flutter speed. The partial feedback linearisation method outperforms the linear control strategy.

Many dynamic systems have uncertain parameters, whether they are constant or varying, as inevitably there will be errors in the measured and modelled descriptions of nonlinearities. Adaptive control is the approach used to account for such uncertain parameters in the system. The process of Backstepping can be used for adaptive control if a system consists of uncertain constant parameters if they are applied linearly in the system equations. The aim is to achieve boundedness of the closed loop states, as well as a convergence of the tracking error to zero [92]. The dynamic part of the controller is designed as a parameter update law, where the static part of the system is continuously adapted with new estimates of the uncertain parameters. Sastry and Isidori outline an adaptive approach to robustify the control of a nonlinear system via state feedback [96].

The method of adaptive control is implemented into Partial Feedback Linearisation by Ko et al. [97–99], where a continuous nonlinear torsional spring is introduced to a pitch-plunge aerofoil without knowing the coefficients of the nonlinear stiffness polynomial. An initial estimation of the stiffness parameters is set, then the controller continuously estimates these parameters during the system response. While the estimation of the parameters does not converge to the true values, the closed loop system still performs well for the numerical results presented. Platanatis and Strganac build on this work with the use of two control surfaces [100]. LQR is used as the linear control theory and it is found that LCO suppression is achieved after roughly 5 seconds. While predicted responses compared well with the closed loop experiments, the performance was limited by the hardware design for higher airspeeds due to the larger aerodynamic loads.

Jiffri et al. implement Adaptive Feedback Linearisation to a flexible wing with cubic hardening stiffness nonlinearity in an engine pylon [101, 102]. A MIMO closed loop system is used for pole placement, with three inputs and three outputs so that the entire system is linearised and no zero dynamics exist. The results in this work show that stability is achieved as LCO is eliminated. Jiffri et al. also considered feedback linearisation for the control for nonlinearities in pitch-plunge aerofoils [103, 104].

Li et al. use adaptive control for a pitch-plunge aerofoil with two control surfaces with polynomial nonlinear stiffness and damping in the pitch degree of freedom [105]. The results indicate that the designed control laws are effective in suppressing flutter, and accounting for damping uncertainty positively impacts flutter control.

While the works discussed so far in this section have looked at linearisation of systems with smooth nonlinearities, Mannarino et al. applied an adaptive control strategy to counteract the effects of freeplay and friction in a nonlinear servo actuator [106]. Additionally, there are aerodynamic nonlinearities present due to the transonic airspeeds used. The controller was developed in two stages, with the first being implementing an Immersion and Invariance (I&I) controller to stabilize flutter beyond the stability boundary, and the second being designed using Nonlinearity Inversion to counteract any occurring LCO. Li et al. also investigated the control of an aeroelastic system with control surface freeplay [107], with a cubic stiffness nonlinearity applied in the pitch DoF. Simulation results show that the effect of the freeplay is a slight increase in flutter speed of the closed loop system.

1.4 Aircraft Innovation

As discussed earlier in the motivation for this work, an industry move towards very high aspect ratio wings is occurring to extend the range, and therefore efficiency, of aircraft, for example High-Altitude Long Endurance (HALE) aircraft [108]. The increased wingspan required or proposed would not adhere to the maximum wing span restrictions at the gates of commercial airports, as well as introducing increased stresses along the wing structure. This has prompted the development of folding wing tips, which have been used on many aircraft before [109]. A recent example of folding wing tip technology being implemented is the Boeing 777X (shown in Figure 1.12), which resulted in an increase of wingspan by 7 m [9].

FIGURE 1.12: Boeing 777X, *Directly Adapted from [9]*

The introduction of a hinged wing by Wilson et al. resulted in a 60% reduction of stresses due to gust loads [110]. They also found that a free hinged wing tip could induce flutter, but this could be stabilised through including a tip mass, the choice of hinge location, and the hinge flare angle, with the latter having the least impact on wing root bending moment.

Balatti et al. considered the effects of an aeroelastic hinged wing tip on worst-case gust loads [111]. Their work investigated the effects of hinge position, orientation and spring stiffness to evaluate hinged wing tip performance for gust load alleviation. Similarly, Castrichini et al. investigated the effects of a folding wing tip for load alleviation by considering a numerical aeroelastic model for a typical commercial jet aircraft, evaluating the effects of stiffness, damping, wingtip mass, and hinge orientation on the static load, gust load and also the flutter behaviour of the wing [112]. Castrichini and others further investigated the effects of folding wing-tips by introducing a nonlinear spring device [113, 114]. Healey et al. considered the dynamic effects of incorporating fuel tanks into the hinged wing tip section [115]. Carrillo et al. introduced a hinge mechanism, allowing the hinge to be locked or released when desired, showing excellent effect on load alleviation in wind tunnel tests when the hinge release is timed [116]. While this work shows an improvement to the standard passive wing tip, there is still an attractive possibility of further gains by using an active wing tip setup, which should therefore be investigated.

Sanghi et al. computationally compare the effects of conventional leading-edge and trailing-edge control surfaces to a free folding wing tips [117]. Gu et al. demonstrated that using a folding wing tip can achieve a 40% reduction in wing weight, leading to a 9% improvement in aircraft range [118]. Mastracci et al. consider the effects of local geometric nonlinearities caused by folding wing tips on the dynamic stability of the wing [119]. Gu et al. investigated the transient response of flared folding wing tips for the case where a locked hinge is released, and for encounters with discrete lateral gusts [120]. Cheung et al. tested a flared folding wing-tip device in a series of steady and dynamic wind tunnel tests [121]. This research was further developed by adding an aerodynamic surface into the wing tip that could control folding action [122]. The series of tests they performed showed that actuating this small surface could improve on already promising results produced by the folding wing tip alone. One drawback of this research is the additional weight added to the wing tip from the motor powering the control surface, and the control surface itself is very small. Also, only open loop control is utilised in the form of a continuous sinusoidal input. This can be limiting in performance compared to closed loop control designed to mitigate wing vibration or root loads. Sanghi et al. computationally investigated flared folding wing tips for high aspect ratio wings during roll maneuvers in a transonic flight regime [123]. Delavenne et al. propose the use of an active wing tip in numerical models, analysing how changing the wing tip fold angle in flight affects drag, loads, and flutter during the flight domain [124]. However, this work does not use any active control law to alleviate gust loads or suppress flutter. Similarly, Sanghi and Cesnik compare the use of passive and active folding wing tips for gust load alleviation and roll maneuvers [125]. The active element in this work again only controls the locked position of the wing tip, and does not implement an active control law to reduce the wing root bending moment.

Another move suggested by the industry is to use cooled hydrogen for power, reducing the effect on climate change from aircraft from an estimated 50 to 90% [126]. From an aeroelasticity and control viewpoint, the benefit of hydrogen power is that no fuel will be stored in the wings, meaning there is a reduction in weight which could be used to implement actuation.

1.5 Summary

This literature review has presented the global aim for the reduction of CO_2 emissions and the push towards clean aviation. Part of this aim is the ATI providing roadmaps for the implementation of flutter suppression and gust load alleviation technologies [2]. This thesis investigates some previously untested solutions for gust load alleviation and flutter extension to address this aim.

First of all, this thesis implements the Receptance Method [75, 79] for use of both gust load alleviation and flutter speed extension of a flexible cantilever wing. This strategy has previously been used on a pitch-plunge aerofoil for flutter speed extension [85, 86], which this thesis builds on by using a flexible wing, which is a more true to life model.

The presence and importance of nonlinearities has also been discussed [33, 37, 44]. This thesis investigates the use of Feedback Linearisation for gust response alleviation of a flexible wing, again this was previously only implemented on a pitch-plunge aerofoil [29, 93, 97, 98].

Finally, there has been a push for high AR wings, which has introduced the discussion of using free folding wing tips for gust load alleviation [110, 113, 121]. While much work has been carried out to investigate passive folding wing tips, active wing tips have only been investigated numerically and without an active control law to target the reduction of wing loads during gusts. This is a significant research gap that has been addressed in this work. This thesis investigates the use of actuating the wing tip with a motor, creating an active folding wing tip for gust load alleviation via PD control.

1.6 Thesis Outline

The work in this thesis deals with various applications of active control, for gust response alleviation and flutter speed extension, in linear and nonlinear systems, and a folding wing tip is also considered for gust load alleviation.

Chapter (1) provides motivation for this work, as well as the general background for aeroelasticity and active control methods. The effects and dangers of gusts and flutter

are discussed. The remainder of the chapter provides the main body of the thesis and demonstrates the novel findings of the work presented.

Chapter (2) provides a detailed explanation of the experimental equipment used and how it is implemented in the work. The various experimental models used for wind tunnel testing are described, as are the corresponding numerical models. Details of the design study carried out for the production of the MODFLEX 2.0 wing are given.

Chapter (3) describes how the Receptance Method is used to implement Pole Placement on a flexible wing for gust response alleviation. The various changes in the Receptance Method are discussed, so that Full or Partial Pole Placement can be implemented on the system using one or both of the control surfaces available on the MODFLEX wing model. Both 1-cosine and harmonic gusts are used to perturb the system numerically and experimentally. (Based on [127, 128])

Chapter (4) focuses on the problem of flutter speed extension. Receptance Method is once again used for Pole Placement in an iterative scheme to extend the flutter speed of a flexible wing system. Gain optimisation is implemented via a genetic algorithm to maximise the effectiveness of the control surface. A study is carried out to evaluate the values of certain parameters in the controller design to find a maximum closed loop flutter speed for the system.

Chapter (5) introduces a Root-Heave Degree of Freedom (RHDoF) to the MODFLEX 2.0 wing so that nonlinearity can be introduced to the system. Pole placement is applied via Feedback Linearisation in order to control and mitigate unstable vibration after the system experiences external perturbation due to a 1-cosine gust. Both SISO and MIMO control are considered (Based on [127, 128])

Chapter (6) considers the implementation of actuation for a folding wing tip. Proportional-Derivative (PD) control is implemented to control the first bending mode of the wing in order to reduce the bending moment at the wing root in the presence of 1-cosine and harmonic gusts. The active tip is compared to a passive tip and fixed tip. (Based on [129–131])

Chapter (7) gives the conclusions of the work carried out in this thesis with suggestions for future studies.

1.7 Original Contributions

Original contributions from this PhD thesis are:

- The use of the the Receptance Method to alleviate gust responses of a flexible wing setup [127, 128].
- Applied a gain scheduling technique using the the Receptance Method to extend the flutter speed of a flexible wing, building on previous literature where a pitch-plunge aerofoil was used. Demonstrated a drawback of the the Receptance Method where if receptance data is unclear due to the combined motion of coupling modes, control cannot be effectively applied using the method.
- Derivation of a root-heave degree of freedom system with lump mass and heave stiffness for a flexible wing, and implemented hardening nonlinearity and nonlinear control via Feedback Linearisation [127, 128].
- Successfully implemented an active hinged wing tip to alleviate wing root bending moments in the presence of gusts using PD control, where the controlling action was proportional to the displacement and velocity of the wing's bending[130–132].

1.7.1 Publications Resulting from This Work

The following is the research outputs of the work performed as part of this thesis in terms of journal publications and conference presentations:

Journal Publication

- **J.D. Ellis**, D. Balatti, H. Haddad Khodaparast, S. Jiffri, & M.I. Friswell, Active Hinged Wing Tip Control for Reducing Wing Root Bending Moment. *AIAA Journal of Aircraft* [131].

Conference Proceedings

- S. Jiffri, **J.D. Ellis**, H. Haddad Khodaparast, & M.I. Friswell, Experimental Active Gust Load Alleviation via an Actuated Wingtip. *AIAA SciTech 2025 Forum*, Orlando (USA) [132]
- **J.D. Ellis**, D. Balatti, H. Haddad Khodaparast, S. Jiffri, & M.I. Friswell (2024). Reduction of Root Loads due to Gusts via Active Hinged Wing Tip Control. *Internation Conference on Noise and Vibration Engineering (ISMA)*, Leuven (Belgium) [130]
- **J.D. Ellis**, D. Balatti, H. Haddad Khodaparast, S. Jiffri, M.I. Friswell, & S. Fichera (2023). Multiple-Input, Multiple-Output Linear and Nonlinear Active Control of a Flexible Wing. *AIAA SciTech 2023 Forum*, Washington D.C. (USA) [128]
- D. Balatti, **J.D. Ellis**, S. Jiffri, H. Haddad Khodaparast, & M.I. Friswell (2023).Active hinged wingtip for gust load alleviation and manoeuvres. *AIAA SciTech 2023 Forum*, Washington D.C. (USA) [129]
- **J.D. Ellis**, S. Jiffri, M.I. Friswell, & S. Fichera (2022). Active Control of a Flexible Wing in the Presence of Gusts and Nonlinearity. *International Forum on Aeroelasticity and Structural Dynamics (IFASD)*, Madrid (Spain) [127]

Conference Presentations

- **J.D. Ellis**, D. Balatti, H. Haddad Khodaparast, S. Jiffri, & M.I. Friswell (2024). Reducing Root Loads due to Gusts Using an Active Hinged Wing Tip. *Airbus DiPaRT Symposium*, 28-29 February 2024, Bristol.

Chapter 2

EXPERIMENTAL SETUPS AND NUMERICAL MODELS

2.1 Introduction

This Chapter will explain in detail all numerical and experimental models used for this work. There are three experimental setups, each requiring a numerical model. Two distinct wing model approaches are used, the first being a traditional wing with leading and trailing edge control surfaces used to change the wing camber for control, the second using a flared folding wing tip. A variety of experiments have been carried out in this work, requiring different test setups. This Chapter will describe each setup in detail. Three cantilever flexible wings have been used in the low-speed, closed return circuit wind tunnel facility at Swansea University (shown in Figure 2.1). The wind tunnel facility designed by AeroTech is capable of airspeeds up to and including 50 m/s. The test section is 1 m in height and 1.5 m in width, with a length of 2.5 m. A gust generator has been designed and installed in the wind tunnel [133], and has been used for much of the work presented. It is used for both 1-Cosine gust profiles and Harmonic gust profiles. The 1-Cosine profile meets airworthiness regulations for gust testing [65, 134], however the gust length is shortened to account for the small test section. Harmonic gusts are used to represent turbulence, as turbulence is measured in the frequency domain and therefore a sinusoidal profile is used for excitation.

FIGURE 2.1: AEROTECH Low-Speed Closed Return Wind Tunnel at Swansea University

Some experiments in this work require the measurement of loads at the wing root, which are obtained using an external balance containing a six-axis load cell, shown in Figure 2.2. The load cell has a temperature range of -17.78 to 51.67°C, with all tests being conducted at a wind tunnel operating temperature between 10 and 20°C depending on the season. The load capacity is 4448 N force and 678 Nm moment, far exceeding any measurements expected from wind tunnel tests.

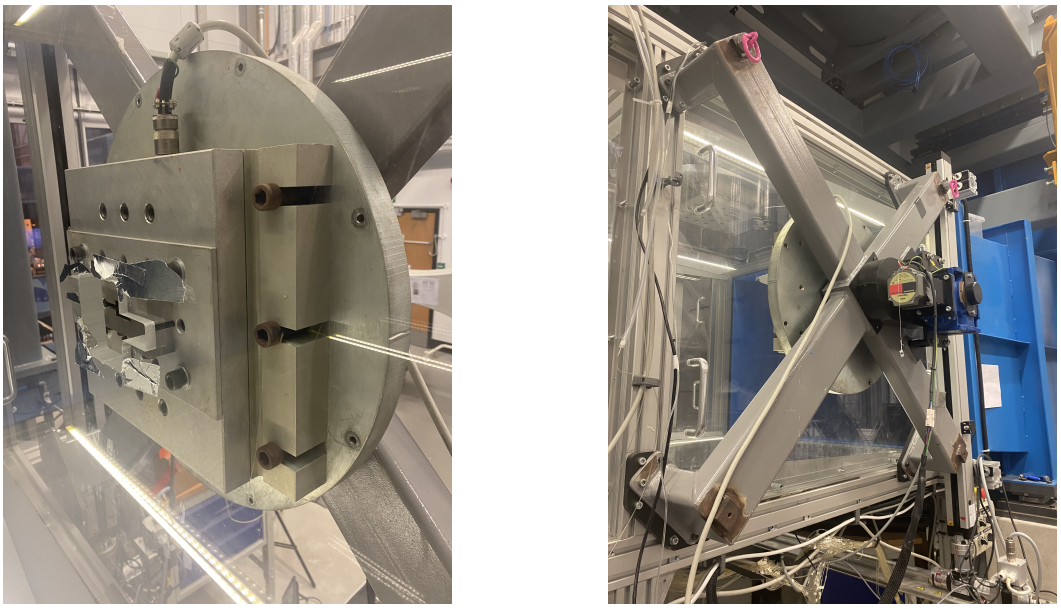

(a) (b)

FIGURE 2.2: Six-Axis Load Cell at Swansea University Wind Tunnel

Any displacement measurements are obtained using Keyence LK-G502 laser displacement sensors (Figure 2.3). The measurement range is -500 to 500 mm so that all wing motion is captured accurately. The laser precision is 0.01 mm, which is more than sufficient for the tests shown in this work.

FIGURE 2.3: Keyence LK-G502 Laser Displacement Sensor

Additionally, the laser sensors are used for calculating angles, whether it is a torsion angle θ or wing tip fold angle θ_t the method is the same and the setup is shown in Figure 2.4.

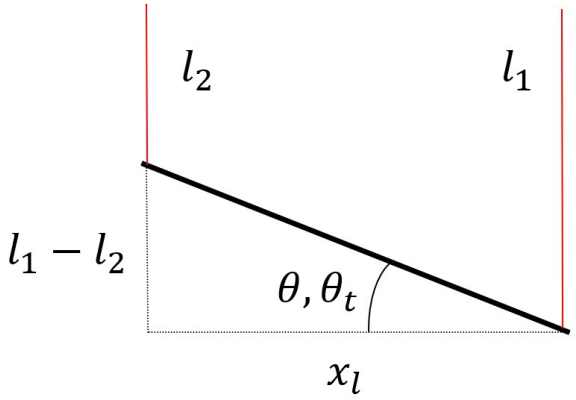

FIGURE 2.4: Laser Sensor Setup for Angle Calculation

The laser sensor readings are given by l_1 and l_2, the distance along the wing between the laser points is x_l. The deflection angle is calculated using the following equation:

$$\theta, \theta_t = \tan^{-1}\left(\frac{l_1 - l_2}{x_l}\right) \tag{2.1}$$

This expression assumes a flat plate, which is acceptable for the folding wing tip shown in this work. However, there is curvature to the aerofoil which introduces errors into this expression. The laser sensors were placed in a way where there was no significant change in curvature when the aerofoil is pitched up or down. This was tested by hand by twisting the wing and measuring the angle with a digital level, then comparing with the measured readings. The error for a deflection of 10° was 0.2°, which is a 2% error, so it was determined that the setup was acceptable and any excitation to the wing, (control surface or gust) would be tuned to ensure the torsion angle did not exceed 10°. The calibration setup is that used by Balatti [10].

Laser sensor readings and motor encoder readings are recorded, and control is applied, using the dSPACE MicroLabBox RTI1202 shown in Figure 2.5. The top panel variant used has 32 BNC analog inputs and 16 BNC analog outputs, as well as two Sub-D 50 I/O connectors which have been utilised in this work. The partnering software, ControlDesk, uses Simulink models as the digital part of the control loop and can record any desired signals within the Simulink model.

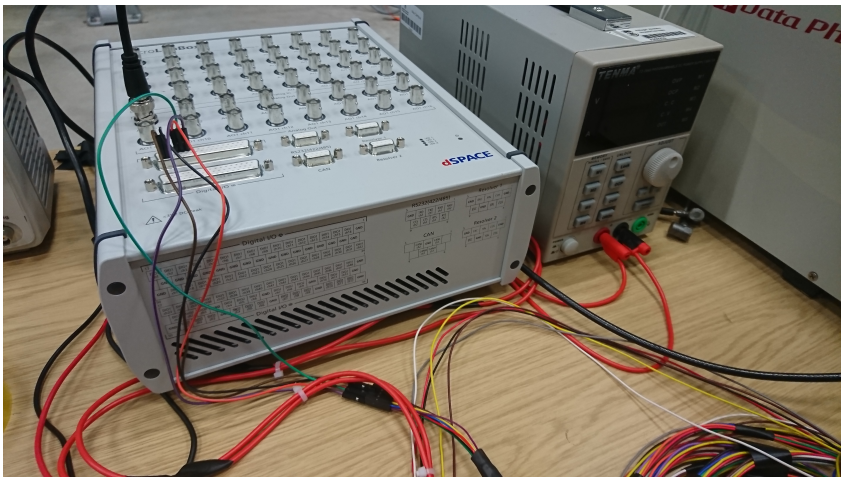

FIGURE 2.5: dSPACE MicroLabBox RTI1202

Originally, a 1 kHz sample rate was used but there was an aliased frequency present in the region of 1 - 10 kHz, which was found to be 5 kHz after conducting a FFT on the laser signal, as shown in Figure 2.6.

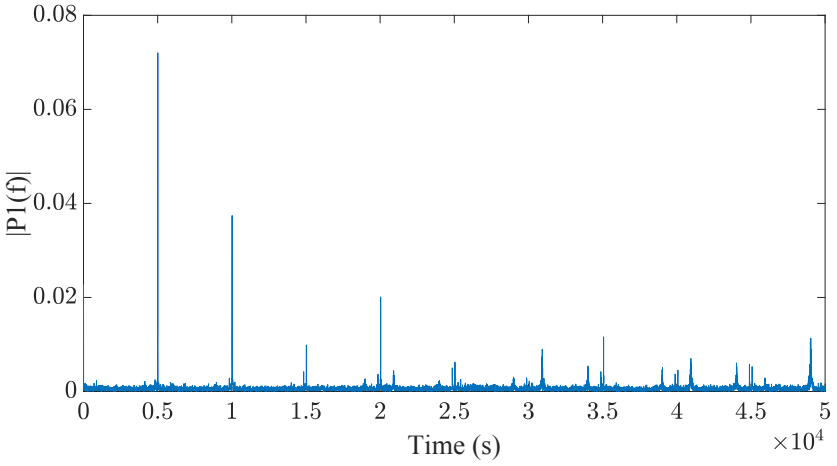

FIGURE 2.6: FFT of an Unfiltered Laser Sensor Reading

Following this, tests were carried out with sample rates of 1, 10 and 100 kHz, where a laser sensor measured a wall with reflective tape to ensure there were minimal losses in the receiving signal and that there was no additional vibration from the environment. The measurements were taken for 30 seconds and passed through a second order low-pass Butterworth filter, the results of which are seen in Figure 2.7:

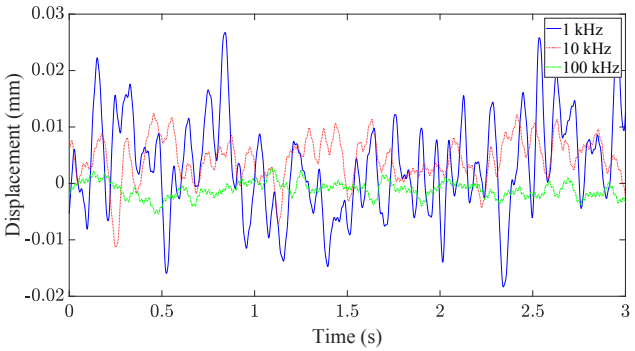

FIGURE 2.7: Laser Sensor Noise for Varying Sample Rates with a Second Order Low-Pass Filter

This meant that the sample rate had to be increased, and while the MicroLabBox is capable of 1 MHz sample rate, the Simulink models used are large and would not successfully compile above 50 kHz, so 10 kHz was selected as a compromise. A second order low-pass Butterworth filter is used on any laser sensor signals to remove signal noise with negligible time delay. A cut-off frequency of 25 Hz is used as any frequency testing or gusts do not exceed 15 Hz, therefore this should filter any higher frequency noise but not affect the genuine wing response measurements.

Simple displacement tests were carried out and the filter order was changed incrementally from first to fourth order to find the effect on signal noise and time delay. It was determined that the second order filter added an acceptable time delay to the system of 0.02 s while reducing the noise level by an order of magnitude. The alternatives were to either reduce the time delay and introduce more noise, to to reduce the noise and have a greater time delay. The results of this can be seen in Table 2.1:

TABLE 2.1: Noise Level and Time Delay for Varying Filter Orders at 10 kHz Sample Rate

Filter Order	Noise level (mm)	Time delay (s)
1	0.08	0.01
2	0.02	0.02
3	0.01	0.03
4	0.01	0.04

Clearly increasing the filter order becomes less effective at reducing the noise level the more the order is increased, with the largest benefit being seen between the first and second order filters. With this in mind, and the time delay being negligible to any tests being carried out, a second order filter was determined to be the most appropriate.

As the laser sensors are merely placed on top of the wind tunnel test section, a vibration test was performed on the test section plexiglass while the wind tunnel was in operation to ensure it was not being displaced by the airflow, thus causing errors in the laser sensor readings. A single axis accelerometer was placed on the plexiglass with the wind tunnel operating at 20 m/s, and for a range of 10 kHz the resulting FRF was a flat line with no clear resonances. Thus, the laser sensors were placed on the plexiglass.

Much of the work presented requires the use of a gust generator (Figure 2.8), designed by Balatti et al. specifically for the Swansea University wind tunnel [133]. This equipment is capable of 1 - cosine and harmonic gusts, as well as other motion if programmed, and is effective up to 28 m/s with a maximum frequency of up to 14 Hz and deflections between -20° to 20°. Two horizontal vanes with NACA 0015 profile and 200 mm chord are powered by Kollmorgen AKM43E motors with a maximum torque of 40 Nm.

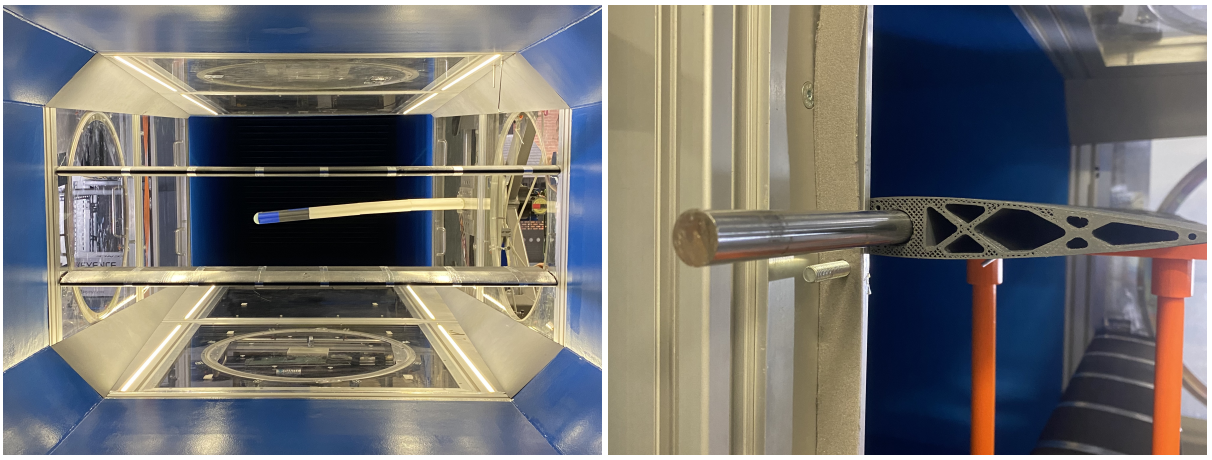

(a) (b)

FIGURE 2.8: Gust Generator (a) in Swansea wind tunnel, (b) vane

2.2 MODFLEX

The first experimental model used is the MODFLEX wing designed at the University of Liverpool [82]. The name is derived from it's modular design and that it is a flexible wing. It has previously been used to implement the Receptance Method [75], with the aim of increasing the damping of the first bending and torsion modes.

2.2.1 Wing Parameters

There are four modular 3D printed sections that can be either passive or active sections. In the case of the Swansea model, a single active section was used at the tip of the wing.

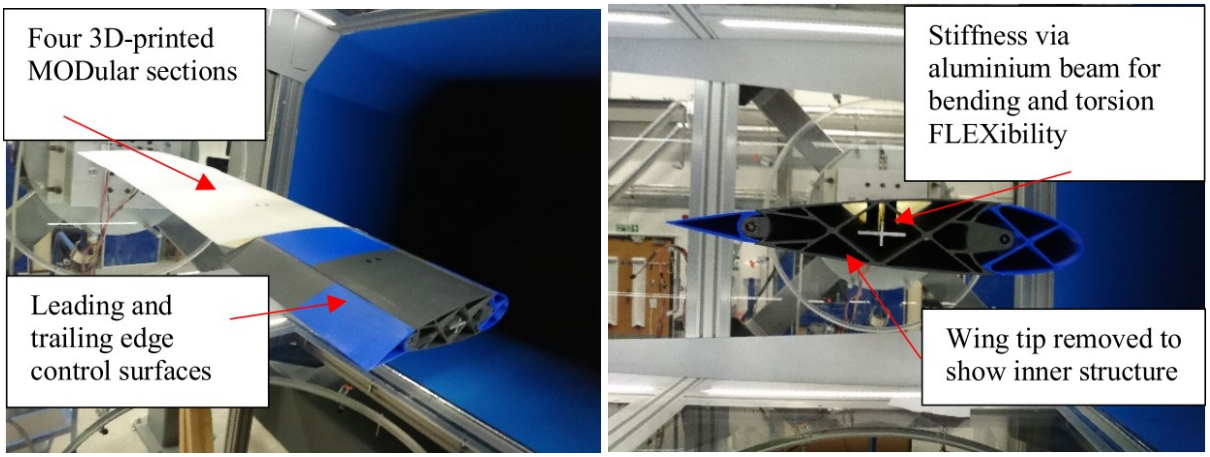

(a) (b)

FIGURE 2.9: MODFLEX (a) Setup in Wind Tunnel, (b) Active Sector Interior Structure

The wing stiffness is provided by a single x-shaped spar, shown in Figure 2.10a , which is mounted to an external balance at the root. A NACA 0018 aerofoil is used for the 3D printed sections, which are rigid and used only to an aerodynamic surface to the wing. They provide no contribution to, or effect on, the structure, other than their mass, and are connected to the spar using two bolts to clamp the aerofoil section to the spar over a small area such that the spar bending is not effected. The NACA 0018 is used as it provides space to include internal actuators. The MODFLEX dimensions are showing in Figure 2.10 and values are given in Table 2.2:

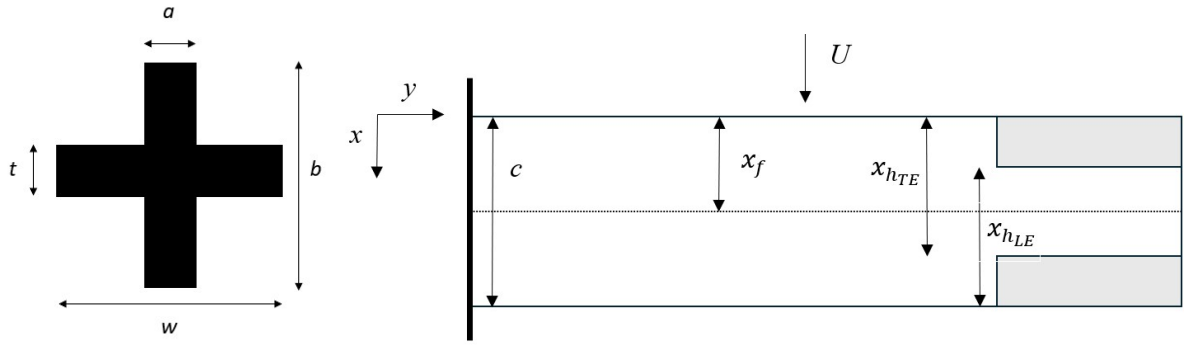

(a) (b)

FIGURE 2.10: MODFLEX Dimensions (a) Spar, (b) Full Wing

TABLE 2.2: MODFLEX Dimensions

Dimension	Notation	Size (mm)
Spar Dimensions (Figure 2.10a)	a	3
	b	17
	w	34
	t	2
Wing Span	s	1000
Chord Length	c	300
Flexural Axis position	x_f	150
Control Surface Hinge Axis	$x_{h_{LE,TE}}$	225

where x_f is the position of the flexural axis from the leading edge. As the wing is rectangular and the stiffness is provided by a single spar, the centre of the spar is the flexural axis. As shown in Figure 2.9, there are two control surfaces in the active section; one in the leading edge and one in the trailing edge. These control surfaces are powered by Maxon ECXSP16L motors with a digital encoder and 103:1 reduction gearboxes which can provide a torque of 1 Nm. The motor can be seen mounted in the active section in Figure 2.11.

FIGURE 2.11: Maxon ECXSP16L Motor in MODFLEX wing

The motors have been used for positional control, against their intended design. In order to achieve this, a PID controller was implemented into the Simulink model paired with ControlDesk, as well as a feedforward system to improve accuracy of the motor position. The PID gains were initially tuned using the Ziegler-Nichols method, with some manual

fine-tuning to reduce motor position error. Then, an estimator was used for feedforward control to again reduce motor position error. In order to apply this, the transfer function of the motor is given as:

$$G(s) = \frac{\Theta(s)}{V(s)} = \frac{K}{s(Js+b)(Ls+R)+K^2} \tag{2.2}$$

with the following motor parameters given in Table 2.3:

TABLE 2.3: Maxon ECXSP16L Parameters

Parameter	Notation	Value	Unit
Rotor Moment of Inertia	J	1.07×10^{-7}	kgm^2
Motor Torque Constant	K	5.25×10^{-3}	Nm/amp
Electrical Inductance	L	5.90×10^{-5}	H
Electrical Resistance	R	0.569	Ohm
Motor Viscous Friction Constant	b	2.28×10^{-7}	Nms

However, as the demanded angle is the input for the feedforward controller, the estimator is the inverse of $G(s)$, denoted as $G^{-1}(s)$. The block diagram for motor control can be seen in Figure 2.12, where the error 'e' is calculated via negative feedback. The encoder reading 'Θ_e' is subtracted from the desired angle 'Θ_d' given by the control law. The gain K_e scales the input to the feedforward control and is tuned manually to reduce error.

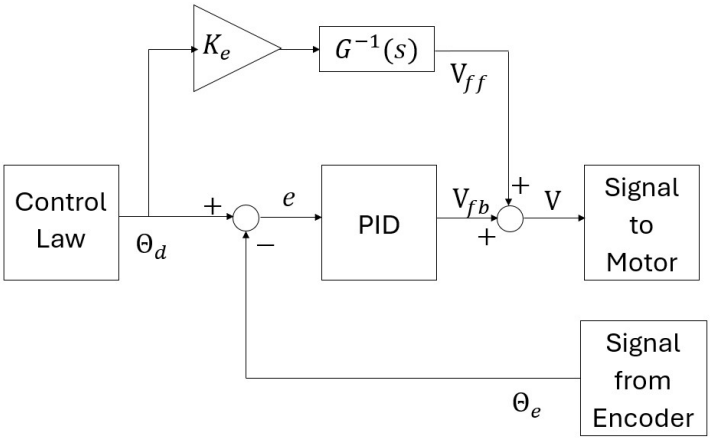

FIGURE 2.12: Block Diagram for Motor Position Control

Both the estimator and the PID controller produce voltage signals which are combined and sent to the motor to achieve the desired position. The voltage signal corresponds to a current that powers the motor, which must not exceed 9 A, so the Simulink block

'Saturation' is used here to prevent motor overload, but has been omitted from the block diagram for brevity and can be seen in Appendix B. In practice, the saturation limit was not reached by the system and therefore had no effect on the results, but was important to include for the safety of the equipment used.

2.2.2 Numerical Model

The numerical model begins as a simple Two-Degree of Freedom (2DoF) aeroelastic model presented by Wright and Cooper [7]. The initial state vector consists of the wing tip displacement due to bending ξ and the aerofoil twist at the wingtip θ.

$$\mathbf{w} = \begin{bmatrix} \xi \\ \theta \end{bmatrix} \tag{2.3}$$

The vertical displacement of any point of the wing can be found at any point of the wing using the following equation:

$$z = \left(\frac{y}{s}\right)^2 q_1 + \left(\frac{y}{s}\right)(x - x_f)q_2 \tag{2.4}$$

where y is the distance in the span-wise direction and x is the distance in the chord-wise direction. Using this relationship, we must transfer into assumed mode coordinates:

$$\begin{aligned} \mathbf{T} &= \begin{bmatrix} y_1^2 & 0 \\ 0 & y_2 \end{bmatrix} \\ \mathbf{q} = \mathbf{T}^{-1}\mathbf{w} &= \begin{bmatrix} q_1 \\ q_2 \end{bmatrix} \end{aligned} \tag{2.5}$$

where q_1, q_2 are generalised coordinates that quantify the amount of bending and torsion modes present in the overall deflection. The assumed shapes describe the quadratic bending of the clamped free wing, hence y_1^2, and the twist θ around the elastic axis, which is presumed to be a linear relationship in the span-wise direction, hence y_2.

The coordinates y_1 and y_2 are the y-coordinates of the measurement positions on the wing, which have been selected to project the wing response onto the first bending and torsion modes. As both measurement positions are situated at the wing tip, $y_1 = y_2 = s$, which in the case of MODFLEX is 1 m. Only the first two modes have been assumed in the numerical model as the natural frequencies of higher modes are sufficiently larger than any gust excitation frequency.

To numerically model the dynamics of the wing, we must first use the Second-Order Equation of Motion [7], which is as follows:

$$\mathbf{A}\ddot{\mathbf{q}} + (\rho U\mathbf{B} + \mathbf{D})\,\dot{\mathbf{q}} + \left(\rho U^2\mathbf{C} + \mathbf{E}\right)\mathbf{q} = \mathbf{G}\mathbf{u} \tag{2.6}$$

All matrices on the left hand side of Eq 2.5 are $n \times n$, and $\mathbf{q}$ is a $n \times 1$. Then, $\mathbf{u}$ is a $j \times 1$ vector, where j is the number of actuators in the system, and $\mathbf{G}$ is a $n \times j$ matrix. In the case of this work, $n = 2$ and $j = 2$. The airspeed is represented by U and the air density is represented by ρ. For all work presented, the air density is the sea level standard of 1.225 kgm^{-3} Then, making $\ddot{\mathbf{q}}$ the subject of Equation (2.7),

$$\ddot{\mathbf{q}} = -\mathbf{A}^{-1}\,(\rho U\mathbf{B} + \mathbf{D})\,\dot{\mathbf{q}} - \mathbf{A}^{-1}\left(\rho U^2\mathbf{C} + \mathbf{E}\right)\mathbf{q} + \mathbf{A}^{-1}\mathbf{G}\mathbf{u} \tag{2.7}$$

where $\mathbf{A}$ is the inertial matrix, defined as:

$$\mathbf{A} = m\begin{bmatrix} \dfrac{sc}{5} & \dfrac{s}{4}\left(\dfrac{c^2}{2} - cx_f\right) \\ \dfrac{s}{4}\left(\dfrac{c^2}{2} - cx_f\right) & \dfrac{s}{3}\left(\dfrac{c^3}{3} - c^2x_f + cx_f^2\right) \end{bmatrix} \tag{2.8}$$

$\mathbf{E}$ is the structural stiffness matrix, defined as:

$$\mathbf{E} = \begin{bmatrix} \dfrac{4EI}{s^3} & 0 \\ 0 & \dfrac{GJ}{s} \end{bmatrix} \tag{2.9}$$

Note that the non-zero terms of $\mathbf{E}$ represent the assumed bending and torsion mode shapes as defined by Wright and Cooper [7], not the equivalent bending and torsional stiffnesses. Then, $\mathbf{B}$ and $\mathbf{C}$ are the aerodynamic damping and stiffness matrices, respectively.

$$\mathbf{B} = \begin{bmatrix} \dfrac{s}{10}ca_w & 0 \\ \dfrac{-c^2s}{8}ea_w & \dfrac{-c^3s}{24}M_{\dot{\theta}} \end{bmatrix}, \quad \mathbf{C} = \begin{bmatrix} 0 & \dfrac{s}{8}ca_w \\ 0 & \dfrac{-c^2s}{6}ea_w \end{bmatrix} \tag{2.10}$$

The term $M_{\dot{\theta}}$ is an Oscillatory Aerodynamic Derivative for the moment about the elastic axis, and is used to create a simplified unsteady aerodynamic model. It is defined as:

$$M_{\dot{\theta}} = \frac{\partial C_M}{\partial\left(\dot{\theta}_c/U\right)} \tag{2.11}$$

The use of an unsteady aerodynamic model is necessary for analysis of the system in flutter and gust response as the behaviour of the model during dynamic motion is required.

Using experimentally obtained natural frequencies and damping ratios, the structural damping matrix $\mathbf{D}$ can be calculated, which will be covered later in this Chapter. The control distribution matrix $\mathbf{G}$ is as follows:

$$\mathbf{G} = \rho U^2 \begin{bmatrix} \mathbf{g_{TE}} \\ \mathbf{g_{LE}} \end{bmatrix} = \rho U^2 \begin{bmatrix} -\dfrac{37 C_{l_\beta} cs}{384} & -\dfrac{37 C_{l_\gamma} cs}{384} \\ \dfrac{7 s c^2 C_{m_{\beta-eff}}}{128} & \dfrac{7 s c^2 C_{m_{\gamma-eff}}}{128} \end{bmatrix} \tag{2.12}$$

Then, the system can be modelled numerically via a state-space transformation, where n is the number of degrees of freedom:

$$\begin{gathered} \tilde{\mathbf{A}} = \begin{bmatrix} \mathbf{0}_{n\times n} & \mathbf{I}_{n\times n} \\ -\mathbf{A}^{-1}\left(\rho U^2 \mathbf{C} + \mathbf{E}\right) & -\mathbf{A}^{-1}\left(\rho U \mathbf{B} + \mathbf{D}\right) \end{bmatrix} \\ \dot{\mathbf{x}} = \begin{bmatrix} \dot{\mathbf{q}} \\ \ddot{\mathbf{q}} \end{bmatrix} = \tilde{\mathbf{A}}\mathbf{x} + \tilde{\mathbf{G}}\mathbf{u}, \text{ where } \mathbf{x} = \begin{bmatrix} \mathbf{q} \\ \dot{\mathbf{q}} \end{bmatrix} \end{gathered} \tag{2.13}$$

$$\tilde{\mathbf{G}} = \begin{bmatrix} \mathbf{0}_{n\times j} \\ -\mathbf{A}^{-1}\mathbf{G} \end{bmatrix}, \quad \mathbf{u} = \begin{bmatrix} \beta & \gamma \end{bmatrix}^T \tag{2.14}$$

where β and γ are the trailing and leading edge surface deflections respectively, measured in radians. Most variables used in the matrix descriptions have already been given in the previous section. The previously undefined variables are given as the following:

Table 2.4: MODFLEX Parameters

Parameter	Notation	Value	Unit
Total mass	m	5.0000	kg
Flexural Rigidity	EI	49.9567	Nm^2
Torsional Rigidity	GJ	7.9825	Nm^2
Oscillatory Aerodynamic Derivative	$M_{\dot{\theta}}$	-1.2000	-
Lift Curve Slope	a_W	2π	-
Elastic Axis Position Constant	e	0.2500	-
TE Surface Lift Coefficient	C_{l_β}	-0.2205	-
LE Surface Lift Coefficient	C_{l_γ}	1.3414	-
Effective Moment Derivatives	$C_{m_{\beta-eff}}$	-0.1765	-
	$C_{m_{\gamma-eff}}$	0.7149	-

where $C_{l_{\beta/\gamma}}$ and $C_{m_{\beta/\gamma}}$ are defined as the change in C_l and C_m with deflection angle, and $C_{m_{\beta/\gamma-eff}}$ are the effective dynamic and control moment derivatives due to trailing and leading edge control surface deflection, defined as:

$$C_{m_{\beta/\gamma-eff}} = (0.5 + a)\, C_{l_{\beta/\gamma}} + 2C_{m_{\beta/\gamma}} \tag{2.15}$$

a_W is the lift curve slope for a three-dimensional finite-span wing and is estimated as 2π. The final term e is used to find the distance, ec, of the elastic axis aft of the aerodynamic centre. The flexural rigidity is calculated using the Young's Modulus E and the second moment of area I, which is calculated using the following:

$$I = \frac{wt^3 + ab^3 - at^3}{12} \tag{2.16}$$

Similarly, the torsional rigidity is calculated by using the modulus of rigidity G and the polar moment of inertia J, which is calculated using the following:

$$J = \left(\frac{tw}{12}\right)\left(t^2 + w^2\right) + \left(\frac{ab}{12}\right)\left(a^2 + b^2\right) - \left(\frac{ta}{12}\right)\left(t^2 + a^2\right) \tag{2.17}$$

where a, b, w, and t are the spar cross sections dimensions shown in Figure 2.10a and given in Table 2.2. The 3D printed sections are not considered as they do not provide structural stiffness to the system.

2.2.3 Design Validation

In order to obtain the natural frequencies and damping ratios of the MODFLEX wing, impact hammer tests were carried out using the DataPhysics Abacus 901 data acquisition system. The test setup can be seen in Figure 2.13:

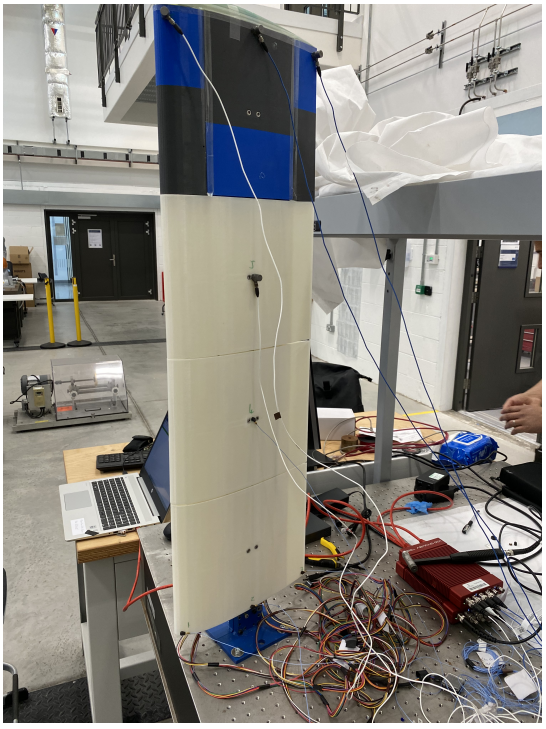

FIGURE 2.13: MODFLEX Hammer Test Setup

A trigger of 5 N was used for the hammer strike to ensure the system is sufficiently excited, and ten acceptable strikes were taken into the average to generate the Frequency Response Function (FRF). After the tests were completed, the natural frequencies and damping ratios were then obtained using the Rational Fraction Polynomial (RFP) Method in Matlab [135].

TABLE 2.5: MODFLEX Natural Frequencies and Damping Ratios

Mode	Natural Frequency (Hz)	Damping Ratio
1st Bending	2.90	0.013
1st Torsion	5.53	0.094
In-plane	8.47	0.020

For model validation, a series of swept-sine tests were carried out in the wind tunnel for a range of airspeeds below flutter. The test frequencies swept from 0.1 Hz to 10 Hz

to capture all the modes of interest, with a sweep rate of 0.0015 Hz/s and a flap angle of 10° magnitude. This meant that the sweep rate was slow enough to allow transient responses to decay before a significant change in excitation frequency. While a stepped-sine test was the preferable option, the DataPhysics Abacus software did not have this capability. It was decided that a swept-sine test with a slow sweep rate was sufficient to approximate a stepped-sine test with a large amount of steps.

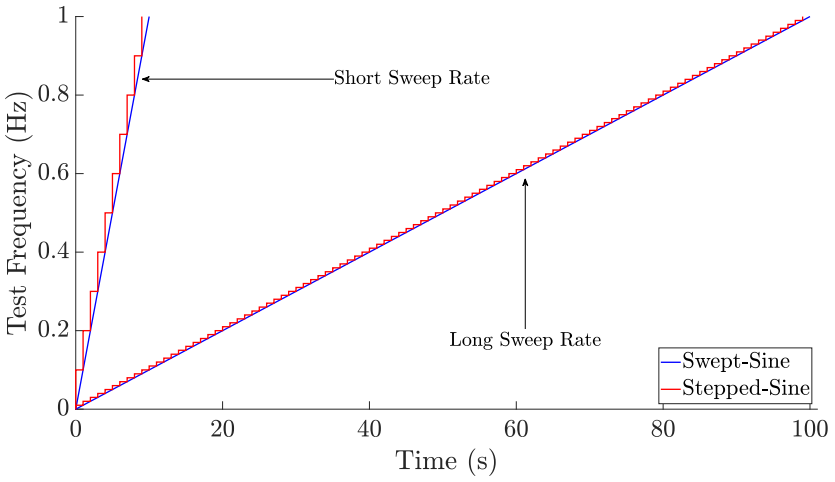

FIGURE 2.14: Comparison of Frequency Ranges in Swept-Sine and Stepped-Sine tests

The downside of the swept-sine test is of course the increased test time when compared to a random excitation or impact hammer test, however this is necessary given the circumstances. Random excitation tests were carried out, with excitation coming from the trailing edge control surface due to the 'Random Source' block in Simulink, but would produce a noisy FRF with no clear resonances. Also there was no way to carry out an impact hammer test with the wind tunnel running. Thus, the swept-sine test was the only viable option. Figure 2.15 shows a comparison between numerical natural frequencies and damping ratios, and experimental natural frequencies and damping ratios obtained from the swept-sine wind tunnel tests. The trailing edge control surface was used for swept-sine excitation, with tests conducted at each of the airspeeds marked in Figure 2.15.

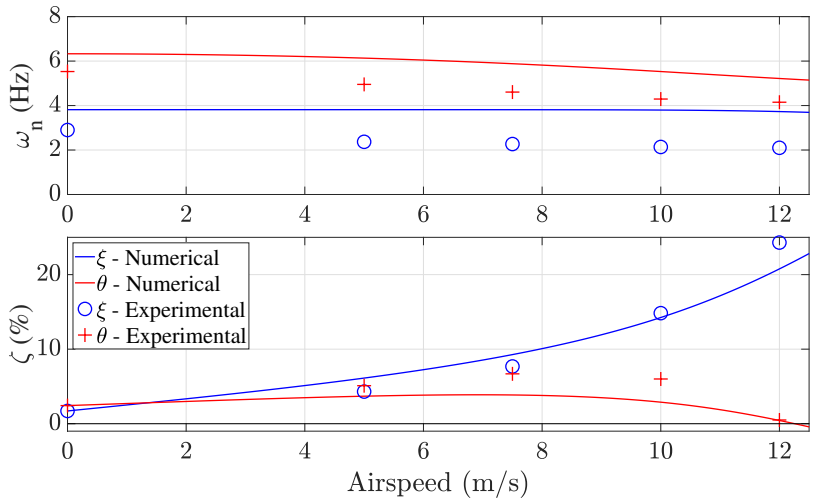

FIGURE 2.15: Natural Frequencies and Damping Ratios of MODFLEX Experimentally and Numerically

The results shown in Figure 2.15 show poor correlation between the numerical and experimental natural frequencies, particularly as airspeed increases. This is because in the model validation, it was deemed more important to more closely match the damping ratios to accurately predict the flutter speed of the system. Due to the simplicity of the assumed modes model, it was not possible to closely match both the damping ratios and natural frequencies of the system. At 12 m/s, the experimentally measured values of the bending and torsional natural frequencies are 2.1 Hz and 4.15 Hz respectively, whereas the numerical values are 3.73 Hz and 5.21 respectively. The stiffness of the spar seems to have been over-estimated in the numerical model, however the most important factor of the model for this work is the flutter speed, which matches the experimental model.

2.3 MODFLEX 2.0

The next experimental model used in this work is an updated version of the MODFLEX wing from the previous section. The following will detail the design considerations for the new wing, as well as vibration test results.

2.3.1 Design Process

The updated MODFLEX 2.0 also utilises the same modular setup as the original MODFLEX, again using a single active sector at the wing tip for this work. The same Maxon

motors are also used for powering the leading and trailing edge control surfaces in the active section. A NACA 0018 aerofoil is also still used for this wing as it provides significant space inside the section to house the motors and fit the spar. All CAD model details can be found in Appendix C

It was identified that the flutter speed of MODFLEX was too low for operation in the Swansea University wind tunnel as the facility experiences some instability in test speed below 10 m/s. Thus, the main aim for a new wing was to increase the flutter speed to make better use of the wind tunnel's range of speed. The target was first to have a large range of airspeed below flutter where the wind tunnel airspeed is sufficiently stable, i.e. increase the flutter speed so it is significantly higher that 10 m/s. Additionally, the gust generator is effective up to 28 m/s, so it was important that the effective range of the gust generator could be used safely and without forcing flutter to occur during gust encounters. Another less significant problem was the large amount of wing bending and pitching down when there was no airflow present. A 3° AOA had to be applied at the root to counteract the pitch down wing twist so that the wing tip had a 0° AOA. The first step was to increase the spar stiffness, as seen in Table 2.6, the thickness t is increased from 2 mm to 3 mm as this would increase the spar stiffness and flutter speed sufficiently without introducing too much additional weight.

Table 2.6: MODFLEX 2.0 Dimensions

Dimension	Notation	Size (mm)
Spar Dimensions	a	3
	b	17
	w	34
	t	3
Wing Span	s	1000
Chord Length	c	250
Flexural Axis position	x_f	100
Leading Edge Hinge Axis	$x_{h_{LE}}$	210
Trailing Edge Hinge Axis	$x_{h_{TE}}$	175

The increase in spar thickness leads to an increase in EI from 49.96 to 89.56 Nm^2 and an increase in GJ from 7.98 to 37.71 Nm^2. The additional mass added to the spar is 83.7g. The next consideration in increasing the flutter speed also helped to solve the static bending and pitch down twisting of the wing. The chord length was reduced from 300 to 250 mm. Finally, the flexural axis was moved forward. The spar was placed at $0.5c$ for the original MODFLEX, but has been moved forward to $0.4c$ so that the centre

of mass was inline with the flexural axis to again act against the drooping seen in the original MODFLEX model. Table 2.7 shows how the flutter speed is increased with each design step:

TABLE 2.7: Change in Flutter Speed with Design Steps

Design Step	U_f (m/s)	ΔU_f (m/s)
MODFLEX	12.5	-
Increase Spar Thickness	24.2	11.7
Reduce Chord Length	29.8	5.6
Move Flexural Axis	31.1	1.3

As the chord length was reduced, the next step was to resize the leading edge (LE) and trailing edge (TE) control surfaces. The original MODFLEX has $x_{h_{LE}} = x_{h_{TE}} = 225$ mm, but due to the aerofoil shape this means the LE surface has a large mass and moment of inertia, causing the connection to the motor shaft to slip during tests. In order to determine a suitable control surface size, xFLR5 was used and three configurations were evaluated. In all configurations, the TE surface was increased to $0.3c$ as reducing the chord length led to a reduction in control surface sizes, so the TE surface was simply increased to compensate for this to where the motor would fit within the aerofoil section without being too close to the spar. The LE surface size was then changed in each configuration:

TABLE 2.8: Leading Edge Control Surface Configurations Analysed

Configuration	$x_{h_{LE}}$ (% of c)	$x_{h_{LE}}$ (mm)	C_{l_γ}	$C_{m_{\gamma-eff}}$
1	84	210	0.6248	0.3455
2	80	200	1.0290	0.5531
3	90	225	0.2021	0.1121

Each configuration had the LE and TE surfaces tested individually from -10° to 10° in increments of 1°.

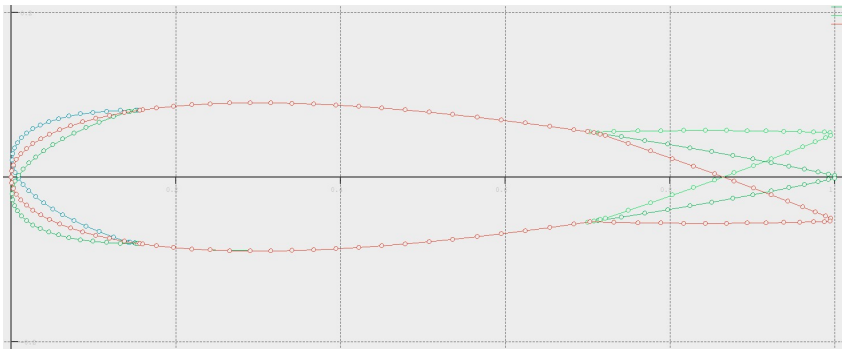

FIGURE 2.16: Configuration 1 in xFLR5 Direct Foil Design

Configuration 1 was then chosen as the C_l and $C_{m_{eff}}$ values had similar relativity between control surfaces to those on MODFLEX for LE and TE. Importantly the sizes of both control surface allowed for space for the motors to be mounted easily, whereas Configuration 2 would have less usability, and was not large enough to cause the slipping effect, which was a concern with Configuration 3. This results in the following lift and moment coefficients for MODFLEX 2.0, shown in Table 2.9:

TABLE 2.9: MODFLEX 2.0 Parameters

Parameter	Notation	Value	Unit
Total mass	m	5.0000	kg
Flexural Rigidity	EI	89.5620	Nm^2
Torsional Rigidity	GJ	37.7056	Nm^2
Oscillatory Aerodynamic Derivative	$M_{\dot{\theta}}$	-1.2000	-
Lift Curve Slope	a_W	2π	-
Elastic Axis Position Constant	e	0.2500	-
TE Surface Lift Coefficient	C_{l_β}	-0.0367	-
LE Surface Lift Coefficient	C_{l_γ}	0.6248	-
Effective Moment Derivatives	$C_{m_{\beta-eff}}$	-0.0294	-
	$C_{m_{\gamma-eff}}$	0.3455	-

The C_l and C_m versus deflection angle plots for the Configuration 1 LE surface can be seen in Figure 2.17.

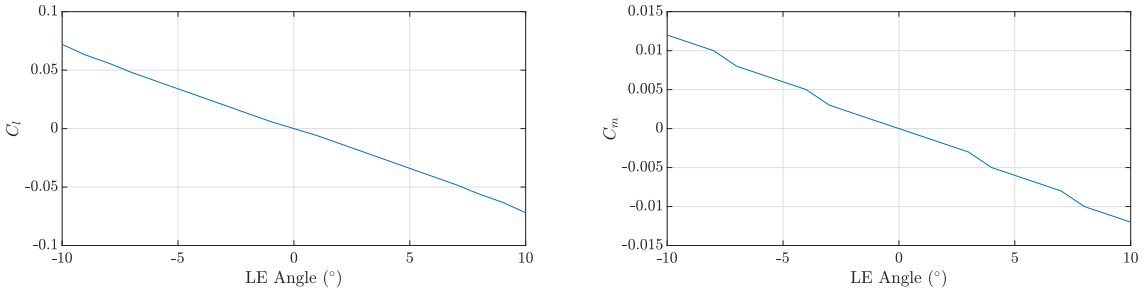

(a) (b)

FIGURE 2.17: (a) C_l, (b) C_m of the Leading Edge Control Surface for MODFLEX 2.0

The final design change was to the motor bushes. In the original MODFLEX model, the connection between the 3D printed control surfaces and the motors was a small M1.6x8 grub screw. This small screw would be forced away from the motor shaft under larger loads, leading to both control surfaces slipping off of the motor after continuous use. The screw head would also be easily worn down, leading it to become stuck in the bush. These issues were rectified by using two Phillips head M4 screws, which would remain in place for much larger loads and eliminated the slipping problem.

(a) (b)

FIGURE 2.18: Motor Bush for (a) MODFLEX, (b) MODFLEX 2.0

The difference between the active sections of both MODFLEX models can be seen in Figure 2.19:

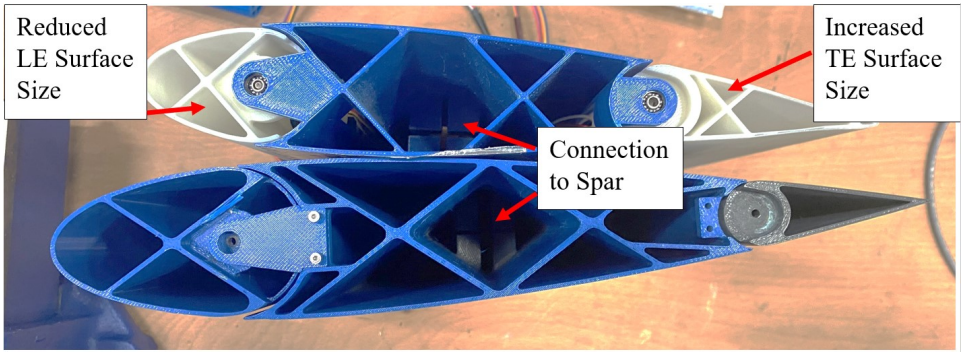

FIGURE 2.19: Comparison of active modules from MODFLEX and MODFLEX 2.0

2.3.2 Design Validation

The same impact hammer test was carried out on MODFLEX 2.0 as on the original MODFLEX model. Table 2.10 shows the natural frequencies and damping ratios of the wing. Clearly the increased spar stiffness has increased the bending and torsion natural frequencies.

TABLE 2.10: MODFLEX 2.0 Natural Frequencies and Damping Ratios

Mode	Natural Frequency (Hz)	Damping Ratio
1st Bending	3.55	0.004
In-plane	9.16	0.008
1st Torsion	14.19	0.02

As the spar width w has not been increased, the in-plane mode has not experienced a large change in natural frequency and it is now between the first bending and torsion modes. Once again, a series of swept-sine tests were carried out for model validation. The test frequencies swept from 0.1 Hz to 15 Hz to capture all the modes of interest, with a sweep rate of 0.0015 Hz/s. While 15 Hz is close to the 1st torsion natural frequency in the static case, it reduced significantly as airspeed increased (as seen in Figure 2.20). Thus, having the sweep end at 15 Hz was acceptable as it is sufficiently higher than the torsional natural frequency.

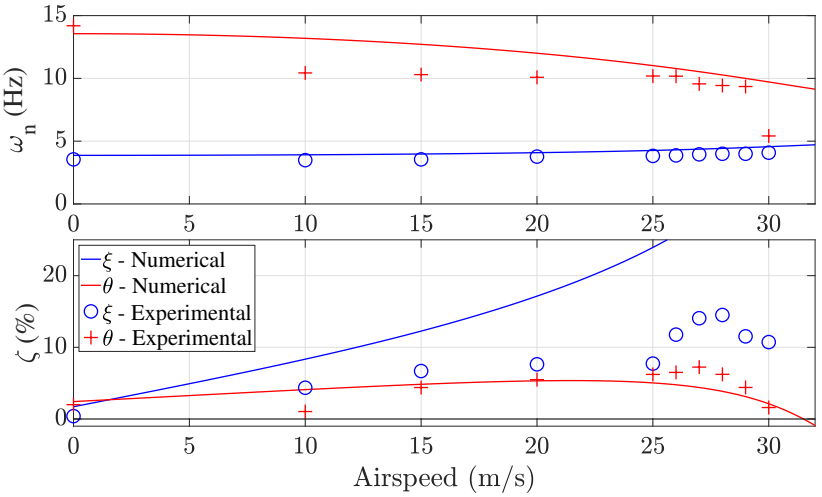

FIGURE 2.20: Natural Frequencies and Damping Ratios of MODFLEX 2.0 Experimentally and Numerically

The experimental results shown in Figure 2.20 confirm the flutter speed of 31.1 m/s, as predicted by the numerical model. As seen with the MODFLEX results in Figure 2.15, the simple numerical model prevents accuracy in both the damping ratios and natural frequencies, so the model was updated to have better matching damping ratios so that the flutter speed was accurate. There is a sudden drop in the torsional natural frequency at 30 m/s due to sudden coupling of the bending and torsional modes. This effect is delayed and sudden due to the presence of the in-plane mode occurring between the bending and torsional mode (Table 2.10), and there is coupling observed in the wind tunnel tests between the in-plane and torsional modes from 27 m/s onwards, until just below the flutter speed at 30 m/s where the large drop occurs. The error in the numerical model is a difference of 4.3 Hz between the experimental value for torsional natural frequency (5.41 Hz) and the numerical value (9.71 Hz).

Chapter 3

GUST RESPONSE ALLEVIATION VIA RECEPTANCE METHOD

3.1 Introduction

In aircraft design, understanding the impact of gusts and the loads they impose on the system is crucial, especially with the industry's shift toward high aspect ratio wings. Repeated loading and unloading of a wing structure, whether from gusts or other factors, can gradually lead to fatigue, particularly in wings with lower stiffness that undergo significant deformations. Moreover, if the flight speed is sufficiently high and close to the flutter boundary, external disturbances like gusts can cause much larger deflections than at lower airspeeds, even leading to instability should there be changes to the airspeed and pressure over the wing. By thoroughly understanding the effects of gust loads, especially the most severe cases, designers can implement structural reinforcements or active control measures to mitigate these risks.

The aim of this Chapter is to alleviate the wing vibration in the presence of gusts. The objective is to use Pole Placement via the Receptance Method [75, 79]. Some examples

of the Receptance Method are the work of Ghandchi et al. [77, 78], and Mokrani et al. [83].

The model used in this Chapter is MODFLEX, designed at the University of Liverpool [82]. This has been described in detail in Chapter 2.

3.2 Gust Modelling

Both Harmonic and 1-cosine gusts have been considered in this work, with the latter being explored experimentally. For the numerical model, the gust models used are those described by Wright and Cooper [7], where the vertical airspeed for a sinusoidal gust is:

$$\begin{aligned} w_g &= w_{g_0} \sin\left(\frac{2\pi U t}{\lambda_g}\right) = w_{g_0} \sin\left(\omega_g t\right) \\ w_{g_0} &= \Delta\theta \cdot U \end{aligned} \tag{3.1}$$

where λ_g is the wavelength of the gust, ω_g is the gust frequency in rad/s and $\Delta\theta$ is the effective angle of incidence due to the gust. Similarly, for a 1-cosine gust:

$$w_g = \frac{w_{g_0}}{2}\left(1 - \cos\left(\frac{2\pi U t}{\lambda_g}\right)\right) \text{ for } 0 < t < \frac{\lambda_g}{U}, \text{ otherwise } w_g = 0 \tag{3.2}$$

The generalised force and pitching moment due to the gust can be expressed in the second-order form as:

$$\mathbf{h} = \rho U \begin{bmatrix} -\dfrac{c a_w s}{6} \\ \dfrac{c^2 e a_w s}{4} \end{bmatrix} = \rho U \begin{bmatrix} h_1 \\ h_2 \end{bmatrix} \tag{3.3}$$

This is converted to state-space as:

$$\tilde{\mathbf{h}} = \begin{bmatrix} \mathbf{0}_{2\times 1} \\ \mathbf{A}^{-1}\mathbf{h} \end{bmatrix} \tag{3.4}$$

The full state-space equation, including gust interference and active control, is then given for the Multiple-Input, Multiple-Output (MIMO) case as:

$$\dot{\mathbf{x}} = \tilde{\mathbf{A}}\mathbf{x} + \tilde{\mathbf{G}}\mathbf{u} + \tilde{\mathbf{h}} w_g \tag{3.5}$$

from which the SIMO case can be derived as:

$$\dot{\mathbf{x}} = \tilde{\mathbf{A}}\mathbf{x} + \tilde{\mathbf{g}}\beta + \tilde{\mathbf{h}}w_g \tag{3.6}$$

The control terms $\tilde{\mathbf{g}}\beta$ and $\tilde{\mathbf{G}}\mathbf{u}$ will be explained further in the following sections.

3.3 Control Approach

Before the details of the receptance method are given, it is important to detail the approach taken to the gust response alleviation problem. The frequency and size of the gust has a significant effect on an aeroelastic system. A larger gust will of course elicit larger vibration from the wing, however the gust frequency and its closeness to any natural frequencies of the wing can also create a significant response from the wing. When selecting closed loop poles for alleviating a gust response, it is important to consider the proximity of the closed loop natural frequencies to the gust frequency and the damping ratios of the vibration modes, as well as the amount of control effort required to place the poles.

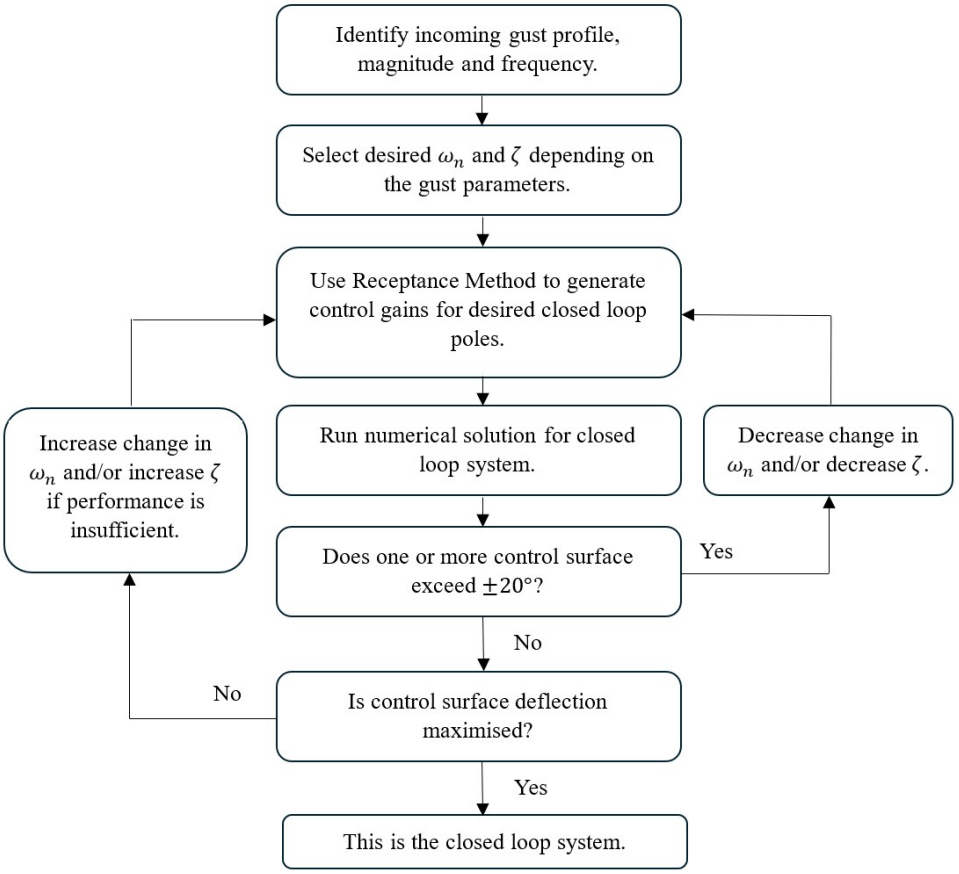

FIGURE 3.1: Flowchart Detailing the Process of Pole Selection for Gust Response Alleviation

Figure 3.1 shows the decisions made to select closed loop poles for results throughout this Chapter. The key step is selecting the desired closed loop natural frequencies and damping ratios depending on the incoming gust. If, for example, an incoming gust has a frequency close to the natural frequency of the bending mode then it makes sense to increase the natural frequency of this mode. However, attempting to set a damping ratio that is too high will result in the demanded control surface angle being too large, particularly if a larger gust is encountered. The numerical results in the following sections will carry out the control approach outlined here, experimenting with different changes to natural frequencies and damping ratios for different airspeed and gust parameters.

3.4 SIMO Receptance Method

The basis of the Receptance Method is to measure the receptance of the system to the input of the controller [75]. In the case of MODFLEX, the control surface contribution

is available numerically and the receptance is also measured experimentally via swept-sine tests using the trailing edge surface for excitation. Using this information, Pole Placement can be applied in the closed loop system for alleviating the wing response to perturbations such as gusts.

3.4.1 Pole Placement

Using a control surface, and the receptance of the system, it is possible to change the poles of the system. Generally the aim is to change the natural frequencies and damping ratios of the system, which are then used to construct desired closed-loop poles. The receptance of a single input system, in the case of MODFLEX where β is the trailing edge flap angle, is:

$$\mathbf{y_x} = \mathbf{R}(s).\beta \tag{3.7}$$

$$\mathbf{R}(s) = \mathbf{H}(s).\tilde{\mathbf{g}} = \begin{bmatrix} \dfrac{N_1(s)}{D(s)} \\ \dfrac{N_2(s)}{D(s)} \end{bmatrix} \tag{3.8}$$

where $\mathbf{R}(s)$ is a $n \times j$ vector (therefore $n \times 1$ in this work), $\mathbf{y_x}$ is the output state vector of the system and $\mathbf{H}(s)$ is the receptance matrix, which may be be determined in practice from the matrix of measured receptances $\mathbf{H}(i\omega)$. For the experiments carried out in this work, the control surface is first used to excite the system using a swept-sine test, meaning the measured receptance of the open loop system is $\mathbf{R}(i\omega)$. In the general case, $\mathbf{H}(s)$ is defined as:

$$\mathbf{H}(s) = \left[\mathbf{M}s^2 + \mathbf{C}s + \mathbf{K}\right]^{-1} \tag{3.9}$$

where $\mathbf{C}$ and $\mathbf{K}$ are the damping and stiffness matrices of the system. However, as it is applied to an aeroelastic system, the receptance matrix is:

$$\mathbf{H}(s) = \left[\mathbf{A}s^2 + (\rho U\mathbf{B} + \mathbf{D})\, s + \left(\rho U^2\mathbf{C} + \mathbf{E}\right)\right]^{-1} \tag{3.10}$$

making $\mathbf{H}(s)$ a $n \times n$ matrix. Using a modified version of the Rational Fraction Polynomial (RFP) method [135], the polynomials needed $(N_1(s), N_2(s), D(s))$ to calculate the transfer function can be obtained from the measured Frequency Response Functions (FRFs). The benefit of the RFP method cited is that the code output after curve fitting provides the natural frequencies, damping ratios and polynomials needed for the transfer function. Once the transfer function $\mathbf{R}(s)$ has been reconstructed, pole placement can

be used through the method of receptances, where the transfer function is evaluated at the locations of the desired poles μ_k, where k is two times the number the degrees of freedom. In order to calculate the control gains, the following transformation is used:

$$\mathbf{r}_k = \mathbf{R}(\mu_k)$$

$$\mathbf{L}\begin{pmatrix}\mathbf{g}\\ \mathbf{f}\end{pmatrix} = \begin{bmatrix}\mathbf{r}_1^T & \mu_1\mathbf{r}_1^T\\ \vdots & \vdots\\ \mathbf{r}_k^T & \mu_k\mathbf{r}_k^T\end{bmatrix}\begin{pmatrix}\mathbf{g}\\ \mathbf{f}\end{pmatrix} = \begin{pmatrix}-1\\ \vdots\\ -1\end{pmatrix} \tag{3.11}$$

In order to obtain the $n \times 1$ control gains $\mathbf{g}$ and $\mathbf{f}$, the $n \times n$ matrix $\mathbf{L}$ must be inverted. However, this is only possible if the system is controllable and μ_k for $k = 1, \ldots, 2n$ are distinct. The check for if the system is controllable is given by Khalil [51], as is given by the controllability matrix Υ:

$$\Upsilon = \begin{bmatrix}\tilde{\mathbf{g}} & \tilde{\mathbf{A}}\tilde{\mathbf{g}} & \tilde{\mathbf{A}}^2\tilde{\mathbf{g}} & \cdots & \tilde{\mathbf{A}}^{n-1}\tilde{\mathbf{g}}\end{bmatrix} \tag{3.12}$$

where Υ is an $n \times (n \cdot j)$ matrix. The system is controllable if Υ is full rank. Then, the control law is obtained as:

$$\beta(t) = -\mathbf{f}^T\dot{\mathbf{z}}(t) - \mathbf{g}^T\mathbf{z}(t) \tag{3.13}$$

3.4.2 Partial Pole Placement

Building on the full pole placement case, it is possible to target specific problematic poles while leaving the stable poles unchanged. This is explored by Tehrani et al. [77], and Ram and Mottershead [79]. The benefit of the reformulation presented in this section is that it can be adapted to a MIMO control system, which will be described later. As in the previous case, the system output state vector is given as:

$$\begin{gathered}\mathbf{y_x} = \mathbf{R}(s)\beta\\ \beta(t) = -\mathbf{f}^T\dot{\mathbf{z}}(t) - \mathbf{g}^T\mathbf{z}(t)\end{gathered} \tag{3.14}$$

$$\mathbf{R}(s) = \mathbf{H}(s).\tilde{\mathbf{g}} = \begin{bmatrix}\dfrac{N_1(s)}{D(s)}\\ \dfrac{N_2(s)}{D(s)}\end{bmatrix} \tag{3.15}$$

Now the difference in methods becomes apparent, as now the closed loop poles placed are distributed into those we wish to change, and those we wish to stay the same. Here, we define two matrices $\mathbf{P}$ and $\mathbf{Q}$ as the following:

$$\mathbf{P} = \begin{bmatrix} \mu_1 \mathbf{r}_1^T & \mathbf{r}_1^T \\ \vdots & \vdots \\ \mu_p \mathbf{r}_p^T & \mathbf{r}_p^T \end{bmatrix}, \quad \mathbf{Q} = \begin{bmatrix} \mu_{p+1} \mathbf{v}_{p+1}^T & \mathbf{v}_{p+1}^T \\ \vdots & \vdots \\ \mu_{2n} \mathbf{v}_{2n}^T & \mathbf{v}_{2n}^T \end{bmatrix} \tag{3.16}$$

where p is the number of poles we wish to place, and n is the number of degrees of freedom in the system. The matrix $\mathbf{P}$ is defined using the the desired close loop poles $\mu_{1:p}$ and their measured receptances $\mathbf{r}_{1:p}$ so that the poles we wish to change are assigned by the control input, whereas the matrix $\mathbf{Q}$ is defined with the poles we wish to leave untouched $\mu_{p+1:2n}$ and their corresponding eigenvectors $\mathbf{v}_{p+1:2n}$. The controller gains are then found using the following relationship:

$$\begin{bmatrix} \mathbf{P} \\ \mathbf{Q} \end{bmatrix} \begin{pmatrix} \mathbf{f} \\ \mathbf{g} \end{pmatrix} = \begin{pmatrix} \mathbf{e} \\ \mathbf{0} \end{pmatrix}, \quad \mathbf{e} = \begin{pmatrix} 1 \\ \vdots \\ 1 \end{pmatrix} \tag{3.17}$$

here, $\mathbf{e}$ is a $p \times 1$ vector, and then the remaining places in the full vector $(p+1:2n)$ are all zero, so that only the desired poles are changed in the closed loop system. The control gain vectors $\mathbf{f}$ and $\mathbf{g}$ are then found by inverting the $\mathbf{P}$, $\mathbf{Q}$ array and multiplying by the $\mathbf{e}$, $\mathbf{0}$ vector.

3.4.3 Results

Tests were carried out both numerically and experimentally, with the latter having drawbacks to their quality which will be discussed. All cases are tested in the presence of 1-cosine and harmonic gusts.

3.4.3.1 Numerical

The numerical model has been described previously in the introduction to this Chapter. The assumed mode model assumes the first bending and torsion modes only. In the experimental model, the control surfaces are capable of up to $\pm 20°$ of rotation (maximum deflections shown in Appendix A, Figure A.9), and this has been reflected in the closed loop poles selected for the results shown in this section. First of all, a 4 Hz 1-cosine gust is applied to the system as this produces the largest (therefore worst case) response.

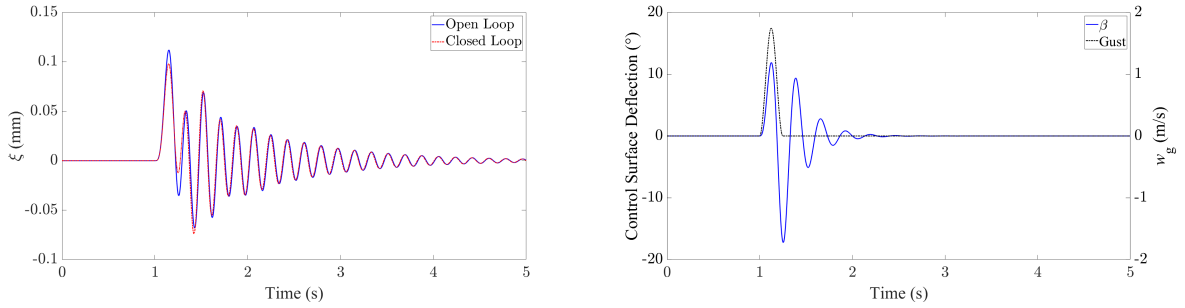

(a) (b)

FIGURE 3.2: Case 1 Response at 10 m/s to 4 Hz 1-Cosine Gust in (a) Wing Bending, (b) Control Surface Deflection

The results shown above will be referred to as Case 1 and will be explained shortly. Multiple cases have been evaluated, so a performance function has been created for better comparison between the closed loop systems. As the aim is not to design an optimum controller, and closed loop poles have been selected based on the maximum possible control surface deflection, any control contribution as been omitted from the performance function. The metric is defined as the following:

$$\varepsilon = [RMS(\xi_{OL}) - RMS(\xi_{CL})] + [RMS(\theta_{OL}) - RMS(\theta_{CL})] \tag{3.18}$$

This gives a performance value in terms of the reduction in the Root Means Square (RMS) of the deflection of the assumed modes, where ξ must be measured in metres and θ must be in radians. Essentially, this measure indicates how much the closed loop system has reduced the overall deflection of the assumed modes. As MATLAB will evaluate the RMS of the full response data, simulations are run until the open loop response has fully decayed after the gust encounter, as running the simulation for longer than this would introduce more zero values, artificially lowering the RMS of the open loop response. The control cases and their ε values are given in Table 3.1:

TABLE 3.1: Summary of Single Input Closed Loop Cases - 4 Hz 1-Cosine Gust, 10 m/s

Case 1 - ζ_1 increased				Case 2 - ζ_1 increased, ω_{n_1} decreased			
Parameter	OL	CL	ε	Parameter	OL	CL	ε
ω_{n_1}	23.861	23.861	0.0018	ω_{n_1}	23.861	23.145	0.0010
ω_{n_2}	34.745	34.745		ω_{n_2}	34.745	34.745	
ζ_1	0.143	0.190		ζ_1	0.143	0.170	
ζ_2	0.029	0.029		ζ_2	0.029	0.029	
Case 3 - $\zeta_{1,2}$ increased				Case 4 - $\zeta_{1,2}$ increased, ω_n separated			
Parameter	OL	CL	ε	Parameter	OL	CL	ε
ω_{n_1}	23.861	23.861	0.0021	ω_{n_1}	23.861	23.145	0.0010
ω_{n_2}	34.745	34.745		ω_{n_2}	34.745	35.787	
ζ_1	0.143	0.160		ζ_1	0.143	0.160	
ζ_2	0.029	0.100		ζ_2	0.029	0.100	

It is clear from the results that changing the natural frequencies of the system does little to improve the gust response. Additionally, a large amount of control power is needed to change the natural frequencies of the system (Cases 2 and 4), which could be better spent increasing the damping ratios instead, as seen in Cases 1 and 3.

As the previous gust case was at 4 Hz, close to the bending natural frequency, it is worthwhile investigating a gust closer to the torsional natural frequency. The next two cases shown are in the presence of a 6 Hz 1-cosine gust, with the first case increasing the damping ratio of the second mode only.

TABLE 3.2: Summary of Single Input Closed Loop Cases - 6 Hz 1-Cosine Gust, 10 m/s

Case 5 - $\zeta_{1,2}$ increased				Case 6 - $\zeta_{1,2}$ increased			
Parameter	OL	CL	ε	Parameter	OL	CL	ε
ζ_1	0.143	0.143	0.0131	ζ_1	0.143	0.160	0.0121
ζ_2	0.029	0.100		ζ_2	0.029	0.080	

Here, the performance metric is much larger than in the previous four cases. As the target is to increase the smallest damping ratio, there is a much larger effect on the system than increasing the larger damping ratio in Cases 1 and 3, especially as the gust frequency is close to the natural frequency of the assumed torsional mode.

The same process is carried out for harmonic gusts, however different closed loop cases must be used to abide by the maximum control surface deflection constraint. Additionally, only cases where the damping ratio/s are changed will be presented as it is clear

that changing the natural frequencies has little effect on the gust response for airspeeds significantly below flutter. Examples are given later in this section for an airspeed close to flutter.

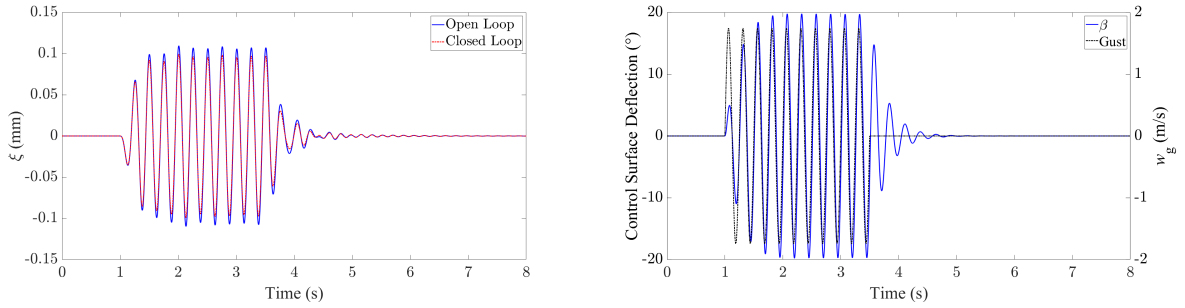

(a) (b)

FIGURE 3.3: Case 7 Response at 10 m/s to a 4 Hz Harmonic Gust in (a) Wing Bending, (b) Control Surface Deflection

There are ten full cycles of the harmonic gust, at a frequency of 4 Hz as this is reflected in the experimental results to be presented. The performance function output can be seen below.

TABLE 3.3: Summary of Single Input Closed Loop Cases - 4 Hz Harmonic Gust, 10 m/s

Case 7 - ζ_1 increased				Case 8 - $\zeta_{1,2}$ increased			
Parameter	OL	CL	ε	Parameter	OL	CL	ε
ζ_1	0.143	0.160	0.0064	ζ_1	0.143	0.155	0.0091
ζ_2	0.029	0.029		ζ_2	0.029	0.070	

It is clear from the results that increasing both damping ratios is more effective than increasing a single damping ratio by a larger amount. The performance function values are much larger for the harmonic gust case when compared to the 1-cos gust, but this is merely because there are ten gust cycles and therefore the responses last longer, forcing the RMS of the responses higher in both the open and closed loop responses compared to the 1-cosine case, and not because the controller is more effective at reducing the harmonic gust response. Similarly to the open loop case, a 6 Hz harmonic gust is applied. The primary aim of the closed loop system is to increase the second damping ratio in the closed loop system.

TABLE 3.4: Summary of Single Input Closed Loop Cases - 6 Hz Harmonic Gust, 10 m/s

Case 9 - ζ_2 increased				Case 10 - $\zeta_{1,2}$ increased			
Parameter	OL	CL	ε	Parameter	OL	CL	ε
ζ_1	0.143	0.143	0.0132	ζ_1	0.143	0.155	0.0122
ζ_2	0.029	0.044		ζ_2	0.029	0.041	

The decrease in performance function value from Case 9 to Case 10 suggests that increasing both damping ratios is not the most efficient controller. It is also seen consistently in all cases shown so far that increasing the smaller damping ratio has had a larger positive effect on the closed loop response.

It has been observed that using controller effort to change the natural frequencies of the system has been inefficient at airspeeds significantly below the flutter speed. However, as the natural frequencies converge with increasing airspeed, it is important to analyse cases closer to flutter. The following closed loop cases are carried out at 12 m/s, just below the flutter speed of 12.5 m/s.

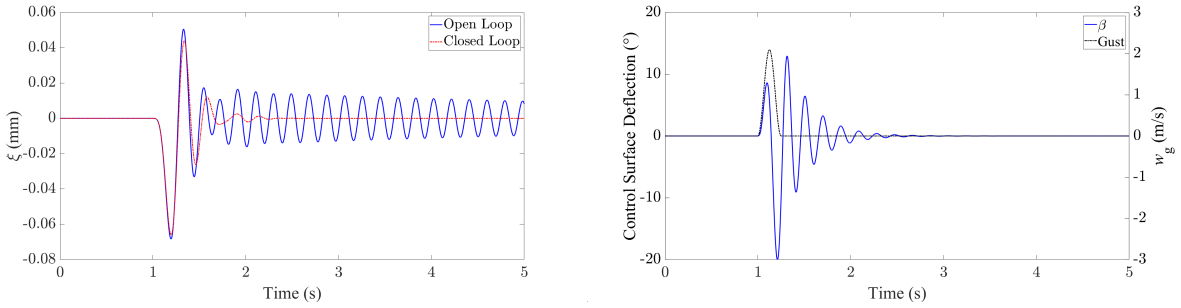

(a) (b)

FIGURE 3.4: Case 11 Response at 12 m/s to 4 Hz 1-Cosine Gust in (a) Wing Bending, (b) Control Surface Deflection

Figure 3.4 shows the first five seconds of the response of Case 11 to highlight the effectiveness of the controller. The open loop response has a settling time of 30 seconds, so both the open and closed loop cases are simulated for this amount of time. A 1-cosine gust of 4 Hz has been used as this is between the two natural frequencies of the system at 12 m/s and should therefore excite both modes effectively.

TABLE 3.5: Summary of Single Input Closed Loop Cases - 4 Hz 1-Cosine Gust, 12 m/s

Case 11 - ζ_2 increased				Case 12 - ζ_2 increased, ω_n separated			
Parameter	OL	CL	ε	Parameter	OL	CL	ε
ω_{n_1}	23.432	23.432	0.0238	ω_{n_1}	23.432	23.145	0.0239
ω_{n_2}	32.782	32.782		ω_{n_2}	32.782	35.404	
ζ_1	0.208	0.208		ζ_1	0.208	0.208	
ζ_2	0.004	0.110		ζ_2	0.004	0.075	
Case 13 - $\zeta_{1,2}$ increased				Case 14 - $\zeta_{1,2}$ increased, ω_n separated			
Parameter	OL	CL	ε	Parameter	OL	CL	ε
ω_{n_1}	23.432	23.432	0.0255	ω_{n_1}	23.432	22.729	0.0230
ω_{n_2}	32.782	32.782		ω_{n_2}	32.782	33.765	
ζ_1	0.208	0.220		ζ_1	0.208	0.215	
ζ_2	0.004	0.100		ζ_2	0.004	0.060	

Table 3.5 shows that changing a natural frequency as well is its corresponding damping ratio can be beneficial to the closed loop gust response, hence the increased ε value in Case 12 when compared to Case 11. However, the same can not be said when two damping ratios are altered. Case 14 is clearly the worst response, showing that shifting natural frequencies is an inefficient use of the control system, particularly when Case 13 provides the largest improvement to the gust response by far. Once again, a harmonic gust has been applied at 12 m/s also.

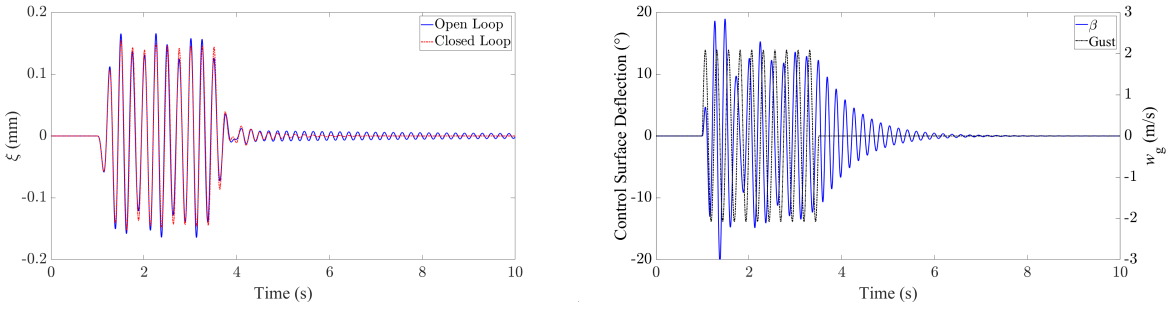

(a) (b)

FIGURE 3.5: Case 11 Response at 12 m/s to 4 Hz 1-Cosine Gust in (a) Wing Bending, (b) Control Surface Deflection

The open loop response decays after 40 seconds, so the closed loop responses are also simulated for the same amount of time for a fair comparison. Again, a gust frequency of 4 Hz is used to excite both modes.

TABLE 3.6: Summary of Single Input Closed Loop Cases - 4 Hz Harmonic Gust, 12 m/s

Case 15 - ζ_2 increased				Case 16 - ζ_2 increased, ω_n separated			
Parameter	OL	CL	ε	Parameter	OL	CL	ε
ω_{n_1}	23.432	23.432	0.0133	ω_{n_1}	23.432	23.145	0.0145
ω_{n_2}	32.782	32.782		ω_{n_2}	32.782	33.765	
ζ_1	0.208	0.208		ζ_1	0.208	0.208	
ζ_2	0.004	0.040		ζ_2	0.004	0.025	
Case 17 - $\zeta_{1,2}$ increased				Case 186 - $\zeta_{1,2}$ increased, ω_n separated			
Parameter	OL	CL	ε	Parameter	OL	CL	ε
ω_{n_1}	23.432	23.432	0.0156	ω_{n_1}	23.432	23.081	0.0123
ω_{n_2}	32.782	32.782		ω_{n_2}	32.782	33.274	
ζ_1	0.208	0.225		ζ_1	0.208	0.210	
ζ_2	0.004	0.035		ζ_2	0.004	0.020	

Cases 15 to 18 show the same trend as Cases 11 to 14 for the 1-cosine gust, with some benefit coming from increasing a single damping ratio and altering a single natural frequency, but not providing the same improvement as simply increasing both damping ratios. So despite being close to the flutter speed, the control aim should still be to increase both damping ratios.

It is clear from the Cases given in this section that the first aim of the gust response alleviation control system design is to increase the smallest damping ratio of modes whose natural frequencies are within the range of expected gusts. If there is substantial control authority available, then all damping ratios in this range should be increased with priority given to the lowest damping ratio. This trend is observed for both 1-cosine and harmonic gusts, for each gust frequency no matter which mode is more likely to be excited, and still applicable at airspeeds close to flutter.

3.4.3.2 Experimental

First of all, the open and closed loop cases must be compared. As described in Chapter 2, swept-sine test were carried out from 1 - 10 Hz. Then $\mathbf{R}(s)$ is extracted from the results of the open loop tests using RFP Method and the control gains are calculated, with the intention of increasing the damping ratios of both modes and leaving the two natural frequencies untouched as the numerical results suggest this is the most effective controller for alleviating gust responses. A sample rate of 1 kHz was used for these tests, which meant substantial signal noise was present as previously discussed in Chapter 2, and is

clearly present in the measured FRFs when plotted. A range of low-pass Butterworth filters were tested, from first order to fourth order and had no effect on the noise level. This analysis has been given in detail in Chapter 2. Again, this introduced errors to the RFP curve fit in the post process and limited the effect of the closed loop system. The comparison of open and closed loop FRFs measured at the spar (see Figure 2.10) can be seen in Figure 3.6:

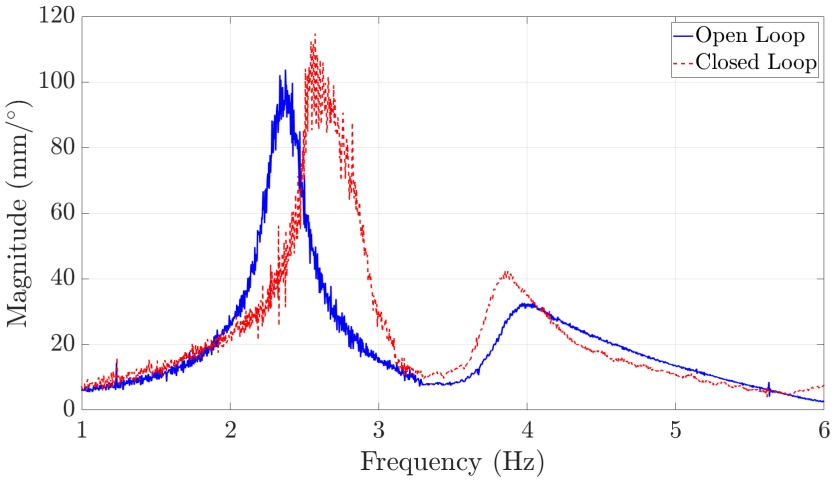

FIGURE 3.6: Comparison of Experimental Open Loop and Closed Loop FRFs at 5 m/s

TABLE 3.7: Natural Frequencies and Damping Ratios at 5 m/s

Parameter	Open Loop	Target Value	Closed Loop	Error (%)
f_{n_1}	2.37	2.37	2.57	8.44
f_{n_2}	3.95	3.95	3.85	2.53
ζ_1	0.0431	0.2	0.0428	78.60
ζ_2	0.0510	0.1	0.0476	52.40

The closed loop gains based on the target poles given in Table 3.7 are $\mathbf{f} = [-0.0312, 0.1180]$, and $\mathbf{g} = [-0.0150, 0.0058]$. It is clear from the results that the control has not worked as intended as the damping ratios have decreased in the closed loop, as well as the natural frequencies shifting closer together. Thus, it is worth discussing here some of the drawbacks to the results presented. First of all, the slipping control surface has already been discussed in Chapter 2, meaning the accuracy of the flap angle measurement from the encoder is uncertain. In addition to this, the motor control did not yet include an estimator feedforward system described in Figure 2.12, meaning there was a large error in the flap angle compared to the desired input, as shown in Figures 3.8, 3.10, 3.14 and 3.14.

Next, instead of measuring the torsional angle using two laser sensors, the displacement reading of the leading edge measurement was used by itself. This meant that as there was an attempt to damp the second mode in the closed loop case, instead the vertical motion of the leading edge measurement point was damped and caused the wing to twist around the measured point as opposed to reducing the torsion about the flexural axis as intended. This is evident in the increased magnitude of the second peak in Figure 3.6.

All displacements were measured in millimetres, and the flap angle in degrees, whereas the bending should have been measured in metres and any angles measured in radians. The significance of this is that the control theory outlined requires the correct units. To compensate for this mistake, the gains were scaled up by 1000 times so that their order of magnitude was correct. While this is not ideal, it did provide some promising results when gusts were applied, which will be discussed later in this section. While the FRF, $\mathbf{R}(s)$ and gain values may not be correct, the trends shown in the time domain results prove useful insight into the efficacy of the control method.

All of these issues were addressed following this wind tunnel campaign, thus will not be present in following Chapters.

After the closed loop FRF was generated, the controlled system was then tested in the presence of both 1-cosine and harmonic gusts. All gusts of a given profile were carried out in the same test, and significant time was given for the wing response to decay before the next gust was encountered to avoid any transient response interfering with the response to the next gust. Full Pole Placement is applied, using the closed loop case given in Table 3.7. Tests were carried out at 5 m/s due to the uncertainty of the closed loop stability, so testing at an airspeed significantly below the flutter speed was necessary. First of all, 1-cosine gusts are explored, with gust frequencies from 1-10 Hz in 1 Hz intervals.

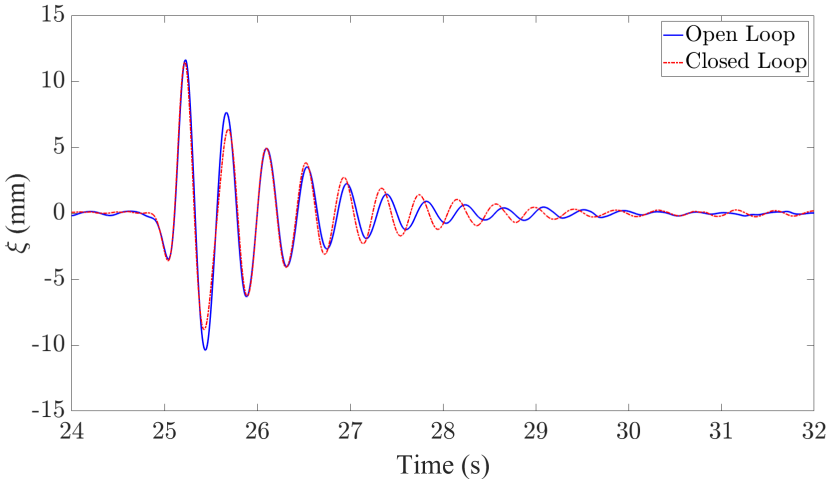

FIGURE 3.7: Open and Closed Loop Responses for a 4 Hz 1-Cosine Gust at 5 m/s

It can be seen in Figure 3.7 that the control is initially effective in reducing the largest peaks of the response, however the response takes longer to decay than the open loop system. One reason contributing to this is the error in control surface deflection angle, as shown by Figure 3.8:

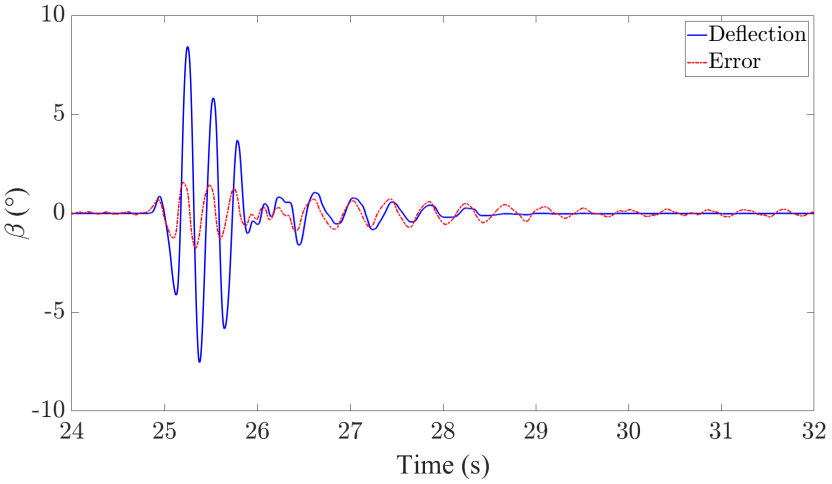

FIGURE 3.8: Control Surface Deflection and Error for a 4 Hz 1-Cosine Gust at 5 m/s

Clearly the control surface deflection is far from the intended input, with nearly 2° error in the initial part of the gust response. This is only the error from the encoder reading, and does not consider the unknown error due to the slipping control surface, however this should be minimal as the connection was checked before and after each test to account for this.

As the controller input is dependent on the bending and twisting of the wing, it is observed that the closed loop system is less effective for smaller wing responses to the gust. Figure 3.9 shows the response to a 1 Hz 1-cosine gust.

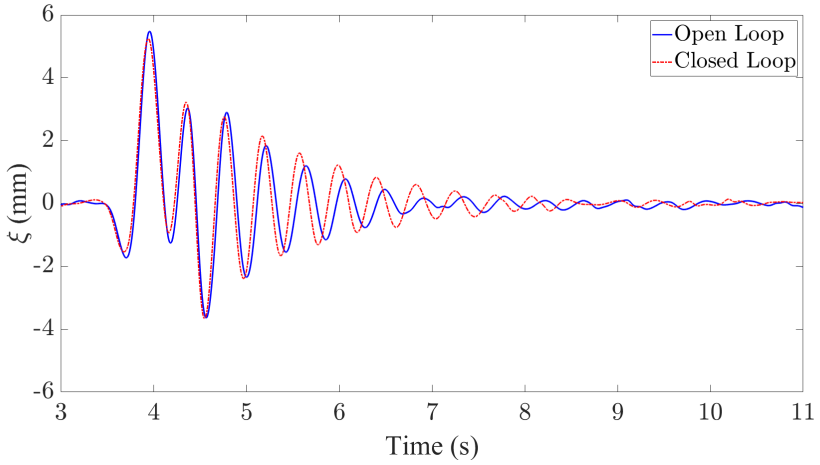

FIGURE 3.9: Open and Closed Loop Responses for a 1 Hz 1-Cosine Gust at 5 m/s

Again, it can be seen that the control is effective in reducing the initial peaks of the response, however after the first cycle the bending in the closed loop case is noticeably larger. The flap angle and error can be seen in Figure 3.10.

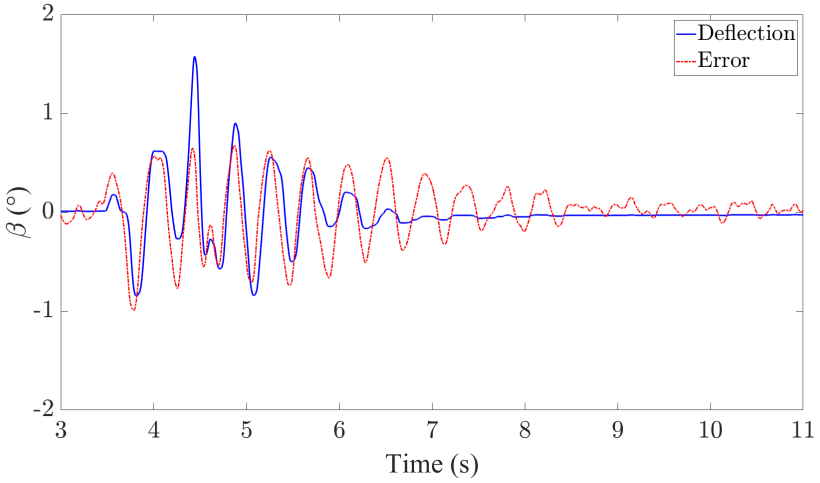

FIGURE 3.10: Control Surface Deflection and Error for a 1 Hz 1-Cosine Gust at 5 m/s

As the controller input is much less than in the 4 Hz case, it is observed that the error is much larger in comparison, particularly beyond 7 seconds where there is a significant period of time where the control surface is not deflected at all due to the lack of estimator in the motor position control. Should the estimator have been included in the motor

control, then perhaps the wing system would have greater damping and the closed loop response would be improved.

Next, harmonic gusts are considered. The gust frequencies were selected to cover the natural frequencies of the modes of interest. Gusts were applied for ten cycles, from 1-4 Hz in increments of 1 Hz. Ten cycles were used as if the gust frequency is close to the natural frequency, it gives time for signs of resonance to show, or for the response to achieve its maximum deflection. As in the 1-cosine test, this was carried out during the same test with sufficient time between gusts given for the wing vibration to decay. The largest wing deflection occurred during the 4 Hz gust and is shown in Figure 3.11.

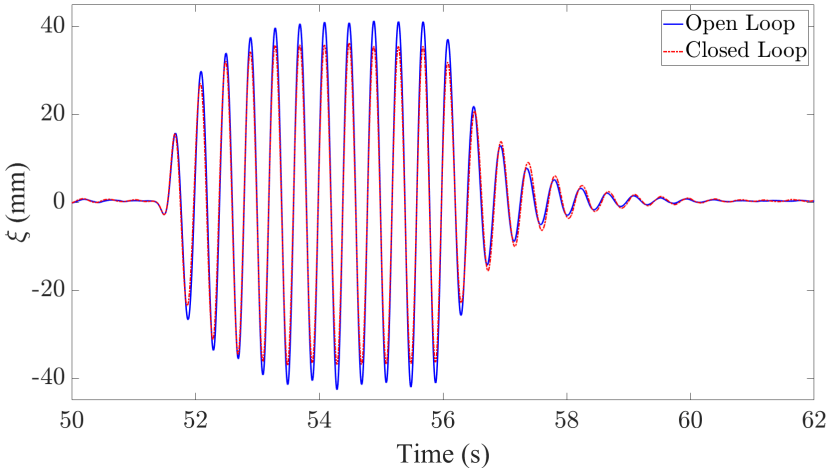

FIGURE 3.11: Open and Closed Loop Responses for a 4 Hz Harmonic Gust at 5 m/s

It can be seen that the controller is effective during the gust encounter and is reducing the response by up to 15%, however once the gust encounter has passed the closed loop response then takes longer to decay than the open loop. Overall, this is still an improvement when compared to the 1-cosine case, however, the flap deflection error is still present as seen in Figure 3.14.

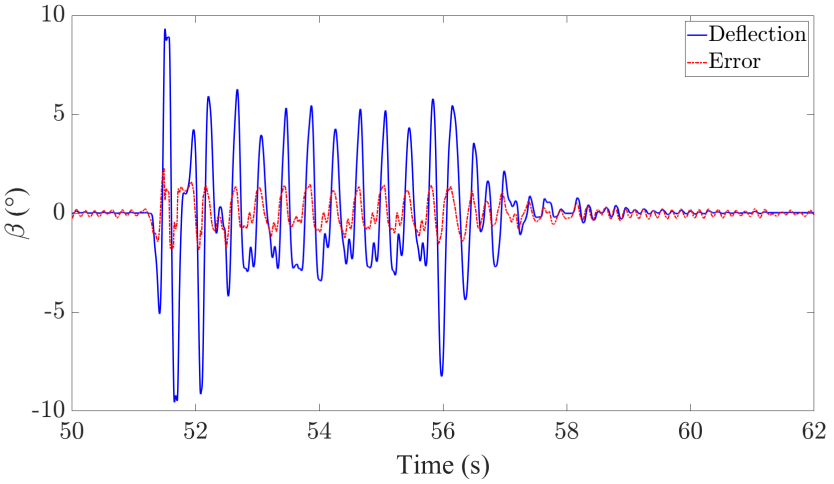

FIGURE 3.12: Control Surface Deflection and Error for a 4 Hz Harmonic Gust at 5 m/s

Similar to the 1-cosine case, the controller is less effective for small wing deflections. Figure 3.13 shows the response to a 1 Hz harmonic gust:

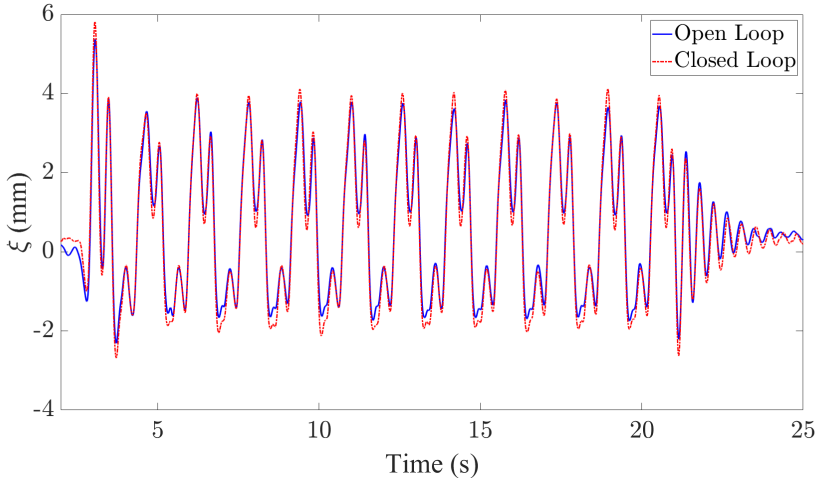

FIGURE 3.13: Open and Closed Loop Responses for a 1 Hz Harmonic Gust at 5 m/s

In this case, the closed loop system is noticeably worse than the open loop system for all stages of the gust response. The flap angle and error can be seen in Figure 3.14.

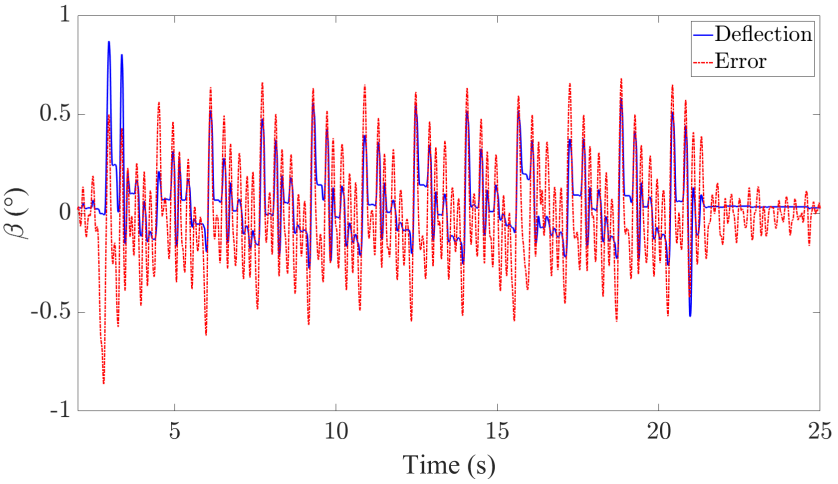

FIGURE 3.14: Control Surface Deflection and Error for a 1 Hz Harmonic Gust at 5 m/s

Now the flap angle error is significantly larger than the flap angle itself. This explains why the closed loop system is completely ineffective at reducing the 1 Hz harmonic gust response.

The results shown here have proven that the Receptance Method can be applied to a flexible wing, however the setup problems discussed have significantly affected the results. With the corrections made to the experimental setup, it is not unreasonable to suggest the Receptance Method would produce promising results. It is consistently seen that the maximum peaks are reduced during both 1-cosine and harmonic gusts of 4 Hz, which is promising despite the longer settling time.

3.5 MIMO Receptance Method

It requires a significant amount of control authority and power to be able to change the natural frequencies and damping ratios of a system. Therefore it makes sense to include more actuators into the system to improve controllability, as is the case with both MODFLEX models. The additional control surface should increase the control authority over the system and enable greater changes to the closed loop poles than using a single control surface. The Receptance Method must also be updated to implement MIMO control. The implementation of the MIMO system is based on the work of Ram and Mottershead [79].

3.5.1 Method

The first thing to consider is that instead of the single input β, the input vector $\mathbf{u}$ is used. In the case of both MODFLEX models, two control surfaces are used:

$$\begin{aligned} \mathbf{y_x} &= \mathbf{R}(s).\mathbf{u} \\ \mathbf{u} = \begin{bmatrix} \beta(t) \\ \gamma(t) \end{bmatrix} &= -\mathbf{F}^T\dot{\mathbf{z}}(t) - \mathbf{G}^T\mathbf{z}(t) \end{aligned} \tag{3.19}$$

Then, similar to Equation 3.11, the receptance matrix is obtained from experimental results and RFP.

$$\mathbf{R}(s) = \mathbf{H}(s) \cdot \mathbf{B}_d = \begin{bmatrix} \dfrac{\mathbf{N}_1(s)}{D(s)} \\ \dfrac{\mathbf{N}_2(s)}{D(s)} \end{bmatrix} \tag{3.20}$$

where $\mathbf{R}(s)$ is a $n \times m$ matrix and $\mathbf{B}_d = [\mathbf{b}_1,\ \mathbf{b}_2, \ldots,\ \mathbf{b}_j]$ is a $n \times j$ matrix of combined control distribution vectors, where m is the number of actuators in the system. Now the key difference in methods, as mentioned earlier, becomes apparent. As opposed to using the Sherman-Morrison formula, it is replaced with the eigen-assignment method to ensure that only the intended poles are placed. With $k = 1, 2, \ldots, p$ and $j = 1, 2, \ldots, m$,

$$\begin{bmatrix} \mathbf{P}_1 \\ \vdots \\ \mathbf{P}_p \\ \mathbf{Q}_{p+1} \\ \vdots \\ \mathbf{Q}_{2n} \end{bmatrix} \begin{pmatrix} \mathbf{g}_1 \\ \vdots \\ \mathbf{g}_m \\ \mathbf{f}_1 \\ \vdots \\ \mathbf{f}_m \end{pmatrix} = \begin{pmatrix} \mathbf{e} \\ \mathbf{0} \end{pmatrix} \tag{3.21}$$

$$\mathbf{P}_k = \begin{bmatrix} \mathbf{w}_k^T & \mathbf{0} & \cdots & \mathbf{0} & \mu_k\mathbf{w}_k^T & \mathbf{0} & \cdots & \mathbf{0} \\ \mathbf{0} & \mathbf{w}_k^T & \cdots & \mathbf{0} & \mathbf{0} & \mu_k\mathbf{w}_k^T & \cdots & \mathbf{0} \\ \vdots & \vdots & \ddots & \vdots & \vdots & \vdots & \ddots & \vdots \\ \mathbf{0} & \mathbf{0} & \cdots & \mathbf{w}_k^T & \mathbf{0} & \mathbf{0} & \cdots & \mu_k\mathbf{w}_k^T \end{bmatrix}$$

$$\text{and } \mathbf{Q}_k = \begin{bmatrix} \mathbf{v}_k^T & \mathbf{0} & \cdots & \mathbf{0} & \lambda_k\mathbf{v}_k^T & \mathbf{0} & \cdots & \mathbf{0} \\ \mathbf{0} & \mathbf{v}_k^T & \cdots & \mathbf{0} & \mathbf{0} & \lambda_k\mathbf{v}_k^T & \cdots & \mathbf{0} \\ \vdots & \vdots & \ddots & \vdots & \vdots & \vdots & \ddots & \vdots \\ \mathbf{0} & \mathbf{0} & \cdots & \mathbf{v}_k^T & \mathbf{0} & \mathbf{0} & \cdots & \lambda_k\mathbf{v}_k^T \\ & & & & & & & \end{bmatrix} \tag{3.22}$$

$$\mathbf{G} = \begin{bmatrix} \mathbf{g}_1 & \cdots & \mathbf{g}_m \end{bmatrix}, \ \mathbf{F} = \begin{bmatrix} \mathbf{f}_1 & \cdots & \mathbf{f}_m \end{bmatrix} \tag{3.23}$$

where m is the number of actuators, n is the number of degrees of freedom and p is the number of poles place. If $m = 1$ and $p = 2$ Equations 3.24-26 become a SISO system. $\mathbf{P}_k$ and $\mathbf{Q}_k$ are both $m \times 2m$ matrices, where $\mathbf{P}_k$ contains the placed eigenvectors $\mathbf{w}_k^T$ and placed poles μ_k, and $\mathbf{Q}_k$ contains the untouched eigenvectors $\mathbf{v}_k^T$ and untouched poles λ_k. The vector $\mathbf{e}$ is used to distribute the controller work according to the desired weighting factors. This also depends on how many actuators are included in the closed loop system. As the model in this work makes use of two actuators, $\mathbf{e}$ is described as the following:

$$\mathbf{e} = \begin{bmatrix} \boldsymbol{\alpha}_1 \\ \vdots \\ \boldsymbol{\alpha}_p \end{bmatrix}, \quad \boldsymbol{\alpha} = \begin{bmatrix} \alpha_1 \\ \vdots \\ \alpha_m \end{bmatrix} \tag{3.24}$$

where $\alpha_{1:m}$ can be tuned to produce the minimum overall control work. For the work presented in this Chapter, flat aerofoil theory has been used which determines control surface authority based on the flap size alone. As the MODFLEX wing has $x_{h_{LE}} = x_{h_{TE}}$, their authority is numerically the same. The values of α are selected as 1, so there is equal distribution to both control surfaces. This means that the two control surfaces have identical responses.

Simply put, if the user still wishes to place all poles using multiple control surfaces (as shown in this work) the $\mathbf{Q}$ matrix is not necessary, and a set of $\mathbf{P}$ matrices are used to include all desired pole pairs. The full pole-placement variation is given as:

$$\begin{bmatrix} \mathbf{P}_1 \\ \vdots \\ \mathbf{P}_p \end{bmatrix} \begin{pmatrix} \mathbf{g}_1 \\ \vdots \\ \mathbf{g}_m \\ \mathbf{f}_1 \\ \vdots \\ \mathbf{f}_m \end{pmatrix} = \begin{pmatrix} \mathbf{e} \end{pmatrix} \tag{3.25}$$

As in the SIMO case, the array of $\mathbf{P}_{1:p}$ is then inverted using the pseudoinverse as it is non-square, and multiplied by $\mathbf{e}$ to obtain the control gain vectors $\mathbf{g}_{1:m}$, $\mathbf{f}_{1:m}$.

3.5.2 Results

Only numerical results are presented here. As shown in the Single Input section, for airspeeds significantly below flutter the additional controller effort required to shift the closed loop natural frequencies results in a worse response than if the aim is to simply increase the damping ratios. Thus, only cases where the damping ratios are increased are explored for a 10 m/s airspeed as the SIMO results show that changing the natural frequencies is not effective at this airspeed. Given that the MIMO system has more control authority, shifting the natural frequencies will be explored at 12 m/s, close to the open loop flutter speed.

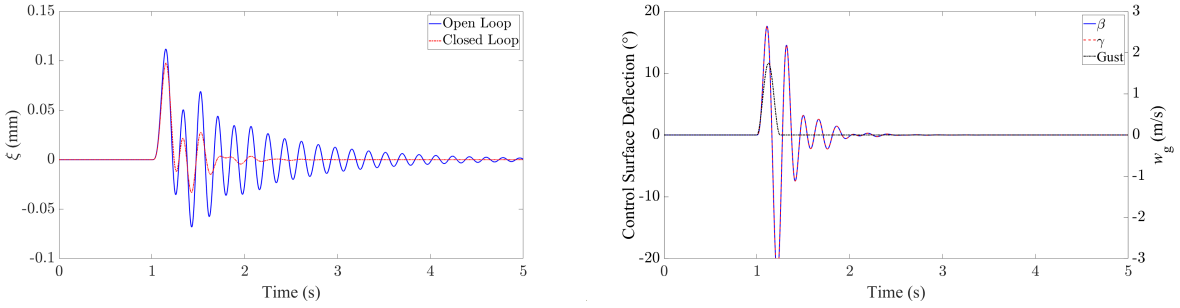

(a) (b)

FIGURE 3.15: Case 19 Response at 10 m/s to 4 Hz 1-Cosine Gust in (a) Wing Bending, (b) Control Surface Deflection

Figure 3.15 shows the first five seconds of the response to a 4 Hz 1-cosine gust at 10 m/s, but now of course the closed loop response benefits from the additional control surface. The improvement compared to Figure 3.2 is clear, and the MIMO cases in this section are subjected to the same performance function as in the SIMO section.

TABLE 3.8: Summary of Multiple Input Closed Loop Cases - 4 Hz 1-Cosine Gust, 10 m/s

Case 19 - ζ_2 increased				Case 20 - $\zeta_{1,2}$ increased			
Parameter	OL	CL	ε	Parameter	OL	CL	ε
ζ_1	0.143	0.143	0.0062	ζ_1	0.143	0.200	0.0068
ζ_2	0.029	0.130		ζ_2	0.029	0.100	

As expected, the increased control authority produces a larger improvement when compared to the SIMO Cases 1 and 3. There is a much larger increase in damping ratios thanks to the additional control authority, and having essentially twice the control authority has yielded three times the performance function value. As in the SIMO section, a 6 Hz gust is now applied to excite the torsion mode.

TABLE 3.9: Summary of Multiple Input Closed Loop Cases - 6 Hz 1-Cosine Gust, 10 m/s

Case 21 - ζ_2 increased				Case 22 - $\zeta_{1,2}$ increased			
Parameter	OL	CL	ε	Parameter	OL	CL	ε
ζ_1	0.143	0.143	0.0142	ζ_1	0.143	0.175	0.0136
ζ_2	0.029	0.115		ζ_2	0.029	0.080	

Again, the trend follows that of the SIMO case, and the improvement to the performance function values are similar to those in the 4 Hz cases. The increased control authority also shows improvement in comparison to SIMO Cases 5 and 6. Now, harmonic gusts are applied.

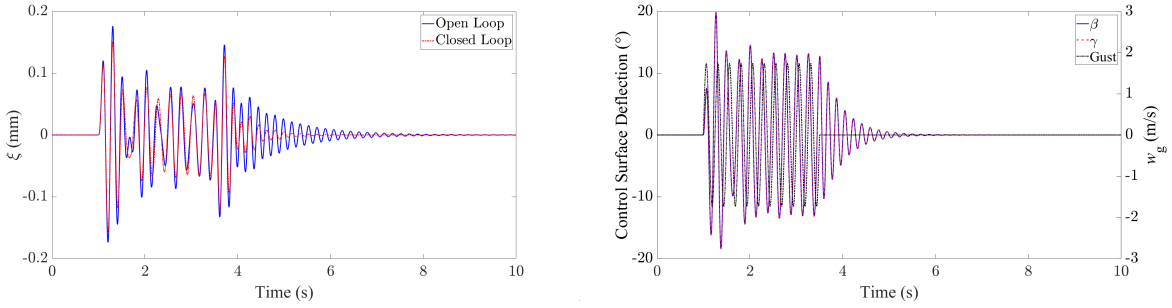

(a) (b)

FIGURE 3.16: Case 21 Response at 10 m/s to 4 Hz Harmonic Gust in (a) Wing Bending, (b) Control Surface Deflection

As in the SIMO case, the responses are simulated for 40 seconds as this is the settling time of the open loop system. Table 3.10 shows the MIMO cases in the presence of a 4 Hz harmonic gust at 10 m/s airspeed.

TABLE 3.10: Summary of Multiple Input Closed Loop Cases - 4 Hz Harmonic Gust, 10 m/s

Case 23 - ζ_2 increased				Case 24 - $\zeta_{1,2}$ increased			
Parameter	OL	CL	ε	Parameter	OL	CL	ε
ζ_1	0.143	0.143	0.0132	ζ_1	0.143	0.170	0.0264
ζ_2	0.029	0.062		ζ_2	0.029	0.055	

It is clear that the increased number of gust cycles demands more from the control system, hence why the damping ratios cannot be increased as high as in the 1-cosine case. However, while in previous cases increasing both damping ratios has made slight improvements to the performance function, Case 24 is twice as effective as Case 23.

TABLE 3.11: Summary of Multiple Input Closed Loop Cases - 6 Hz Harmonic Gust, 10 m/s

Case 25 - ζ_2 increased				Case 26 - $\zeta_{1,2}$ increased			
Parameter	OL	CL	ε	Parameter	OL	CL	ε
ζ_1	0.143	0.143	0.0174	ζ_1	0.143	0.160	0.0253
ζ_2	0.029	0.060		ζ_2	0.029	0.048	

Similarly to previous cases, it is given that increasing both damping ratios has the greatest effect on the closed loop gust response. However, the improvement is less than for the 4 Hz case, further suggesting that increasing the damping ratio of the natural frequency closest to the gust frequency has a larger improvement on the system's response.

As there is now more control authority than in the SIMO case, the following cases at 12 m/s once again include changing the natural frequencies of the system. The aim is to have a greater change of the natural frequencies than in the SIMO study to see if the gust response is improved and to confirm if the control authority was indeed a limiting factor.

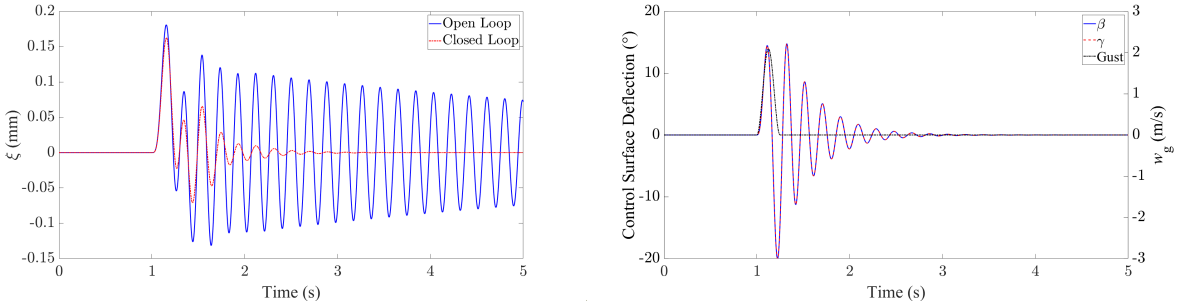

(a) (b)

FIGURE 3.17: Case 27 Response at 12 m/s to 4 Hz 1-Cosine Gust in (a) Wing Bending, (b) Control Surface Deflection

Figure 3.17 again shows the response to a 4 Hz 1-cosine gust at 12 m/s, this time showing closed loop Case 25, which is given in Table 3.12 below.

TABLE 3.12: Summary of Multiple Input Closed Loop Cases - 4 Hz 1-Cosine Gust, 12 m/s

Case 27 - ζ_2 increased				Case 28 - ζ_2 increased, ω_n separated			
Parameter	OL	CL	ε	Parameter	OL	CL	ε
ω_{n_1}	23.432	23.432	0.0242	ω_{n_1}	23.432	23.432	0.0253
ω_{n_2}	32.782	32.782		ω_{n_2}	32.782	33.438	
ζ_1	0.208	0.208		ζ_1	0.208	0.208	
ζ_2	0.004	0.115		ζ_2	0.004	0.070	
Case 29 - $\zeta_{1,2}$ increased				Case 30 - $\zeta_{1,2}$ increased, ω_n separated			
Parameter	OL	CL	ε	Parameter	OL	CL	ε
ω_{n_1}	23.432	23.432	0.0260	ω_{n_1}	23.432	22.963	0.0232
ω_{n_2}	32.782	32.782		ω_{n_2}	32.782	33.437	
ζ_1	0.208	0.250		ζ_1	0.208	0.220	
ζ_2	0.004	0.080		ζ_2	0.004	0.050	

The results in Table 3.12 confirm what was seen in Table 3.6, where increasing a damping ratio and changing the natural frequency of a single mode does show positive results, however attempting to do this for both modes actually produces the worst result of all four cases.

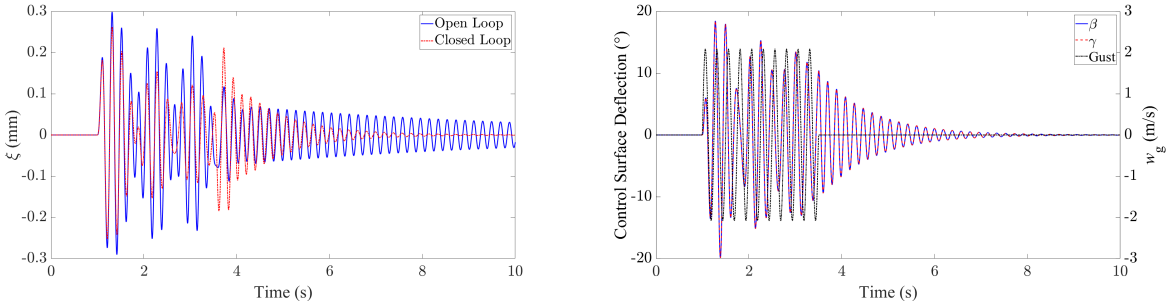

(a) (b)

FIGURE 3.18: Case 31 Response at 12 m/s to 4 Hz Harmonic Gust in (a) Wing Bending, (b) Control Surface Deflection

Figure 3.18 shows the first ten seconds of the Case 31 response. The details of which can be seen in Table 3.13 below.

TABLE 3.13: Summary of Multiple Input Closed Loop Cases - 4 Hz Harmonic Gust, 12 m/s

Case 31 - ζ_2 increased				Case 32 - ζ_2 increased, ω_n separated			
Parameter	OL	CL	ε	Parameter	OL	CL	ε
ω_{n_1}	23.432	23.432	0.0142	ω_{n_1}	23.432	23.432	0.0146
ω_{n_2}	32.782	32.782		ω_{n_2}	32.782	33.274	
ζ_1	0.208	0.208		ζ_1	0.208	0.208	
ζ_2	0.004	0.046		ζ_2	0.004	0.027	
Case 33 - $\zeta_{1,2}$ increased				Case 34 - $\zeta_{1,2}$ increased, ω_n separated			
Parameter	OL	CL	ε	Parameter	OL	CL	ε
ω_{n_1}	23.432	23.432	0.0165	ω_{n_1}	23.432	23.081	0.0128
ω_{n_2}	32.782	32.782		ω_{n_2}	32.782	33.274	
ζ_1	0.208	0.230		ζ_1	0.208	0.210	
ζ_2	0.004	0.035		ζ_2	0.004	0.022	

Finally, Cases 29 to 32 confirm the trends seen throughout this Chapter. The results highlight the importance of carefully selecting how to affect the closed loop poles to best improve the gust response. Generally, the first point of call is to increase the minimum damping ratio, however the natural frequencies of the two modes in the MODFLEX model are very close together. The results have also revealed that it is important to increase the damping ratio of a certain mode if its natural frequency is close to the gust frequency, so this should also be a priority, particularly in a system where the natural frequencies have a much larger separation than MODFLEX. While changing the natural frequency and damping ratio of a single mode proves to be marginally beneficial when compared to only increasing the damping ratio, this effect could be amplified for a different system. One thing is clear, that attempting to separate the natural frequencies is an inefficient use of the available control authority and the main focus should be to increase the system damping during gust encounters.

3.6 Summary

Pole Placement via Receptance Method for gust response alleviation has been considered both numerically and experimentally. Numerically it was shown that for airspeeds significantly below the flutter speed, control effort is best spent increasing at least one of the damping ratios, as changing the natural frequencies of the system did very little

to improve the gust response, even when the gust frequency was close to the natural frequencies of one of the modes. Including a second control surface and using MIMO control gave the same results, however more changes could be made to the closed loop poles due to the increased control authority.

Experimentally, the SIMO Receptance Method was applied with the aim of increasing the damping ratios of the bending and torsion modes. Due to time constraints and problems with the test setup, experimental results did not reflect the intended closed loop system and therefore do not successfully validate the numerical results. A suggestion for future work would be to correct the problems in the experimental setup and repeat the tests carried out. Additionally, the MIMO receptance method should be implemented and explored under the same conditions.

In order to carry out the work in future and to obtain more effective results, the motor control loop should include a feedforward estimator to reduce the large error between demanded and actual control surface deflection. This was included in the experimental work in Chapter 4, successfully reducing the control surface error to 0.1° for high deflection and natural frequencies. Additionally, an update to the wing design to prevent the control surfaces from slipping off of the motor would prevent further error. This is implemented into the design of the MODFLEX 2.0 wing, as shown in Chapter 2.

Chapter 4

FLUTTER SPEED EXTENSION VIA ITERATIVE GAIN SCHEDULING

4.1 Introduction

The method proposed in this Chapter utilises the previously described Receptance Method applied iteratively for a range of airspeeds with the aim of extending the flutter speed. Flutter is induced by two natural frequencies of the system converging and coupling, and by one or more of the damping ratios becoming negative. The aim behind gain scheduling is to optimise controller gains based on an ideal separation of the natural frequencies and increasing of the damping ratios of the first bending and torsion modes for each airspeed [85, 86, 136]. Theoretically, this should extend the speed at which flutter is onset. Single and multiple input systems are both studied, with the key differences in their respective formulations being highlighted. The single input system is investigated both numerically and experimentally, whereas the multiple input system is only investigated numerically due to problems faced with the single input tests and time constraints. While this was previously applied to a pitch-plunge aerofoil [86], this work uses a simplified flexible wing model both numerically for single and multiple input, and experimentally for the single

input configuration. The model used in this Chapter is MODFLEX 2.0, which has been described in detail in Chapter 2.

It is worth noting that all problems with experimental setup described in Chapter 3 were acknowledged and rectified before the work in this Chapter was carried out.

4.2 Control Approach

Before the details of the receptance method are given, it is important to outline the approach taken towards the flutter speed extension problem. First, consider an arbitrary aeroservoelastic system with an open loop flutter speed of U_f. This is demonstrated in Figure 4.1, where the green area represents where receptance measurements can be taken, the red area is immeasurable. U_{lim} is the largest airspeed where receptance measurements can be taken as receptance data cannot be measured at airspeeds close to, or above, U_f due to the increasing instability and interaction/coupling between modes. The interaction of multiple vibration modes leads to unpredictable vibration behaviour and difficulty interpreting receptance data. Practically speaking, in wind tunnel tests the conditions may not be constant and a small change in the test airspeed could lead to instability, so even if receptance data were clear close to flutter there is a higher risk in carrying out tests above U_{lim}.

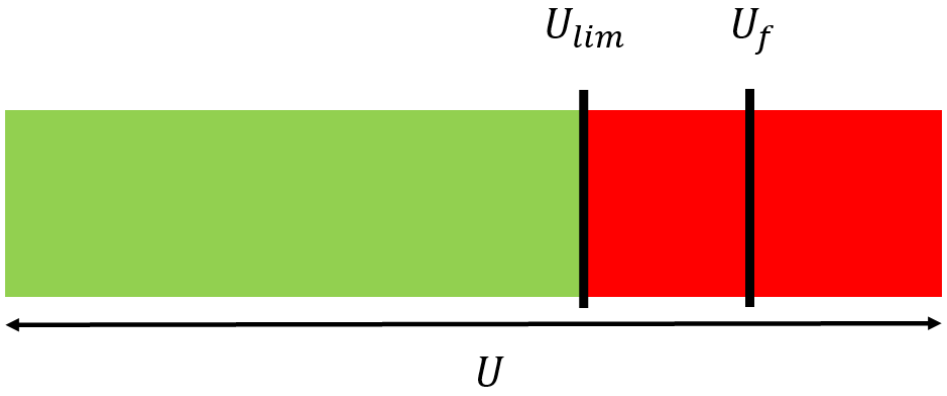

FIGURE 4.1: Demonstration of Measurable and Immeasurable Receptance For Certain Airspeeds in an Arbitrary System

First, the receptance is measured at an airspeed up to U_{lim} and a controller is designed at this airspeed, with the aim of increasing the damping ratios of both modes and separating

their natural frequencies. Then, the controller is implemented and receptance data is gathered from the closed loop system at the same airspeed. The closed loop system then will have increased U_{lim} so that it is higher than in the open loop system. This can be carried out iteratively, causing U_{lim} and U_f to be increased with each controller iteration. The iterations will eventually stop when U_{lim} and U_f cannot be increased any further due to limits of the control surface inputs, meaning the controller has reached its final form.

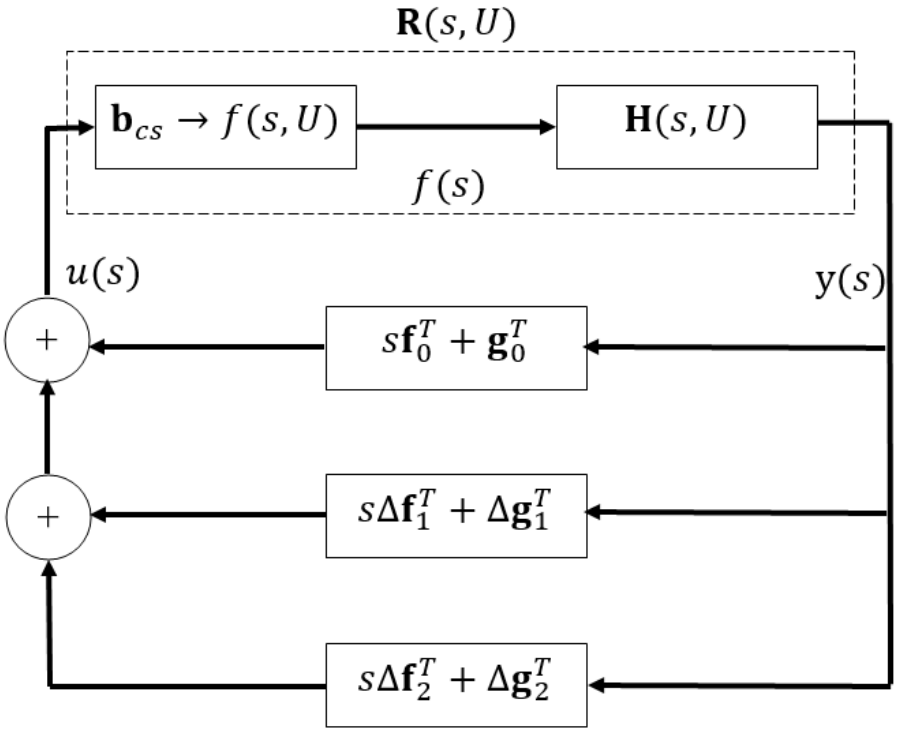

FIGURE 4.2: Block Diagram Demonstrating Iterative Control Process

Figure 4.2 shows the block diagram of the iterative control process for the first three iterations of a single input system. The input to the system $\mathbf{u}(s)$ is given by

$$\mathbf{u}(s) = \mathbf{u}_0(s) + \Delta\mathbf{u}(s) \tag{4.1}$$

which is equivalent to

$$\mathbf{u}(s) = \left(s\mathbf{f}_0^T + \mathbf{g}_0^T\right)\mathbf{y}(s) + \sum_{j=1}^{i}\left(s\Delta\mathbf{f}_i^T + \Delta\mathbf{g}_i^T\right)\mathbf{y}(s) \tag{4.2}$$

where $\mathbf{y}(s)$ is the system output, $\mathbf{f}_0$ and $\mathbf{g}_0$ are the control gains obtained via Receptance method for the first iteration, and $\Delta\mathbf{f}_i$ and $\Delta\mathbf{g}_i$ are the incremental difference in control gains between each iteration. The control gains for each iteration are given by

$$\begin{aligned} \mathbf{f}_i &= \mathbf{f}_0 + \sum_{j=1}^{i} \Delta\mathbf{f}_j \\ \mathbf{g}_i &= \mathbf{g}_0 + \sum_{j=1}^{i} \Delta\mathbf{g}_j \end{aligned} \tag{4.3}$$

Then, $\mathbf{b}_{cs}$ is the force distribution vector for the control surface, $f(s,U) = \mathbf{b}_{cs}\mathbf{u}(s)$ is the force applied to the system by the control surface. $\mathbf{H}(s,U)$ is the measured receptance of the system and $\mathbf{R}(s,U)$ is the receptance of the system to the control surface input. The full second-order Equation of Motion is then given for any iteration of the controller as:

$$\begin{aligned} &\mathbf{A}\ddot{\mathbf{q}} + (\rho U\mathbf{B} + \mathbf{D})\,\dot{\mathbf{q}} + \left(\rho U^2\mathbf{C} + \mathbf{E}\right)\mathbf{q} = \mathbf{b}_{cs}\mathbf{u} \\ &\text{where} \quad \mathbf{u} = \mathbf{f}_i\dot{\mathbf{q}} + \mathbf{g}_i\mathbf{q} \end{aligned} \tag{4.4}$$

4.2.1 Genetic Algorithm

One drawback of the closed loop systems in Chapter 3 is that closed loop poles were selected through trial and error and gradually changed until the control surface deflection limits were reached. Additionally, the control aim has now changed and the need for altering the closed-loop natural frequencies has risen. This introduced the need for a more effective method of selecting the closed loop poles, as described in the previous Section 4.2, and led to the inclusion of Derivative Evolution to optimise the closed loop poles based on the available control authority. Derivative Evolution is used to find a global minimum for the given constraints [87]. In this work, the constraint is the control surface angle, i.e. control authority available, and a range of closed loop natural frequencies and damping ratios (and therefore poles) are tested via the genetic algorithm to minimise an objective function that weights the increase of damping ratios against the natural frequency separation. The resulting control gains from the receptance method are tested

in a constraint function to check if the maximum control surface angle is exceeded. The objective and constraint functions will be detailed throughout this Chapter, as they change depending on the system used.

The first detail required for the use of Genetic Algorithm is the initial population. This is selected as the values that will be tested in the objective function, in the case of this work that is the two natural frequencies and damping ratios of the open loop system. Ten populations are then used for the first generation of the genetic algorithm; the initial population and nine randomly generated populations based on selected upper and lower bounds of the four values within the population. Ten populations were selected to balance between solution time and computing power.

TABLE 4.1: Upper and Lower Bounds for Genetic Algorithm Populations

Value	Lower Bound	Upper Bound
$\zeta_{1,2}$	0	1
ω_{n_1}	0	ω_{n_1}
ω_{n_2}	ω_{n_2}	$2\omega_{n_2}$

Table 4.1 shows the values selected for the upper and lower bounds of each parameter in the populations. These are selected so that the system cannot become overdamped and the natural frequency separation is forced to remain the same, or increase.

4.3 SIMO Control

Initially, single-input multiple-output (SIMO) control is implemented and uses the receptance method discussed in the previous Chapter. The trailing edge control surface is used for control, meaning it is also used for excitation experimentally to generate the open loop FRFs so that the receptance can be found. Both open and closed loop FRFs are generated using swept-sine tests, as detailed in Chapter 2. Both numerical and experimental results will be presented here.

4.3.1 Receptance Method

For a single-input, linear aeroservoelastic system with n-degrees of freedom, the input-output equation is given as:

$$\mathbf{y}(s) = \mathbf{r}(s, U)u(s) \tag{4.5}$$

where $\mathbf{y}(s)$ is the output vector, $\mathbf{r}(s, U)$ is the transfer function vector and $u(s)$ is the input. In the case of this work, the input for a single input system is deflection from the trailing edge control surface, β. For the standard Receptance Method described in Chapter 3.4, the input is selected as:

$$u(s) = \left(s\mathbf{f}^T + \mathbf{g}^T\right)\mathbf{y}(s) \tag{4.6}$$

The control gain vectors are represented by $\mathbf{f}$ and $\mathbf{g}$. For this study, the input equation is modified so that the input is scheduled according to the airspeed U:

$$u(s, U) = \left(s\mathbf{f}(U)^T + \mathbf{g}(U)^T\right)\mathbf{y}(s) \tag{4.7}$$

This means that the controller is only engaged at the given airspeed, which is key to the iterative process as each controller iteration is created for its given airspeed. Then, substituting Equation 4.7 into Equation 4.5 gives

$$\mathbf{y}(s) = \mathbf{r}(s, U)\left(s\mathbf{f}(U)^T + \mathbf{g}(U)^T\right)\mathbf{y}(s) \tag{4.8}$$

The aim is to design a controller and determine gains for a range of airspeeds. The set of reference speeds $U_1, U_2, \ldots, U_p$ is chosen, and at each speed U_j the set of closed-loop poles is $\boldsymbol{\mu}_j = [\mu_{j_1}, \mu_{j_2}, \ldots, \mu_{j_{2n}}]$, resulting in sets of $\mathbf{f}_p$ and $\mathbf{g}_p$ after controller design is complete.

4.3.2 Controller Iteration

Now that the updated Receptance Method has been presented, we can define the iteration process. First, let each pole μ_{j_i} be decomposed as:

$$\mu_{j_i} = -\zeta_{j_i}\omega_{j_i} \pm \mathbf{i}\omega_{j_i}\sqrt{1 - \zeta_{j_i}^2} \tag{4.9}$$

where ζ_{j_i} and ω_{j_i} are the damping ratio and natural frequency of each pole, respectively. At each airspeed U_j an objective function is defined as:

$$\begin{gathered}\rho_j = -\min\left(\zeta_{j_i}\right) + \alpha \max\left(\frac{\min\left(\omega_{j_i}, \omega_{j_k}\right)}{\left(\omega_{j_i} - \omega_{j_k}\right)^2}\right) \\ \zeta_j \in \left\{\zeta_{j_i}\right\}_{i=1}^{n}, \omega_{j_{i,k}} \in \left\{\omega_{j_{i,k}}\right\}_{i=1}^{n}\end{gathered} \tag{4.10}$$

The controller iteration number is given by the subscript j, and the number of modes is represented by i.The genetic algorithm works to minimise the objective function. The damping ratio term selects the smallest damping ratio, and the negative sign ensures that increasing the damping ratio will lower the value of ρ_j. Similarly, in the natural frequency term, the difference between the natural frequencies is present in the denominator so that increasing the spacing will again reduce the value of ρ_j. A weighting factor α is used as a penalty of the frequency separation to the minimum damping. This can be changed through trial and error to have greater effect on either of the terms, depending on user preference. One of the drawbacks of the receptance method presented in the previous Chapter was that there was no way to select closed loop poles, knowing that the limits of the control surface would not be reached. A set of gain constraints can be written so that the control surface will not exceed a given deflection angle, and the constraint is defined as:

$$\begin{gathered}\sqrt{\mathbf{f}^T \mathbf{\Lambda}_f \mathbf{f}} + \sqrt{\mathbf{g}^T \mathbf{\Lambda}_g \mathbf{g}} \leq \beta_{max} \\ \mathbf{\Lambda}_f = \begin{bmatrix} 0.23 & 0 \\ 0 & 0.262 \end{bmatrix}, \quad \mathbf{\Lambda}_g = \begin{bmatrix} 0.1 & 0 \\ 0 & 0.096 \end{bmatrix}\end{gathered} \tag{4.11}$$

where $\mathbf{\Lambda}_f, \mathbf{\Lambda}_g \in \mathbb{R}^{n \times n}$ are diagonal matrices with entries weighting the control gains associated with $\mathbf{f}$ and $\mathbf{g}$ using the maximum open loop values of displacement and velocity of each degree of freedom or assumed mode, which in the case of this model were found during the swept sine tests at 30 m/s. To implement gain scheduling, the closed loop system for the first iteration will be used as the new 'open loop' system at the next airspeed, so that the next iteration of the control can be calculated. The iteration steps are as follows:

(1) Obtain receptance r_1 and speed U_1.

(2) At speed U_1, choose desired eigenvalues (using Derivative Evolution and constraints for optimisation) and solve for $\mathbf{f}_1$ and $\mathbf{g}_1$.

(3) With the controller active, measure r_2 at speed U_2 so that the transfer function is as follows:

$$\hat{\mathbf{r}}_2 = \hat{\mathbf{H}}(s).\mathbf{b} = \begin{bmatrix} \dfrac{N_1(s)}{D(s)} \\ \dfrac{N_2(s)}{D(s)} \end{bmatrix}$$

$$\text{where } \hat{\mathbf{H}}(s) = \mathbf{H}(s) - \frac{\mathbf{H}(s)\mathbf{b}\left(\mathbf{g} + s\mathbf{f}\right)^T \mathbf{H}(s)}{1 + \left(\mathbf{g} + s\mathbf{f}\right)^T \mathbf{H}(s)\mathbf{b}}$$

(4) At U_2, choose desired eigenvalues and calculate new $\mathbf{f}$ and $\mathbf{g}$ gains using $\hat{\mathbf{r}}_2$.

(5) Repeat 3-4 for each airspeed.

4.3.3 Results

This section will describe in detail the studies carried out numerically in order to validate the described method and to find ideal parameters for the closed loop system to carry out tests in the wind tunnel. Several parameters can be arbitrarily selected in the controller design, so each should be investigated to find an ideal controller.

4.3.3.1 Numerical

First of all, numerical studies were carried out to determine the effects of certain parameters on the final, extended flutter speed of the system. These considerations are as follows:

(1) Value of the objective function weighting factor, α.

(2) Maximum allowed control surface deflection, β_{max}.

(3) Airspeed where the iterative process begins, U_1.

(4) Step size of the airspeed between controller iterations, ΔU.

Each of these variables need to be investigated so that the iterative controller system can be optimised and result in the highest flutter speed for the system. It is important to note that the four considerations have been carried out in an order selected by the author, and the final result shown in this section may not be a global optimum. Further

experimentation with swapping the order of these selected parameters may yield a better optimum.

First of all, the value of α has been considered. For this study, the other variables have been selected as $\beta_{max} = 5°$ as in experiments the same control surface is also used for swept-sine excitation, so the combined control surface deflection must be less than 20°. Then $U_1 = 25$ m/s and $\Delta U = 1$ are selected so that sufficient controller iterations occur before the open loop flutter speed to ensure that it is increased.

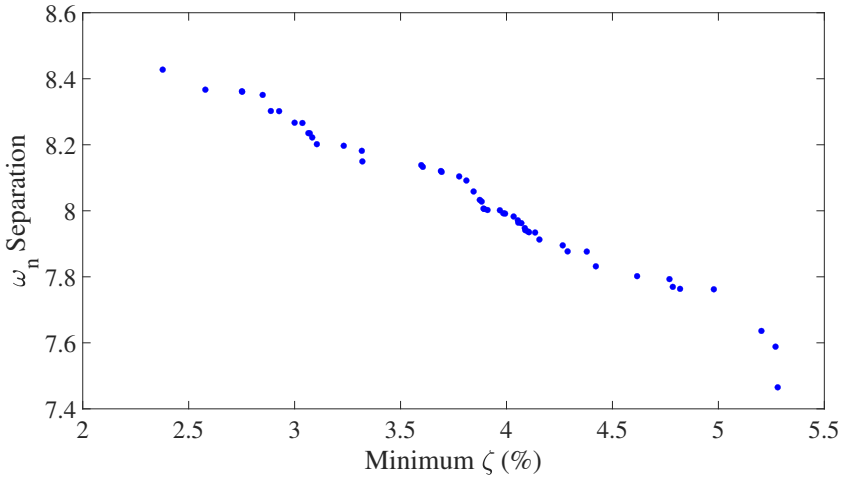

FIGURE 4.3: Pareto Analysis of the SIMO Controller's First Iteration at 25 m/s

Figure 4.3 shows the Pareto analysis performed on the first iteration of the controller at 25 m/s. 53 values of α are tested from 0.0001 to 1, however no real trend or ideal value was found. This means that the value of α needs to be tested against the overall aim of increasing the flutter speed. The results of this are shown in Table 4.2:

TABLE 4.2: Closed Loop Flutter Speed for Varying α

α	U_f (m/s)
0.0001	31.67
0.001	32.40
0.01	33.88
0.1	33.86
1	33.84

Table 4.2 shows that the closed loop flutter speed has experienced a small increase of 2.7 m/s in the best case. Increasing the weighting factor α seems to be beneficial until a point, suggesting that increasing the natural frequency spacing is more important to

increasing flutter than increasing the damping ratios, especially as increasing α beyond 0.01 yields the same flutter speed to one decimal place. In order to determine the flutter speed to the level of accuracy given in Table 4.2, the poles of the closed loop state-space matrix $\tilde{\mathbf{A}}_{CL}$ are evaluated above the last integer airspeed so that the exact airspeed where a damping ratio becomes negative is found.

$$\tilde{\mathbf{A}}_{CL} = \begin{bmatrix} \mathbf{0}_{n\times n} & \mathbf{I}_{n\times n} \\ -\mathbf{A}^{-1}\left(\rho U^2\mathbf{C} + \mathbf{E} - \mathbf{b}\mathbf{g}^T\right) & -\mathbf{A}^{-1}\left(\rho U\mathbf{B} + \mathbf{D} - \mathbf{b}\mathbf{f}^T\right) \end{bmatrix} \tag{4.12}$$

The next variable to consider is β_{max}. From the results in Table 4.2, $\alpha = 0.01$, and then $U_1 = 25$ m/s, and $\Delta U = 1$ as in the previous study. Table 4.3 shows the resulting flutter speeds for each β_{max} tested:

TABLE 4.3: Closed Loop Flutter Speed for Varying β_{max}

β_{max} (°)	U_f (m/s)
1	32.11
3	33.88
4	34.27
5	33.88
7	33.32
10	32.51

It is clear from Table 4.3 that simply increasing the control surface deflection available does not produces the highest closed loop flutter speed. Due to the relatively high airspeeds, small control surface deflections cause larger forces on the wing than at lower airspeeds. Table 4.3 suggests that larger deflections of β would apply too much force to the system, which may cause larger reactions from the wing, resulting in less damping than for smaller control surface deflections. $\beta_{max} = 4$ is selected for the next study, where U_1 is varied. As in the previous studies, $\alpha = 0.01$ and $\Delta U = 1$.

TABLE 4.4: Closed Loop Flutter Speed for Varying U_1

U_1 (m/s)	U_f (m/s)
15	33.44
20	36.82
25	34.27
30	31.38

Based on the results given in Table 4.4, it is clear that beginning the closed loop iterations at 20 m/s provides the best closed loop flutter speed, therefore this shall be implemented into the final study. If the iterative process begins at a higher speed, then there are not enough iterations to reach the maximum airspeed. However, if the process begins at lower airspeeds then the controller reaches its limit sooner and again does not result in the optimum closed loop flutter speed. The final variable to consider is ΔU, the results of which can be found in Table 4.5.

TABLE 4.5: Closed Loop Flutter Speed for Varying ΔU

ΔU (m/s)	U_f (m/s)
0.5	33.42
1	36.82
2	31.08

As in the results from Table 4.4, the effectiveness of the controller and the final closed loop flutter speed is dependent on the number of iterations. Too many iterations at lower airspeeds will result in the controller being maximised too soon, and too few iterations will not increase the flutter speed high enough. From the final study in Table 4.5, it is clear for this system that the final optimum values are $\alpha = 0.01$, $\beta_{max} = 4°$, $U_1 = 20$ m/s, and $\Delta U = 1$

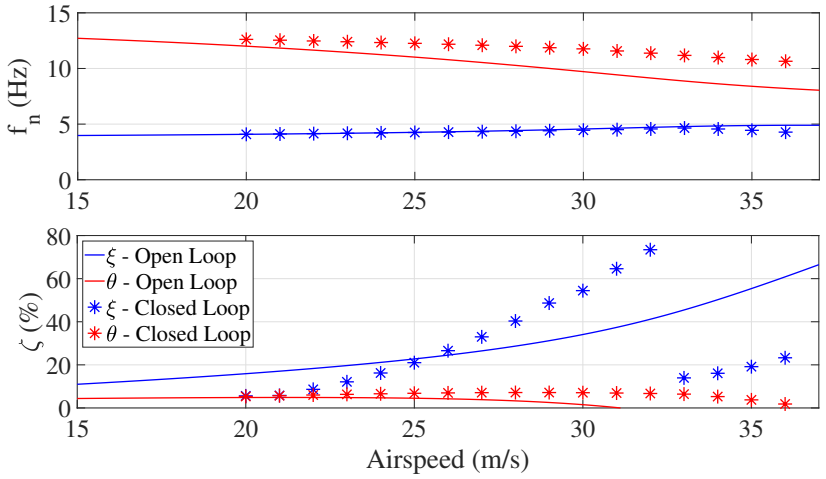

FIGURE 4.4: Comparison of Open and Closed Loop Natural Frequencies and Damping Ratios - SIMO Numerical

Figure 4.4 shows the comparison of open and closed loop natural frequencies and damping ratios for MODFLEX 2.0 following the controller design process shown throughout this section. The closed loop flutter speed is 36.82 m/s, which is an increase of 18.35% increase

compared to the open loop flutter speed of 31.11 m/s. It shows how the control effort shifts from effectively increasing the damping and separating the natural frequencies until 33 m/s, which is the 14 th iteration of the controller. At this point, the damping ratio for the bending mode reduces dramatically, because the damping is approaching critical damping, which is the upper limit for the damping ratio in the genetic algorithm, as stated in Section 4.2.1. Only three more controller iterations were able to be carried out before reaching the new flutter speed due to negative damping, and therefore the onset of flutter. This suggests that perhaps decreasing the objective function weighting constant α could be beneficial for these higher iterations, as the natural frequencies are still well separated but the damping ratios need to be increased further.

4.3.3.2 Experimental

Experimental tests have been carried out on the MODFLEX 2.0 flexible wing model. Initially, swept-sine tests are carried out for a range of airspeeds to confirm the open loop flutter speed in the numerical model. The trailing edge control surface is used for excitation so that the system receptance to this control surface is found and control can be applied. The leading edge control surface is fixed to a zero angle of deflection as to have no effect on the system. As detailed in Chapter 2, The frequency range is selected as 0.01 to 15 Hz to ensure all frequencies of interest are captured with a 0.0015 Hz/s sweep rate.

Once the open loop swept sine tests are completed, the Receptance Method can be applied. It was attempted to carry this out following the iterative approach described previously in this section. All of the control design considerations from the numerical studies were followed and the same values for each parameter are used in the experiments with the exception of $U_1 = 25$ m/s due to time constraints in wind tunnel testing. Table 4.6 gives a reminder of the values used from the study in the numerical section:

Table 4.6: Closed Loop Flutter Speed for Varying α

Parameter	Notation	Value
Objective Function Weighting Constant	α	0.01
Maximum Control Surface Deflection	β_{max}	4°
Airspeed of first iteration	U_1	25 m/s
Airspeed Step Size	ΔU	1 m/s

The experimental results can be seen in Figure 4.5:

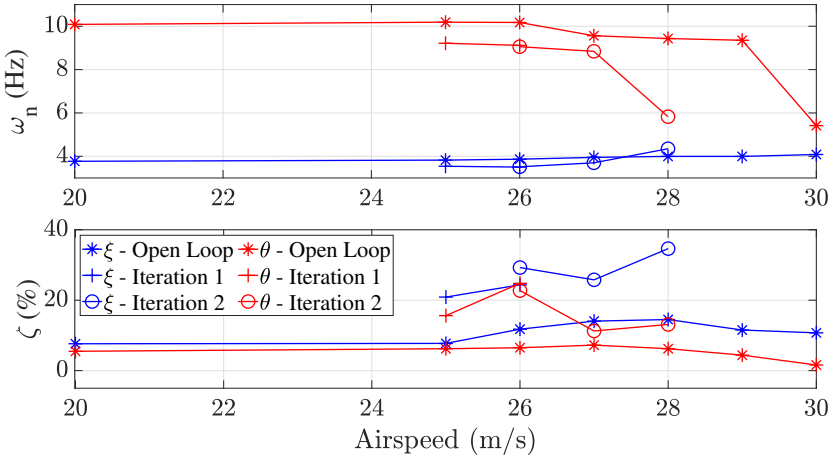

FIGURE 4.5: Comparison of Open and Closed Loop Natural Frequencies and Damping Ratios - Experimental

Control Gains	Iteration 1	Iteration 2
f	0.0541	0.1217
	-0.0149	-0.0135
g	10.5295	5.0496
	1.8457	1.5189

TABLE 4.7: Control Gains for Each Experimental Controller Iteration

Table 4.7 shows the control gains for each iteration. In the second iteration, there is a reduction in the gains that affect the torsional mode in both **f** and **g**. This explains the reduced damping ratio of the torsional mode between the two iterations at 26 m/s as the controller is less reactive to torsional displacement. While the **g** gain pertaining to the bending mode has roughly halved between the two iterations, the **f** gain has more than doubled. The effect of this can be seen in the bending mode damping ratio increasing by roughly 3% for the second iteration. Again, there is little change in the natural frequency between the two iterations. This phenomenon is to be expected as the **f** gains are multiplied by the velocity of the assumed modes, and therefore have a direct effect on damping, whereas the **g** gains are multiplied by the displacements and have a direct effect on the stiffness of the system, and therefore the natural frequencies. It is unclear why such a large change in the first **g** gain between iterations has very little effect on the closed loop natural frequency.

It is clear from the results shown in Figure 4.5 that the closed loop system has not worked as expected, as the flutter speed has reduced to around 29 m/s. While the damping ratios are successfully increased, the natural frequency separation has decreased which has led

to a lower flutter speed. A possible explanation for this is that the damping ratio increase is weighting too highly in the objective function, as the damping ratios are consistently larger in the closed loop system.

The largest issue encountered in this work is that the in-plane mode had a resonance between the 1st bending and 1st torsion natural frequencies (Table 2.10). This meant that as the airspeed was increased, there was coupled motion between the in-plane mode and 1st torsional mode as the natural frequency of the latter decreased, leading to unclear receptance data in the region of these two resonances, which is reflected in Figure 4.5. This is also an explanation as to why there is a sudden drop in the torsional natural frequency above 29 m/s. An easy solution to this is to increase the length of dimension w in Figure 2.10 which increases the stiffness and therefore natural frequency of the first in-plane mode.

Another issue is that the gain scheduling method has only been tested on a pitch-plunge aerofoil [86]. The pitch-plunge aerofoil model only has two distinct degrees of freedom, as opposed to an infinite amount of vibration modes, as in the MODFLEX 2.0 model. Future work must focus on increasing the number of modelled and measured modes to ensure that either higher modes are sufficiently damped, or that the closed loop system can control higher modes if necessary.

The experimental results in Figure 4.5 have a poor match with those in the numerical results (Figure 4.4). The main reason for this is the absence of the in-plane mode from the numerical model, whereas in the experiments the coupled motion between the torsion and in-plane modes prevented clear receptance data from being measured. If the receptance data is unclear, it is not possible to apply accurate control. The error cannot be quantified as the control application is also different, most notably the airspeed of the first iteration and the number of iterations carried out. The experimental results were partially successful as the damping ratios were increased when compared to the open loop system. However, the numerical results show a larger increase in damping ratio as more iterations were carried out, and in practice the control surfaces are less effective.

4.4 MIMO Control

As previously discussed, introducing a second control surface will increase the controllability of the system and may allow for greater change in the closed loop natural frequencies and damping ratios. This section will outline how the MIMO system is implemented and can be used iteratively in the same manner as the SIMO system. Numerical results will be presented and compared to the SIMO results.

4.4.1 Receptance Method

For a multiple-input, linear aeroservoelastic system with n-degrees of freedom, the input-output equation is given as:

$$\mathbf{y}(s) = \mathbf{R}(s, U)\mathbf{u}(s) \tag{4.13}$$

where $\mathbf{y}(s)$ is the output vector, $\mathbf{R}(s, U)$ is the transfer function matrix and $\mathbf{u}(s)$ is the input. However, the second input is now present in the system so that the input is a column vector of the two control surface deflections. For the standard Receptance Method the input is selected as:

$$\mathbf{u}(s) = \begin{bmatrix} \gamma \\ \beta \end{bmatrix} = \left(s\mathbf{F}^T + \mathbf{G}^T\right)\mathbf{y}(s) \tag{4.14}$$

The gain matrices $\mathbf{F}$ and $\mathbf{G}$ are obtained from the MIMO receptance method for full pole placement presented in Chapter 3. Again, the input equation is modified so that the input is scheduled according to the airspeed U:

$$\mathbf{u}(s, U) = \left(s\mathbf{F}(U)^T + \mathbf{G}(U)^T\right)\mathbf{y}(s) \tag{4.15}$$

Then, substituting Equation 4.15 into Equation 4.13 gives

$$\mathbf{y}(s) = \mathbf{R}(s, U)\left(s\mathbf{F}(U)^T + \mathbf{G}(U)^T\right)\mathbf{y}(s) \tag{4.16}$$

As in the SIMO case, the aim is to design a controller and determine gains for a range of airspeeds until further iterations no longer produce a higher flutter speed.

4.4.2 Controller Iteration

Now that the updated Receptance Method has been presented, we can now define the iteration process. The iteration follows the same process as the SIMO system, however the gain constraint must be updated for the MIMO case. The new constraint is defined as:

$$||\mathbf{\Lambda}_f\mathbf{F}||_F+||\mathbf{\Lambda}_g\mathbf{G}||_F\leq c_{max}$$
$$\text{where } \; c_{max}=\beta_{max}+\gamma_{max} \tag{4.17}$$

The selection of $\mathbf{\Lambda}_f$ and $\mathbf{\Lambda}_g$ as the maximum (positive) expected velocities and displacements respectively of the bending and torsion essentially generates a 'worst case' for the controller. This ensures that neither control surfaces is demanded to exceed their maximum deflections, as the maximum velocity and displacement for a given mode cannot occur at the same time. The Frobenius norm is used to essentially calculate the magnitude of the matrix, considering all of its elements, whereas the Euclidean norm used in the SIMO case finds the magnitude of a vector, considering the length of the vector. The iteration process is then carried out in the same way as the SIMO case, however with updated equations to apply the additional control surface:

(1) Obtain receptance $\mathbf{r_1}$ and speed U_1

(2) At speed U_1, choose desired eigenvalues (using Derivative Evolution and constraints for optimisation) and solve for $\mathbf{F}$ and $\mathbf{G}$

(3) With the controller active, measure $\mathbf{r_2}$ at speed U_2 so that the transfer function is as follows:

$$\hat{\mathbf{r}}_2=\hat{\mathbf{H}}(s).\mathbf{B}=\begin{bmatrix}\dfrac{\mathbf{N}_1(s)}{D(s)}\\[2ex]\dfrac{\mathbf{N}_2(s)}{D(s)}\end{bmatrix}$$

$$\text{where } \; \hat{\mathbf{H}}(s)=\mathbf{H}(s)-\frac{\mathbf{H}(s)\mathbf{b}\left(\mathbf{G}+s\mathbf{F}\right)^T\mathbf{H}(s)}{1+\left(\mathbf{G}+s\mathbf{F}\right)^T\mathbf{H}(s)\mathbf{b}}$$

(4) At U_2, choose desired eigenvalues and calculate new $\mathbf{f}$ and $\mathbf{g}$ gains using $\hat{\mathbf{r}}_2$

(5) Repeat 3-4 for each airspeed

4.4.3 Results

Given time constraints and high demand of the wind tunnel facility from other users, as well as shortcomings from the SIMO wind tunnel tests, it was not possible to implement the MIMO method in wind tunnel testing. This section will cover numerical results only. The same studies have been carried out as in the SIMO section.

First of all, the value of α has been considered. For this study, the other variables have been selected as $c_{max} = 5°$ as in experiments the same control surface is also used for swept-sine excitement, so the combined control surface deflection must be less than 20°. Then $U_1 = 25$ m/s and $\Delta U = 1$ are selected so that sufficient controller iterations occur before the open loop flutter speed to ensure that it is increased. As in the SIMO method, a Pareto analysis has been carried out on the first iteration.

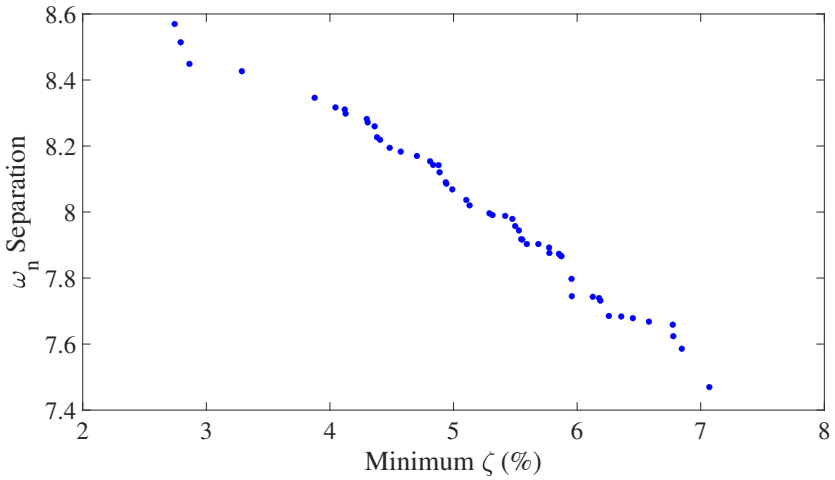

FIGURE 4.6: Pareto Analysis of the MIMO Controller's First Iteration at 25 m/s

Figure 4.6 shows the Pareto analysis performed on the first iteration of the controller at 25 m/s. 53 values of α are tested from 0.0001 to 1, however no real trend or ideal value was found. This means that the value of α needs to be tested against the overall aim of increasing the flutter speed. The results of this are shown in Table 4.8:

TABLE 4.8: Closed Loop Flutter Speed for Varying α

α	U_f (m/s)
0.0001	31.84
0.001	32.96
0.01	34.68
0.1	34.65
1	34.62

Table 4.8 shows the same trend as in the SIMO case, with increasing α being beneficial until a point. The closed loop flutter speed has increased by 3.5 m/s in the best case, again with α set as 0.01. The flutter speed has increased for the same inputs as the SIMO system due to the increased controllability of the system thanks to the additional control surface.

The next variable considered is c_{max}. From the results in Table 4.8, $\alpha = 0.01$, and then $U_1 = 25$ m/s, and $\Delta U = 1$ as in the previous study. Table 4.9 shows the resulting flutter speeds for each c_{max} tested:

TABLE 4.9: Closed Loop Flutter Speed for Varying c_{max}

c_{max} (°)	U_f (m/s)
1	33.31
3	34.18
4	35.24
5	36.67
6	37.42
7	36.34
10	33.44

Again, the same trend is seen as in the SIMO case. It is clear that simply increasing the control surface deflection available does not produce the highest closed loop flutter speed. However, the difference in SIMO and MIMO systems can now be seen as $\beta_{max} = 4$ is selected for the SIMO case, but $c_{max} = 6$ provides the highest closed loop flutter speed in the MIMO case. This is likely due to the fact that both control surfaces will be active, combining to a maximum of 6° deflection, and both control surfaces will likely have similar maximum deflections of around 3°.

The maximum combined control deflection of $c_{max} = 6$ is selected for the next study, where U_1 is varied. As in the previous studies, $\alpha = 0.01$ and $\Delta U = 1$.

TABLE 4.10: Closed Loop Flutter Speed for Varying U_1

U_1 (m/s)	U_f (m/s)
15	35.89
20	38.02
25	37.42
30	31.38

Based on the results given in Table 4.10, the trend seen in the SIMO case is the same, where the number of control iterations must be selected so there are enough to sufficiently increase the closed loop flutter speed, without reaching the limit of the controller too early. The final variable to consider is ΔU, the results of which can be found in Table 4.11.

TABLE 4.11: Closed Loop Flutter Speed for Varying ΔU

ΔU (m/s)	U_f (m/s)
0.5	36.23
1	38.02
2	35.16

As in the results from Table 4.10, and in the SIMO system, the effectiveness of the controller and the final closed loop flutter speed is dependent on the number of iterations. The ideal value for this system is $\Delta U = 1$ From the final study in Table 4.11, it is clear for this system that the final optimum values are $\alpha = 0.01$, $c_{max} = 4°$, $U_1 = 20$ m/s, and $\Delta U = 1$

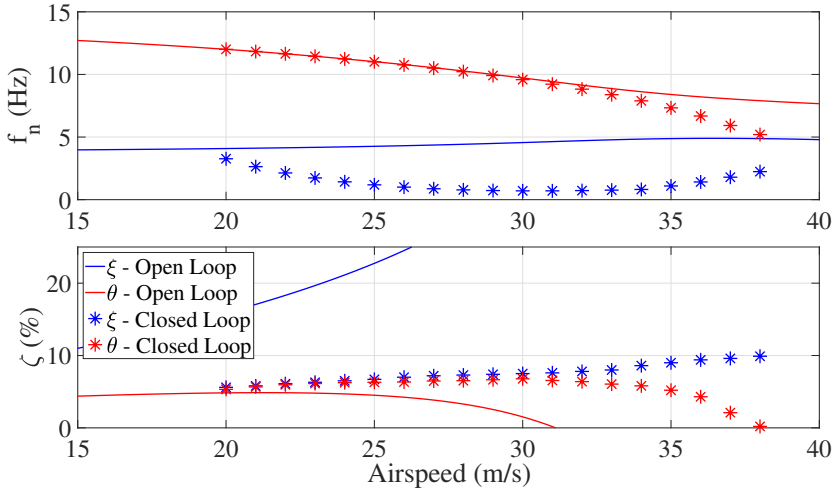

FIGURE 4.7: Comparison of Open and Closed Loop Natural Frequencies and Damping Ratios - MIMO Numerical

Figure 4.7 shows the comparison of open and closed loop natural frequencies and damping ratios for MODFLEX 2.0 when both control surfaces are used as inputs. The closed loop flutter speed is 38.02 m/s, which is an increase of 22.21% increase compared to the open loop flutter speed of 31.11 m/s.

4.5 Summary

The gain scheduling method has been successfully implemented numerically for a SIMO system, and studies were carried out to find ideal values for various parameters. However, the numerical model has the advantage of simplicity as it is a reduced model and only includes the first bending and torsional modes. In reality, the experimental model and tests had numerous problems preventing a successful implementation of the method, the most significant of which was the in-plane mode affecting the clarity of the measured receptance due to some coupled motion with the torsion mode at higher airspeeds. This highlights the importance of wing design and also a limit to the practical application of the receptance method in this application. A simple solution for this has been identified as changing the spar dimensions so that the in-plane mode is higher than the torsional mode, and this can be implemented in future work. While the experimental results did not successfully extend the flutter speed, the increased damping ratios and reduced natural frequency of the bending mode show that this method could still be implemented if not for the presence of the in-plane mode.

The numerical results for the MIMO system reflect the trends seen with the SIMO system, however the flutter speed was increased further due to the increased controllability of the system. A suggestion for future work is to implement the MIMO method in wind tunnel experiments following the completion of successful SIMO experiments.

Chapter 5

LINEAR CONTROL OF A FLEXIBLE WING WITH NONLINEAR ROOT-HEAVE DEGREE OF FREEDOM SYSTEM IN THE PRESENCE OF GUSTS

5.1 Introduction

In Chapter 4, the Receptance Method was used to apply Pole Placement to a linear system to extend the flutter speed. For a nonlinear system, the dynamics around flutter can be more complicated, with effects such as Limit Cycle Oscillations (LCO) occurring [33]. This Chapter will investigate the control of a flexible wing with cubic nonlinearity in a flexible wing system with a Root-Heave Degree of Freedom (RHDoF). This system was designed as a concentrated nonlinearity is simpler to implement and control than a distributed nonlinearity, making it easier to prove the effectiveness of the selected control method. Additionally, as a research group, the broader research goal was to implement hybrid testing. This necessitates the implementation of heave and pitch motion at the

root so that full aircraft dynamics could be implemented outside of the wind tunnel using actuators, however this is beyond the scope of this Chapter and project.

In order to control the nonlinear system, feedback linearisation has been selected as the control method [29, 93, 94]. As the name suggests, the system is linearised through full-state feedback using one or more control surfaces so that a linear control law can be applied by using the controller input to replace the nonlinear dynamics of the system. This work numerically investigates the use of pole placement via feedback linearisation. Experiments could not be carried out due to time constraints. The model used in this work is the MODFLEX 2.0 flexible wing used in Chapter 4, and has been described in detail in Chapter 2.

5.2 Feedback Linearisation

The process of Feedback Linearisation is applied to a nonlinear system to essentially transform it into a linear system [137]. The process results in an exact linearisation, presuming the model of the nonlinearity is known exactly with no modelling errors, and therefore does not require any approximation at any stage, meaning the linearisation is totally accurate for the full range of motion. The Feedback Linearisation method is implemented by transforming a nonlinear system, given by:

$$\dot{\mathbf{x}} = \mathbf{f}(\mathbf{x}) + \mathbf{G}(\mathbf{x})\mathbf{u} \tag{5.1}$$

into an equivalent, linear system given by:

$$\dot{\boldsymbol{\phi}} = \tilde{\mathbf{A}}_{\boldsymbol{\phi}}\boldsymbol{\phi} + \tilde{\mathbf{G}}_{\boldsymbol{\phi}}\mathbf{u}_{\boldsymbol{\phi}} \tag{5.2}$$

based on a choice of output $\mathbf{y} = \mathbf{h}(\mathbf{x})$. The inputs to the nonlinear and the linear systems are represented by $\mathbf{u}$ and $\mathbf{u}_{\boldsymbol{\phi}}$ respectively. In order to transform from the nonlinear domain to the linear domain, a non-singular coordinate transform $\boldsymbol{\phi} = \mathbf{T}_{\boldsymbol{\phi}}\mathbf{x}$ is used. The resulting linearisation may be either complete or partial depending on the Relative Degree, defined as the number of times the output has been differentiated with respect to time before the input terms explicitly appear. A complete linearisation occurs in a SISO system when the Relative Degree is equal to the length of state vector $\mathbf{x}$, in which ensuring stability of the linearised system will also ensure stability of the original nonlinear system. Conversely, if the Relative Degree of the SISO system is less than the

length of $\mathbf{x}$, the resulting system is only partially linearised. In this case, it is imperative to ensure the stability of the remaining nonlinear portion of the system in addition to stabilising the linearised sub-system. The stability of the Zero Dynamics must by verified to achieve this, where the Zero Dynamics are defined as the behavior of the unlinearised subsystem when all coordinates associated with the linearised subsystem are set to zero. The Zero Dynamics may be linear or nonlinear, but are uncontrollable as they do not contain any input terms. For all systems shown in this Chapter, the closed loop systems are only partially linearised.

5.3 Root-Heave Degree of Freedom Model

A new Root-Heave Degree of Freedom system has been derived for this work for the MODFLEX 2.0 model described in Chapter 2. The aim is to allow vertical motion of the wing at the root, with no allowed rotation. The full derivation of this system can been found in Appendix D. Following the derivation of the model, we can form the Second-Order Equation of Motion:

$$\mathbf{A}\ddot{\mathbf{q}} + (\rho V\mathbf{B} + \mathbf{D})\,\dot{\mathbf{q}} + \left(\rho V^2\mathbf{C} + \mathbf{E}\right)\mathbf{q} = \mathbf{g}\beta + \mathbf{h}_g \tag{5.3}$$

where $\mathbf{A}$ is the inertial matrix, $\mathbf{B}$ and $\mathbf{D}$ are the aerodynamic and structural damping respectively, and $\mathbf{C}$ and $\mathbf{E}$ are the aerodynamic and structural stiffness respectively. These matrices have been described in detail in Chapter 2, with the RHDoF derivations for these matrices described in Appendix A. However, this is for the case of linear stiffness in the RHDoF. In the case where cubic hardening stiffness is included, a nonlinearity vector is introduced:

$$\begin{gathered}\mathbf{A}\ddot{\mathbf{q}} + (\rho V\mathbf{B} + \mathbf{D})\dot{\mathbf{q}} + \left(\rho V^2\mathbf{C} + \mathbf{E}\right)\mathbf{q} + \mathbf{F_{nl}} = \mathbf{g}\beta + \mathbf{h}_g \\ \text{where } \mathbf{F_{nl}} = \begin{bmatrix} 0 \\ 0 \\ f_{nl} \end{bmatrix},\ f_{nl} = k_{r_{nl}} z^3\end{gathered} \tag{5.4}$$

The vector for applying the nonlinearity $\mathbf{F_{nl}}$ is a 3×1 vector, which ensures the nonlinearity is applied to the RHDoF only. The 3×1 vector $\mathbf{q}$ is the state vector of the assumed modes for bending, torsion and root-heave. For a MIMO system, $\mathbf{g}\beta$ is replaced with $\mathbf{Gu}$, where $\mathbf{u}$ is a column vector of the control surface deflections β and γ. Then,

making $\ddot{\mathbf{q}}$ the subject of the equation,

$$\ddot{\mathbf{q}} = -\mathbf{A}^{-1}\left(\rho V \mathbf{B} + \mathbf{D}\right)\dot{\mathbf{q}} - \mathbf{A}^{-1}\left(\rho V^2 \mathbf{C} + \mathbf{E}\right)\mathbf{q} - \mathbf{A}^{-1}\mathbf{F_{nl}} + \mathbf{A}^{-1}\mathbf{g}\beta \tag{5.5}$$

which gives rise to the state-space matrix:

$$\tilde{\mathbf{A}} = \begin{bmatrix} \mathbf{0}_{3\times3} & \mathbf{I}_{3\times3} \\ -\mathbf{A}^{-1}\left(\rho V^2 \mathbf{C} + \mathbf{E}\right) & -\mathbf{A}^{-1}\left(\rho V \mathbf{B} + \mathbf{D}\right) \end{bmatrix} \tag{5.6}$$

For the linear case, the state-space equation is

$$\dot{\mathbf{x}} = \begin{bmatrix} \dot{\mathbf{q}} \\ \ddot{\mathbf{q}} \end{bmatrix} = \tilde{\mathbf{A}}\mathbf{x} + \tilde{\mathbf{g}}\beta, \text{ where } \mathbf{x} = \begin{bmatrix} \mathbf{q} \\ \dot{\mathbf{q}} \end{bmatrix} \text{ and } \tilde{\mathbf{g}} = \begin{bmatrix} \mathbf{0}_{3\times1} \\ g_1 \\ g_2 \\ g_3 \end{bmatrix} \tag{5.7}$$

Then, for the nonlinear case:

$$\dot{\mathbf{x}} = \mathbf{f}(\mathbf{x}) = \tilde{\mathbf{A}}\mathbf{x} + \tilde{\mathbf{F}}_{\mathbf{nl}} + \tilde{\mathbf{g}}\beta \tag{5.8}$$

where $\mathbf{f}(\mathbf{x})$ is a vector consisting of nonlinear terms and as shown in Equation 5.8 can be replicated using the linear state-space equation and an additional nonlinear term, defined as:

$$\tilde{\mathbf{F}}_{\mathbf{nl}} = \begin{bmatrix} \mathbf{0}_{3\times1} \\ -\mathbf{A}^{-1}\mathbf{F_{nl}} \end{bmatrix} \tag{5.9}$$

The change in natural frequencies and damping ratios for increasing airspeed of the linear system can be seen in Figure 5.1:

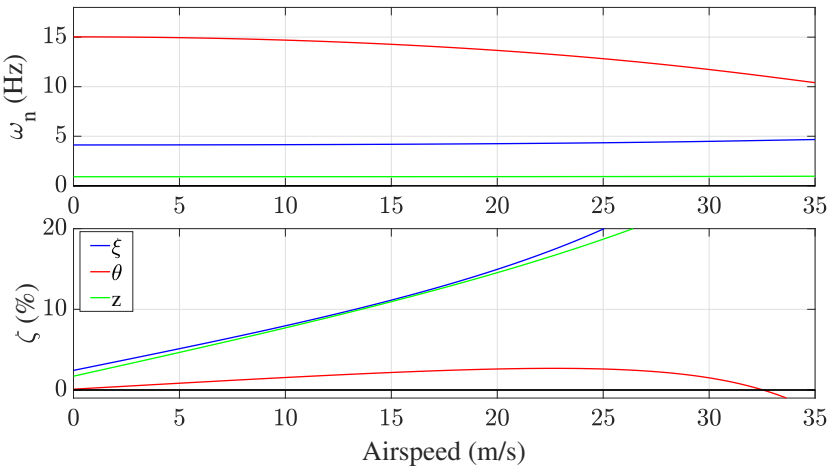

FIGURE 5.1: Natural Frequencies and Damping Ratios of the RHDoF system

Figure 5.1 shows the natural frequencies and damping ratios for the bending, torsion and root-heave modes, which become coupled when airflow is introduced. It is seen that the torsional mode causes instability to the system as its damping ratio becomes negative, so the system has a flutter speed of 32.55 m/s. The validity of the RHDoF system has been checked by increasing the RHDoF stiffness until it is essentially rigid, then comparing the natural frequencies and damping ratios with the fixed-root system. The plots were seemingly identical, which gives confidence that the RHDoF system is valid. The values for the introduced RHDoF terms are given in Table 5.1:

TABLE 5.1: RHDoF Parameters

Parameter	Value	Units
k_{r_0}	10	Nm^{-1}
$k_{r_{nl}}$	1000	Nm^{-3}
ζ_{r_0}	0.001	-

The aim of selecting the values given in Table 5.1 is that the stiffness coefficients k_{r_0} and $k_{r_{nl}}$ are of a realistic value that could be implemented into an experimental setup. The stiffness values are selected to be stiff enough that a maximum displacement would still be within the bounds of the Swansea University wind tunnel test section (see Chapter 2 for details), but not so stiff that very small deflections occur. Additionally, $k_{r_{nl}}$ is selected to be sufficiently larger than k_{r_0} so that there is a clear nonlinear stiffness profile in the region of displacement. The damping is selected to be minimal for system stability and because no additional damping would be implemented into the experimental system.

5.4 SISO Control

Initially, a single input, single output system is considered. In Feedback Linearisation, a control surface is required for each mode the user wishes to control. For the case of MODFLEX 2.0, even in the RHDoF system it is identified that the torsional mode causes instability in the system, and therefore this mode is selected for control in the SISO system. This section will detail how the control is implemented and shows numerical results.

5.4.1 Control Theory

In order to control the nonlinear RHDoF system, pole placement is still used however the system must first be linearised, hence the introduction of Feedback Linearisation. The unstable mode should be selected as the output and in the case of this work this is the torsional mode.

$$y_1 = x_2 = \phi_1$$

$$\dot{y}_1 = \dot{x}_2 = x_5 = \phi_2 = \dot{y}_1 \tag{5.10}$$

$$\ddot{y}_1 = \ddot{x}_2 = \dot{x}_5 = \tilde{\mathbf{A}}_{(5,:)}\mathbf{x} + \tilde{\mathbf{F}}_{nl_5} + \tilde{\mathbf{g}}_{(5,:)}\beta = \dot{\phi}_2$$

The system coordinates are represented by x, the output represented by y, and we define ϕ to represent the linearised coordinate system. The subscripts $(5,:)$ represents the 5th row of the given matrix, and the subscript 5 represents the fifth entry of the associated vector. Then, an artificial input v_1 pertaining to the linearised system is defined, and this is selected as:

$$v_1 = \dot{\phi}_2$$

$$\dot{\mathbf{\Phi}}_{[1,2]} = \begin{bmatrix} 0 & 1 \\ 0 & 0 \end{bmatrix} \mathbf{\Phi}_{[1,2]} + \begin{bmatrix} 0 \\ 1 \end{bmatrix} v_1 \tag{5.11}$$

where $\mathbf{\Phi}_{[1,2]} = [\phi_1 \;\; \phi_2]'$. The linear control law is then defined as:

$$v_1 = -\omega_{n_1}^2 \phi_1 - 2\zeta_1 \omega_{n_1} \phi_2 = -k_1 \phi_1 - k_2 \phi_2 \tag{5.12}$$

where ω_{n_1} and ζ_1 are the desired closed loop undamped natural frequency and damping ratio respectively. Substituting Equation 5.12 into 5.11, the closed loop linearised system is then obtained as:

$$\dot{\mathbf{\Phi}}_{[1,2]} = \begin{bmatrix} 0 & 1 \\ -\omega_{n_1}^2 & -2\zeta_1\omega_{n_1} \end{bmatrix} \mathbf{\Phi}_{[1,2]} \tag{5.13}$$

The Assumed Modes Coordinates in the original, nonlinear domain must then be transformed to Linearised Coordinates using the following matrix:

$$\mathbf{T_\phi} = \begin{bmatrix} 0 & 1 & 0 & 0 & 0 & 0 \\ 0 & 0 & 0 & 0 & 1 & 0 \\ 1 & 0 & 0 & 0 & 0 & 0 \\ 0 & 0 & 0 & -g_3 & 0 & g_1 \\ 0 & 0 & 1 & 0 & 0 & 0 \\ 0 & 0 & 0 & 0 & g_3 & -g_2 \end{bmatrix} \tag{5.14}$$

The transform matrix must be full rank so that it has an inverse. Control distribution terms are included in the fourth and sixth rows to satisfy the full rank condition, as well as ensuring that control is not applied to these states. Then, the coordinate system and state-space matrix are transformed into linearised coordinates:

$$\boldsymbol{\phi} = \mathbf{T_\phi x}, \quad \tilde{\mathbf{A}}_{\boldsymbol{\phi}} = \mathbf{T_\phi \tilde{A} T_\phi^{-1}} \tag{5.15}$$

The control surface contribution must now be introduced. The control distribution vector must be transformed into linearised coordinates.

$$\tilde{\mathbf{g}}_{1_{\boldsymbol{\phi}}} = \mathbf{T_\phi \tilde{g}_1} \tag{5.16}$$

This results in the following state-space equation in linearised coordinates:

$$\dot{\boldsymbol{\phi}} = \tilde{\mathbf{A}}_{\boldsymbol{\phi}} \boldsymbol{\phi} + \mathbf{T_\phi \tilde{F}_{nl}} + \tilde{\mathbf{g}}_{1_{\boldsymbol{\phi}}} \beta \tag{5.17}$$

The required flap angle is obtained by removing the nonlinear dynamics of ϕ_2 and replacing them with the artificial input v_1. This leads to β being given as:

$$\beta = \frac{v_1 - \tilde{\mathbf{A}}_{\boldsymbol{\phi}_{[\mathbf{2},\mathbf{1:6}]}} \boldsymbol{\phi} - \left[\mathbf{T_\phi \tilde{F}_{nl}}\right]_{[\mathbf{2},\mathbf{1:6}]}}{g_2} \tag{5.18}$$

An important aspect of feedback linearisation is ensuring that the zero dynamics are stable. The zero dynamics relate to the dynamics of the system that have not been linearised by control, known as the internal dynamics, and are also uncontrolled. If the zero dynamics are unstable, the overall closed loop system will also unstable. The linearised subsystem has a dimension of 2, meaning the unlinearised internal dynamics has a dimension of 4. The stability of the internal dynamics are a prerequisite for the overall stability of the closed loop system. This can be ensured if the stability of the

zero dynamics is verified, found by setting the coordinates of the linearised subsystem to zero, i.e. $\phi_1 = \phi_2 = 0$.

$$\begin{bmatrix} \dot{\phi}_3 \\ \vdots \\ \dot{\phi}_6 \end{bmatrix} = \begin{bmatrix} \tilde{\mathbf{A}}_{\boldsymbol{\Phi}_{[3,3]}} & \cdots & \tilde{\mathbf{A}}_{\boldsymbol{\Phi}_{[3,6]}} \\ \vdots & \ddots & \vdots \\ \tilde{\mathbf{A}}_{\boldsymbol{\Phi}_{[6,3]}} & \cdots & \tilde{\mathbf{A}}_{\boldsymbol{\Phi}_{[6,6]}} \end{bmatrix} \begin{bmatrix} \phi_3 \\ \vdots \\ \phi_6 \end{bmatrix} \tag{5.19}$$

If the zero dynamics are linear, the stability is simply found by eigenvalue assessment of the state-space matrix shown in Equation 5.19. For nonlinear zero dynamics, as in the system shown in this Chapter, to validate the transformation is viable the stability of the Jacobian must be considered [29]. For the uncontrolled system in Equation 5.17, the state-space equation is written as:

$$\dot{\boldsymbol{\Phi}} = \tilde{\mathbf{A}}_{\boldsymbol{\Phi}} \boldsymbol{\Phi} + \mathbf{T}_{\boldsymbol{\Phi}} \tilde{\mathbf{F}}_{\mathbf{nl}} = \mathbf{f}(\boldsymbol{\Phi}) \tag{5.20}$$

where $\mathbf{f}(\boldsymbol{\Phi})$ is a nonlinear function of the state variables $\boldsymbol{\Phi}$. The Jacobian with respect to the state variable is then given as:

$$\mathbf{J} = \frac{\partial \mathbf{f}(\boldsymbol{\Phi})}{\partial \boldsymbol{\Phi}} \tag{5.21}$$

The stability of the system is then found by evaluating the eigenvalues of $\mathbf{J}$ when using the coordinates of a known equilibrium point of $\boldsymbol{\Phi}$. It is important to note that stability of the zero dynamics only guarantees the local stability of the internal dynamics. This is sufficient for small perturbations about the equilibrium point.

5.4.2 Results

In the results presented in this section, a 1-cosine gust with frequency of 2 Hz is used to excite the system. This causes a small perturbation in the controlled torsional mode to cause flutter. The airspeed is 33 m/s, above the system flutter speed to demonstrate how pole placement applied via feedback linearisation can be used to stabilise an unstable system. The MODFLEX 2.0 wing used is capable of up to 20° control surface deflection, so as in Chapter 3 it is important to select gains that do not cause the control surface to exceed this deflection. The closed loop artificial input parameters are given in Table 5.2:

TABLE 5.2: Closed Loop Inputs for SISO Control

Parameter	Value	Dimension
$\bar{\omega}_1$	62.83	rad/s
$\bar{\zeta}_1$	0.2	-

The natural frequency has been selected as 10 Hz, which is close to the open loop value for the linear system at 33 m/s. This was to minimise the controller work as primarily the damping ratio needed to be increased due to the instability of the system. The comparison of open and closed loop results is shown in Figure 5.2.

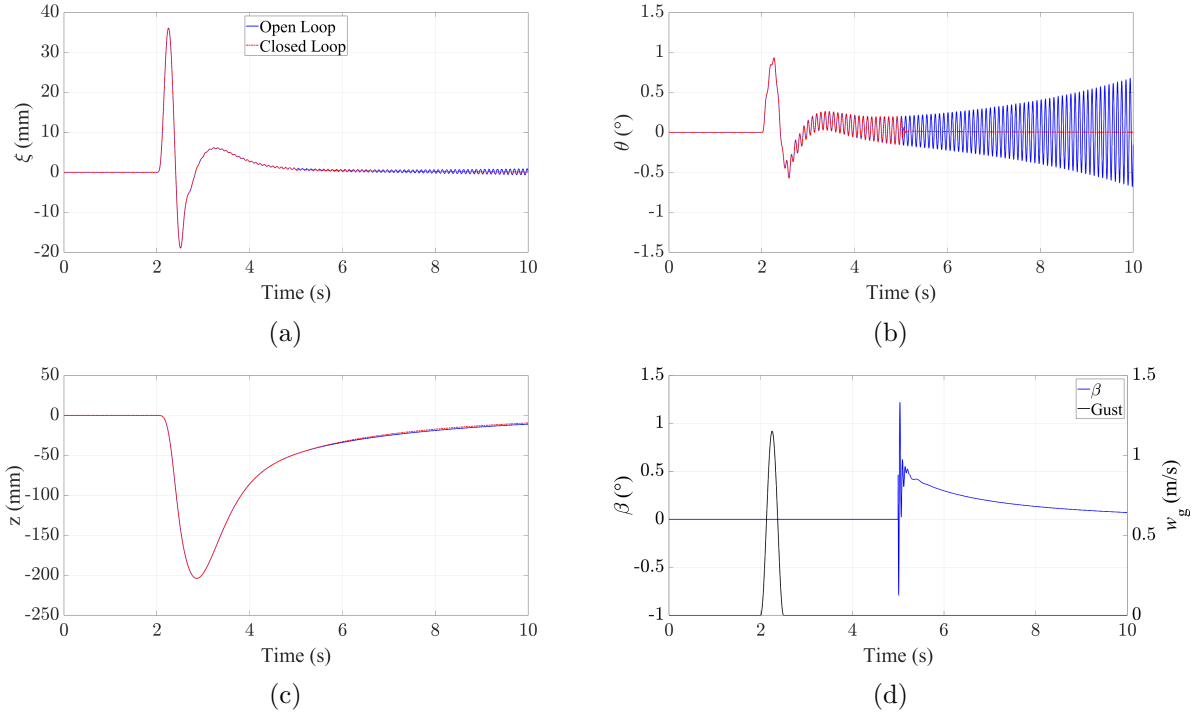

FIGURE 5.2: Open and Closed Loop Responses to a 2 Hz 1-Cosine Gust at 33 m/s using SISO Feedback Linearisation

As expected, the gust input provides a small perturbation and causes instability in the system. Once the controller is engaged at 5 seconds, the open loop dynamics have been replaced by the controller with the desired dynamics. While the control completely decouples the torsion mode from the system, it is seen that the whole system is stabilised as the zero dynamics have had their stability checked via Jacobian Stability for the all-zero initial conditions used in this simulation. Figure 5.3 shows the torsion and control surface deflections after the controller is engaged.

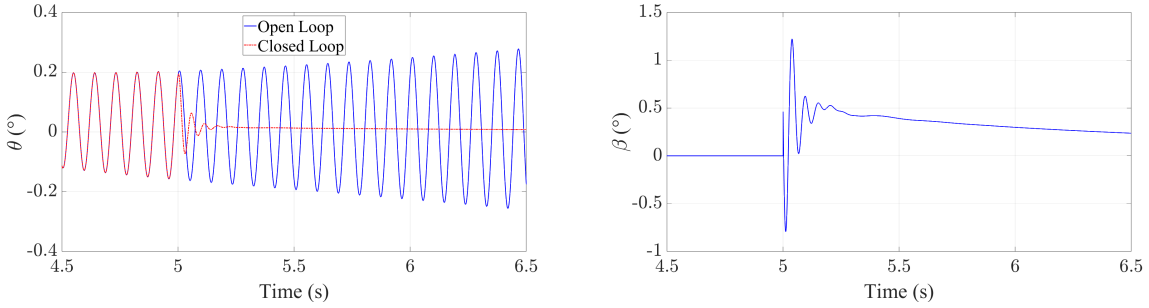

(a) (b)

FIGURE 5.3: Open and Closed Loop Responses to a 2 Hz 1-Cosine Gust at 33 m/s using SISO Feedback Linearisation

The large increase in damping causes a quick decay in the response. Due to the small deflections of the torsion mode, there is little deflection required from the control surface, however the change in deflection is of high frequency, matching the 10 Hz closed loop natural frequency applied. One key behaviour to note is how the torsional mode seemingly stabilises within 0.5 seconds, but the control surface is still deflecting up to and beyond 10 seconds as the response has not completely decayed after 0.5 seconds. This shows that despite the harmonic motion damping out quickly, there is still time required to stabilise the system. The large amount of damping and low natural frequency in the heave response is a reflection of the damping and natural frequency seen in Figure 5.1, as well as the high frequency component of the bending response.

As the initial perturbation due to the 2 Hz gust, and unstable response until 5 seconds is very low, the control law has not been tested for a larger perturbation and therefore it is unknown if the selected closed loop natural frequency and damping ratio will cause the maximum control surface angle to be exceeded. The following results in Figures 5.4 and 5.5 show the same control system in response to a 10 Hz gust gives higher excitement of the torsional mode.

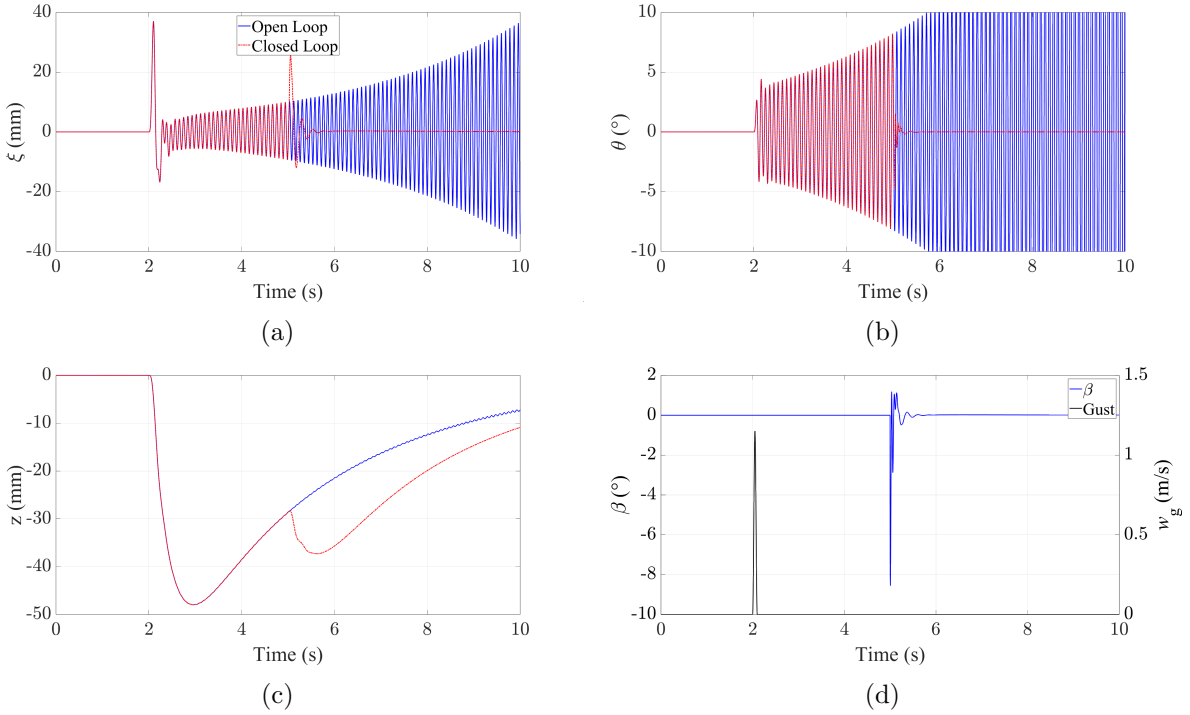

FIGURE 5.4: Open and Closed Loop Responses to a 10 Hz 1-Cosine Gust at 33 m/s using SISO Feedback Linearisation

As the gust frequency is much closer to the torsional natural frequency, a much larger response is experienced from the torsion mode. Additionally, the z displacement due to the gust has decreased significantly as the gust frequency is much higher than the root-heave natural frequency. Figure 5.5 shows the torsion and control surface deflections in detail after the controller is enabled.

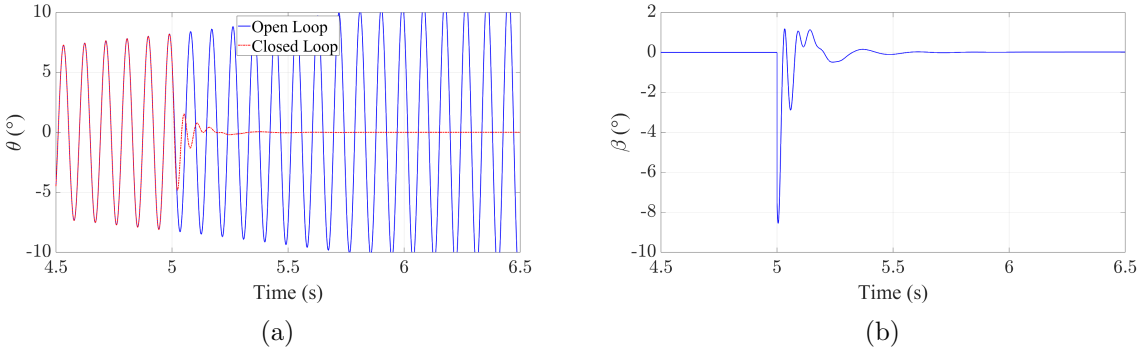

FIGURE 5.5: Open and Closed Loop Responses to a 10 Hz 1-Cosine Gust at 33 m/s using SISO Feedback Linearisation

Due to the larger torsional deflection, and that it is approaching a peak in the harmonic motion when the controller is engaged, the β response experiences a large spike as the

controller is engaged. This causes a large change in the torsional displacement, but has a knock-on effect on the bending and root-heave modes and causes large changes in their deflections also. This shows the importance of the time that the controller is engaged, as if the torsional deflection is passing through zero as the controller is activated then less initial work is demanded from the control surface and a spike in the bending and heave displacements wouldn't occur.

5.5 MIMO Control

As stated in the previous section, one control surface corresponds to one controlled mode. In order to improve the closed loop response, it is beneficial to control multiple modes. This section details the MIMO feedback linearisation problem and provides results for two closed loop cases.

5.5.1 Control Theory

In the feedback linearisation problem, one control surface is required per mode we wish to control. As MODFLEX 2.0 uses two control surfaces, two modes can be controlled. The torsional mode must be controlled as it causes instability, meaning there are two two possible cases where an additional mode can be controlled, first where the bending is controlled and second where the mode associated with the RHDoF is controlled. The derivation for Case 1 will be shown, but can also be followed for Case 2. As in the SISO case, we must first define the outputs of the system, where the first output is the assumed torsion mode,

$$y_1 = x_2 = \phi_1$$

$$\dot{y}_1 = \dot{x}_2 = x_5 = \phi_2 = \dot{y}_1 \tag{5.22}$$

$$\ddot{y}_1 = \ddot{x}_2 = \dot{x}_5 = \tilde{\mathbf{A}}_{(5,:)}\mathbf{x} + \tilde{\mathbf{F}}_{nl_5} + \tilde{\mathbf{G}}_{(5,:)}\mathbf{u} = \dot{\phi}_2$$

and second output is selected as the assumed bending mode:

$$y_2 = x_1 = \phi_3$$

$$\dot{y}_2 = \dot{x}_1 = x_4 = \phi_4 = \dot{y}_1 \tag{5.23}$$

$$\ddot{y}_2 = \ddot{x}_1 = \dot{x}_4 = \tilde{\mathbf{A}}_{(4,:)}\mathbf{x} + \tilde{\mathbf{F}}_{nl_4} + \tilde{\mathbf{G}}_{(4,:)}\mathbf{u} = \dot{\phi}_4$$

As there are now two control surfaces, the controller input has been updated to accommodate this with the single control input $\tilde{\mathbf{g}}\beta$ being replaced with a control distribution matrix $\tilde{\mathbf{G}}$ and input vector $\mathbf{u} = [\beta,\ \gamma]'$. Similarly, we must update the artificial inputs.

$$v_1 = \dot{\phi}_2, \quad v_2 = \dot{\phi}_4$$

$$\dot{\phi} = \begin{bmatrix} 0 & 1 & 0 & 0 \\ 0 & 0 & 0 & 0 \\ 0 & 0 & 0 & 1 \\ 0 & 0 & 0 & 0 \end{bmatrix} \phi + \begin{bmatrix} 0 \\ 1 \\ 0 \\ 0 \end{bmatrix} v_1 + \begin{bmatrix} 0 \\ 0 \\ 0 \\ 1 \end{bmatrix} v_2 \tag{5.24}$$

Then, the linear control law is defined as:

$$\begin{aligned} v_1 &= -\omega_{n_1}^2\phi_1 - 2\zeta_1\omega_{n_1}\phi_2 = -k_1\phi_1 - k_2\phi_2 \\ v_2 &= -\omega_{n_2}^2\phi_3 - 2\zeta_2\omega_{n_2}\phi_4 = -k_3\phi_3 - k_4\phi_4 \end{aligned} \tag{5.25}$$

Again, the desired closed loop natural frequencies and damping ratios are denoted by $\omega_{n_{1,2}}$ and $\zeta_{1,2}$. The linearised system is then obtain by substituting Equation 5.25 into Equation 5.24.

$$\dot{\boldsymbol{\Phi}}_{[1:4]} = \begin{bmatrix} 0 & 1 & 0 & 0 \\ -\omega_{n_1}^2 & -2\zeta_1\omega_{n_1} & 0 & 0 \\ 0 & 0 & 0 & 1 \\ 0 & 0 & -\omega_{n_2}^2 & -2\zeta_2\omega_{n_2} \end{bmatrix} \boldsymbol{\Phi}_{[1:4]} \tag{5.26}$$

The Assumed Modes Coordinates must then be transformed to Linearised Coordinates using the following matrix:

$$\mathbf{T_\Phi} = \begin{bmatrix} 0 & 1 & 0 & 0 & 0 & 0 \\ 0 & 0 & 0 & 0 & 1 & 0 \\ 1 & 0 & 0 & 0 & 0 & 0 \\ 0 & 0 & 0 & 1 & 0 & 0 \\ 0 & 0 & 1 & 0 & 0 & 0 \\ 0 & 0 & 0 & T_{\phi_{6,4}} & T_{\phi_{6,5}} & 1 \end{bmatrix} \tag{5.27}$$

$$T_{\phi_{6,4}} = \frac{\tilde{g}_2\tilde{g}_6 - \tilde{g}_3\tilde{g}_5}{\tilde{g}_1\tilde{g}_5 - \tilde{g}_2\tilde{g}_5}, \quad T_{\phi_{6,5}} = -\frac{\tilde{g}_1\tilde{g}_6 - \tilde{g}_3\tilde{g}_4}{\tilde{g}_1\tilde{g}_5 - \tilde{g}_2\tilde{g}_5}$$

The final row of $\mathbf{T_\Phi}$ is the null-space of $\tilde{\mathbf{G}}$ as this ensures that the final entry in $\boldsymbol{\Phi}$ is not controlled. This has been calculated using Symbolic Math in MATLAB. As previously mentioned, there are two control cases as there is the option of controlling bending or root heave. The same derivation can be used for Case 2, and produces the following transfer matrix:

$$\mathbf{T_\Phi} = \begin{bmatrix} 0 & 1 & 0 & 0 & 0 & 0 \\ 0 & 0 & 0 & 0 & 1 & 0 \\ 0 & 0 & 1 & 0 & 0 & 0 \\ 0 & 0 & 0 & 0 & 0 & 1 \\ 1 & 0 & 0 & 0 & 0 & 0 \\ 0 & 0 & 0 & T_{\mathbf{\Phi}_{6,4}} & T_{\mathbf{\Phi}_{6,5}} & 1 \end{bmatrix} \tag{5.28}$$

As in the SISO case, one must assess the stability of the zero dynamics before control can be applied. In the MIMO case, the dimension of the linearised subsystem is 4, which leaves an uncontrolled set of internal dynamics with dimension of 2. The zero dynamics are then obtained by setting the coordinates of the linearised subsystem to zero, $\phi_1 = \phi_2 = \phi_3 = \phi_4 = 0$, and assessing the stability of the remaining zero dynamics, given by:

$$\begin{bmatrix} \dot{\phi}_5 \\ \dot{\phi}_6 \end{bmatrix} = \begin{bmatrix} \tilde{\mathbf{A}}_{\mathbf{\Phi}_{[5,5]}} & \tilde{\mathbf{A}}_{\mathbf{\Phi}_{[5,6]}} \\ \tilde{\mathbf{A}}_{\mathbf{\Phi}_{[6,5]}} & \tilde{\mathbf{A}}_{\mathbf{\Phi}_{[6,6]}} \end{bmatrix} = \begin{bmatrix} \phi_5 \\ \phi_6 \end{bmatrix} \tag{5.29}$$

Once again, the stability of the zero dynamics is found via eigenvalue assessment for linear zero dynamics, which is true for the case where torsion and root heave are controlled. However, for the case of controlling torsion and bending, there is again nonlinear zero dynamics and the stability is found by evaluating the Jacobian, as described in the SISO

section. For the results shown in this section, the Jacobian is evaluated using the all-zero initial conditions used in each simulation and the stability has been confirmed by the negative real parts of the eigenvalues. If the zero dynamics are stable, then the internal dynamics are locally stable and we can proceed with the control implementation.

5.5.2 Results

As in the results for the SISO system, first a 1-cosine gust with frequency of 2 Hz is used to excite the system as this causes a small perturbation to the bending and torsion modes so that an unstable response begins. The airspeed is 33 m/s, above the system flutter speed. Each control surface on the MODFLEX 2.0 wing used is capable of up to 20° deflection, so again it is import to select gains that do not cause the control surfaces to exceed this deflection. As there are two control surfaces available, two possible MIMO cases have been identified in the Control theory of this section, however the case where torsion and root-heave are controlled has unstable zero dynamics and therefore is not explored in this results section due to being unfeasible. The closed loop artificial input parameters for the case of controlling torsion and bending are given in Table 5.3:

TABLE 5.3: Closed Loop Inputs for MIMO Control

Parameter	Value
$\bar{\omega}_1$	62.83
$\bar{\zeta}_1$	0.2
$\bar{\omega}_2$	31.42
$\bar{\zeta}_2$	0.4

As in the SISO method, closed loop natural frequencies have been selected close to respective open loop values to reduce the control effort required. The results in response to a 2 Hz 1-cosine gust are shown in Figure 5.6.

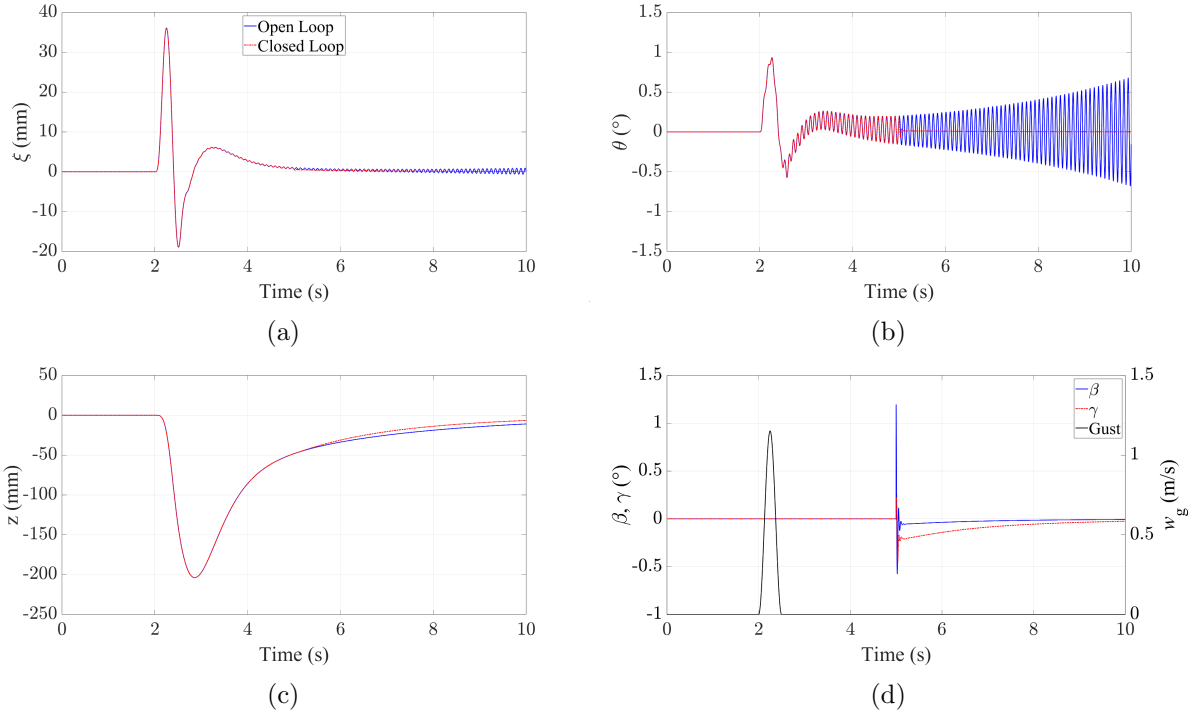

FIGURE 5.6: Open and Closed Loop Responses to a 2 Hz 1-Cosine Gust at 33 m/s using MIMO Feedback Linearisation

Now that two control surfaces are used, both the torsion and bending are controlled. The effect of this is that the system is still stabilised as the torsional mode is controlled, however controlling two modes has an improved effect on the full response. The root-heave mode has a slightly reduced settling time compared to the SISO and open loop systems, which shows how increased control improves the response of the internal dynamics of the system. Figure 5.7 shows a detailed view of the bending and torsion responses to the 2 Hz gust after the controller is engaged, as well as the control surface deflections.

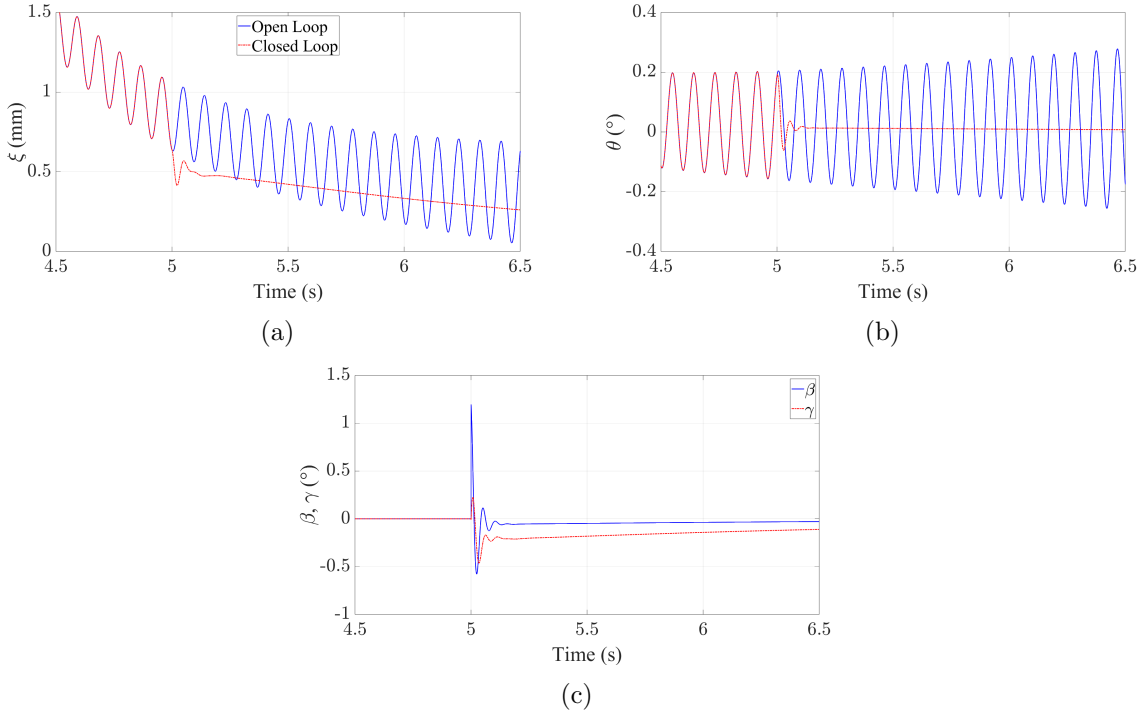

FIGURE 5.7: Open and Closed Loop Responses to a 2 Hz 1-Cosine Gust at 33 m/s using MIMO Feedback Linearisation - Detailed View

It is seen that the torsion and bending modes vibrate at the applied natural frequencies. The large damping ratios applied lead to harmonic motion quickly settling, with each mode returning to rest shortly thereafter. As in the SISO system, very little is demanded of the control surfaces due to the small deflections in the bending and torsion modes. Again, despite the bending and torsion being completely decoupled from each other and the root-heave, the effect of controlling the unstable torsion mode has reduced the responses of the other modes. The combined control of bending and torsion has lead to a marginal decrease in settling time for the root-heave mode, both compared to the open loop system and the SISO system as the root-heave mode is still coupled to the other modes.

As in the SISO analysis, a gust of 10 Hz is applied to see the effects of larger displacements on the controller. While the bending mode has an open loop frequency of roughly 4.5 Hz, the 10 Hz gust is still selected to excite the torsion mode. Figures 5.8 and 5.9 show the responses to the 10 Hz gust.

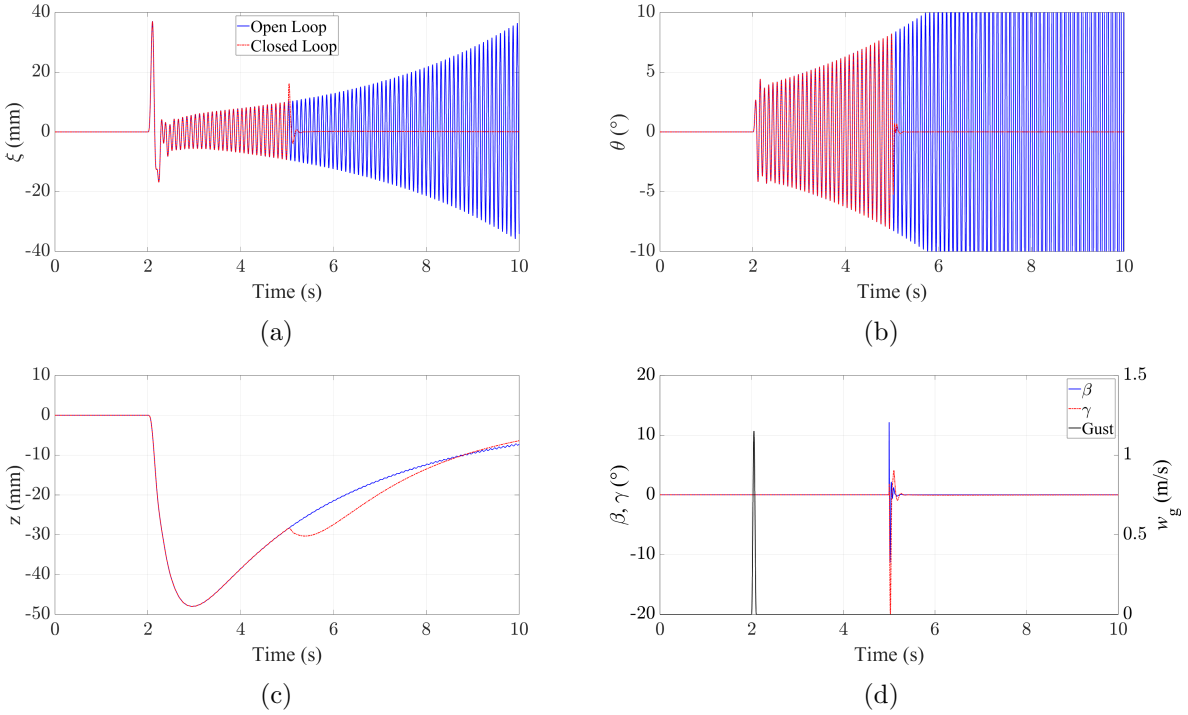

FIGURE 5.8: Open and Closed Loop Responses to a 10 Hz 1-Cosine Gust at 33 m/s using MIMO Feedback Linearisation

A similar response can be seen to that of the SISO system, where due to the controller being engaged as the torsional response is reaching a peak in its oscillation, there is a spike in the bending and root-heave responses as there is an abrupt change in the β deflection. A more detailed view of the controlled modes and control surface deflections are shown in Figure 5.9.

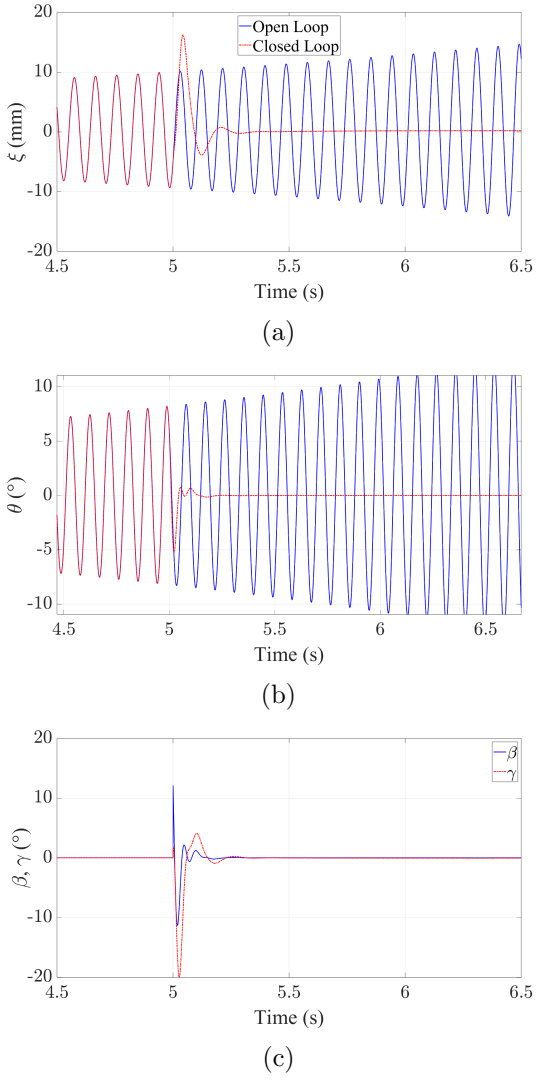

FIGURE 5.9: Open and Closed Loop Responses to a 10 Hz 1-Cosine Gust at 33 m/s using MIMO Feedback Linearisation - Detailed View

As in previous simulations, the bending and torsion modes take on their new dynamics as applied by the control. Similar to the SISO input, there is a large spike in the bending and root-heave modes due to the controller engagement however they are less pronounced as the bending is now also controlled. With the MIMO system, there is a difficulty introduced on choosing when the control is engaged. When only the torsion was controlled in the SISO section, the controller could simply be activated when the torsion deflection was passing through zero to avoid a spike in control surface deflection. Due to the phase difference between the bending and torsion modes in the flutter response, one mode will pass through zero as the other is at a peak, meaning activating the controller at any point will cause a spike in at least one of the control surfaces and therefore alter the response of the other modes. One option to avoid this, is to gradually ramp up

the control effort, rather than simply switching the controller on. This would mean the system takes longer to stabilise, but is overall safer and prevents large peaks in the response. To avoid the danger of causing further instability or damage to the wing, a solution would be to increase the number of control surfaces so that more modes are controlled, which increases the stability of the system. Suggestions for further work would be to develop an experimental test rig and to include more actuators so that more modes can be controlled. Additionally, the effect of error in the modelling of nonlinearity should be explored and the implementation of Adaptive Feedback Linearisation would be required [97].

5.5.2.1 SISO and MIMO Comparison

As previously discussed, it is important to understand the effect of increased control power. Figure 5.10 shows a comparison between the SISO and MIMO responses for a 2 Hz 1-Cosine gust.

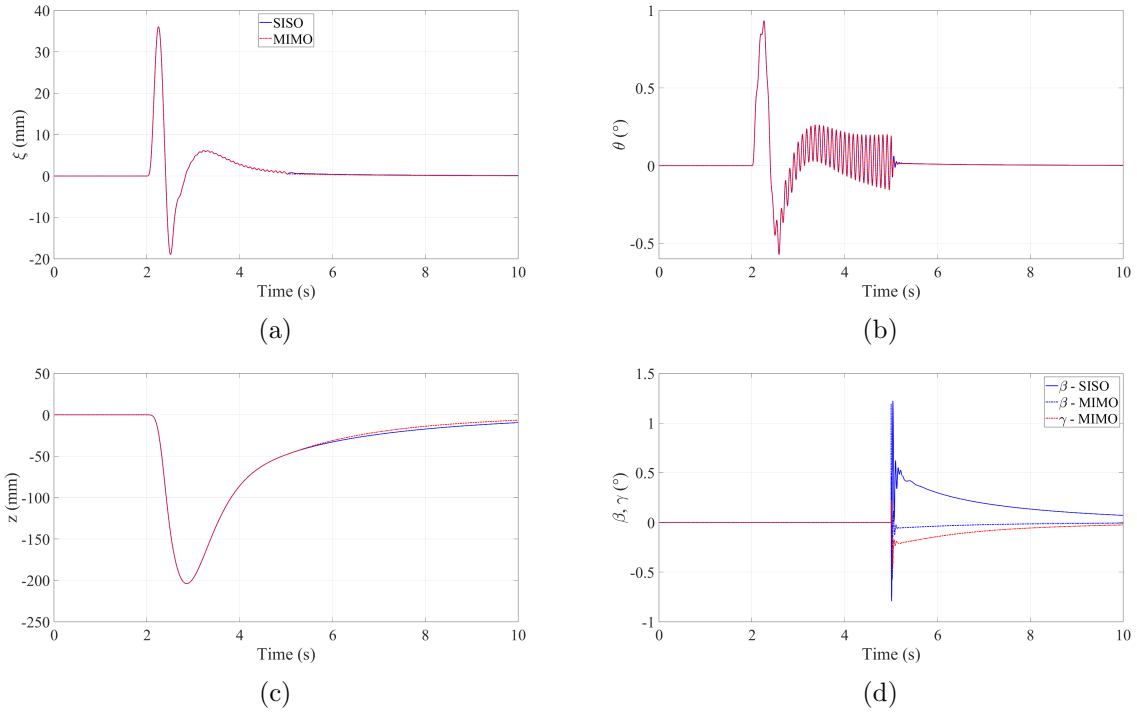

FIGURE 5.10: Comparison of SISO and MIMO Responses to a 2 Hz 1-Cosine Gust at 33 m/s

There is very little improvement to the controlled responses between the SISO and MIMO methods for ythe particular control requirements set in the simulations shown. Figure

5.11 shows a detailed view of the controlled modes and control surface deflections when the controller is enabled.

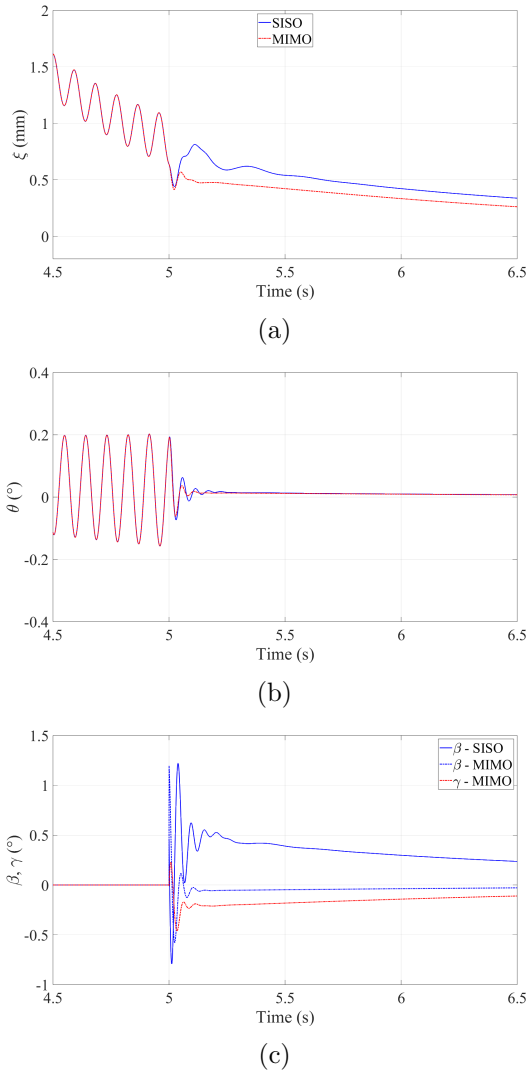

FIGURE 5.11: Comparison of SISO and MIMO Responses to a 2 Hz 1-Cosine Gust at 33 m/s - Detailed View

It is seen that the additional control surface allows for greater damping of the harmonic motion in both the bending and torsional modes. The trailing edge control surface in the SISO system is in use for significantly longer than the two control surfaces in the MIMO system, resulting in a similar amount of control power being used in each system. This shows that there is benefit to using the MIMO system due to the increased controllability. These trends are also true for the 10 Hz gust case, so a comparison is not shown here for brevity.

5.6 Summary

Both single input, single output and multiple input, multiple output systems have been considered numerically for Feedback Linearisation of a flexible wing model with cubic hardening nonlinearity in the Root-Heave Degree of Freedom. The motivation for using feedback linearisation is to linearise the nonlinear system so that a linear control law can be applied to the system. Two control surfaces are available, meaning the pole placement was applied as the linear control law after the system was linearised, with the primary aim of increasing the damping of the unstable torsional mode. As a 1-cosine gust was used to unsettle the system, gust frequencies of 2 Hz and 10 Hz were used to excite the uncontrolled mode associated with the Root-Heave Degree of Freedom and the controlled torsional mode respectively. It was found that the SISO configuration was effective at stabilising the response after either gust frequency, with the MIMO system marginally improving the response, due to the increased control authority available. While this suggests that the additional control power is not particularly beneficial for this model as only one mode is primarily responsible for the instability that causes flutter, this is not true for all systems and should be investigated for different models.

Chapter 6

ACTIVE HINGED WING TIP CONTROL FOR REDUCING WING ROOT BENDING MOMENTS DUE TO GUSTS

6.1 Introduction

Following on from work carried out by Balatti et al. [10] where a passive folding wing tip is used for gust load alleviation, a folding wing tip model was developed for active control to investigate the effects of gusts on the wing root bending moment.

6.1.1 Wing Parameters

A wing of 1.1 m span with a chord of 160 mm has been designed to fit various wing tips, The wing stiffness is provided by a similar "x-shaped" aluminium spar to that used in the MODFLEX wings (Figure 2.10a), which is 780 mm in length. Eight identical 3D-printed aerofoil sections are connected along the spar's span and the wing tips are attached to the tip of the spar. The wing tip is made of a single 3D printed section for

a strong connection to the hinge, and three light-weight foam sections as previous work identified a need to reduce the wingtip mass [111].

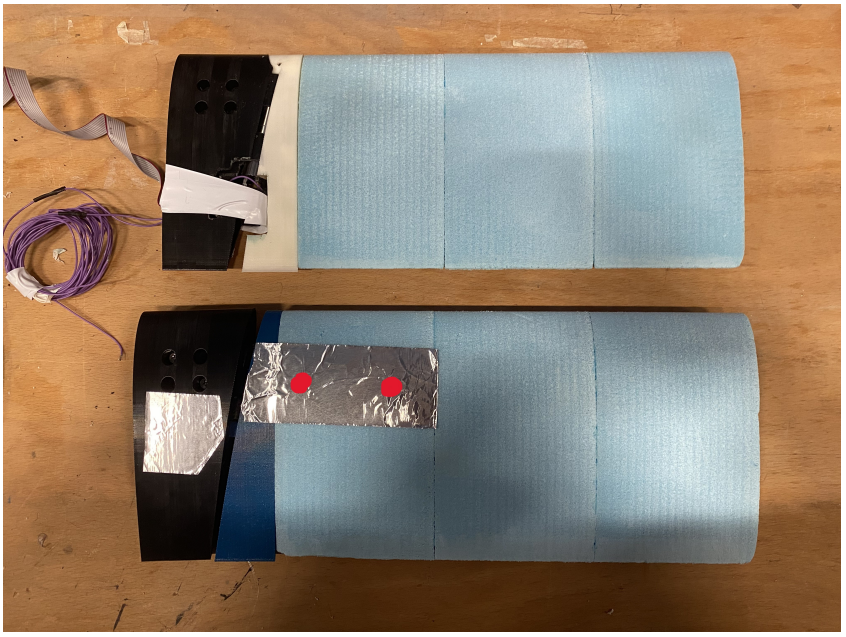

FIGURE 6.1: Active (Top) and Passive (Bottom) Wing Tips (*Red dots represent laser positions*)

Two wing tip configurations have been utilised for this work: a passive hinged wing tip, and an active wing tip with a motor acting as the hinge, as shown in Figure 6.1. The wing tip fold angle for the passive tip is calculated using the method shown in Figure 2.4, and Equation 2.1. Details on the CAD used to make the wing is given in Appendix E. Both the passive hinge and motor are located at 800 mm from the root in their respective tip configurations. The hinge consists of a steel shaft, a metal bush, and two bearings. The metal bush is attached to the steel shaft, which rotates within the two metal bearings. The shaft is secured to a metal bush connected to the 3D-printed section of the wingtip. The bearings are attached to the 3D-printed section of the main wing and prevent the bush from moving in the hinge direction. The wing has a maximum fold angle of 25°, and a flare angle Λ_f of 10°.

TABLE 6.1: Wing Dimensions

Dimension	Size (mm)
a	3
b	13
w	25
t	3
s	1100
y_h	800
y_t	300
c	160
x_f	40

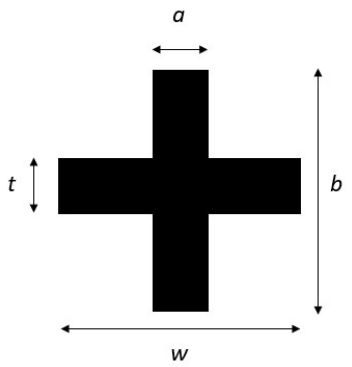

FIGURE 6.2: Spar Cross Section Dimensions

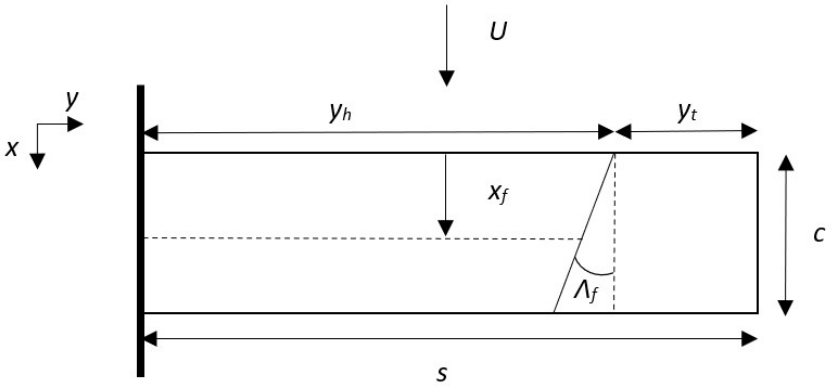

FIGURE 6.3: Dimensions of Folding Wing Tip Model

For active control and the fixed-tip case, a high-torque Maxon DCX22S motor is used. Similar to the work of Carillo et al [116], the motor can be used as a hinge locking mechanism, with the additional benefit of locking at a desired fold angle.

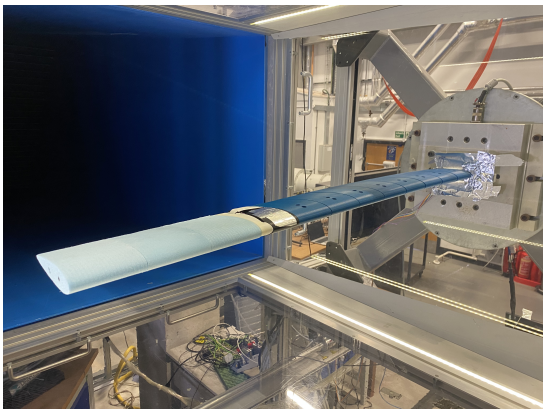

(a)

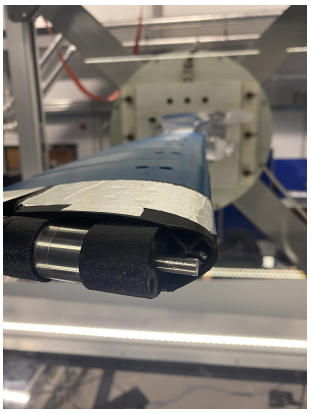

(b)

FIGURE 6.4: Active Folding Wing Tip (a) Wing Setup in wind tunnel and (b) Motor

TABLE 6.2: Maxon DCX22S Parameters

Parameter	Notation	Value	Unit
Rotor Moment of Inertia	J	5.55×10^{-7}	kgm^2
Motor Torque Constant	K	18.40×10^{-3}	Nm/amp
Electrical Inductance	L	23.10×10^{-5}	H
Electrical Resistance	R	3.69	Ohm
Nominal Current	I_{nom}	0.869	A

In order to control the motor position, the same PID controller setup is used as seen in Figure 2.12, however the PID alone was enough to achieve the desired wing tip angle for all experiments within an error of 0.1°, so there was no need to include an estimator. The main concern with the DCX22S is the small nominal current, which will be discussed later.

6.1.2 Nastran Model

Two aeroelastic models were developed in MSC/Nastran, considering the active and passive wing tips. This work is a continuation of work done by Balatti et al. [10, 129], so the available Nastran model of the passive wing tip has been edited to allow for active control. The only difference between models is the wingtip hinge stiffness. The aluminium spar is modelled with beam elements. The weight and inertia of each 3D printed wing section, foam tip sections and motor where applicable are modelled as a concentrated mass and inertia at their actual position. Solidworks calculated the inertia and centre of mass position of each part after manually correcting the mass density so

that the Solidworks part weight matches the weight of the manufactured part. Each concentrated mass was connected to the spar through a rigid beam.

The hinge is modelled using CBUSH elements for their flexibility of use and local co-ordinate system, and PBUSH elements to define the detailed properties of the CBUSH elements. This allows for precise, customisable modelling of whatever the desired spring-damper connection is. In the case of this work, the connection is either a very low stiffness spring for the free tip, or a very high stiffness spring for the active tip. To apply control to the system, the Nastran node where the hinge is located is identified and is set as the controller mechanism in MATLAB. This enables the folding of the wing tip to the local coordinate system of the CBUSH used to generate the hinge stiffness, which has been set to emulate the flare angle of the tip.

After convergence studies carried out in previous work by Balatti [10], 205 elements were used to model the wing spar, resulting in an element size of 3.9 mm. and 3000 panels were used for the aerodynamic model in both models.

TABLE 6.3: Nastran Model Parameters (*Adapted from [10]*)

	Number of Elements						
Mode (Hz)	10	20	40	60	80	100	200
1	9.8	9.8	9.8	9.8	9.8	9.8	9.8
2	60.5	61.4	61.6	61.6	61.6	61.6	61.6
3	167.0	171.1	171.1	172.2	172.3	172.3	172.3
4	239.9	240.1	240.1	240.2	240.2	240.2	240.2
5	322.3	333.7	336.3	336.7	336.9	337.0	337.0

The aerodynamic model is divided into two sections, the first being from wing root to the hinge, and the second being the wing tip. The convergence study is shown in Figure 6.5, where the maximum vertical displacement of the tip is considered due to a gust. 20 quadratic aerodynamic panels are used in the chord-wise direction, with a total of 2400 panels for the main wing and 600 panels for the wing tip.

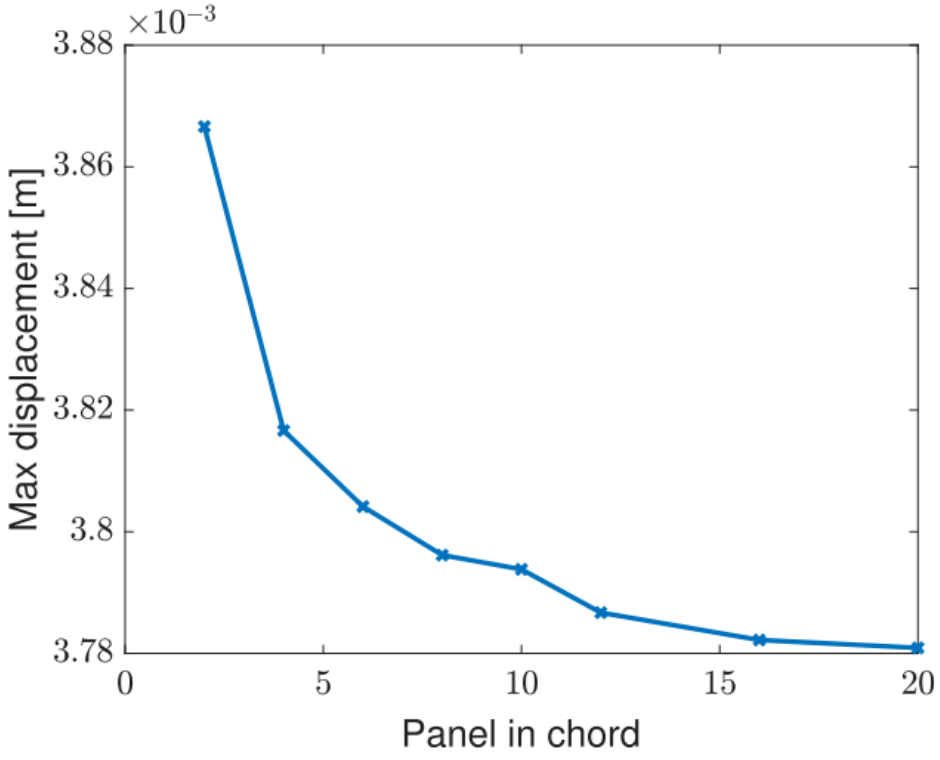

FIGURE 6.5: Convergence of Aerodynamic Panels in Model (*Adapted from [10]*)

Figure 6.6 shows the wing structural and aerodynamic models and Table 6.4 summarises the Nastran model.

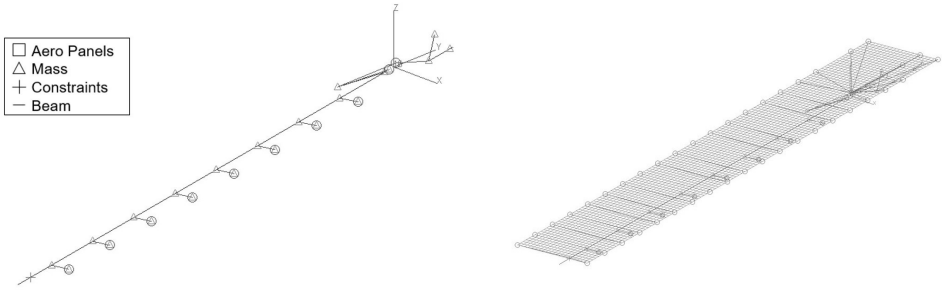

(a) (b)

FIGURE 6.6: Nastran model (a) without and (b) with Aerodynamic Panels

TABLE 6.4: Nastran Model Parameters

Element	Amount
Nodes	276
Beam Elements	205
Concentrated Masses	35
Rigid Beams	56
Aerodynamic Panels	3000

In order to apply the control shown in Chapter 6, first the structural system matrices are extracted from Nastran. The aerodynamic matrices are then estimated using Rational Function Approximation (RFA), as detailed by Eversman and Tewari [26]. This estimates Aerodynamic Influence Coefficient (AIC) functions for a given flight condition for a range of reduced frequencies. The AIC matrix relates the lift on each wing element to the dynamic pressure and the angle of incidence, and is detailed by Wright and Cooper [7]. First, the classical aeroelastic model is considered but with the aerodynamic terms moved to the right hand side of the equation.

$$\mathbf{A}\ddot{\mathbf{q}} + \mathbf{D}\dot{\mathbf{q}} + \mathbf{E}\mathbf{q} = \mathbf{Q}_{Aero}(t) \tag{6.1}$$

where $\mathbf{Q}_{Aero}$ is the generalised aerodynamic force vector. Equation (2.16) above is represented in the Laplace domain as

$$\left(\mathbf{A}s^2 + \mathbf{D}s + \mathbf{E}\right)\mathbf{q}(s) = \frac{\rho U^2}{2}\mathbf{Q}_{RFA}(s)\mathbf{q}(s) \tag{6.2}$$

where $\mathbf{Q}_{RFA}(s)$ is the RFA to the AIC expressed in modal space. Then, $\mathbf{Q}_{RFA}(s)$ is expanded via a RFA in terms of their Laplace variable $s = j\omega$ (where $j = \sqrt{-1}$), to give

$$\mathbf{Q}_{RFA}(s) = \mathbf{A}_0 + \mathbf{A}_1\frac{sb}{U} + \mathbf{A}_2\left(\frac{sb}{U}\right)^2 + \frac{U}{b}\sum_{n=1}^{N}\frac{\mathbf{A}_{n+2}}{(s + \frac{U}{b}p_n)} \tag{6.3}$$

where $\mathbf{A}_i,\ i = 0, 1, \ldots N+2$ are unknown matrices to be found and p_n are the N_L poles (lag parameters). The RFA approach allows for nonlinear effects to be examined in the state-space time domain using a 3D aerodynamic panel approach, however nonlinearities have not been considered in this work.

Following Nastran's model reduction and the extraction of the aerodynamic state-space matrices, a state-space model of the wing is then available for time domain analysis. This will be explained in detail in Chapter 6.

6.1.3 Model Validation

Similar to the tests carried out on the MODFLEX wings (Chapter 2), impact hammer tests were conducted on the folding wing tip setup. Two laser sensors were used, positioned at the flexural axis and towards the trailing edge, both just before the hinge section so that the bending and torsion modes could be measured. The fixed/active tip setup was tested in a fixed-free condition as the hinge is locked by the motor. To test the pendulum mode of the free wing tip, the tip was hung by itself in a fixed-free condition. The hammer test setup for the active tip can be seen in Figure 6.7, with red dots added to clearly see the laser positions.

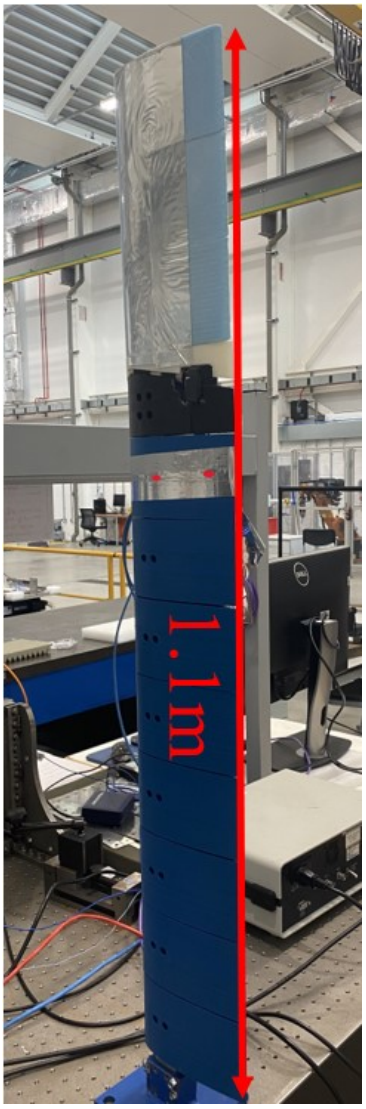

FIGURE 6.7: Hammer Test Setup for Folding Wing Tip Model

These laser positions were chosen to measure large deflections to obtain accurate results for the first bending and torsional modes. The natural frequencies and damping ratios of the two wing configurations can be seen in Table 6.5:

TABLE 6.5: Natural Frequencies and Damping Ratios for Fixed and Passive Wing Tips Setups

	Fixed Tip		Passive Tip	
Mode	f_n	ζ	f_n	ζ
Pendulum	-	-	0.62	0.06
1st Bending	2.85	0.02	3.57	0.03
1st Torsion	15.98	0.02	22.54	0.01

Ten hammer strikes were used to take an average FRF for each wing tip setup. Any double strikes, or poor strikes, were removed from the average, resulting in clear FRFs. The damping ratios are obtained using the Rational Fraction Polynomial code in MATLAB [135], which calculates the damping ratios based on the FRFs generated from the impact hammer tests. Higher modes have not been considered as no wind tunnel testing will be carried out in higher frequency regions. It is clear from Table 6.5 that the additional mass from the motor in the fixed tip variation has reduced the natural frequencies of the system compared to the passive tip case.

Figure 6.8 shows the passive wing tip, and the first three mode shapes for the fixed wing tip model in Patran:

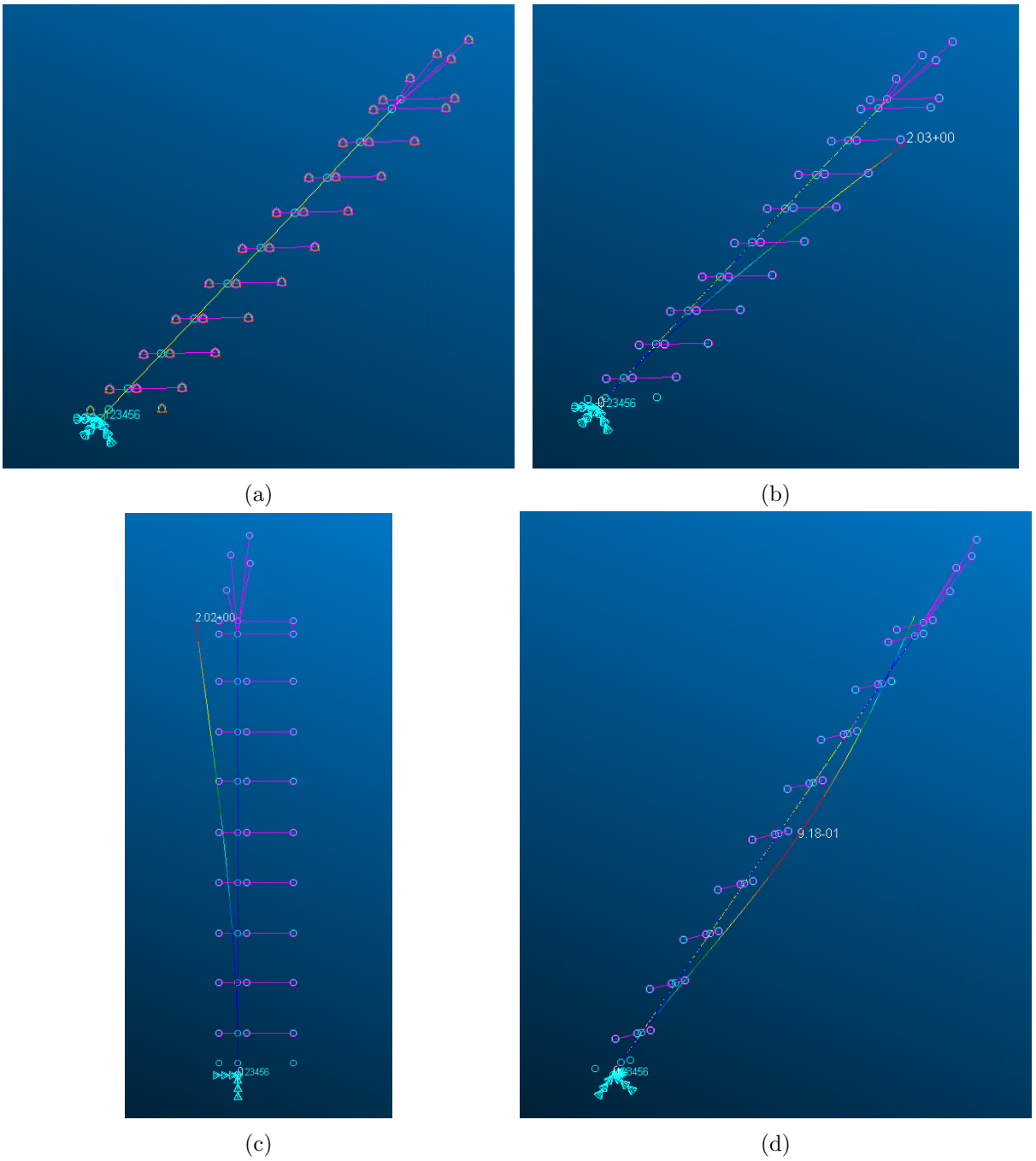

(a) (b) (c) (d)

FIGURE 6.8: Comparison of Fixed Wing Tip Mode Shapes (a) Static (b) Mode 1 (c) Mode 2, and (d) Mode 3

Mode 1 is the out of plane first bending mode, Mode 2 is the first in-plane bending mode, and Mode 3 is a combination of the second bending and first torsional mode. For comparison, the active folding wing tip mode shapes are shown in Figure 6.9:

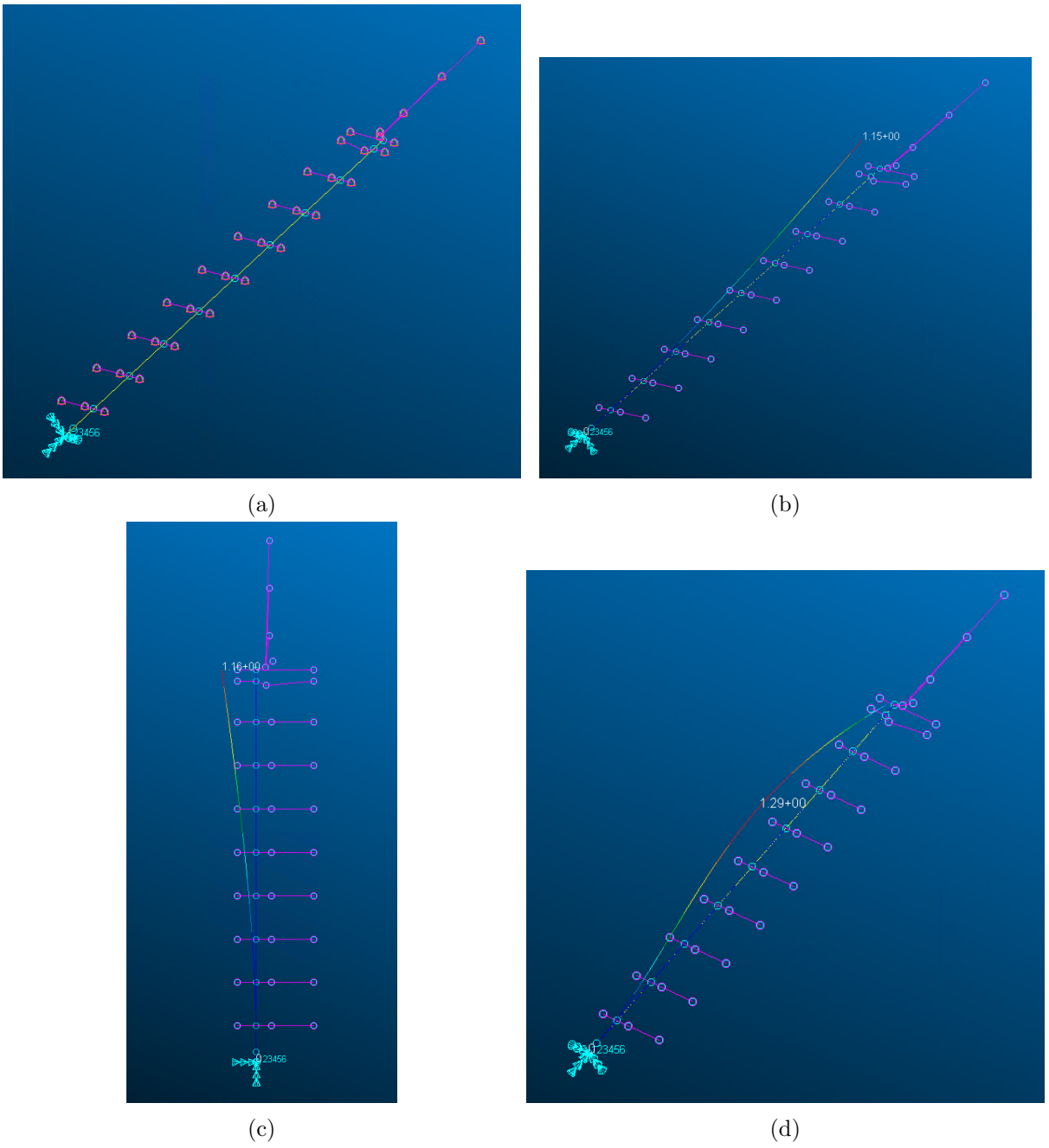

(a) (b) (c) (d)

FIGURE 6.9: Comparison of Passive Folding Wing Tip Mode Shapes (a) Static (b) Mode 1 (c) Mode 2, and (d) Mode 3

It is seen that the mode shapes remain the same, however the maximum deflections of each have changed. Generally the deflections have decreased, however Mode 3 has increased slightly.

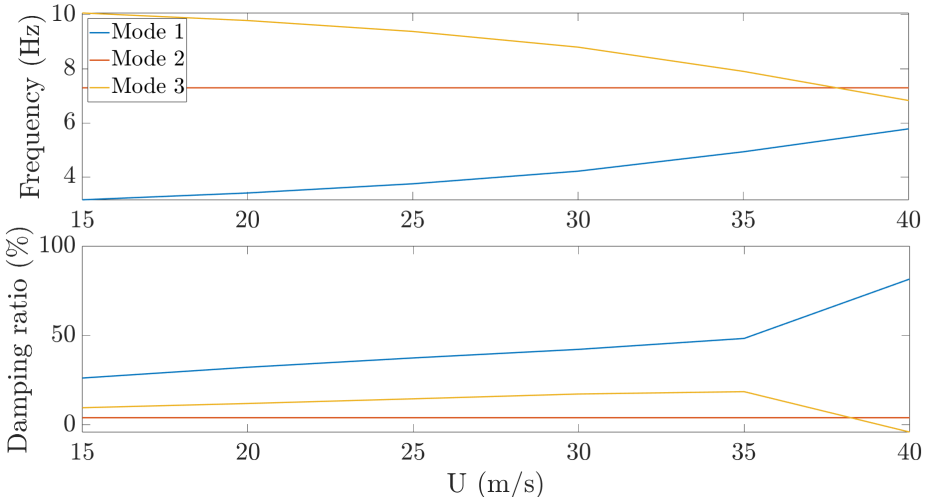

FIGURE 6.10: Natural Frequencies and Damping Ratios for the Folding Wing Tip Model

Figure 6.10 shows the natural frequencies and damping ratios for the passive folding wing tip model in Patran, with values obtained in intervals of 5 m/s. This gives a flutter speed of 39.25 m/s, caused by the instability of Mode 3.

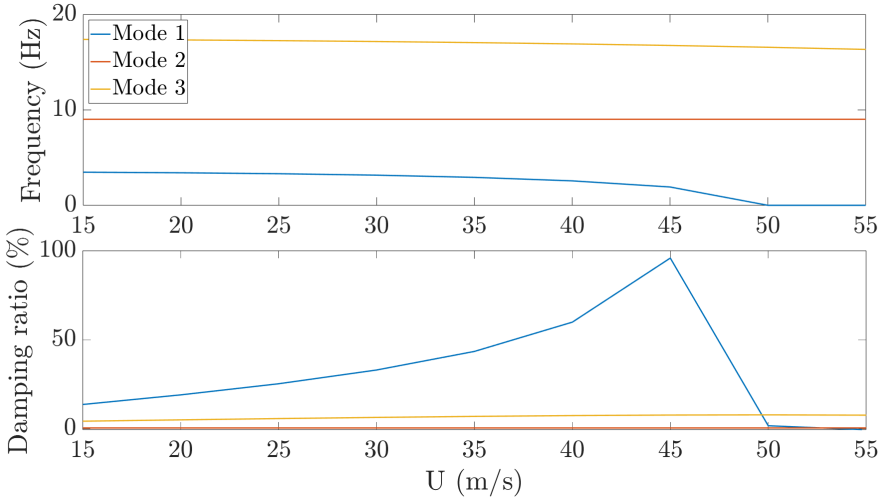

FIGURE 6.11: Natural Frequencies and Damping Ratios for the Folding Wing Tip Model

Figure 6.11 shows the natural frequencies and damping ratios for the active folding wing tip model in Patran. This gives a flutter speed of 53.21 m/s, caused by the instability of Mode 3.

6.2 Control Theory

This section outlines the control theory used in this study. PD control has been selected for this preliminary research as a proof of concept due to its simplicity and the ease with which the effects of the controller can be observed. PD control requires the measurement of displacement and velocity of the wing, with the aim of reducing the root bending moment. The first bending mode of the fixed wing section is selected for control, which directly affects the root bending moment. The PD control then commands a wingtip fold angle to reduce the bending of the wing, thereby reducing the root bending moment. The aeroelastic equation is formulated in state-space as:

$$\begin{aligned} \dot{\mathbf{x}} &= \mathbf{A}\mathbf{x} + \mathbf{b}_g w_g + \mathbf{b}_c \theta \\ \mathbf{y} &= \mathbf{C}\mathbf{x} \end{aligned} \tag{6.4}$$

where $\mathbf{x}$ is the $n \times 1$ state vector and contains all system state variables represented in the modal domain from Nastran after model reduction, $\mathbf{A}$ is the $n \times n$ system state matrix, $\mathbf{b}_g$ and $\mathbf{b}_c$ are the $n \times 1$ force distribution vectors due to the gust disturbance w_g and tip fold angle θ respectively, where θ is the input to the system. Then, $\mathbf{y}$ is the 2×1 state-space output and $\mathbf{C}$ is the $2 \times n$ output matrix, which acts to transform the two entries of interest in $\mathbf{x}$ from modal to physical values. As described in the previous section, RFA has been used to estimate the unsteady aerodynamics of the system. The set of reduced frequencies used to represent the aerodynamic modes, as well as the displacements and velocities of the first 20 structural modes of the wing, result in 173 states, so that $n = 173$.

The assumption made in this model is that higher modes are sufficiently damped and well separated, so that all states in $\mathbf{x}$ are negligible in comparison to the out of plane bending displacement and velocity, thus making them zero in comparison. As these additional states are zero, the only rows required in $\mathbf{C}$ are the two rows pertaining to displacement and velocity of the first bending mode, hence $\mathbf{C}$ is $2 \times n$.

The control objective of the system is to reduce wing vibration, which in turn reduces the stresses acting on the wing. In this case, the wing displacement at the hinge ξ and the velocity of this point $\dot{\xi}$ were measured for use as the control objective. Using PD control, the closed loop wingtip fold angle is calculated as:

$$\theta = -\mathbf{g}^T \mathbf{y}, \quad \text{where} \quad \mathbf{y} = [\xi \;\; \dot{\xi}]^T, \quad \mathbf{g} = [K_p \; K_d]^T \tag{6.5}$$

where K_p and K_d are the proportional and derivative gains respectively, ξ is the displacement of assumed bending mode of the wing and $\dot{\xi}$ is the velocity of the assumed bending mode. Then, the full closed loop state-space equation is given as

$$\dot{\mathbf{x}} = \left(\mathbf{A} - \mathbf{b}_c \mathbf{g}^T \mathbf{C}\right) \mathbf{x} + \mathbf{b}_g w_g \tag{6.6}$$

6.3 Numerical Results

Following the creation of the numerical model and the definition of the control system, numerical results have been calculated to check the validity of using an active hinged wing tip for gust alleviation. Root Locus plots have been generated to see the effects of the K_p and K_d gains on the closed loop system for an airspeed of 25 m/s and air density of 1.225 kg/m^3. First of all, Figure 6.12 shows the effects of $K_p = -10^{-8}$ to -10^{-3} for three distinct values of K_d.

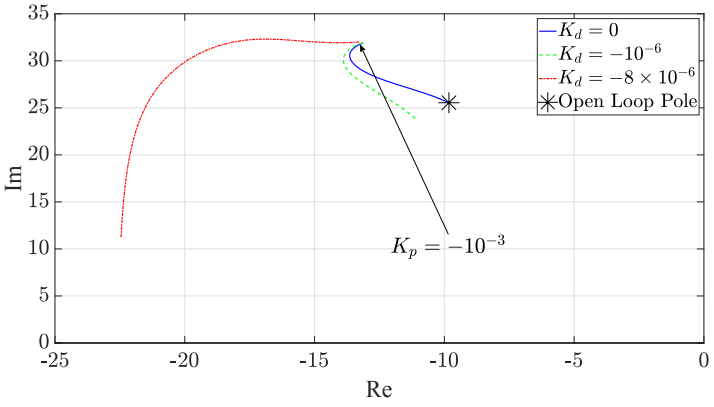

FIGURE 6.12: Root Locus Plot Showing Change in ξ Pole for Varying K_p and Three Values of K_d at 25 m/s

For all values of K_d, increasing K_p results in an increase in the damped natural frequency. This trends to a closed loop pole pair of $-13.1 \pm j31.9$, resulting in a closed loop natural frequency of 5.49 Hz and a damping ratio of 0.38. However, should the control aim be to increase the damping ratio, then a small value of K_p and large value of K_d should be used, as shown by the $K_d = -8 \cdot 10^{-6}$ case.

Next, three distinct values of K_p are analysed with $K_d = -10^{-8}$ to -10^{-5}. The Root Locus plot of this investigation is shown in Figure 6.13.

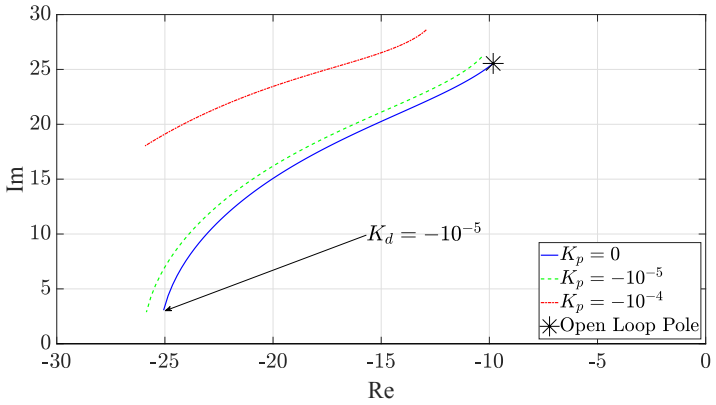

FIGURE 6.13: Root Locus Plot Showing Change in ξ Pole for Varying K_d and Three Values of K_p at 25 m/s

Again, it is clear that increasing K_p increases the damped natural frequency, and the damping ratio is increased as K_d is increased. The closed loop natural frequency is also increased with increasing K_d, but only to a certain point. This is shown for $K_p = 0, -10^{-5}$ where the imaginary part of the pole closely approaches zero, the real part does not decrease.

The values of K_p and K_d should be tuned based on the desired effects of the user. An optimal solution has not been considered for this work, as it depends on the frequency of the incoming gust. For example, if a gust is encountered with a frequency close to the bending resonance, then may be beneficial to shift the natural frequency. Alternatively, if the frequency of the incoming gust is significantly different to the bending resonance then simply increasing the damping ratio may suffice.

6.4 Experimental Results

Numerous experimental tests were carried out for three distinct airspeeds: 20, 22.3, and 24.5 m/s. Both 1-cosine and harmonic gust responses were analysed for different angles of attack (AOA) as well as different initial wing tip fold angles, in the fixed and active tip cases. In the active wing tip- cases, two sets of gains have been used for both gust types to demonstrate the effect of tuning controller gains on the wing vibration. Figure 6.14 shows the time response of the Wing Root Bending Moment (WRBM) to a 4 Hz 1-cosine gust at 20 m/s and an AOA of 0°. The first positive and negative peaks have

been highlighted as these will be used in all of the following figures, where WRBM is defined as positive for the wing bending vertically up.

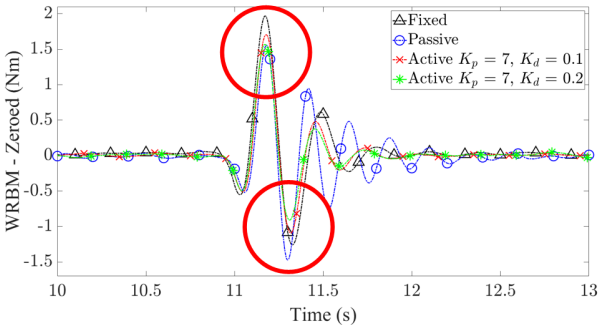

FIGURE 6.14: WRBM for all Wing Tip Cases at 20 m/s with 4 Hz 1-Cosine Gust

Some limitations to the tests were found. For instance, the passive wing tip could not be used at an AOA greater than 2° as it would fold to the maximum limit, therefore unable to fold more to have any effect on the response. Next, the motor used for the active cases has a current limit which would be exceeded in some harmonic gust cases at 24.5 m/s, specifically for non-zero AOA or coast angle. Additionally, after the motor PID was tuned effectively to give a low error, the current limit prevented any deflection above 6° as the angular velocity would cause the demanded current to exceed the motor's limit. This meant that PD gains were selected to prevent the wing tip from folding more than ±6°, meaning the results shown for the active tip are not optimum. These limitations will be considered in a new design for future work. One key consideration for an active tip is the additional weight added to the wing, resulting in an increase in WRBM.

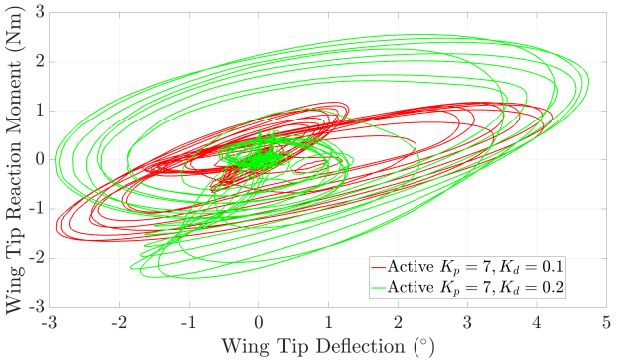

FIGURE 6.15: Reaction Moment for the Active Tip Deflections at 20 m/s

Figure 6.15 shows the reaction moments as a function of the wing tip deflection for the two active tip cases at 20 m/s for all 1-cos gusts, with the reaction moment calculated as the difference in WRBM between the fixed tip case and the active tip cases. As expected,

the larger K_d case produces a larger wing tip deflection and therefore a larger reaction moment.

TABLE 6.6: Static WRBM For Passive and Active Wing Tips

Airspeed (m/s)	WRBM - Passive Tip (Nm)	WRBM - Active Tip (Nm)
20.0	1.44	-0.92
22.3	1.45	-0.89
24.5	1.46	-0.87

Table 6.6 gives the static WRBM for the active and passive tips for each airspeed tested. As in the figures shown in this work, a positive WRBM relates to the wing bending up, and a negative WRBM is for the wing bending down. It is clear that the increase in weight has a significant effect on the WRBM, with an additional -2.3 Nm applied at the root as the lift produced in the static airflow is not enough to counteract the effect of the additional weight, which is a drawback to the active tip system. In future work, other motor positions and configurations will be considered to alleviate the static WRBM of the wing.

	Angle of Attack (°)			Initial Fold Angle (°)		Gust Type	
Wing Tip	0	2	4	0	5	1-Cosine	Harmonic
Fixed	✓	✓	✓	✓	✓	✓	✓
Passive	✓	✓				✓	✓
Active	✓	✓	✓	✓	✓	✓	✓

TABLE 6.7: List of Tests Carried Out for Each Wing Tip Configuration

Table 6.7 shows which tests are carried out for each wing tip. Considering the three airspeeds, and two sets of PD gains for the active tip, a total of 116 tests were carried to account for every possible configuration of airspeed, AOA, initial fold angle, gust type, and PD gains.

6.4.1 1-Cosine Gusts

The tests used for 1-cosine gusts used one cycle of each gust from 1-10 Hz. Sufficient time was given for the wing to come to rest before the next gust encounter. A vane rotation of 10° was used. The vertical airspeed changes depending on gust frequency and airspeed, but remains within the range of 1.5 to 2 m/s.

6.4.1.1 Airspeed Comparison

Initially, tests were carried at 0° AOA and initial fold angle for the airspeeds previously mentioned. Figure 6.16 shows the consistent trends as the airspeed increases, where the overall WRBM increases with airspeed but each wing tip configuration maintains relative performance to the others. The WRBM is defined as positive in the direction of the wing tip bending upwards.

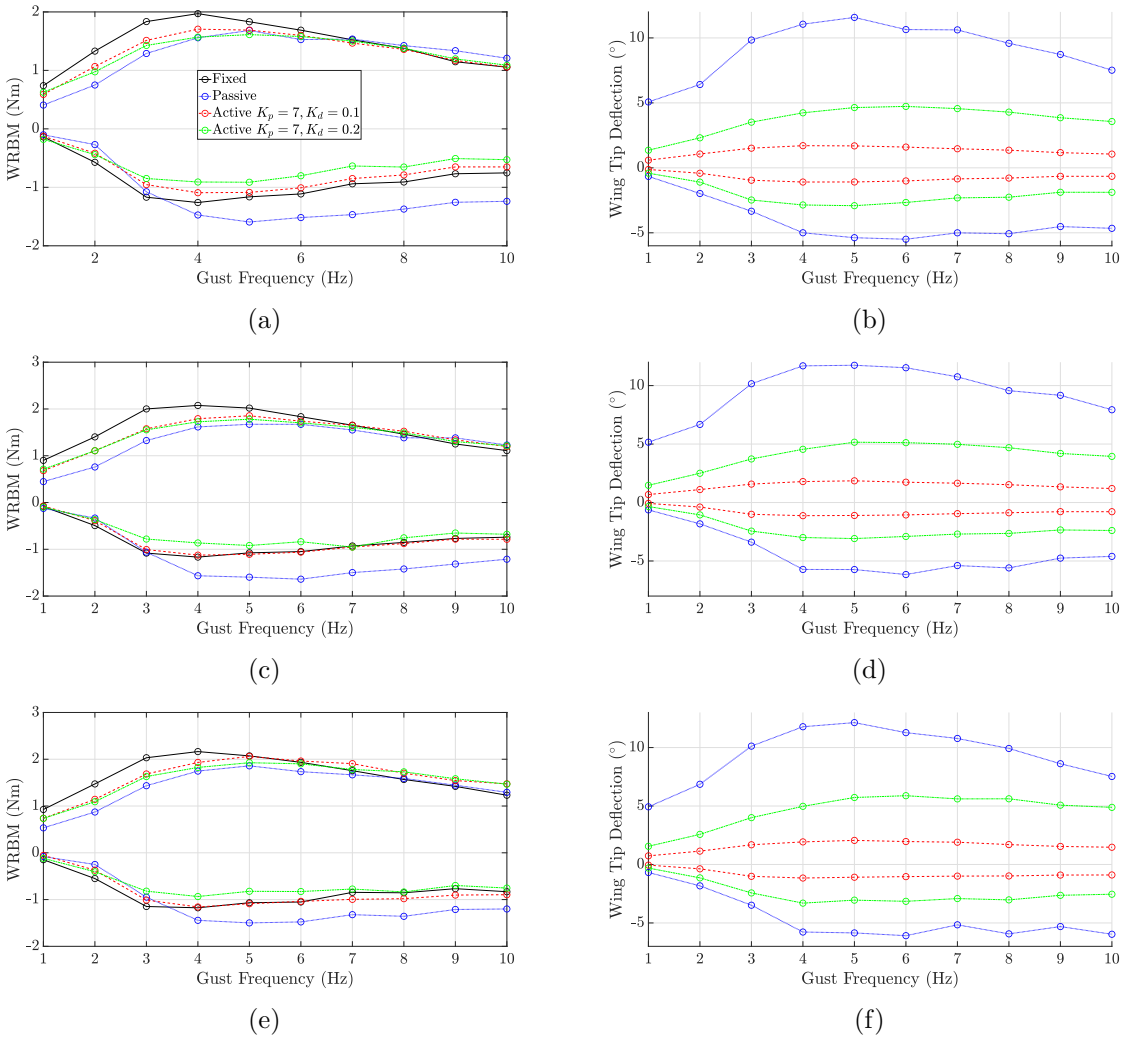

FIGURE 6.16: Response due to 1-Cosine Gusts at (a,b) 20.0 m/s (c,d) 22.3 m/s, (e,f) 24.5 m/s

All wing tips cases improved the WRBM for the largest gust responses compared to the fixed tip, before declining in effectiveness thereafter. The largest response for all tip configurations is at 4 Hz due to the natural frequency of the first out-of-plane bending mode being close to 4 Hz. One significant observation is that as the gust frequency increases, the passive wing tip worsens the WRBM when compared to the fixed tip case,

specifically from 7 Hz and particularly in the negative peak. This shows that an active wing tip is a valid consideration, especially as it can be tuned to combat incoming gusts depending on the frequency if the gust can be detected. Additionally, the active tips required significantly smaller deflection angles than the passive tip, so is more efficient in terms of deflection, but of course requires increased power input for an aircraft. As previously mentioned, the active cases were tuned so that the motor limits were not exceeded. This suggests that with an improved design, an active tip can further improve the WRBM if a larger range of fold angle was available. The active tip is less effective for smaller wing deflections because the PD control implemented means that the wing tip deflection is directly determined by the wing bending. The response can be improved in these areas simply by increasing the control gains depending on the incoming gust to ensure the wing tip deflection is increased.

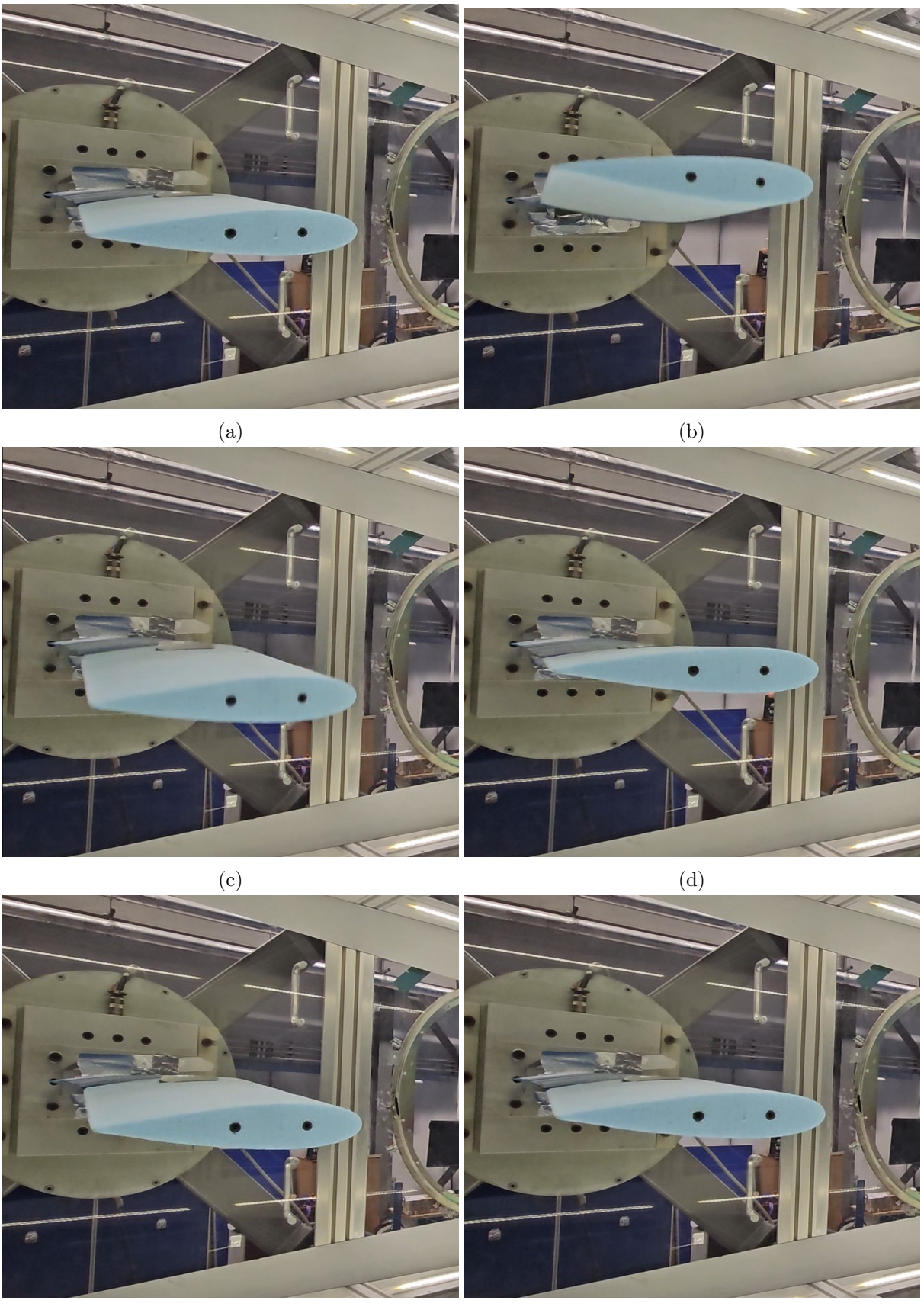

(a) (b) (c) (d) (e) (f)

FIGURE 6.17: Photos of the Active Wing Tip Responding to a 4 Hz 1-Cosine Gust at 20 m/s

Figure 6.17 shows the physical response of the active folding wing tip in response to a 4 Hz 1-cos gust at 20 m/s. Figure 6.17a shows the wing at rest before encountering the gust. The first four peaks of the response in Figure 6.14 are clearly shown in Figures 6.17b to 6.17e, with the wing tip deflecting in the appropriate direction to counteract the deflection caused by the incoming gust. It is shown that the wing tip effectively reduces the deflection, as seen by the reduced deflection in Figures 6.17d and 6.17e when compared to the first two peaks in Figures 6.17b to 6.17c. Figure 6.17f then shows the wing at rest following the gust encounter and wing response.

6.4.1.2 Effect of Angle of Attack

The next series of tests involves increasing the AOA of the wing to represent climb conditions of a full aircraft. Additionally, the aim is to see how varying AOA affects the passive wing tip deflection and the effectiveness of the control system for the active tip. As results follow the same trend at all airspeeds, only results for 20 m/s will be discussed for brevity. Figure 6.18 shows the effect on the WRBM of increasing the AOA on the fixed wing case.

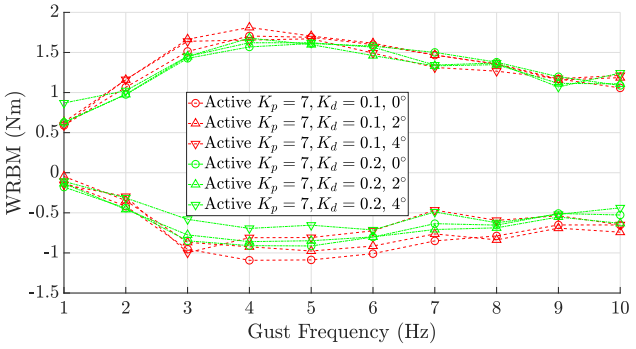

FIGURE 6.18: WRBM for the Fixed Wing Tip Case at 20 m/s for Different AOA with 1-Cosine Gusts

As expected, an increase in AOA leads to increased lift and therefore greater WRBM. The active case where $K_d = 0.2$ seems to be more effective at higher frequencies than the lower gain case when AOA is increased, however there was a larger variation in static WRBM for higher AOA so there are some outliers in these results. The largest change in WRBM due to gust encounter is at 4 Hz, and thus the WRBM comparison of each wing tip for each AOA will be compared for the 4 Hz gust in Table 6.8:

TABLE 6.8: Percentage Difference in Respect to the Fixed Tip in Maximum WRBM due to a 4 Hz 1-Cosine Gust at 20 m/s

	Maximum Peak			Minimum Peak		
Wing Tip	% Dif, 0°	% Dif, 2°	% Dif, 4°	% Dif, 0°	% Dif, 2°	% Dif, 4°
Passive	-20.4	-18.2	-	+16.9	+18.3	-
$K_d = 0.1$	-13.2	-6.3	-17.3	-13.3	-16.7	-17.4
$K_d = 0.2$	-20.2	-13.3	-19.2	-27.9	-22.5	-29.3

As previously mentioned, the passive wing tip will fold to its maximum position when the AOA is increased to 4°, hence this has been omitted from the table. It is clear from Table 6.8 that the active tip significantly improved the minimum peak in particular as AOA is increased, whereas the passive tip has a significantly worse effect on the WRBM negative peak.

6.4.1.3 Effect of Initial Fold Angle

The aim with introducing an initial fold angle is to reduce the WRBM when the gust initially hits, i.e. target the first positive peak of the gust response. As the passive wing tip has no locking capability, it was not used in this test.

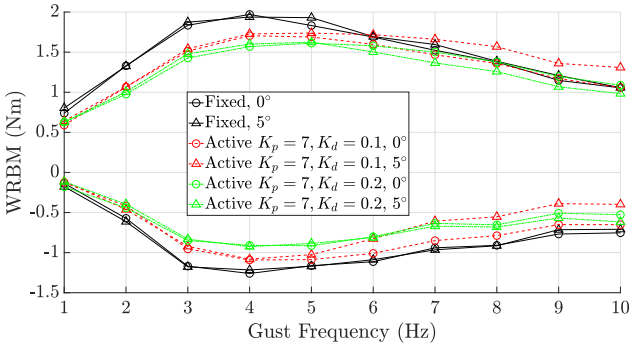

FIGURE 6.19: WRBM for the Fixed Wing Tip Case at 20 m/s for Different Initial Fold Angles with 1-Cosine Gusts

It is seen in Figure 6.19 that for the fixed tip case there is very little change in the WRBM, suggesting that an initial wing tip fold angle has very little effect on the gust response. However, when active control is introduced we see significant changes depending on the control gains used. For the lower K_d case, there is significant improvement to the negative peaks above 5 Hz at the expensive of an increase the positive peak, which is the opposite effect intended for this test. On the other hand, the larger K_d case shows an

improvement in the positive peak above 5 Hz with small expense on the negative peak. However, the negative peaks are still smaller than in the fixed case, meaning an initial 5° fold angle has improved the WRBM overall compared to the fixed tip case. This suggests that using an initial fold angle in the presence of 1-cosine gusts can be effective when paired with a controller if the gains are tuned adequately to reduce the WRBM.

6.4.2 Harmonic Gusts

The tests used for harmonic gusts used ten cycles of each gust frequency of 1, 4, 5, 7 and 8 Hz as this captures an appropriate range of frequencies, while focusing on key frequencies that produce large displacements. Ten gust cycles were used as if the gust frequency is close to the natural frequency, it gives time for signs of resonance to show, or for the response to achieve its maximum deflection. Sufficient time was given for the wing to come to rest before the next gust encounter. Again, a vane rotation of 10° was used. The responses to a 4 Hz Harmonic gust at 20 m/s can be seen in Figure 6.20.

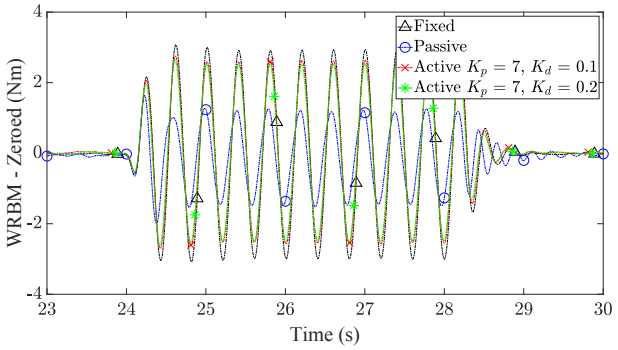

FIGURE 6.20: WRBM for all Wing Tip Cases at 20 m/s with 4 Hz Harmonic Gust

As increasing the value of K_d effectively increases the damping of the system, it is seen in the active cases that the wing bending is reduced across all cycles of the gust, thus reducing the WRBM. However, while the passive tip is still the most effective at certain gusts frequencies, the advantage of the active tip will be discussed in this section.

6.4.2.1 Airspeed Comparison

As with the 1-cosine tests, initial tests were carried out at 0° AOA and initial fold angle for the three airspeeds previously mentioned. Figure 6.21 shows the WRBM for each airspeed.

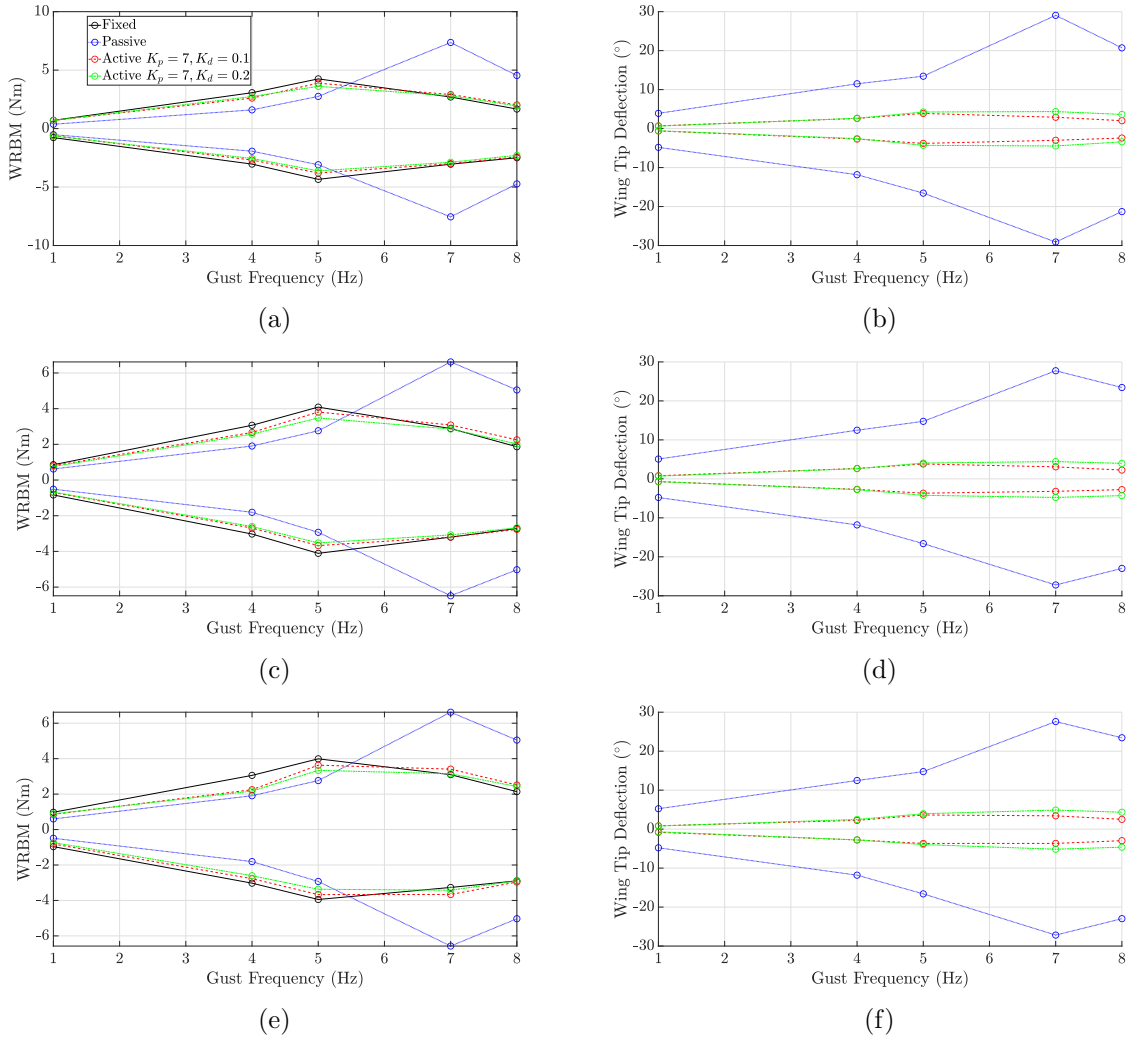

FIGURE 6.21: Response due to Harmonic Gusts at (a,b) 20.0 m/s (c,d) 22.3 m/s, (e,f) 24.5 m/s

Similar to the 1-cosine responses, all non-fixed wing tip cases improve on the fixed tip case from 1-5 Hz, but then lose effectiveness and worsen the WRBM above 5 Hz. This is particularly prevalent in the passive wing tip case.

One key difference between passive and active tips occurs at frequencies above 5 Hz. It was seen in testing that for the 7 and 8 Hz gusts, the passive tip would fold in the opposite direction, causing a 'flapping' motion and contributing to increased bending. There is no resonance near enough to 7 Hz in this model to cause this phenomenon, and a likely cause is snap-through buckling, however this was not investigated further in the tests. Conversely, the nature of the control ensures that the active tip configuration works to reduce the peaks as it is forced to fold in the correct direction. The percentage difference in peak WRBM can be seen in Table 6.9:

TABLE 6.9: Percentage Difference in Minimum WRBM due to Harmonic Gust at 20 m/s

Tip	% Dif, 4 Hz	% Dif, 7 Hz
Fixed	-	-
Passive	-58.5	+221.2
$K_d = 0.1$	-10.0	+14.8
$K_d = 0.2$	-15.7	+10.9

6.4.2.2 Effect of Angle of Attack

As in the 1-cosine section, the following will show the effect of AOA on the WRBM for an airspeed of 20 m/s, but now using the harmonic gust profile. Figure 6.22 shows the WRBM of the fixed wing tip for each AOA.

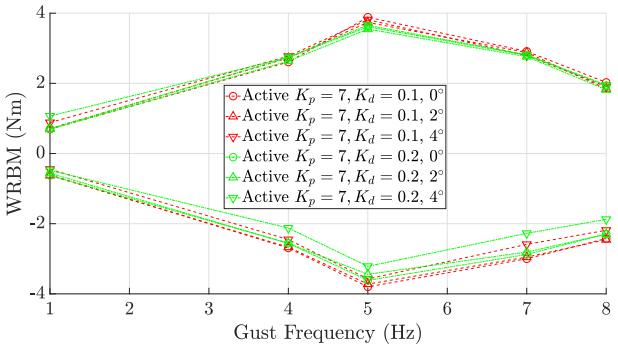

FIGURE 6.22: WRBM for the Fixed Wing Tip Case at 20 m/s for Different AOA with Harmonic Gusts

Again, the WRBM is increased due to the increase in lift caused by a non-zero AOA. However, the increased K_d gain case consistently improves the negative peaks more effectively than in the 1-cosine case when compared to the smaller K_d gain case.

6.4.2.3 Effect of Initial Fold Angle

Similar to the 1-cosine gust tests, an initial fold angle was explored for the harmonic gust tests. The biggest difference is that the gusts now act upwards and downwards on the wing across the cycles, so an initial positive fold angle could be more detrimental to the negative peak than in the 1-cosine tests. The results of these tests can be seen in Figure 6.23.

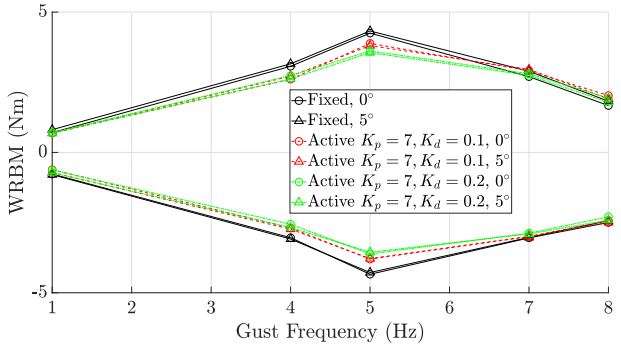

FIGURE 6.23: WRBM for the Fixed Wing Tip Case at 20 m/s for Different AOA with 1-Cosine Gusts

Across all frequencies tested, there seems to be no benefit in using an initial fold angle for the active cases as the WRBM readings remain similar. The only noticeable effect is that the fixed tip case has a larger positive WRBM at higher frequency, meaning using an initial fold angle has made the response worse.

6.5 Summary

First of all, a numerical model was produced and analysed to test the validity of using PD control by exploring the effects of the controller gains in root locus plots. Following this, two experimental wing tip configurations have been tested under gust loads for various conditions. In previous research, it is observed that while a passive wing tip reduces the first positive peak in the WRBM during 1-cosine gusts, it always increases the first negative peak, and it is not possible to reduce the negative peak using a passive tip. Additionally, it is seen in this work that a passive wing tip can have a flapping motion in the presence of harmonic gusts, significantly worsening the WRBM when compared to a standard fixed wing tip. The active wing tip configuration explored in this work has shown that it is possible to reduce the negative peak significantly during 1-cosine gusts, as well as preventing a flapping motion during harmonic gusts due to the control law forcing the wing tip to always fold in the direction that opposes wing bending. The active configuration can also be used to lock the wing tip if necessary, as it has been used for the fixed tip tests.

This work also explored increasing AOA to simulate take-off conditions. One significant drawback of a free-hinged wing tip is that increasing AOA significantly will cause the tip

to fold to fold to its maximum, meaning it is essentially locked and will have no effect on WRBM if a gust is encountered. Again, it was observed that an active wing tip can positively affect WRBM in the presence of gusts depending on how the PD gains are tuned. Increasing the derivative gain increases the damping of the system, which clearly reduces the negative peak in the 1-cosine case and improves the overall response in the presence of harmonic gusts.

Finally, an initial fold angle was introduced for the fixed and active wing tip cases. It was seen that with a well tuned controller, the response is significantly improved in the presence of 1-cosine gusts. However, when harmonic gusts are encountered there is little effect on the active tip response or a negative effect on the fixed tip response when an initial wing tip angle is used. This prompts the need for gust detection.

There were several limits to the results in this work. The most significant being the motor used in active control. One solution would be to increase the flare angle of the wing tip, meaning there is a greater aerodynamic effect for the same wing tip fold angle. An improved motor setup could also be used to remove the limit entirely. Another improvement to this work would be to investigate feedforward control. If a gust can be detected before the encounter, for instance with a LiDAR sensor, then this would improve the WRBM throughout the gust if a feedforward controller is also implemented. Finally, some effects of changing PD gains were shown. If a full PID controller were introduced, the gains could be tuned for each gust frequency to minimise the WRBM, as well as reducing the settling time of the response after a gust encounter.

Several considerations have been made for future work. For instance, the flapping motion seen in the passive wing tip for responses to certain harmonic gusts is concerning and should be investigated further to pinpoint the source of the phenomenon. One significant consideration for active wing tips is the additional weight and control power required. Future work must look at different tip configurations to reduce both of these before an active wing tip can be considered for a full-sized aircraft. One benefit of an active wing tip that has not been explored in this work is for controlling flutter, which will also be an important consideration for future work.

Chapter 7

CONCLUSIONS AND FUTURE WORK

7.1 Conclusions

This thesis has presented numerical and experimental studies on control methods for linear and nonlinear aeroelastic systems for the purposes of gust alleviation and flutter suppression. Generally, binary flutter models were considered using MATLAB for their simplicity in flutter prediction and ease of modelling, allowing for control to be applied effectively. While binary flutter models are excellent for simplifying numerical practices, they lack detail and therefore predict the characteristics of the physical experimental models less accurately than higher order models. In later work, a reduced order Nastran model was used for the folding wing tip setup for greater accuracy in the numerical modelling. Both 1-cosine and harmonic gusts have been investigated and controlled, numerically and experimentally using different control methods and control surface configurations. The effects of flutter are well documented in the literature, so flutter suppression techniques have been explored for linear and nonlinear models.

Chapter 3 uses the Receptance Method for gust load alleviation of the MODFLEX wing model. While numerical studies showed this is a viable technique, experimental results were limited by the noisy receptance data collected and physical limitations of the model

itself. Considering these experimental issues, the MODFLEX 2.0 wing was designed and used in Chapter 4, where the receptance method was used in an iterative process to extend the flutter speed of the system. Numerically, the flutter speed could be extended by 18.35% for the single-input case, and as much as 22.21% when two control surfaces are used. However, it was identified that the presence of the in-plane mode between the first bending and torsional modes prevented receptance data from being recorded at higher airspeeds. This highlights the importance of being mindful of all potential modes and their interactions during the design process, or selecting a control method that is compatible with the wing dynamics. A Root-Heave Degree of Freedom was designed and implemented in Chapter 5 as a preliminary investigation to move towards hybrid testing, as the greater aim was to replicate the motion of a full aircraft while only using a wing model inside the wind tunnel. Pole Placement via Feedback Linearisation was selected as the control method, with the aim of counteracting LCO occurring after a gust is encountered. It was found that flutter occurred in the system, instead of LCO, as the RHDoF was not one of the coupling modes, thus the nonlinearity was not present in the unstable dynamics to cause LCO. It was found numerically that the Feedback Linearisation method successfully prevents flutter from occuring, with the MIMO system marginally improving on the SISO system. Finally, Chapter 6 investigates the use of an active folding wing tip model for the reduction of WRBM in response to 1-Cosine and harmonic gusts, and compares this approach to a standard fixed tip, and a passive hinged wing tip. Both the tests in this chapter, and in the literature, show that the first negative peak of the WRBM following a gust is worse when a passive tip is used instead of a fixed tip. The active wing tip used in this work definitively improves on the first negative peak when compared to both fixed and passive tips, however the PD controller should be tuned depending on the gust profile and frequency.

In general, this work has investigated numerous control methods for gust alleviation and flutter suppression, both of which are key in aircraft design and must be explored to help improve aircraft efficiency and contribute to the environmental initiatives shown in Chapter 1. While the work has been carried out with varying success, any problems in numerical modelling or experiments have been identified and this work can be used as a stepping stone towards further research.

7.2 Recommendations for Future Work

The work discussed in this thesis introduces the possibility of the following future work:

- Improve numerical modeling of the MODFLEX type wing models using MSC/Nastran so that gust response and flutter prediction can be obtained more accurately. This would also aid in the design process for future MODFLEX iterations.
- Repeat gust response alleviation via the Receptance Method tests using the MODFLEX 2.0 wing (or newly designed iteration of the MODFLEX wing) and develop the MIMO controller. Following changes in the test setup, and the introduction of the second controller, a better investigation can be carried out into gust response and load alleviation using the the Receptance Method.
- Increase the width of the spar in the MODFLEX 2.0 wing to increase the natural frequency of the in-plane mode so that it does not couple with the torsional mode as it converges with the bending mode close to flutter. This would result in clearer receptance data that can be post processed for control to be applied.
- Following the previous suggestions, develop and implement MIMO control experimentally to the gain scheduling problem and attempt to further increase the flutter speed of the flexible wing model.
- Develop an experimental rig for the Root-Heave Degree of Freedom system to apply the Feedback Linearisation method demonstrated numerically in this work.
- Introduce pitch motion at the root, combined with the RHDoF model, allowing for the exploration of two nonlinearities in a single model.
- Numerically, a detailed full-aircraft model should be implemented with the RHDoF system for the use of hybrid testing.
- An additional improvement is to include more actuators in the MODFLEX design series so that more modes can be controlled in the Feedback Linearisation problem.
- Numerically and experimentally test the effects of different flare angles for the same motor configuration in the folding wing tip setup.
- Explore different motor placements and configurations for the active folding wing tip model so that static WRBM is reduced.

- Introduce a servomotor to control the folding wing tip as a light-weight alternative to the high torque motor used in this work.
- Develop a controller that directly combats the WRBM in the folding wing tip model, as opposed to reducing only the bending motion.
- Numerically and experimentally test the active folding wing tip with increased wing span and tip span. This would help to address the industry move towards HALE aircraft as described in Chapter 1.
- Carry out flutter analysis both numerically and experimentally on the folding wing tip model. Various control laws should be explored to develop an active flutter suppression system as an active folding wing tip has not been used in this capacity before. This is necessary research before an active folding wing tip can be considered for use in commercial aircraft.
- All work in this thesis has been carried out using rectangular wings. Before any of the proposed control methods can be introduced to commercial aircraft, they must be tested on wing models that are tapered and swept, as well as a full aircraft model as these are more true to life.
- Each of the wing models used in this work should be developed iteratively with the aim of reducing mass by reducing the support structure. This would result in more flexible wings which would further test the effectiveness of the control systems used. The aim of reducing the mass then relates to the environmental initiatives described in Chapter 1, as showing active control implementation leads to reducing the wing mass then results in increasing an aircraft's range and fuel efficiency.

Appendix A

CAD MODELS AND DRAWINGS FOR MODFLEX WING

All CAD models and drawings are available upon request at ellis.james2018@gmail.com

A.1 Milled Parts

Some metal work is required in order to produce the MODFLEX wing. First of all, an aluminium spar is required to provide stiffness for the system.

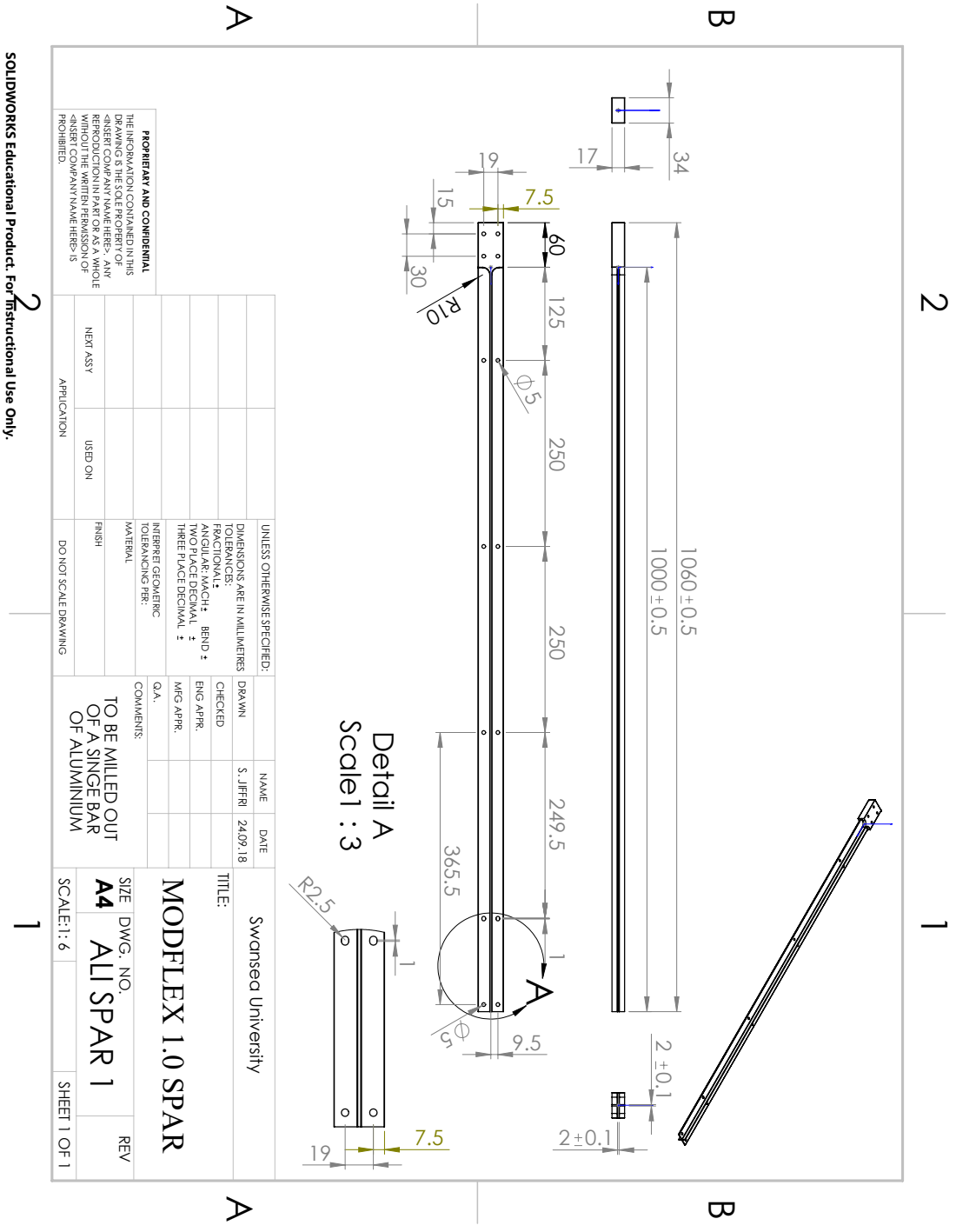

FIGURE A.1: Technical Drawing for MODFLEX Aluminium Spar

Figure A.1 shows the technical drawing for the aluminium spar used to provide stiffness to the wing. Only one spar is required for the wing.

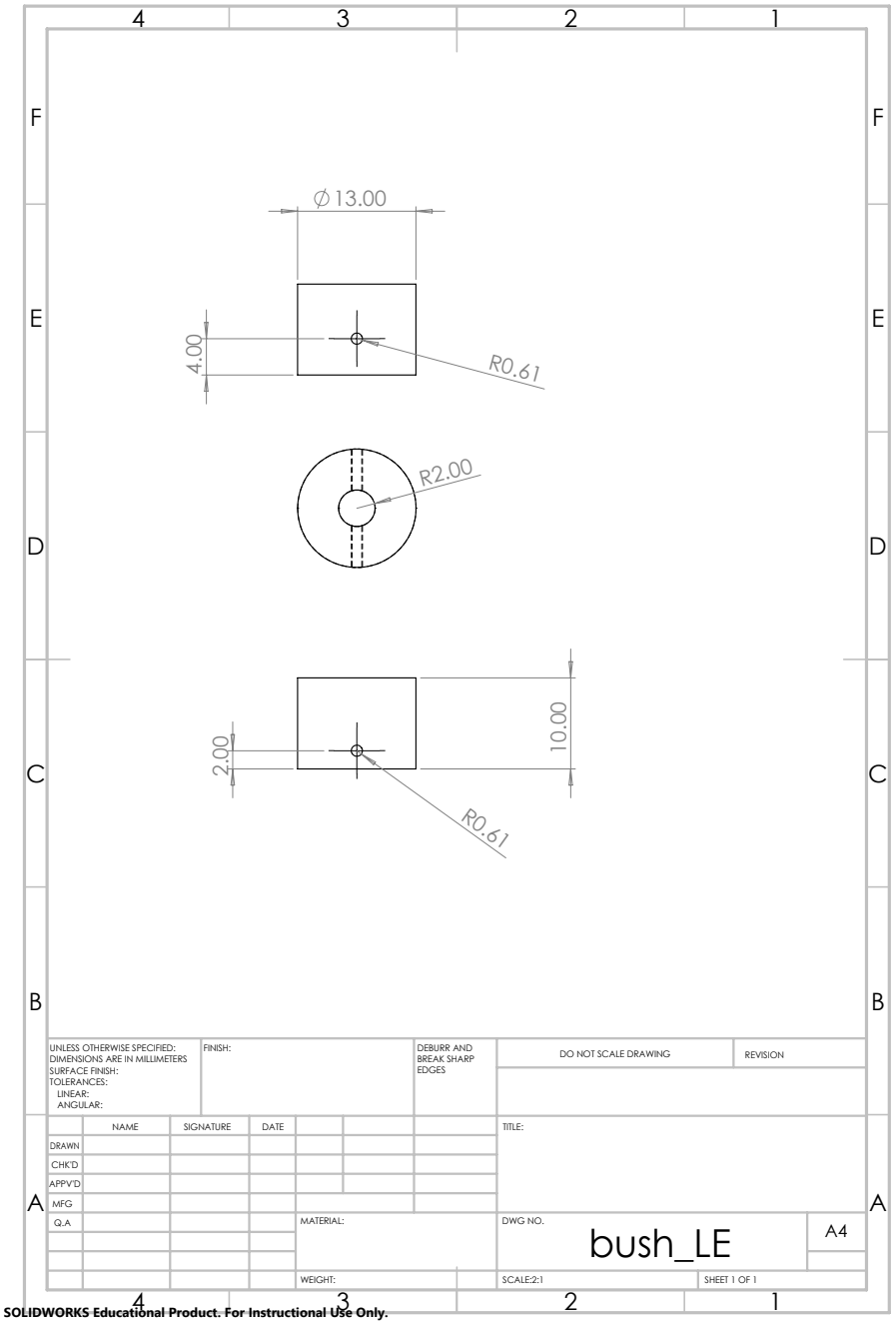

FIGURE A.2: Technical Drawing for MODFLEX Metal Bush

Figure A.2 shows the technical drawing for the metal bush used in the connection of the control surfaces to the motors. One bush is required per control surface used, therefore two are used in this work.

A.2 3D Printed Sections

All 3D printed sections are made from ABS-M30 FDM Thermoplastic Filament. Under compression, the material has a yield strength of 30MPa and an elastic modulus of 2.2 GPa, which allows the assumption of rigidity of 3D printed parts during wind tunnel testing.

A.2.1 Passive Section

The first 3D printed part necessary for the MODFLEX wing is the passive quarter section. Three are used in the work presented, however they can be substituted for additional active sections if necessary. The passive section acts as an aerodynamic surface only, and does not provide any structural stiffness.

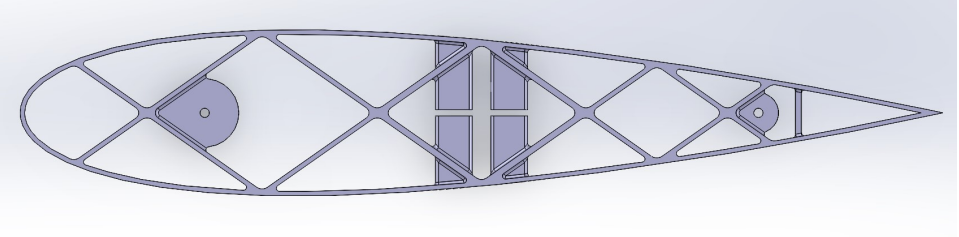

FIGURE A.3: Passive Aerofoil Section for MODFLEX Wing

Figure A.3 shows the passive quarter section used on the MODFLEX wing. A lattice structure is used to ensure the rigidity of the section. The lattice structure and outside surface are both 1.5mm thick, which balances the mass and the structural rigidity.

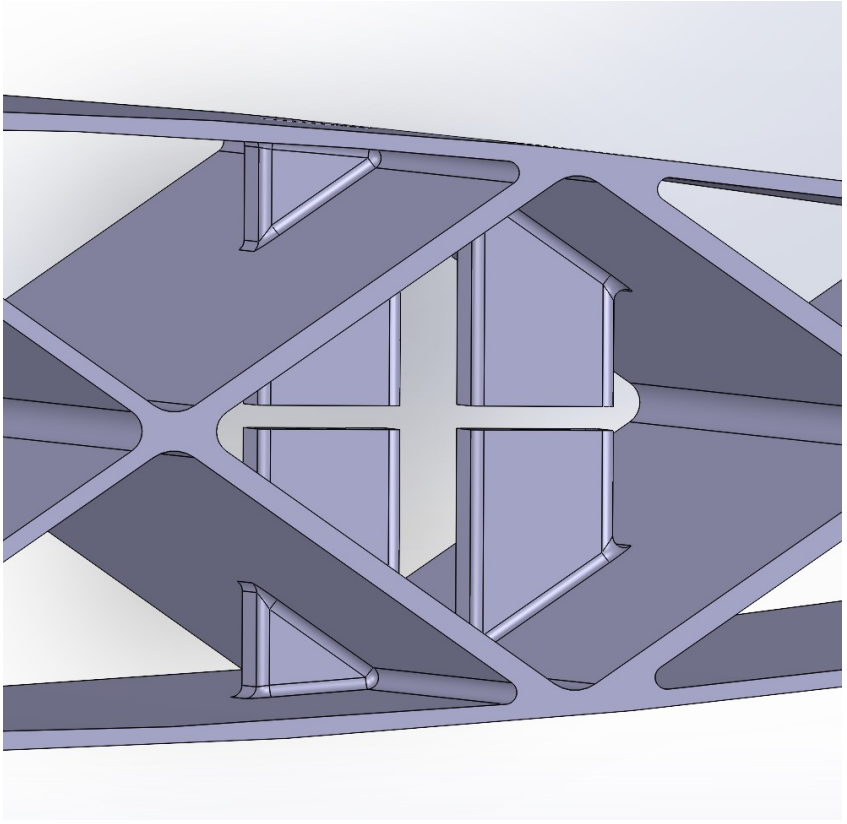

FIGURE A.4: Passive Aerofoil Section Fixing for MODFLEX Wing

Figure A.4 shows the structure made to fix the passive section to the spar. Four rectangular columns are used as clamps using M2.5×25 bolts and nuts that run through the entire 3D pinted section, with a + shaped space for the spar. The rectangular columns are 12×14mm as this provides a significant clamping surface without preventing a large section of the wing from bending. Two bolts are used for each quarter section. The flat surfaces of the columns are 2mm apart in the centre to allow space for the spar to have a close fit. The bolt holes are centred in the middle of the section spanwise, and 140.5mm and 159.5mm from the leading edge respectively.

A.2.2 Active Section

In order to provide control, an active section must be used. A leading edge and trailing edge control surface are attached to a central active section, which in turn is fixed to the spar.

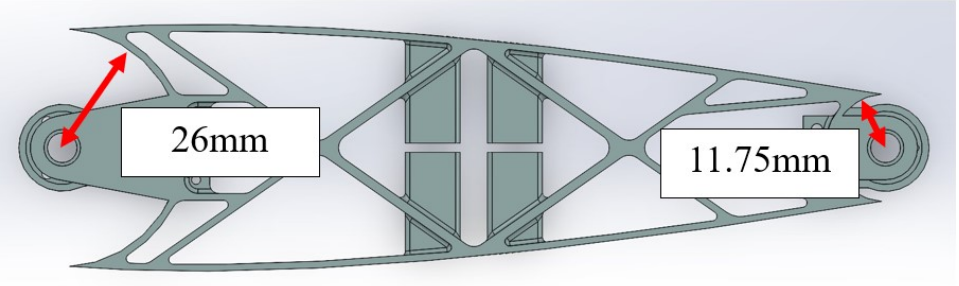

FIGURE A.5: Central Active Aerofoil Part for MODFLEX Wing

Figure A.5 shows the main part for the active section, without the control surfaces. It has the same lattice structure and connection to the spar as the passive section. The radii of the cutaway sections are shown so that the control surfaces can move without resistance when in use. It is worth noting that the centres are the hinge axes for the control surfaces, meaning that the centres are 75mm and 225mm from the leading edge of the full aerofoil.

A.2.2.1 Control Surface and Motor Fixings

A number of elements are used to attach the motors and control surfaces to the main active sector part. Figure A.6 shows the additions required and their dimensions.

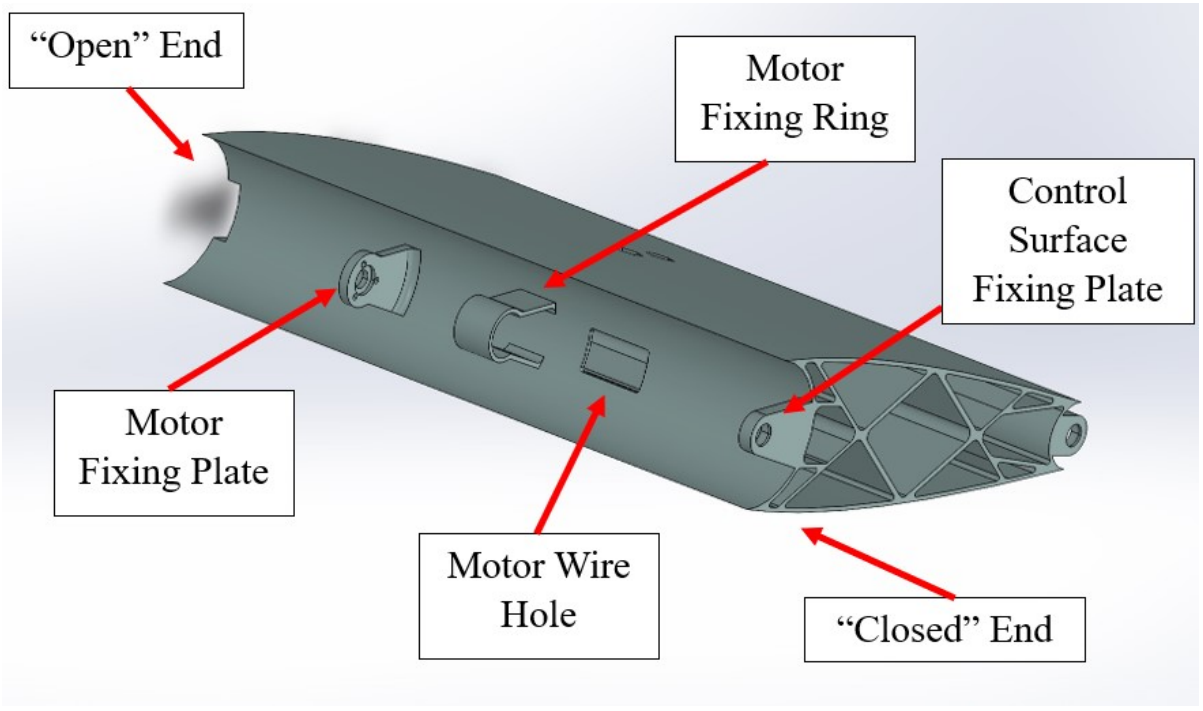

(a)

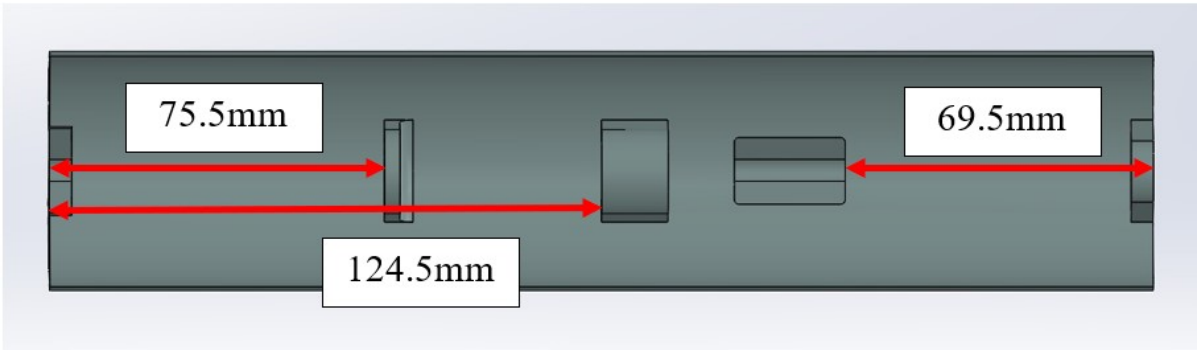

(b)

FIGURE A.6: Leading Edge Motor and Control Surface Fixings (a) Labels and (b) Dimensions

The motor fixing plate has a thickness of 3.5mm with three 2.4mm diameter holes separated equally in a circlular layout that is 6.5mm radius from centre to centre, which are used to screw in the Maxon motor. There is also a central hole for the motor shaft that is 6.5mm in diameter. The motor fixing ring is 1.5mm thick and 15mm wide, with an inner diameter of 16mm. The motor is held in this ring, however the single ring allows for too much movement and the design is updated for MODFLEX 2.0 (see Appendix C for details). The motor wire hole is 25mm by 15mm, however in practice this was made wide to avoid damage to the motor wire connections. Again, this feature is updated on MODFLEX 2.0. These dimensions are all repeated for the trailing edge surface.

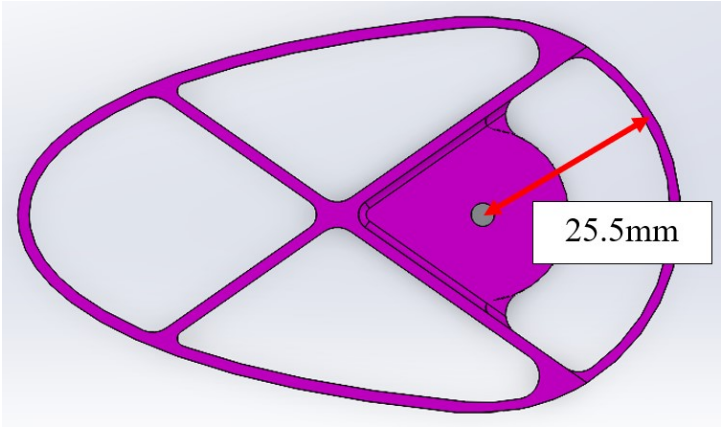

(a)

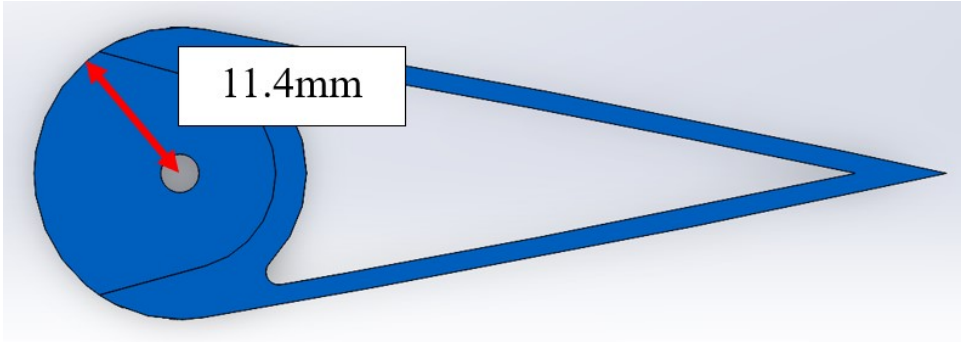

(b)

FIGURE A.7: End View of (a) Leading Edge and (b) Trailing Edge Control Surfaces

Figure A.7 shows the structure of the leading and trailing edge control surfaces. The leading edge has the same lattice structure to ensure rigidity, however the trailing edge does not, making it prone to breaking under handling stress. The lattice structure is added to the MODFLEX 2.0 trailing edge control surface to rectify this. The radii shown in Figure A.7 are smaller than those shown in Figure A.5 so that there is no friction between the parts when the control surfaces are in operation.

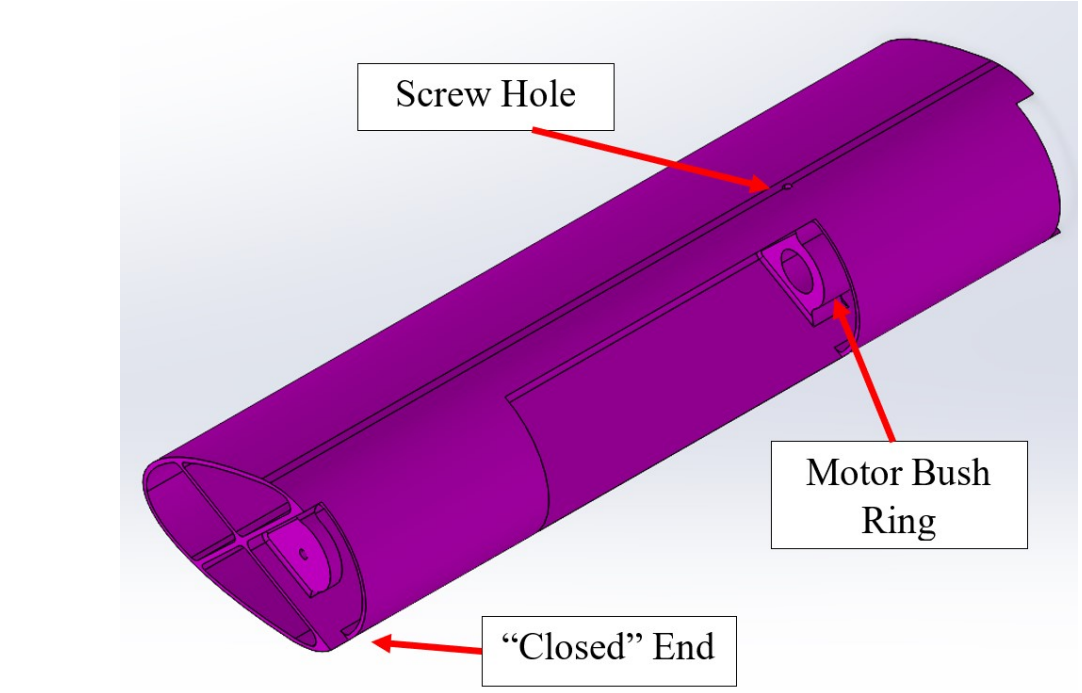

(a)

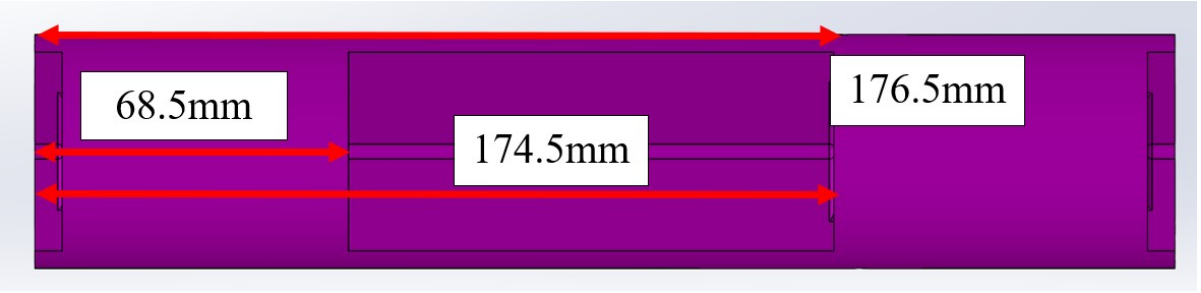

(b)

FIGURE A.8: Leading Edge Control Surface (a) Label and (b) Dimensions

Figure A.8 shows the key features and dimensions for the leading edge control surface. These dimensions are the same for the trailing edge surface. A large rectangular hole of 43.36mm by 106mm is 68.5mm from the "closed" end of the control surface to accommodate the motor and ensure the surface can rotate freely without collision with the motor up to ±20°. The Motor Bush Ring is 174.5mm from the closed end, with a width of 10mm, an inner diameter of 13mm, and a thickness of 4.6mm. A screw hole of 2.5mm diameter is centred at 176.5mm from the closed end. This hole runs through the whole part so that two screws can be used to fix the surface to the motor. As discussed in Chapter 2, the small M1 grub screw is prone to coming loose. This design flaw is updated in the MODFLEX 2.0 wing and will be discussed in Appendix C.

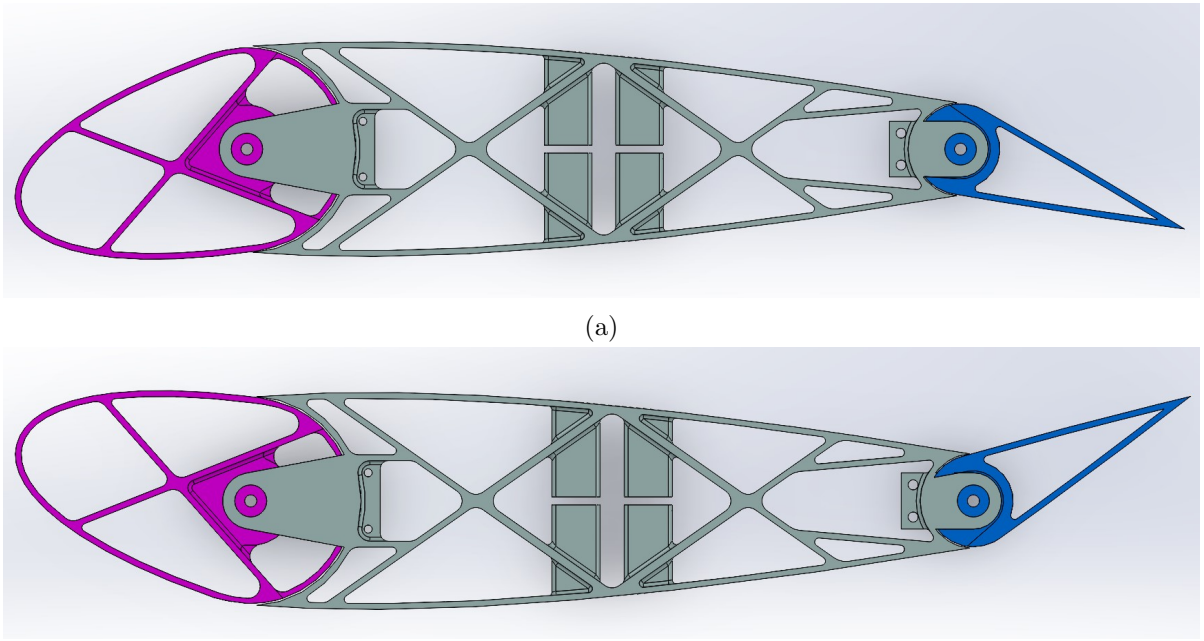

(a)

(b)

FIGURE A.9: Control Surface Maximum Rotation

Figure A.9 shows the maximum deflections possible for each control surface.

A.2.3 Tip Section

A wing tip is added to the wing to cover the opening of the final quarter section so that airflow is not disrupted by a large opening at the tip of the wing.

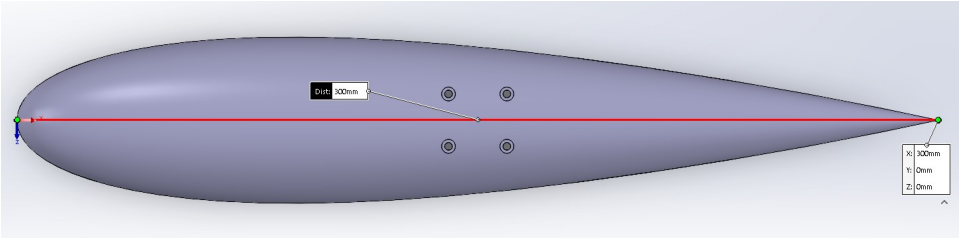

FIGURE A.10: Tip Part for MODFLEX Wing

Figure A.10 shows the tip section, with a chord length of 300mm. Unthreaded holes 2.5mm in diameter are used for M2.5 bolts to fix the tip section to the aluminium spar. The two pairs bolt holes are placed 140.5mm and 159.5mm from the leading edge respectively, and 8.5mm from the centre line.

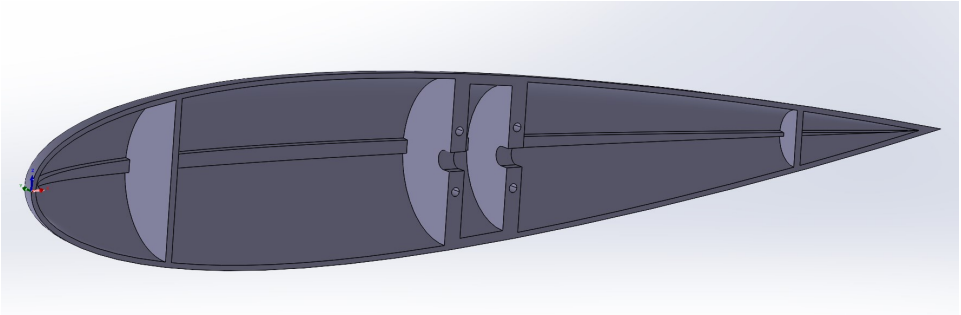

FIGURE A.11: Inside of Tip Part for MODFLEX Wing

Figure A.11 shows the inside of the tip part. It is mostly hollow to reduce the necessary mass and material required. There are two thin strips of support material starting at 46mm and 252mm from the leading edge, which are 2mm in thickness. This helps to ensure the rigidity of the part. The outer shell of the part is also 2mm thick. The two inner supports are 5mm thick to support the bolts. There are notches in each support that are 5.4mm wide to fit the end of the aluminium spar.

The tip section is fixed to the aluminium spar using four L-shaped 3D printed brackets, as shown in Figure A.12 below:

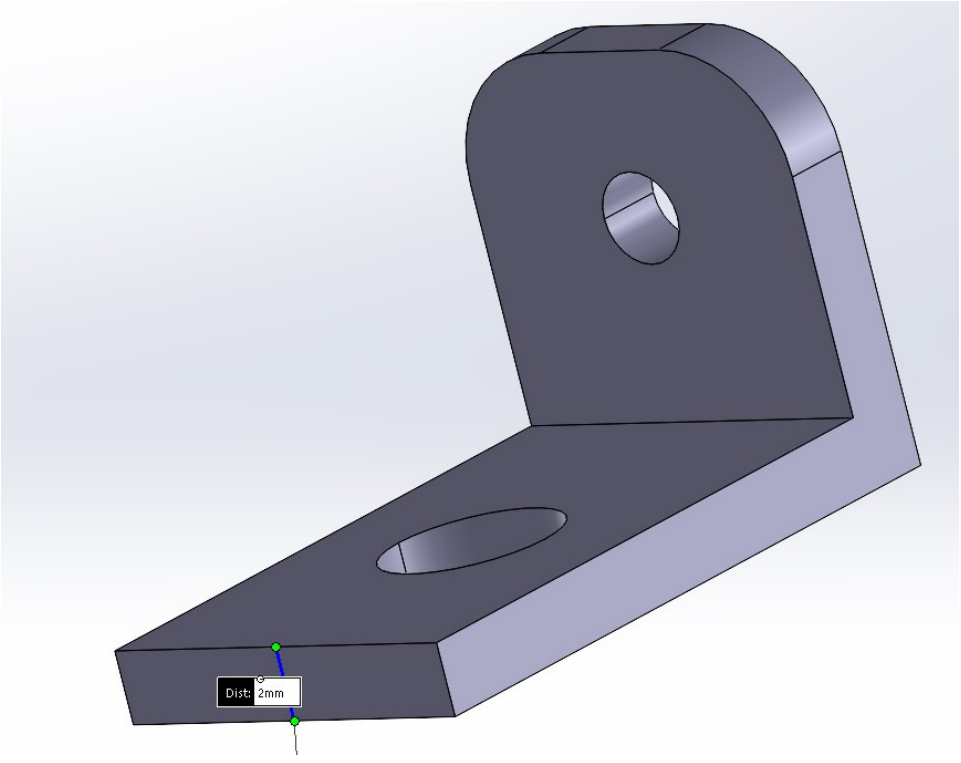

FIGURE A.12: Inside of Tip Part for MODFLEX Wing

The brackets have a thickness of 2mm. There are two holes to accommodate the bolts needed to fix the brackets to the spar, and the tip section to the brackets.

(a) (b)

FIGURE A.13: L-Bracket view from (a) Top and (b) Front

Figure A.13 shows the top and front views of the L-bracket. Figure A.13a shows a 5mm diameter hole used for attaching the L-bracket to the spar. The vertical height shown is 19mm, with a width of 11mm. Figure A.13b shows a 2.5mm diameter hole used for attaching the wing tip part to the L-bracket. The height is 12mm, with two rounded corners of 3.5mm radius.

Appendix B

SIMULINK SATURATION BLOCK

As stated in Chapter 2, a saturation block is used in the Simulink models involved in experiments. This is to prevent overloading the motors used to power the control surfaces. The block and parameters can be see in Figure B.1:

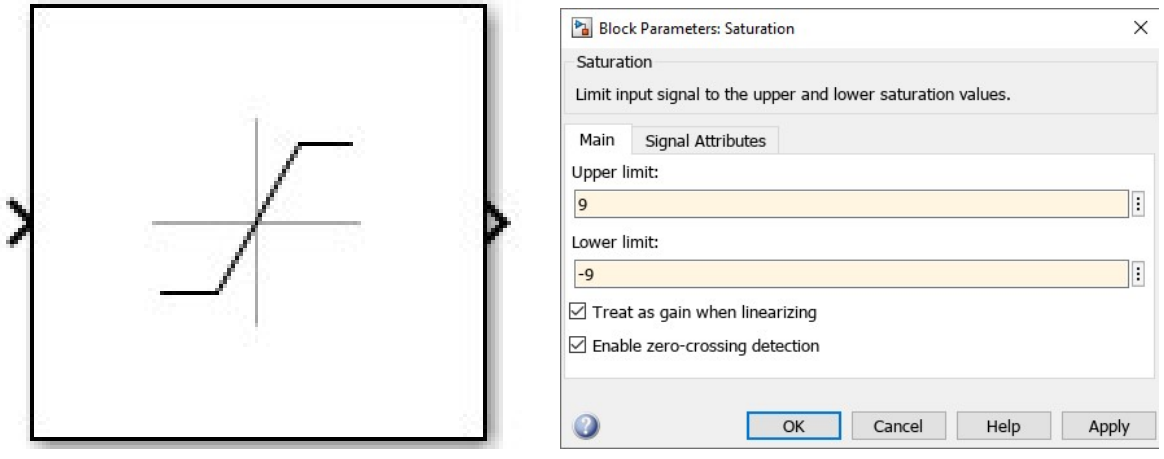

(a) (b)

FIGURE B.1: Saturation (a) Block and (b) Block Parameters

Other than changing the upper and lower limits, all block parameters are left as default.

Appendix C

CAD MODELS AND DRAWINGS FOR MODFLEX 2.0 WING

All CAD models and drawings are available upon request at ellis.james2018@gmail.com

C.1 Milled Parts

Some metal work is required in order to produce the MODFLEX 2.0 wing. First of all, an aluminium spar is required to provide stiffness for the system.

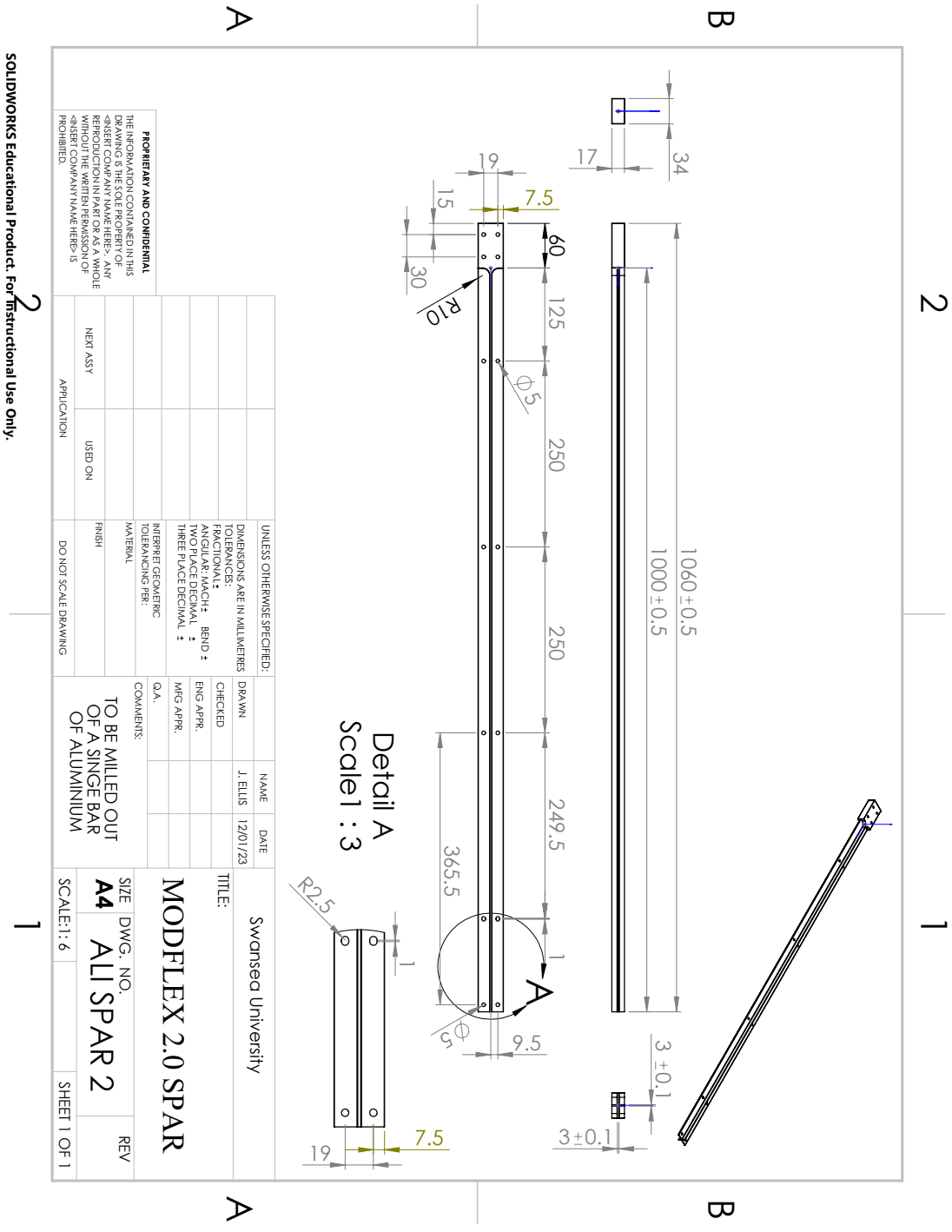

FIGURE C.1: Technical Drawing for MODFLEX 2.0 Aluminium Spar

Figure C.1 shows the technical drawing for the aluminium spar used to provide stiffness to the wing. Only one spar is required for the wing.

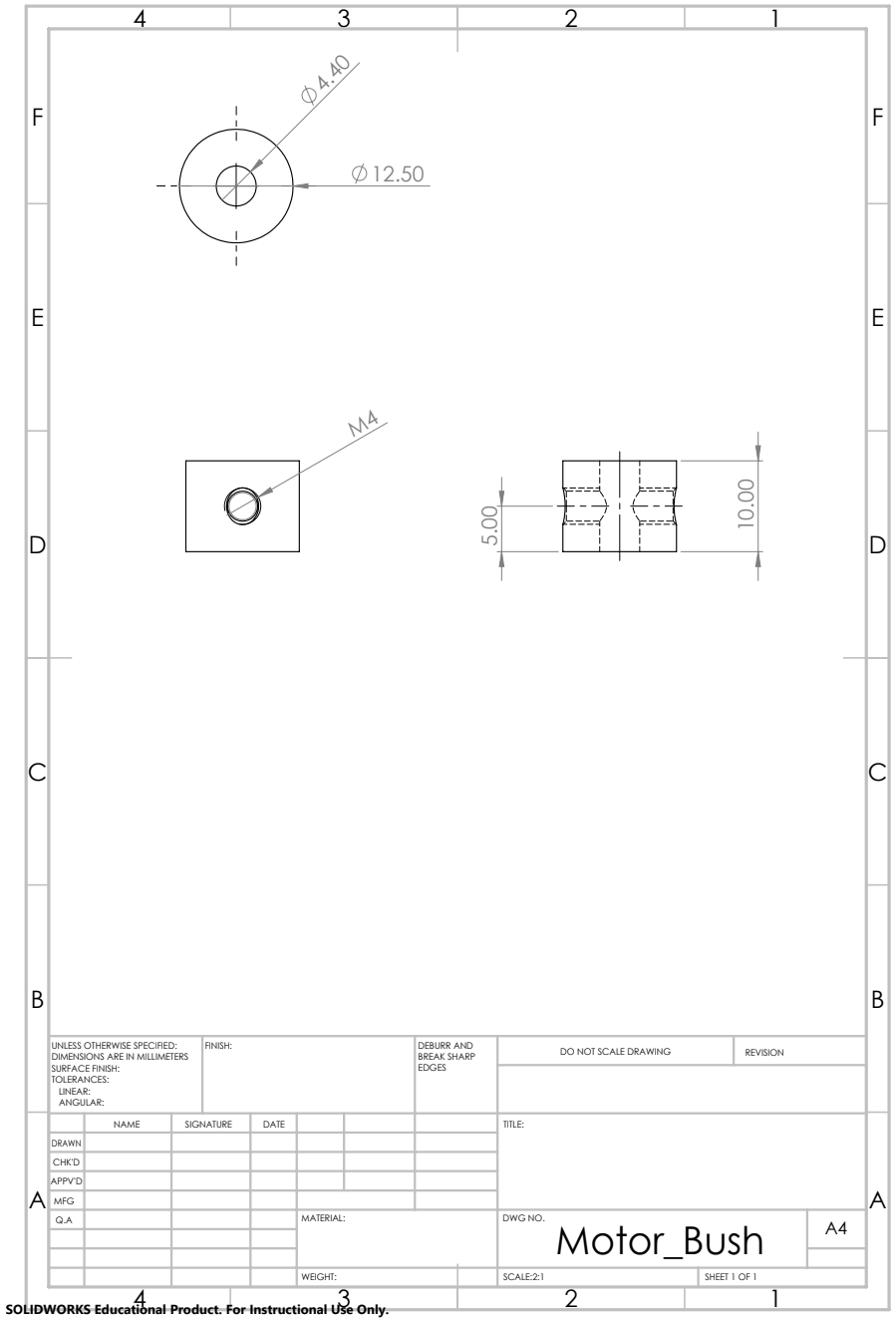

FIGURE C.2: Technical Drawing for MODFLEX 2.0 Metal Bush

Figure C.2 shows the technical drawing for the metal bush used in the connection of the control surfaces to the motors. One bush is required per control surface used, therefore two are used in this work.

C.2 3D Printed Sections

All 3D printed sections are made from ABS-M30 FDM Thermoplastic Filament. Under compression, the material has a yield strength of 30MPa and an elastic modulus of 2.2 GPa, which allows the assumption of rigidity of 3D printed parts during wind tunnel testing.

C.2.1 Passive Section

The first 3D printed part necessary for the MODFLEX wing is the passive quarter section. Three are used in the work presented, however they can be substituted for additional active sections if necessary. The passive section acts as an aerodynamic surface only, and does not provide any structural stiffness.

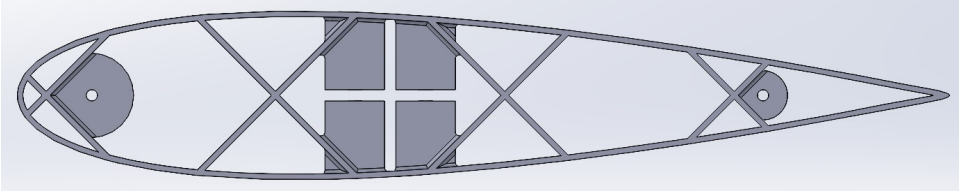

FIGURE C.3: Passive Aerofoil Section for MODFLEX 2.0 Wing

Figure C.3 shows the passive quarter section used on the MODFLEX wing. A lattice structure is used to ensure the rigidity of the section. The lattice structure and outside surface are both 1.5mm thick, which balances the mass and the structural rigidity.

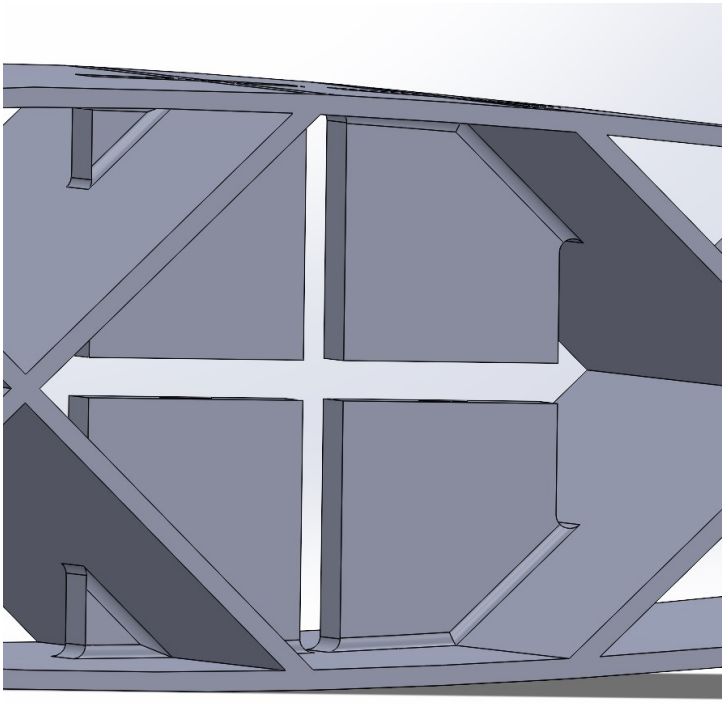

FIGURE C.4: Passive Aerofoil Section Fixing for MODFLEX 2.0 Wing

Figure C.4 shows the structure made to fix the passive section to the spar. Four rectangular columns are used as clamps using M2.5×20 bolts and nuts that run through the entire 3D pinted section, with a + shaped space for the spar. The rectangular columns are 12×14mm as this provides a significant clamping surface without preventing a large section of the wing from bending. Two bolts are used for each quarter section. The flat surfaces of the columns are 3mm apart in the centre to allow space for the spar to have a close fit. The bolt holes are centred in the middle of the section spanwise, and 90.5mm and 109.5mm from the leading edge respectively.

C.2.2 Active Section

In order to provide control, an active section must be used. A leading edge and trailing edge control surface are attached to a central active section, which in turn is fixed to the spar.

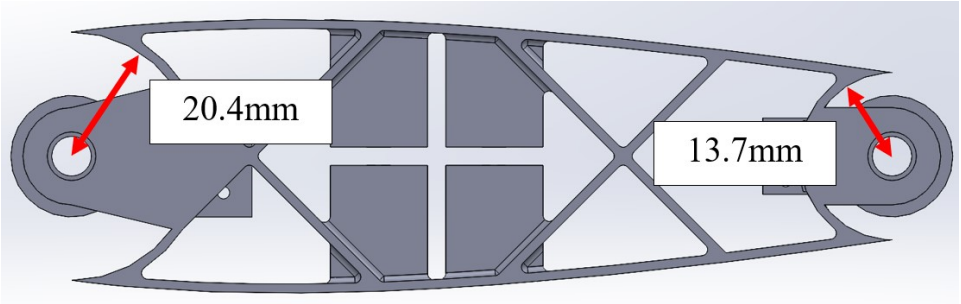

FIGURE C.5: Central Active Aerofoil Part for MODFLEX 2.0 Wing

Figure C.5 shows the main part for the active section, without the control surfaces. It has the same lattice structure and connection to the spar as the passive section. The radii of the cutaway sections are shown so that the control surfaces can move without resistance when in use. It is worth noting that the centres are the hinge axes for the control surfaces, meaning that the centres are 40mm and 175mm from the leading edge of the full aerofoil.

C.2.2.1 Control Surface and Motor Fixings

A number of elements are used to attach the motors and control surfaces to the main active sector part. Figure C.6 shows the additions required and their dimensions.

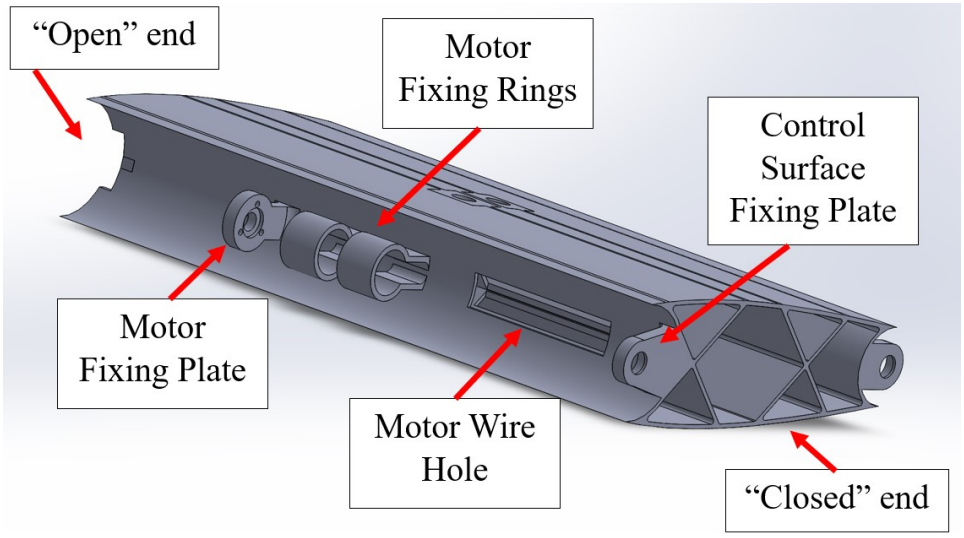

(a)

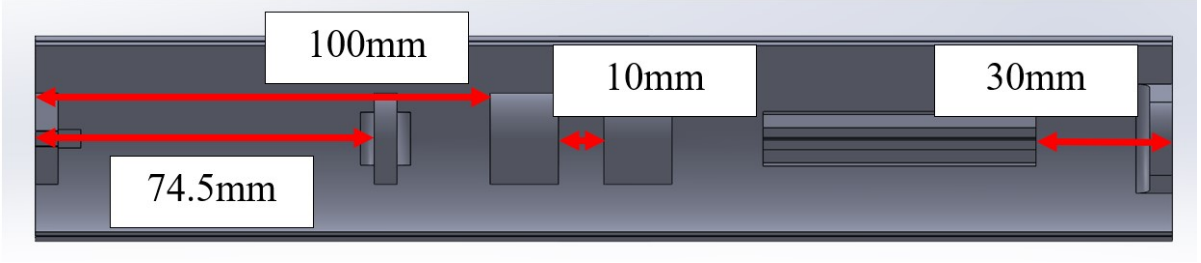

(b)

FIGURE C.6: Leading Edge Motor and Control Surface Fixings (a) Labels and (b) Dimensions

The motor fixing plate has a thickness of 5mm with three 2.4mm diameter holes separated equally in a circlular layout that is 6.5mm radius from centre to centre, which are used to screw in the Maxon motor. The motor fixing plate thickness was increased compared to that on MODFLEX as it was previously prone to snapping off. There is also a central hole for the motor shaft that is 6.5mm in diameter. The motor fixing rings are 2mm thick (again, increased to prevent breaks) and 15mm wide, with an inner diameter of 16mm. The additional motor fixing ring prevents movement of the motor should the motor fixing plate become damaged. This design also prevents movement during testing, which was a recurring problem with the original MODFLEX wing. The motor wire hole is 60mm by 12mm, which is larger that on the original MODFLEX wing to avoid damage to the motor wires. These dimensions are all repeated for the trailing edge surface.

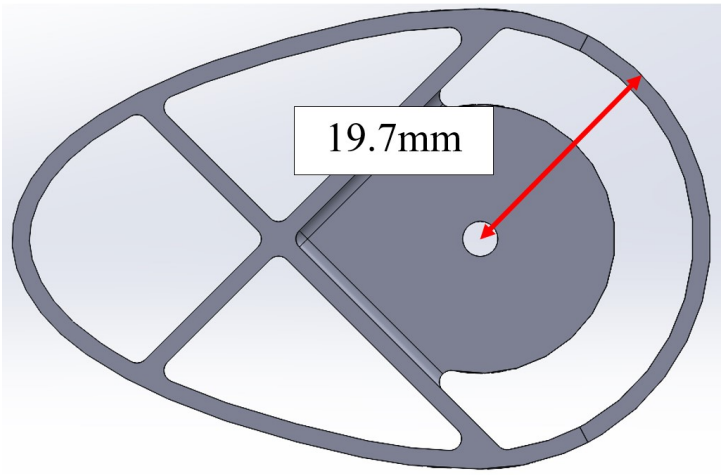

(a)

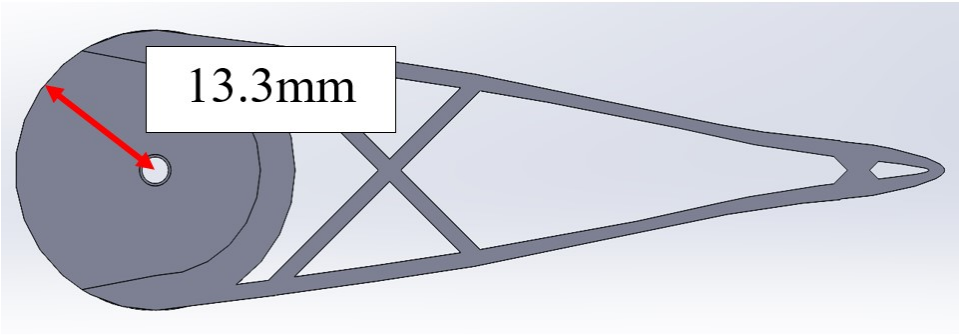

(b)

FIGURE C.7: End View of (a) Leading Edge and (b) Trailing Edge Control Surfaces

Figure C.7 shows the structure of the leading and trailing edge control surfaces. The leading edge has the same lattice structure to ensure rigidity, and after a design update from the original MODFLEX wing the trailing edge now also has a lattice structure to help rigidity and eliminate breaking under handling stress. The radii shown in Figure C.7 are smaller than those shown in Figure C.5 so that there is no friction between the parts when the control surfaces are in operation.

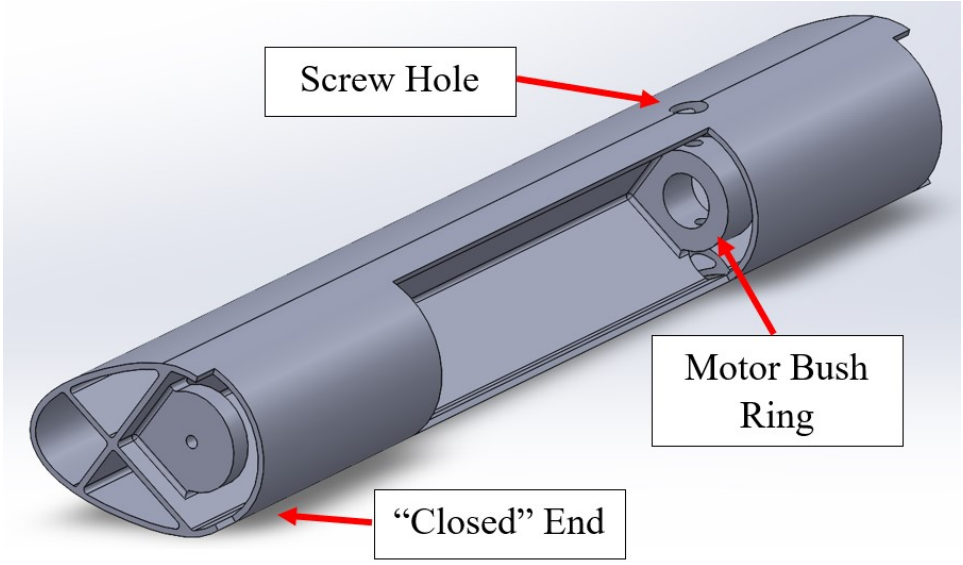

(a)

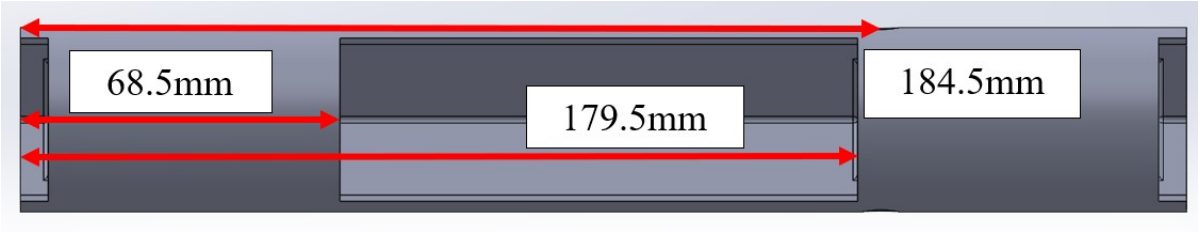

(b)

FIGURE C.8: Leading Edge Control Surface (a) Label and (b) Dimensions

Figure C.8 shows the key features and dimensions for the leading edge control surface. These dimensions are the same for the trailing edge surface. A large rectangular hole of 34.85mm by 111mm is 68.5mm from the "closed" end of the control surface to accommodate the motor and ensure the surface can rotate freely without collision with the motor up to $\pm 20°$. The Motor Bush Ring is 179.5mm from the closed end, with a width of 10mm, an inner diameter of 13mm, and a thickness of 4.6mm. A screw hole of 8.4mm diameter is centred at 184.5mm from the closed end so that M4 phillips head screws can be used to fix the control surface to the motor. A 4mm diameter hole runs through the whole part with the same centre placement that the screws can be used to fix the surface to the motor. This is a key improvement on the MODFLEX 2.0 wing design as no control surface slipping was experienced during testing.

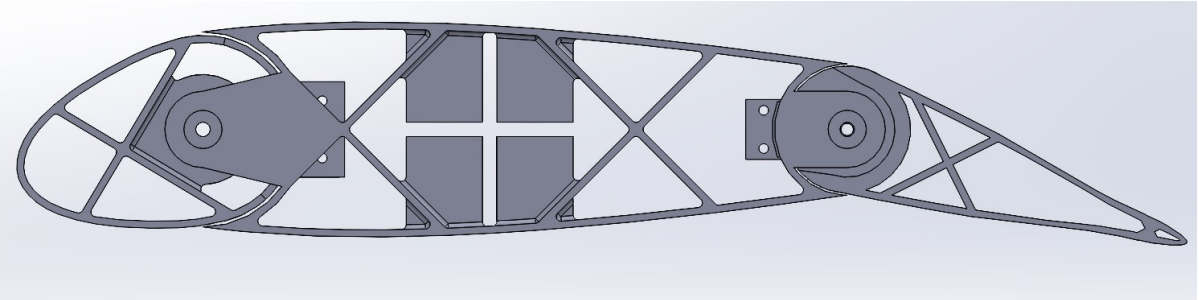

(a)

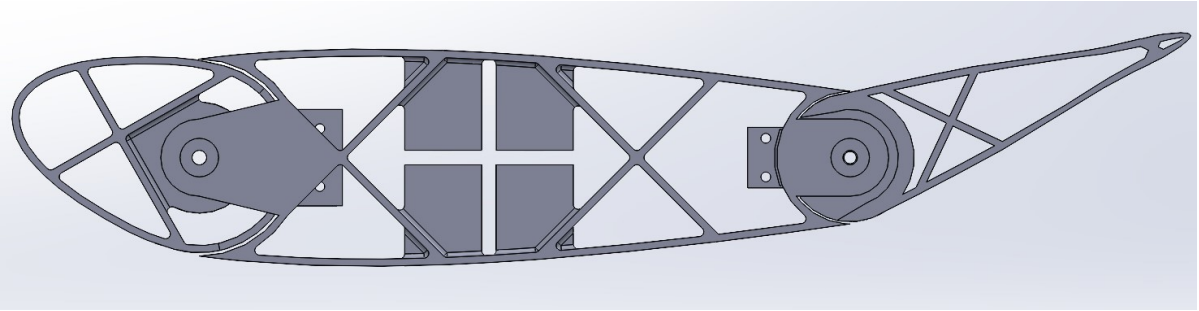

(b)

FIGURE C.9: Control Surface Maximum Rotation

Figure C.9 shows the maximum deflections possible for each control surface.

C.2.3 Tip Section

A wing tip is added to the wing to cover the opening of the final quarter section so that airflow is not disrupted by a large opening at the tip of the wing.

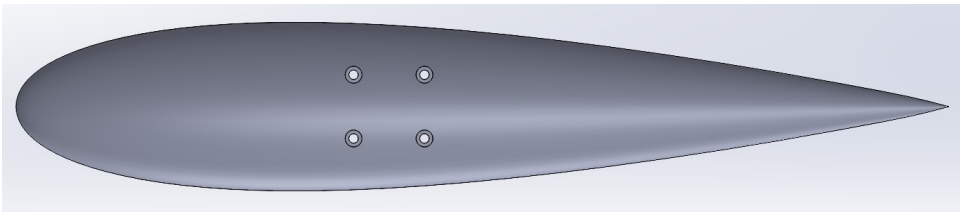

FIGURE C.10: Tip Part for MODFLEX 2.0 Wing

Figure C.10 shows the tip section, with a chord length of 250mm. Unthreaded holes 2.5mm in diameter are used for M2.5 bolts to fix the tip section to the aluminium spar. The two pairs bolt holes are placed 90.5mm and 109.5mm from the leading edge respectively, and 8.5mm from the centre line.

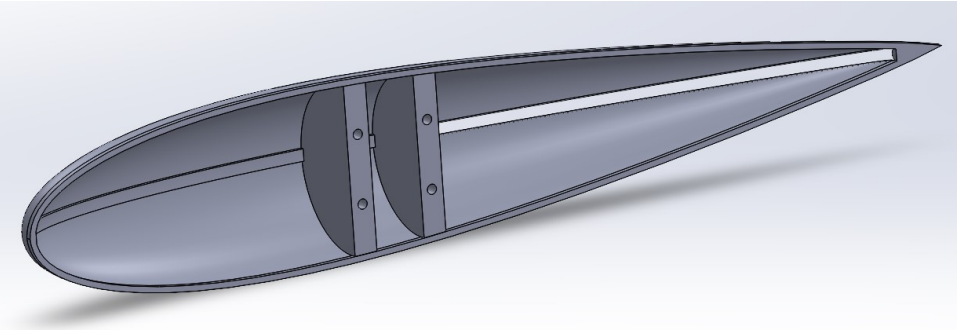

FIGURE C.11: Inside of Tip Part for MODFLEX Wing

Figure C.11 shows the inside of the tip part. It is mostly hollow to reduce the necessary mass and material required. The two strips of supporting material have been removed compared to the MODFLEX wing tip part to save material as the part can withstand stresses from handling and testing, thus they were not required. The outer shell of the part is 1.5mm thick. The two inner supports are 5mm thick to support the bolts.

The tip section is fixed to the aluminium spar using the same four L-shaped 3D printed brackets shown in Figure A.12.

Appendix D

FLEXIBLE WING WITH ROOT-HEAVE DEGREE OF FREEDOM DERIVATION

D.1 Root Heave Degree of Freedom Model

For the implementation of nonlinear control via Feedback Linearisation, a Root Heave Degree of Freedom (RHDoF) system has been derived with the inclusion of a cubic hardening nonlinearity. This Appendix will describe in detail how this system is derived.

D.1.1 Assumed Modes

The method for determining the model equations in the root-heave case is similar to that in the fixed root case, with the initial state vector defined as:

$$\mathbf{w} = \begin{bmatrix} \xi \\ \theta \\ z \end{bmatrix} \tag{D.1}$$

where ξ is the bending displacement, θ is the torsional displacement, and z is the root-heave displacement. Then, we must transfer into assumed mode coordinates:

$$\mathbf{T} = \begin{bmatrix} y_1^2 & 0 & 0 \\ 0 & y_2 & 0 \\ 0 & 0 & 1 \end{bmatrix}$$

$$\mathbf{q} = \mathbf{T}^{-1}\mathbf{w} = \begin{bmatrix} q_1 \\ q_2 \\ q_3 \end{bmatrix} \tag{D.2}$$

The final entry of the transformation matrix $\mathbf{T}$ is 1 as the root-heave has no mode shape and therefore the generalised coordinate of the assumed heave mode q_3 is the same as the real displacement. This means that all assumed mode coordinates are directly representing each degree of freedom.

D.1.2 Inertia Matrix

The derivation for the Inertia Matrix is based on using the Lagrange equation to define the Equation of Motion [7]. First, the displacement τ (downwards positive) of a general point on the wing is:

$$\tau(x, y, t) = \left(\left(\frac{y}{s}\right)^2 \dot{q}_b + \left(\frac{y}{s}\right)(x - x_f)\dot{q}_t + \dot{q}_r \right) \tag{D.3}$$

To find the first row of the Inertia Matrix, we must differentiate *tau* with respect to $\dot{q}_b$, so that:

$$\frac{\partial \tau}{\partial \dot{q}_b} = 2\left(\frac{y}{s}\right)^4 \dot{q}_b + 2\left(\frac{y}{s}\right)^3 (x - x_f)\dot{q}_t + 2\left(\frac{y}{s}\right)^2 \dot{q}_r \tag{D.4}$$

The Lagrange equation is then applied to the kinetic energy T for the generalised bending coordinate:

$$\begin{aligned} \frac{\partial T}{\partial \dot{q}_b} &= \frac{m}{2} \int_0^s \int_0^c \frac{\partial \tau}{\partial \dot{q}_b} dx dy \\ &= m\left[\frac{sc}{5}\dot{q}_b + \frac{s}{4}\left(\frac{c^2}{2} - cx_f\right)\dot{q}_t + \frac{sc}{3}\dot{q}_r \right] \end{aligned} \tag{D.5}$$

Then, differentiating over time:

$$\frac{d}{dt}\left(\frac{\partial T}{\partial \dot{q}_b}\right) = m\left[\frac{sc}{5}\ddot{q}_b + \frac{s}{4}\left(\frac{c^2}{2} - cx_f\right)\ddot{q}_t + \frac{sc}{3}\ddot{q}_r\right] \tag{D.6}$$

The coefficients of each $\ddot{q}$ term are then entries into the first row of the A matrix. The second row can then be found as follows:

$$\frac{\partial \tau}{\partial \dot{q}_t} = 2\left(\frac{y}{s}\right)^3 (x - x_f)\dot{q}_b + 2\left(\frac{y}{s}\right)(x - x_f)^2\dot{q}_t + 2\left(\frac{y}{s}\right)(x - x_f)\dot{q}_r \tag{D.7}$$

The Lagrange equation is then applied to the kinetic energy T for the generalised torsional coordinate:

$$\begin{aligned}\frac{\partial T}{\partial \dot{q}_t} &= \frac{m}{2}\int_0^s \int_0^c \frac{\partial \tau}{\partial \dot{q}_t} dx dy \\ &= m\left[\frac{s}{4}\left(\frac{c^2}{2} - cx_f\right)\dot{q}_b + \frac{s}{2}\left(\frac{c^3}{3} - c^2x_f + cx_f^2\right)\dot{q}_t + \frac{s}{2}\left(\frac{c^2}{2} - cx_f\right)\dot{q}_r\right]\end{aligned} \tag{D.8}$$

Then, differentiating over time:

$$\frac{d}{dt}\left(\frac{\partial T}{\partial \dot{q}_t}\right) = m\left[\frac{s}{4}\left(\frac{c^2}{2} - cx_f\right)\ddot{q}_b + \frac{s}{2}\left(\frac{c^3}{3} - c^2x_f + cx_f^2\right)\ddot{q}_t + \frac{s}{2}\left(\frac{c^2}{2} - cx_f\right)\ddot{q}_r\right] \tag{D.9}$$

The coefficients of each $\ddot{q}$ term are then entries into the second row of the $\mathbf{A}$ matrix. The third row can then be found as follows:

$$\frac{\partial \tau}{\partial \dot{q}_r} = 2\left(\frac{y}{s}\right)^2 \dot{q}_b + 2\left(\frac{y}{s}\right)(x - x_f)\dot{q}_t + \dot{q}_r \tag{D.10}$$

The Lagrange equation is then applied to the kinetic energy T for the generalised root-heave coordinate:

$$\begin{aligned}\frac{\partial T}{\partial \dot{q}_r} &= \frac{m}{2}\int_0^s \int_0^c \frac{\partial \tau}{\partial \dot{q}_r} dx dy \\ &= m\left[\frac{sc}{5}\dot{q}_b + \frac{s}{2}\left(\frac{c^2}{2} - cx_f\right)\dot{q}_t + sc\dot{q}_r\right]\end{aligned} \tag{D.11}$$

Then, differentiating over time:

$$\frac{d}{dt}\left(\frac{\partial T}{\partial \dot{q}_r}\right) = m\left[\frac{sc}{5}\ddot{q}_b + \frac{s}{2}\left(\frac{c^2}{2} - cx_f\right)\ddot{q}_t + sc\ddot{q}_r\right] \tag{D.12}$$

This gives a final inertia matrix of:

$$\mathbf{A} = \begin{bmatrix} \frac{sc}{5} & \frac{s}{4}\left(\frac{c^2}{2} - cx_f\right) & \frac{sc}{3} \\ \frac{s}{4}\left(\frac{c^2}{2} - cx_f\right) & \frac{s}{3}\left(\frac{c^3}{3} - c^2x_f + cx_f^2\right) & \frac{s}{2}\left(\frac{c^2}{2} - cx_f\right) \\ \frac{sc}{3} & \frac{s}{2}\left(\frac{c^2}{2} - cx_f\right) & sc \end{bmatrix} \tag{D.13}$$

D.1.3 Structural Stiffness Matrix

The structural stiffness matrix is based on the elastic potential energy of the system, which is as follows:

$$U = \frac{1}{2}\int_0^s EI\left(\frac{2q_b}{s^2}\right)^2 dy + \frac{1}{2}\int_0^s GJ\left(\frac{q_t}{s}\right)^2 dy + \frac{1}{2}k_{r_0}q_r^2 \tag{D.14}$$

Then each row is found as follows:

$$\frac{\partial U}{\partial q_b} = \int_0^s EI\left(\frac{4q_b}{s^4}\right) dy = \frac{4EI}{s^3}q_b \tag{D.15}$$

$$\frac{\partial U}{\partial q_t} = \int_0^s GJ\left(\frac{q_t}{s^2}\right) dy = \frac{GJ}{s}q_t \tag{D.16}$$

$$\frac{\partial U}{\partial q_r} = k_{r_0}q_r \tag{D.17}$$

The final structural stiffness matrix is then given as:

$$\mathbf{E} = \begin{bmatrix} \frac{4EI}{s^3} & 0 & 0 \\ 0 & \frac{GJ}{s} & 0 \\ 0 & 0 & k_{r_0} \end{bmatrix} \tag{D.18}$$

D.1.4 Aerodynamic Stiffness and Damping Matrices

The aerodynamic stiffness and damping matrices are found via the incremental work done over the wing, corresponding to the aerodynamic force and moment doing work

through the incremental deflections δq_b, δq_t and δq_r.

$$\delta W = \int_{Wing} \left[dL \left(-\left(\frac{y}{s}\right)^2 \delta q_b - \delta q_r \right) + dM \left(\frac{y}{s} \delta q_t \right) \right] \tag{D.19}$$

where dL and dM are the expressions for lift and nose up pitch moment about the elastic axis for each elemental strip dy, and are defined as follows:

$$\begin{aligned} dL &= \frac{1}{2}\rho V^2 c dy a_w \left(\frac{y^2 \dot{q}_b}{s^2 V} + \frac{y q_t}{s} + \frac{\dot{q}_r}{V} \right) \\ dM &= \frac{1}{2}\rho V^2 c^2 dy \left[e a_w \left(\frac{y^2 \dot{q}_b}{s^2 V} + \frac{y q_t}{s} + \frac{\dot{q}_r}{V} \right) + M_{\dot{\theta}} c \frac{y \dot{q}_t}{4 s V} \right] \end{aligned} \tag{D.20}$$

The generalised forces are then:

$$\begin{aligned} Q_{q_b} &= \frac{\partial(\delta W)}{\partial(\delta q_b)} = -\int_0^s \left(\frac{y}{s}\right)^2 dL \\ &= -\frac{1}{2}\rho V^2 c a_w \left[\frac{s}{5V}\dot{q}_b + \frac{s}{4} q_t + \frac{s}{3V}\dot{q}_r \right] \end{aligned} \tag{D.21}$$

$$\begin{aligned} Q_{q_t} &= \frac{\partial(\delta W)}{\partial(\delta q_t)} = \int_0^s \left(\frac{y}{s}\right) dM \\ = -\frac{1}{2}\rho V^2 c^2 &\left[e a_w \left(\frac{s}{4V}\dot{q}_b + \frac{s}{3} q_t + \frac{s}{2V}\dot{q}_r \right) + M_{\dot{\theta}} \left(\frac{s}{12V}\dot{q}_t \right) \right] \end{aligned} \tag{D.22}$$

$$\begin{aligned} Q_{q_r} &= \frac{\partial(\delta W)}{\partial(\delta q_r)} = -\int_0^s dL \\ &= -\frac{1}{2}\rho V^2 c a_w \left[\frac{s}{3V}\dot{q}_b + \frac{s}{3} q_t + \frac{s}{V}\dot{q}_r \right] \end{aligned} \tag{D.23}$$

The aerodynamic damping matrix is therefore given as:

$$\mathbf{B} = \begin{bmatrix} \frac{s}{10} c a_w & 0 & \frac{s}{6} c a_w \\ \frac{-c^2 s}{8} e a_w & \frac{c^3 s}{24} M_{\dot{\theta}} & \frac{-c^2 s}{4} e a_w \\ \frac{s}{6} c a_w & 0 & \frac{s}{2} c a_w \end{bmatrix} \tag{D.24}$$

and the aerodynamic stiffness matrix is given as:

$$\mathbf{C} = \begin{bmatrix} 0 & \frac{s}{8}ca_w & 0 \\ 0 & \frac{-c^2 s}{6}ea_w & 0 \\ 0 & \frac{s}{4}ca_w & 0 \end{bmatrix} \tag{D.25}$$

D.1.5 Introducing Control Surfaces

Two control surfaces are implemented into the wing; one at the leading edge (β) and one at the trailing edge (γ). Both control surfaces have a span that is one-quarter the total span and are positioned at the wing tip. The derivation shown below is for the trailing edge surface, but is also applicable to the leading edge, simply substituting β values for γ values.

The expressions dM and dL now include contributions from the control surface, as follows:

$$dL = \frac{1}{2}\rho V^2 c dy \left[a_w \left(\frac{y^2 \dot{q}_b}{s^2 V} + \frac{y q_t}{s} + \frac{\dot{q}_r}{V} \right) + C_{l_\beta}\beta \right] \tag{D.26}$$

$$dM = \frac{1}{2}\rho V^2 c^2 dy \left[e a_w \left(\frac{y^2 \dot{q}_b}{s^2 V} + \frac{y q_t}{s} + \frac{\dot{q}_r}{V} \right) + M_{\dot{\theta}} c \frac{y \dot{q}_t}{4sV} + \frac{1}{2} C_{m_{\beta-eff}}\beta \right] \tag{D.27}$$

where $C_{m_{\beta-eff}}$ is defined as:

$$C_{m_{\beta-eff}} = \left(\frac{1}{2} + a \right) C_{l_\beta} + 2C_{m_\beta} \tag{D.28}$$

Following the same derivation for the generalised forces on the wing, but only integrating the control surface over $\frac{3}{4}s$ to s, gives us:

$$Q_{q_b} = -\frac{1}{2}\rho V^2 c \left[a_w \left[\frac{s}{5V}\dot{q}_b + \frac{s}{4}q_t + \frac{s}{3V}\dot{q}_r \right] + \frac{37 s C_{l_\beta}}{192}\beta \right] \tag{D.29}$$

$$Q_{q_t} = -\frac{1}{2}\rho V^2 c^2 \left[e a_w \left(\frac{s}{4V}\dot{q}_b + \frac{s}{3}q_t + \frac{s}{2V}\dot{q}_r \right) + M_{\dot{\theta}} \left(\frac{s}{12V}\dot{q}_t \right) + \frac{7s}{64} C_{m_{\beta-eff}}\beta \right] \tag{D.30}$$

$$Q_{q_r} = -\frac{1}{2}\rho V^2 c \left[a_w \left[\frac{s}{3V}\dot{q}_b + \frac{s}{3}q_t + \frac{s}{V}\dot{q}_r \right] + \frac{C_{l_\beta} s}{4}\beta \right] \tag{D.31}$$

The gain vector is then made up of the coefficients of β:

$$\mathbf{g}_1 = \rho V^2 \begin{bmatrix} -\dfrac{37 C_{l_\beta} cs}{384} \\ \dfrac{7 s c^2 C_{m_{\beta-eff}}}{128} \\ -\dfrac{C_{l_\beta} cs}{8} \end{bmatrix} \tag{D.32}$$

Following the same steps, the gain matrix for leading edge control surface deflection γ is:

$$\mathbf{g}_2 = \rho V^2 \begin{bmatrix} -\dfrac{37 C_{l_\gamma} cs}{384} \\ \dfrac{7 s c^2 C_{m_{\gamma-eff}}}{128} \\ -\dfrac{C_{l_\gamma} cs}{8} \end{bmatrix} \tag{D.33}$$

D.1.6 Including Gust Terms

The incremental lift and moment due to gusts, dL_{gust} and dM_{gust} respectively, are as follows:

$$\begin{aligned} dL_{gust} &= \frac{1}{2}\rho V^2 c dy a_W \frac{w_g}{V} \\ dM_{gust} &= \frac{1}{2}\rho V^2 c^2 dy e a_W \frac{w_g}{V} \end{aligned} \tag{D.34}$$

where w_g is the uniform vertical gust velocity. The generalised forces are then:

$$\begin{aligned} Q_{q_{b_{gust}}} &= -\int_0^s \left(\frac{y}{s}\right)^2 dL_{gust} \\ &= -\frac{1}{6}\rho V a_W s w_g \end{aligned} \tag{D.35}$$

$$\begin{aligned} Q_{q_{t_{gust}}} &= \int_0^s \left(\frac{y}{s}\right) dM_{gust} \\ &= -\frac{1}{4}\rho V c^2 e a_W s w_g \end{aligned} \tag{D.36}$$

$$\begin{aligned} Q_{q_{r_{gust}}} &= -\int_0^s dL_{gust} \\ &= -\frac{1}{2}\rho V c a_W s w_g \end{aligned} \tag{D.37}$$

Then we can obtain the gust distribution matrix using the coefficients of w_g.

$$\mathbf{h} = \rho V \begin{bmatrix} -\frac{ca_w s}{6} \\ \frac{c^2 e a_w s}{4} \\ -\frac{ca_w s}{2} \end{bmatrix} = \rho V \begin{bmatrix} h_1 \\ h_2 \\ h_3 \end{bmatrix} \tag{D.38}$$

Appendix E

CAD MODELS AND DRAWINGS FOR FOLDING WING TIP WING

All CAD models and drawings are available upon request at ellis.james2018@gmail.com

E.1 Milled Parts

Some metal work is required in order to produce the wing. First of all, an aluminium spar is required to provide stiffness for the system.

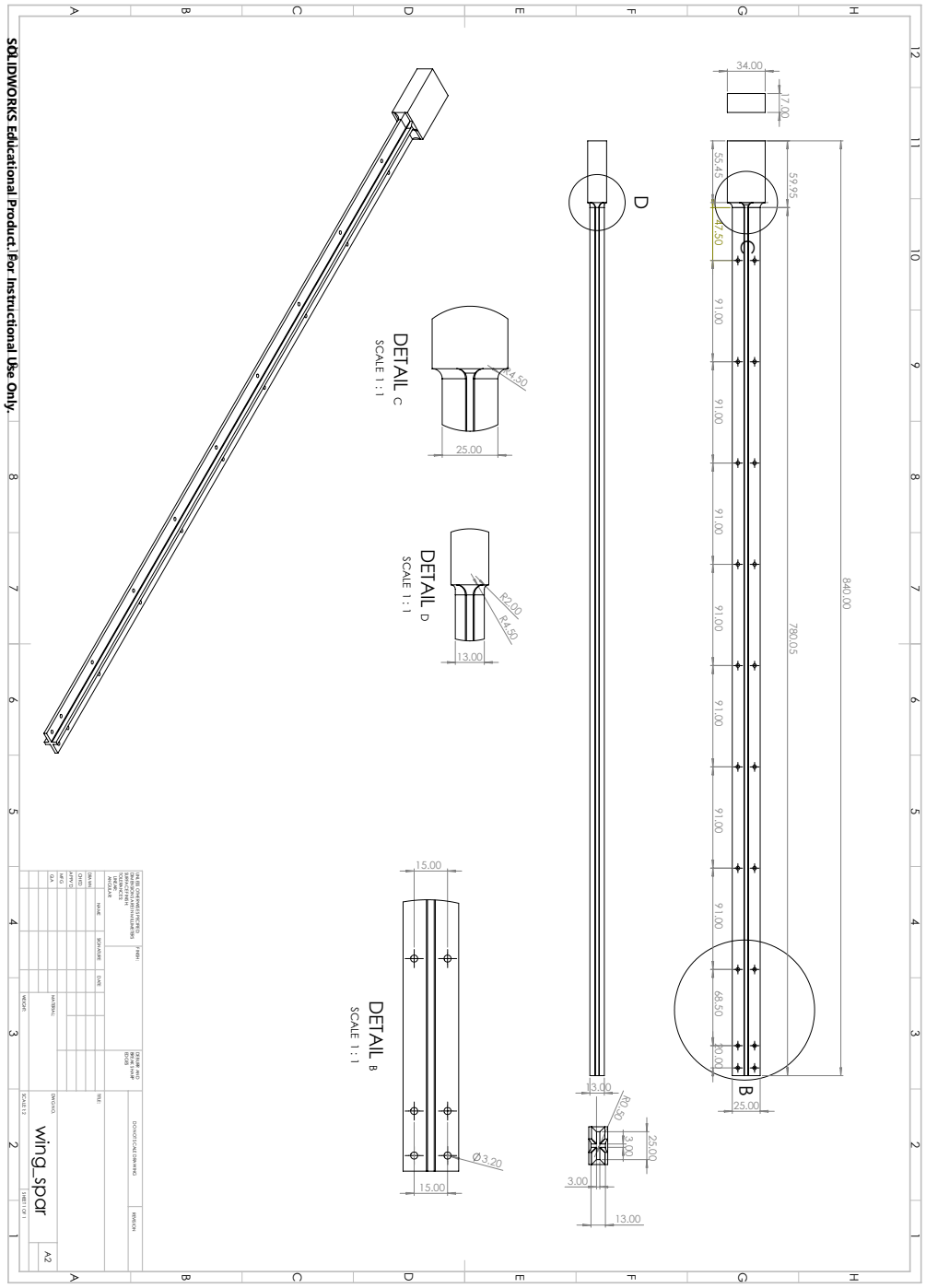

FIGURE E.1: Technical Drawing for Folding Wing Tip Wing Aluminium Spar

Figure E.1 shows the technical drawing for the aluminium spar used to provide stiffness to the wing. Only one spar is required for the wing.

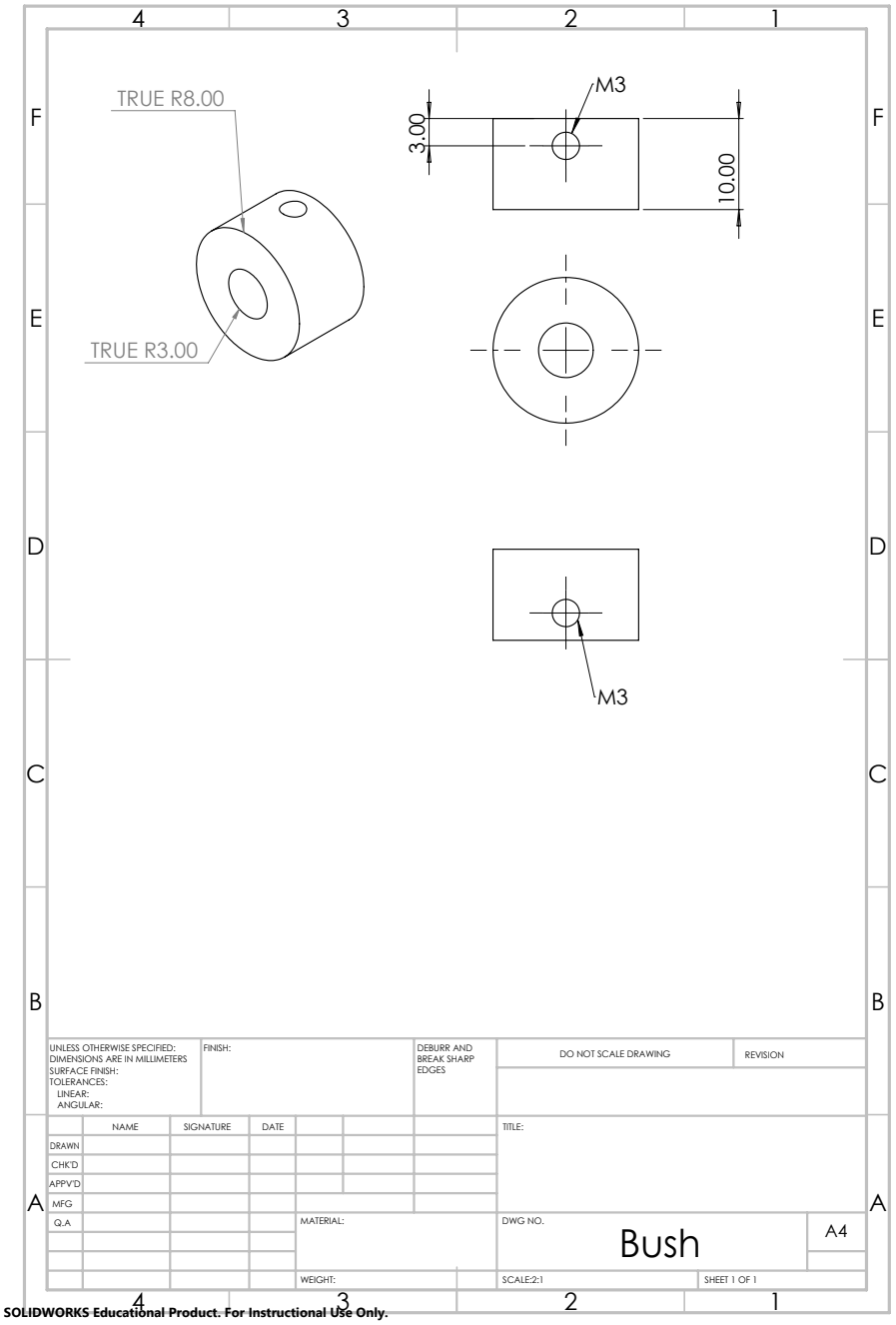

FIGURE E.2: Technical Drawing for Metal Bush Used on the Active Folding Wing Tip Model

Figure E.2 shows the technical drawing for the metal bush used in the connection of the active wing tip to the motor.

E.2 3D Printed Parts

All 3D printed sections are made from ABS-M30 FDM Thermoplastic Filament. Under compression, the material has a yield strength of 30MPa and an elastic modulus of 2.2 GPa, which allows the assumption of rigidity of 3D printed parts during wind tunnel testing.

E.2.1 Aerofoil Part

Firstly, a passive aerofoil section is used simply as an aerodynamic surface, and provides no stiffness to the system. Eight of these sections are required in total.

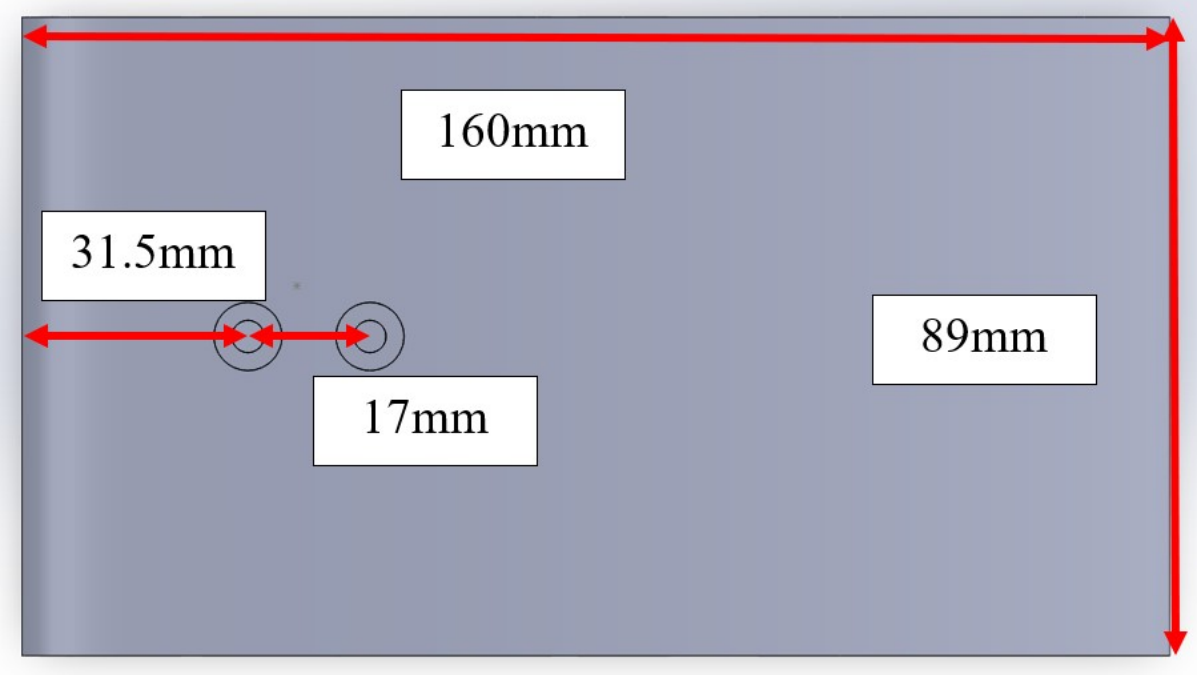

(a)

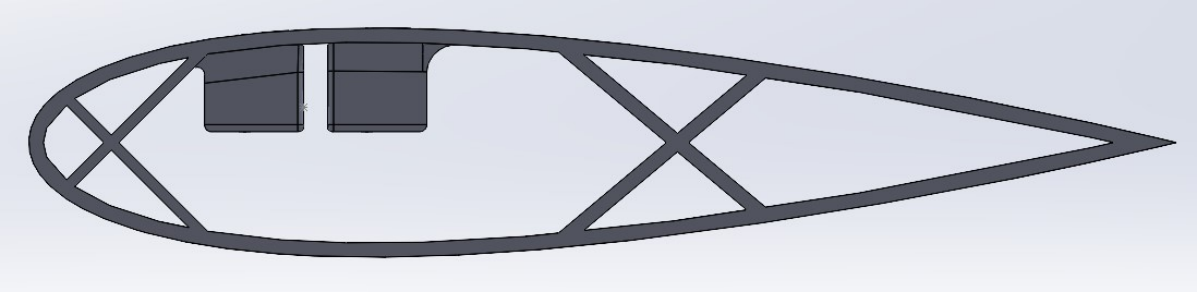

(b)

FIGURE E.3: Passive Aerofoil Section Viewed from (a) Top and (b) Side

Figure E.3 shows the passive aerofoil section,as well as key dimensions. The wing has a chord length of 160mm and each section has a span-wise width of 89mm. As in the MODFLEX wings, a lattice structure is used to ensure rigidity of the part, and the material has a thickness of 2mm. Two 4.5mm holes are used in the top of the part so that it can be attached to the spar using screws. As in the MODFLEX wings, there are two columns used to attach the section to the spar. These extend from the top of the part to 1.5mm above the centre line of the aerofoil, with a gap of 3.4mm to make room for the spar thickness. These columns have a 14mm square base.

E.2.2 Passive Wing Tip Parts

As discussed in Chapter 6, two wing tips are used in testing. The first of which is the passive folding wing tip. The hinge is made of two sections, a 'wing-side' and a 'tip-side'.

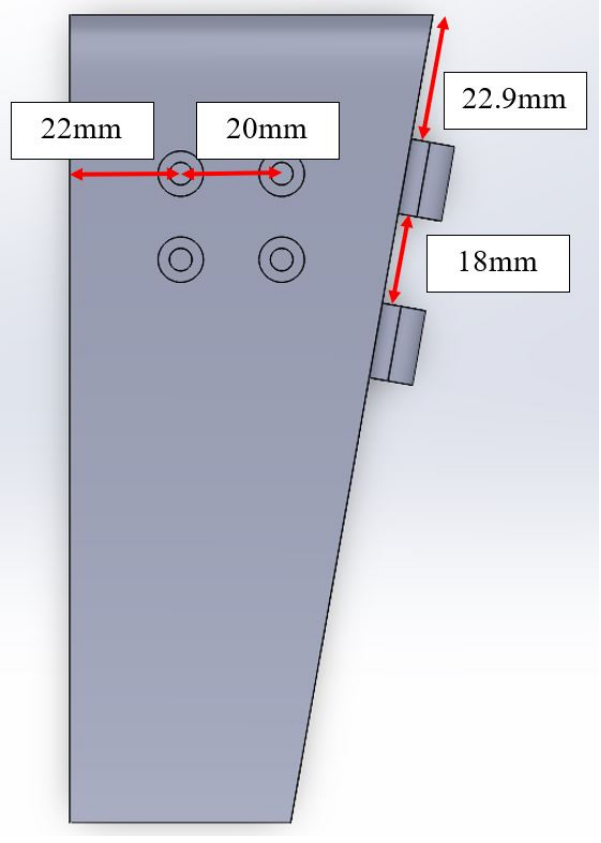

FIGURE E.4: 'Wing-Side' Part of the Passive Hinge

Figure E.4 shows the 'wing-side' part of the hinge mechanism. All material has a thickness of 2mm, other than the two rings which are 3mm thick and house bearings for the free hinge movement. The rings have an inner diameter of 7mm, and a width of 15mm. Four 4.5mm screw holes are used to fix the part to the spar, with the same placement

from the leading edge as in the passive aerofoil section shown in Figure E.3. The same lattice structure and support columns are used as in the passive aerofoil section. The leading edge has a spanwise width of 72mm, and the trailing edge is 45mm, due to the hinge flare angle.

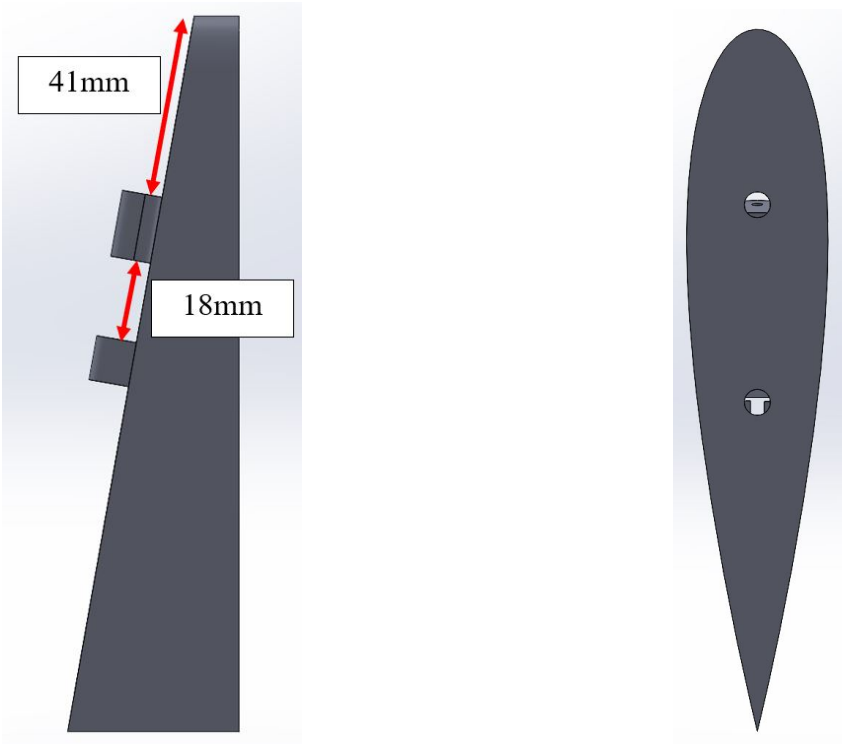

(a) (b)

FIGURE E.5: 'Tip-Side' Part of the Passive Hinge Viewed from (a) Top and (b) Side

Figure E.5 shows the 'Tip-side' part of the hinge mechanism. All material has a thickness of 2mm, other than the two rings which are 3mm thick and house bearings for the free hinge movement. The rings have an inner diameter of 7mm, and a width of 15mm and 10mm. The same lattice structure and support columns are used as in the passive aerofoil section. The leading edge has a spanwise width of 10mm, and the trailing edge is 37mm, due to the hinge flare angle. Two holes with 6mm diameter are placed in the flat side, with the same placement as the holes shown in E.7 so that two carbon rods can attach the different wing tip parts together.

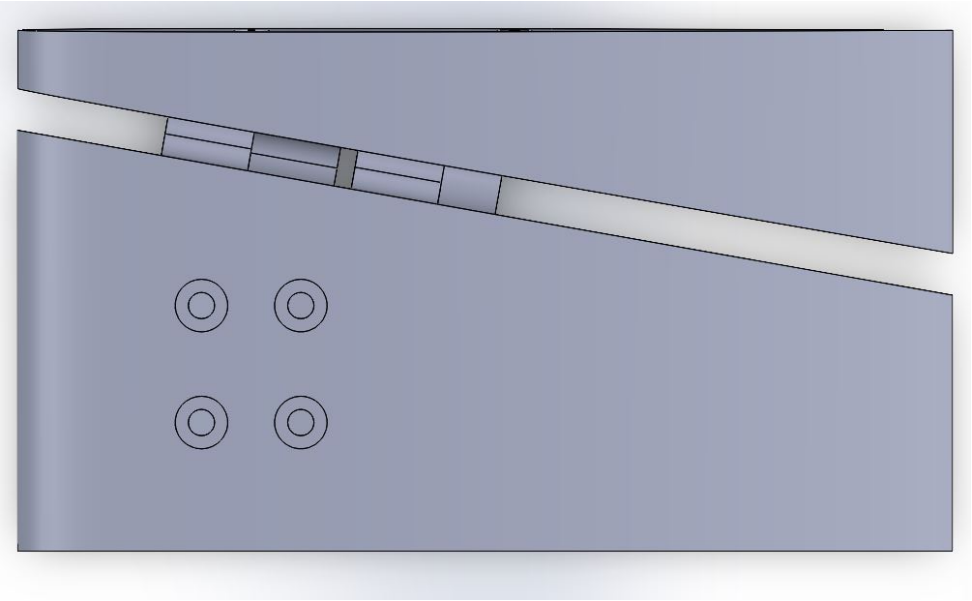

FIGURE E.6: Assembly of Passive Wing Tip Hinge Mechanism

Figure E.6 shows the assembled passive hinged wing tip section. It is capable of wing tip rotations of $\pm 25^{\circ}$ before making contact with itself and preventing further deflection.

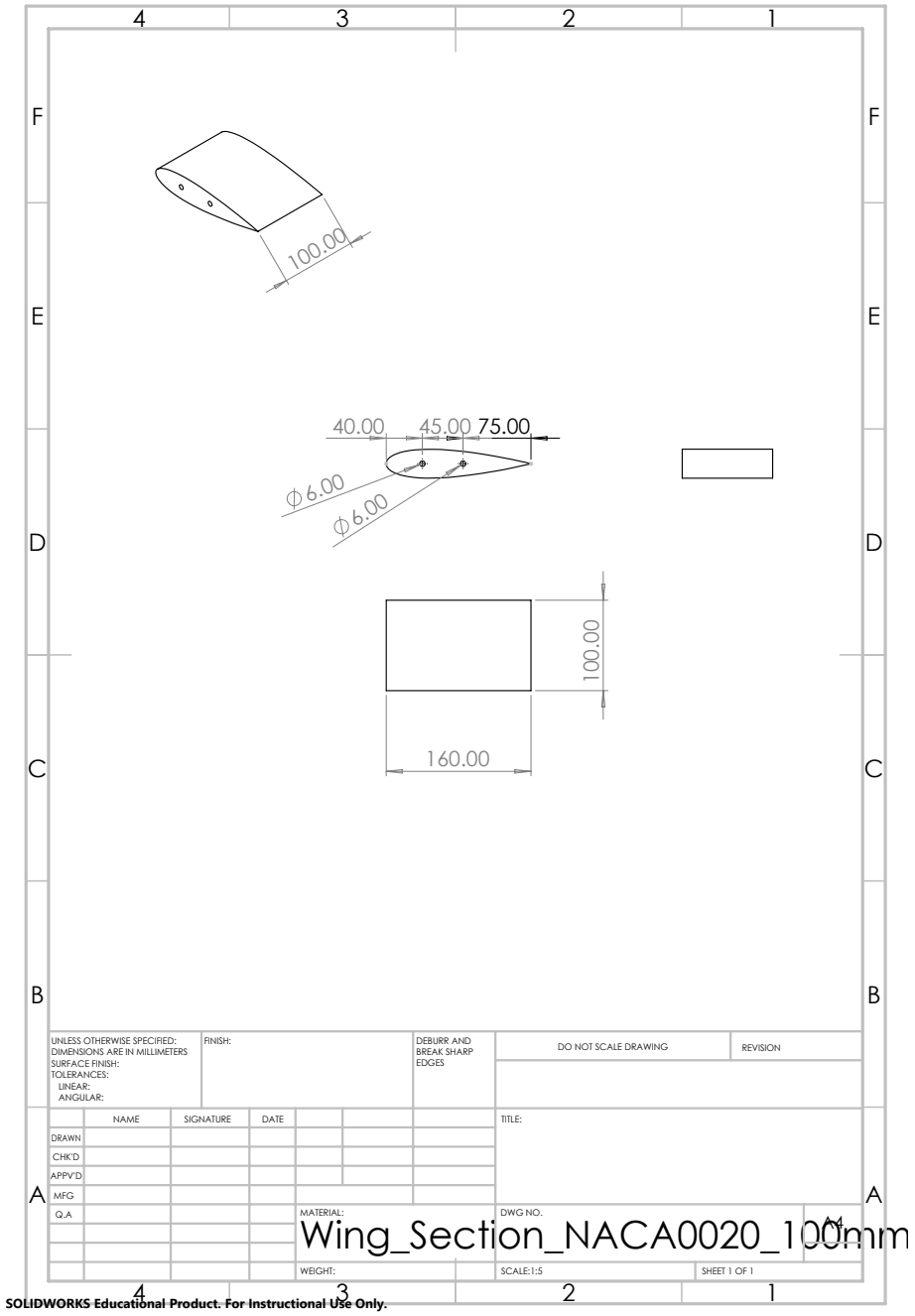

FIGURE E.7: Foam Aerofoil Profile Used for Wing Tip

Figure E.7 shows the technical drawing for the foam aerofoil profile used for the wing tip. It is cut using a CNC machine and has the same NACA0020 aerofoil as the rest of the wing, as well as the same 160mm chord length and a spanwise width of 100mm. Three foam sections are used for the wing tip, held together using lightweight carbon fibre rods with a 6mm diameter and a 30mm length, which are subsequently fixed into the tip hinge part.

E.2.3 Active Wing Tip Parts

As with the passive wing tip, the folding hinge section is made of two key parts. The 'wing-side' part holds the motor which acts as the hinge and powers the wing tip. The 'tip-side' part is then attached to the motor using the metal bush shown in Figure E.2. The 'wing-side' part is split into two parts, with a removable trailing edge so that the motor can be inserted.

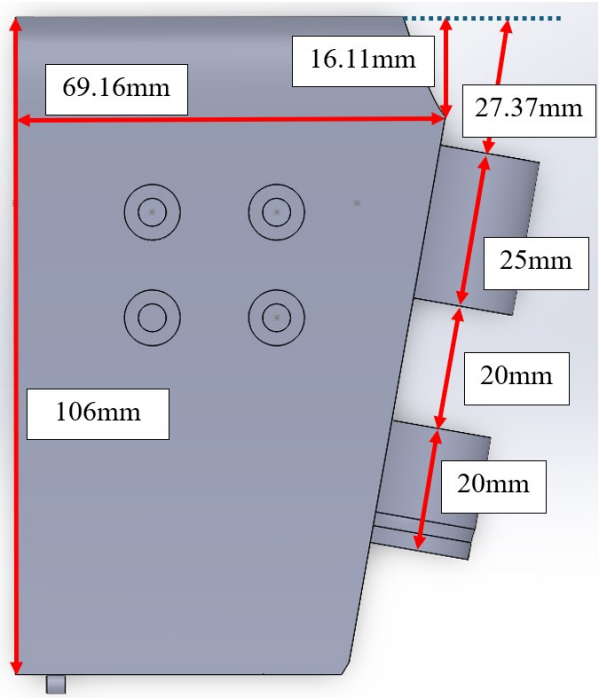

FIGURE E.8: 'Wing-Side' Part of the Active Hinge Viewed from (a) Top and (b) Rear

Figure E.8 shows the 'wing-side' part of the hinge mechanism. All material has a thickness of 2mm, other than the two rings which are 1.75mm thick as to not cause friction in the full assembly. The rings have an inner diameter of 22mm to fit the motor. The same lattice structure and support columns are used as in the passive aerofoil section. The leading edge has a spanwise width of 62.35mm, and the trailing edge is 52.47mm, due to the hinge flare angle and the cutaway in the leading edge.

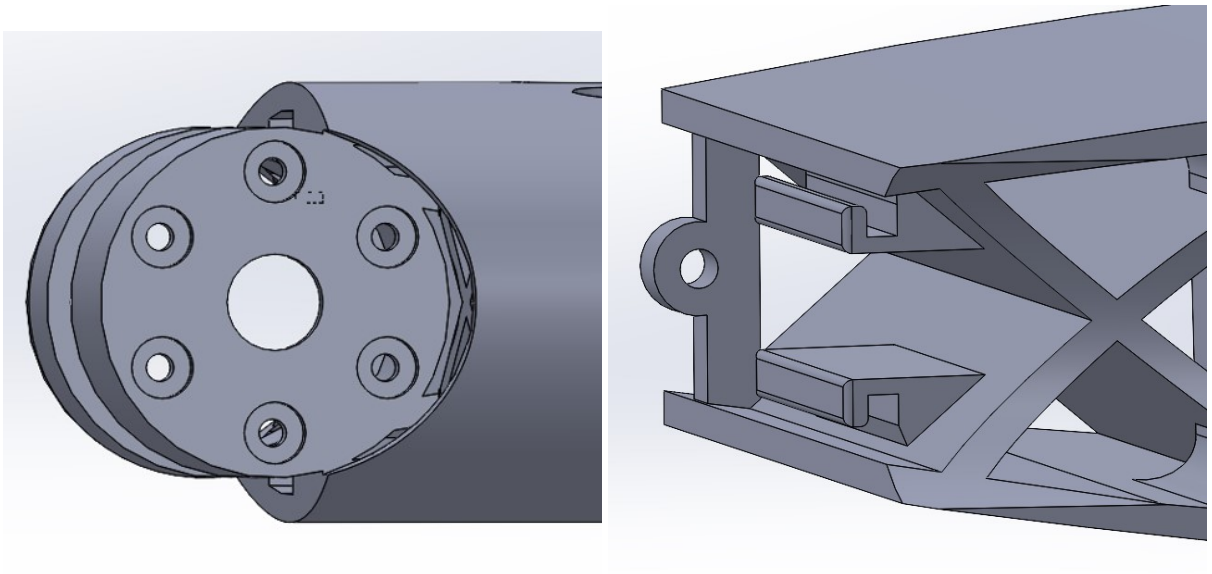

(a) (b)

FIGURE E.9: 'Wing-Side' Part of the Active Hinge Viewed from (a) Front and (b) Rear

Figure E.9 shows the front and rear details of the wing-side part. The front cutaway has a 13mm radius so that no friction is caused in the full assembly. The motor ring has six holes with 2mm diameter so that the motor can be screwed on, and the cap is 3mm thick. The rear of the part shows the fixing needed to connect the trailing edge to the main part. These brackets rely on friction with the corresponding feature on the trailing edge part to make the connection. While this may seem loose and insufficient, in practice the trailing edge part never came loose throughout the test period.

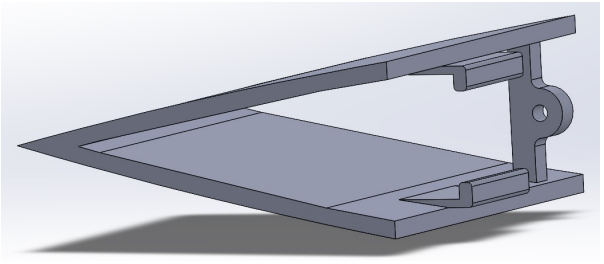

FIGURE E.10: 'Wing-Side' Part of the Active Hinge Viewed from (a) Top and (b) Rear

Figure E.10 shows the trailing edge part for the wing-side hinge mechanism. The material thickness is 2mm and the L-shaped features link with those shown in Figure E.9b.

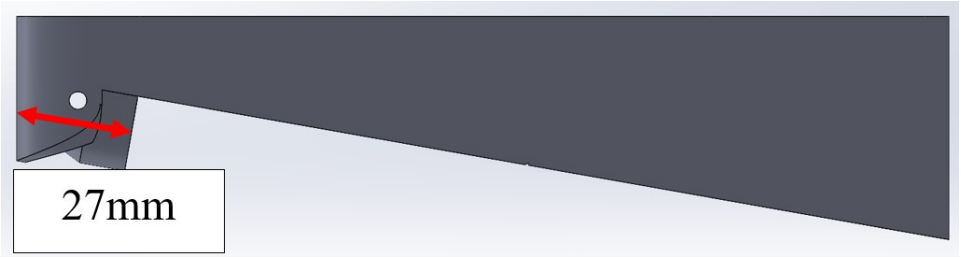

(a)

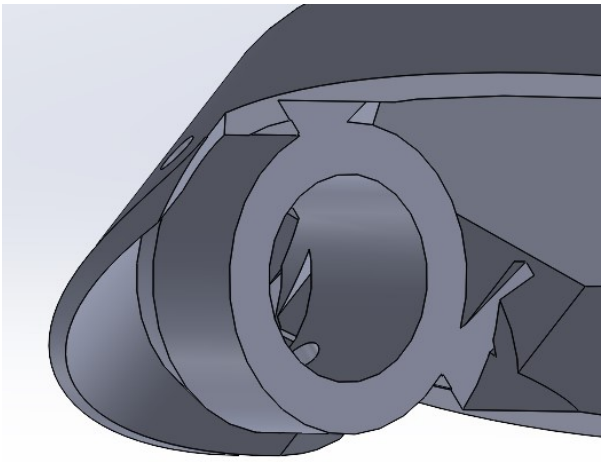

(b)

FIGURE E.11: 'Tip-Side' Part of the Active Hinge View (a) Top and (b) Bush Ring

Figure E.11 shows the tip-side part for the hinge mechanism. As it is a single part, it has a full chord length of 160mm. The leading edge has a length of 24.66mm, the trailing edge is 38.18mm. The angled edge on the 'inside' of the part is 149.17mm and angled at the 10° flare angle. The material has a 2mm thickness, except the bush ring which has a 3.5mm thickness. A 3mm diameter hole runs through the entire part so that M3 grub screws can be used to secure the motor and bush. The hole is centred 10.56mm from the leading edge and 14.4mm from the flat edge. Two 6mm diameter holes are placed in the flat edge in the same place as the foam section shown in Figure E.7.

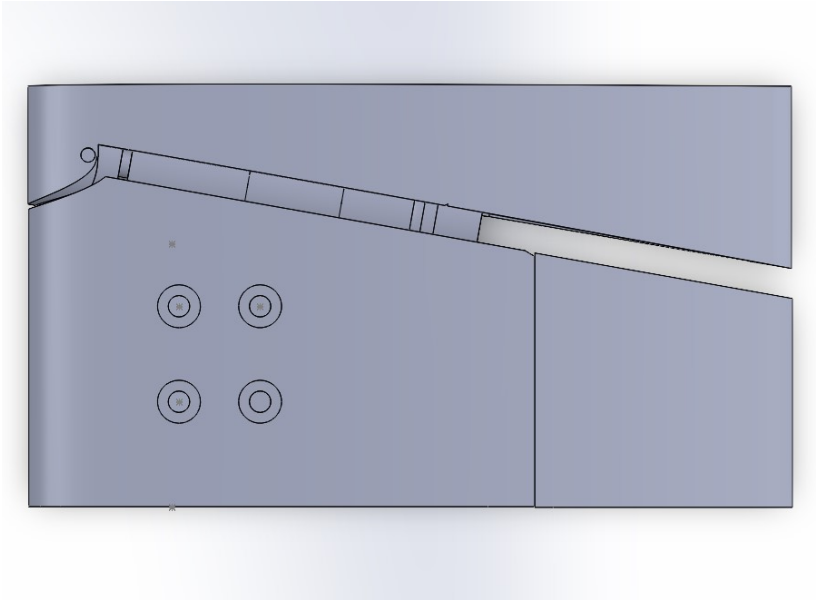

FIGURE E.12: Assembly of Active Wing Tip Hinge Mechanism

Figure E.12 shows the assembled active hinged wing tip section. It is capable of wing tip rotations of $\pm 25°$ before making contact with itself and preventing further deflection.

The active wing tip uses the same foam sections for the tip as the passive wing tip, as shown in Figure E.7.

REFERENCES

[1] International Air Transport Association. IATA - Fly Net Zero;. Available from: https://www.iata.org/en/programs/environment/flynetzero/.

[2] Aerospace Technology Institute. Aerospace Technology Institute Destination Zero Strategy;. Available from: https://www.ati.org.uk/strategy/.

[3] European Union. Clean Aviation;. Available from: https://www.clean-aviation.eu/.

[4] Air Transport Action Group. Waypoint 2050; 2021. Available from: www.bluesky-d2d.com.

[5] Castellani M, Cooper JE, Lemmens Y. Nonlinear Static Aeroelasticity of High-Aspect-Ratio-Wing Aircraft by Finite Element and Multibody Methods. Journal of Aircraft. 2017 3;54(2):548-60. Available from: https://arc.aiaa.org/doi/10.2514/1.C033825.

[6] Collar AR. The First Fifty Years of Aeroelasticity. Aerospace. 1978;5:12-20.

[7] Wright JR, Cooper JE. Introduction to Aircraft Aeroelasticity and Loads. 2nd ed. Wiley; 2015.

[8] Stanford B, Beran P. Direct flutter and limit cycle computations of highly flexible wings for efficient analysis and optimization. Journal of Fluids and Structures. 2013 1;36:111-23.

[9] Boeing Website;. Available from: https://www.boeing.com/commercial/777x#overview.

[10] Balatti D. Numerical and experimental studies of aeroelastic hinged wingtips. Swansea University; 2023.

[11] ACARE. Aeronautics and Air Transport: Beyond Vision 2020 (Towards 2050). Advisory Council for Aeronautics Research in Europe. 2010.

[12] International Air Transport Association. IATA forecast predicts 8.2 billion air travelers in 2037. International Air Transport Association. 2018;1:2019.

[13] ICAO. Presentation of 2018 Air Transport Statistical Results;. Available from: https://www.icao.int/annual-report-2018/Documents/Annual.Report.2018_Air%20Transport%20Statistics.pdf.

[14] International Civil Aviation Organization. The World of Air Transport in 2017;. Available from: https://www.icao.int/annual-report-2017/Pages/the-world-of-air-transport-in-2017.aspx.

[15] European Union Aviation Safety Agency. European aviation environmental report 2019;. Available from: https://www.easa.europa.eu/eco/eaer/system/files/usr_uploaded/219473_EASA_EAER_2019_WEB_LOW-RES.pdf.

[16] Flight Plan. Airbus and Boeing Report April 2024 Commercial Aircraft Orders and Deliveries; 2024. Available from: https://flightplan.forecastinternational.com/2024/05/20/airbus-and-boeing-report-april-2024-commercial-aircraft-orders-and-deliveries/.

[17] Button K. Low-Cost Airlines: A Failed Business Model? Transport Journal. 2012;51(2):197-229.

[18] Drela M. Integrated simulation model for preliminary aerodynamic, structural, and control-law design of aircraft. In: 40th Structures, Structural Dynamics, and Materials Conference and Exhibit. Reston, Virigina: American Institute of Aeronautics and Astronautics; 1999. .

[19] Klimmek T, Ohme P, Ciampa PD, Handojo V. Aircraft Loads - An Important Task From Pre-Design to Loads Flight Testing. In: Deutscher Luft- und Raumfahrtkongress; 2016. .

[20] Bisplinghoff RL, Ashley H, Halfman RL. Aeroelasticity. Addison-Wesley Publishing Company Inc; 1955.

[21] Bisplinghoff RL, Ashley H. Principles of Aeroelasticity. New York: Wiley and Sons Inc; 1962.

[22] Xiang J, Yan Y, Li D. Recent advance in nonlinear aeroelastic analysis and control of the aircraft. Chinese Journal of Aeronautics. 2014 2;27(1):12-22.

[23] Banerjee AK. Flexible Multibody Dynamics: Efficient Formulations and Applications. vol. 1. 1st ed. John Wiley & Sons; 2016.

[24] Bathe KJ. Finite Element Procedures. vol. 1. 1st ed. Prentice Hall; 1996.

[25] Theodorsen T. General Theory of Aerodynamic Instability and the Mechanism of Flutter; 1949.

[26] Eversman W, Tewari A. Consistent rational-function approximation for unsteady aerodynamics. Journal of Aircraft. 1991 9;28(9):545-52. Available from: https://doi.org/10.2514/3.46062https://arc.aiaa.org/doi/10.2514/3.46062.

[27] Tang D, Conner MD, Dowell EH. Reduced-order aerodynamic model and its application to a nonlinear aeroelastic system. Journal of Aircraft. 1998;35(2):332-8.

[28] Vio GA, Dimitriadis G, Cooper JE, Badcock KJ, Woodgate MA, Rampurawala AM. Aeroelastic system identification using transonic CFD data for a wing/store configuration. Aerospace Science and Technology. 2007 3;11(2-3):146-54.

[29] Ko J, Kurdila AJ, Strganac TW. Nonlinear Control of a Prototypical Wing Section with Torsional Nonlinearity. Journal of Guidance, Control and Dynamics. 1997;20(6).

[30] Edwards JW, Ashley H, Breakwell JV. Unsteady aerodynamic modeling for arbitrary motions. AIAA Journal. 1979;17(4):365-74.

[31] Karpel M. Design for Active and Passive Flutter Suppression and Gust Alleviation; 1980.

[32] Fung YC. An Introduction to the Theory of Aeroelasticity. New York: Dover Publications; 1993.

[33] Dowell EH, Edwards J, Strganac T. Nonlinear Aeroelasticity. Journal of Aircraft. 2003;40(5):489-533. Available from: https://link.springer.com/10.1007/978-3-030-74236-2_11.

[34] Tang D, Dowell EH. Experimental aeroelastic models design and wind tunnel testing for correlation with new theory. Aerospace. 2016 6;3(2).

[35] Tang D, Dowell EH, Virgin LN. Limit Cycle Behavior of an Airfoil with a Control Surface; 1998.

[36] Tang D, Dowell EH. Experimental and theoretical study of gust response for a wing-store model with freeplay. Journal of Sound and Vibration. 2006 8;295(3-5):659-84.

[37] Lee BHK, Price SJ, Wong YS. Nonlinear aeroelastic analysis of airfoils: bifurcation and chaos. Progress in Aerospace Sciences. 1999;35:205-334.

[38] Dimitriadis G, Cooper JE. Characterisation of the Behaviour of a Simple Aeroservoelastic System with Control Nonlinearities. Journal of Fluids and Structures. 2000;14:1173-93.

[39] Woolston DS, Runyan HL, Byrdsong TA. Some Effects of System Nonlinearities in the Problem of Aircraft Flutter; 1955.

[40] Woolston DS, Runyan HL, Andrews RE. An Investigation of Effects of Certain Types of Structural Nonlinearities on Wing and Control Surface Flutter. Journal of Aeronautical Sciences. 1957 1;24(1).

[41] Shen SF, Hsu CC. Analytical Results of Certain Nonlinear Flutter Problems. Journal of Aerospace Sciences. 1958 8;25(2).

[42] Breitbach E. Effects of Structural Non-Linearities on Aircraft Vibration and Flutter. AGARD; 1977.

[43] Worden K, Tomlinson GR. Nonlinearity in Structural Dynamics: Detection, Identification and Modelling. New York: Institute of Physics Publishing; 2001.

[44] Dowell EH, Tang D. Nonlinear aeroelasticity and unsteady aerodynamics. AIAA Journal. 2002;40(9):1697-707.

[45] Dowell EH, Ilgamov M. Studies in Nonlinear Aeroelasticity. Springer; 2012.

[46] Dowell E. A Modern Course in Aeroelasticity. 6th ed. Dowell E, editor. Springer; 2021.

[47] Silva W. Identification of Nonlinear Aeroelastic Systems Based on the Volterra Theory: Progress and Opportunities; 2005.

[48] Patil MJ, Hodges DH. On the importance of aerodynamic and structural geometrical nonlinearities in aeroelastic behavior of high-aspect-ratio wings. Journal of Fluids and Structures. 2004 8;19(7):905-15.

[49] Ericsson LE, Reding JP. Fluid mechanics of dynamic stall part I. Unsteady flow concepts. Journal of Fluids and Structures. 1988 1;2(1):1-33.

[50] Dimitriadis G. Introduction to Nonlinear Aeroelasticity. John Wiley & Sons; 2017. Available from: https://ebookcentral.proquest.com/lib/swansea-ebooks/reader.action?docID=4817836.

[51] Khalil H. Nonlinear Systems. 3rd ed. Pearson; 2014.

[52] O'neil T, Gilliatt H, Strganac TW. Investigations of aeroelastic response for a system with continuous structural nonlinearities; 1996.

[53] O'neil T, Strganac TW. Aeroelastic Response of a Rigid Wing Supported by Nonlinear Springs. JOURNAL OF AIRCRAFT. 1998;35(4):616.

[54] Thompson DE. Nonlinear analysis of store-induced limit cycle oscillations. Texas A&M University; 2001.

[55] Thompson DE, Strganac TW. Nonlinear Analysis of Store-Induced Limit Cycle Oscillations; 2005.

[56] Conner MD, Virgin LN, Dowell EH. Accurate numerical integration of state-space models for aeroelastic systems with free play. AIAA Journal. 1996;34(10):2202-5.

[57] Conner MD, Tang DM, Dowell EH, Virgin LN. Nonlinear Behaviour of a Typical Airfoil Section with Control Surface Freeplay: A Numerical and Experimental Study; 1997.

[58] Henon M. On the Numerical Integration of Poincare Maps; 1982.

[59] Al-Mashhadani WJ, Dowell EH, Wasmi HR, Al-Asadi AA. Aeroelastic response and limit cycle oscillations for wing-flap-tab section with freeplay in tab. Journal of Fluids and Structures. 2017 1;68:403-22.

[60] Khalil H. Nonlinear Control. Global ed. Pearson Education; 2015.

[61] Verstraelen E, Dimitriadis G, Rossetto GDB, Dowell EH. Two-domain and three-domain limit cycles in a typical aeroelastic system with freeplay in pitch. Journal of Fluids and Structures. 2017 2;69:89-107.

[62] Hoblit FM. Gust Loads on Aircraft: Concepts and Applications. Washington DC: American Institute of Aeronautics and Astronautics; 1988. Available from: https://arc.aiaa.org/doi/book/10.2514/4.861888.

[63] Regan CD, Jutte CV. Survey of Applications of Active Control Technology for Gust Alleviation and New Challenges for Lighter-weight Aircraft; 2012. Available from: http://www.sti.nasa.gov.

[64] Fuller J. Evolution and future development of airplane gust loads design requirements. In: 1997 World Aviation Congress. Reston, Virigina: American Institute of Aeronautics and Astronautics; 1997. .

[65] Federal Aviation Administration. AC 25.341-1 - Dynamic Gust Loads; 2014.

[66] Haddad Khodaparast H, Georgiou G, Cooper JE, Ricci S, Vio Ga, Denner P. Efficient Worst Case "1-Cosine" Gust Loads Prediction. ASDJournal. 2012;2(3):33-54.

[67] Haddad Khodaparast H, Cooper JE. Rapid prediction of worst-case gust loads following structural modification. AIAA Journal. 2014 2;52(2):242-54.

[68] Scott RC, Vetter TK, Penning KB, Coulson DA, Heeg J. Aeroservoelastic testing of a sidewall mounted free flying wind-tunnel model. Collection of Technical Papers - AIAA Applied Aerodynamics Conference. 2008.

[69] Scott RC, Castelluccio MA, Coulson DA, Heeg J. Aeroservoelastic wind-tunnel tests of a free-flying, Joined-Wing SensorCraft model for gust load alleviation. Collection of Technical Papers - AIAA/ASME/ASCE/AHS/ASC Structures, Structural Dynamics and Materials Conference. 2011;(April).

[70] Brown C, McGowan G, Cooley K, Deese J, Josey T, Dowell EH, et al. Convolution/Volterra Reduced-Order Modeling for Nonlinear Aeroelastic Limit Cycle Oscillation Analysis and Control. AIAA Journal. 2022 12;60(12):6647-64. Available from: https://arc.aiaa.org/doi/10.2514/1.J061845.

[71] Bueno DD, Gonsalez Bueno CG, Dowell EH. A modal approach for designing controllers for active flutter suppression. Journal of the Brazilian Society of Mechanical Sciences and Engineering. 2021 1;43(1).

[72] Datta BN, Elhay S, Ram YM. Orthogonality and partial pole assignment for the symmetric definite quadratic pencil. Linear Algebra and Its Applications. 1997;257(1-3):29-48.

[73] Mottershead JE, Kyprianou A, Ouyang H. Structural modification. Part 1: Rotational receptances. Journal of Sound and Vibration. 2005 6;284(1-2):249-65.

[74] Mottershead JE, Ram YM. Inverse eigenvalue problems in vibration absorption: Passive modification and active control. Mechanical Systems and Signal Processing. 2006 1;20(1):5-44.

[75] Ram YM, Mottershead JE. Receptance method in active vibration control. AIAA Journal. 2007 3;45(3):562-7.

[76] Mottershead JE, Tehrani MG, Ram YM. Assignment of eigenvalue sensitivities from receptance measurements. Mechanical Systems and Signal Processing. 2009 8;23(6):1931-9. Available from: www.elsevier.com/locate/jnlabr/ymssp.

[77] Ghandchi Tehrani M, Elliott RNR, Mottershead JE. Partial pole placement in structures by the method of receptances: Theory and experiments. Journal of Sound and Vibration. 2010 11;329(24):5017-35.

[78] Ghandchi Tehrani M, Mottershead JE, Shenton AT, Ram YM. Robust pole placement in structures by the method of receptances. Mechanical Systems and Signal Processing. 2011 1;25(1):112-22.

[79] Ram YM, Mottershead JE. Multiple-input active vibration control by partial pole placement using the method of receptances. Mechanical Systems and Signal Processing. 2013 11;40(2):727-35.

[80] Singh KV, McDonough LA, Kolonay R, Cooper JE. Receptance-based active aeroelastic control using multiple control surfaces. Journal of Aircraft. 2014;51(1):335-41.

[81] Singh KV, Brown RN, Kolonay R. Receptance-based active aeroelastic control with embedded control surfaces having actuator dynamics. Journal of Aircraft. 2016;53(3):830-45.

[82] Fichera S, Jiffri S, Mottershead JE. Design and wind tunnel test of a MODular aeroelastic FLEXible wing (MODFLEX). Proceedings of ISMA 2016 - International Conference on Noise and Vibration Engineering and USD2016 - International Conference on Uncertainty in Structural Dynamics. 2016:445-55.

[83] Mokrani B, Palazzo F, Mottershead JE, Fichera S. Multiple-input multiple-output experimental aeroelastic control using a receptance-based method. AIAA Journal. 2019;57(7):3066-77.

[84] Adamson LJ, Fichera S, Mokrani B, Mottershead JE. Pole placement in uncertain dynamic systems by variance minimisation. Mechanical Systems and Signal Processing. 2019 7;127:290-305.

[85] Adamson LJ, Braun O, Fichera S, Mottershead JE. Gain scheduling in receptance-based control of aeroelastic systems. In: Proceedings of ISMA 2020 - International Conference on Noise and Vibration Engineering and USD 2020 - International Conference on Uncertainty in Structural Dynamics; 2020. p. 195-205.

[86] Adamson LJ. Receptance-Based Control and Uncertainty Quantification of Aeroservoelastic Systems. 2021;(June).

[87] Storn R, Price K. Differential Evolution-A Simple and Efficient Heuristic for Global Optimization over Continuous Spaces. Journal of Global Optimization. 1997;11:341-59.

[88] Ghandchi Tehrani M, Wilmshurst L, Elliott SJ. Receptance method for active vibration control of a nonlinear system. Journal of Sound and Vibration. 2013 9;332(19):4440-9.

[89] Slotine JJ, Li W. Applied Nonlinear Control. 1st ed. Prentice Hall; 1991.

[90] Perruquetti W, Barbot JP. Sliding Mode Control in Engineering. Marcel Dekker, Inc.; 2002.

[91] Cao L, Tang S, Zhang D. Fractional-Order Sliding Mode Control of Air-Breathing Hypersonic Vehicles Based on Linear-Quadratic Regulator. Journal of Aerospace Engineering. 2018;31(3).

[92] Krstic M, Kanellakopoulos I, Kokotovic P. Nonlinear and Adaptive Control Design. 1st ed. John Wiley and Sons; 1995.

[93] Ko J, Strganac TW, Kurdila AJ. Stability and Control of a Structurally Nonlinear Aeroelastic System. JOURNAL OF GUIDANCE, CONTROL, AND DYNAMICS. 1998;21(5).

[94] Block JJ, Strganac TW. Applied Active Control for a Nonlinear Aeroelastic Structure; 1998. 6.

[95] Da Ronch A, Tantaroudas ND, Jiffri S, Mottershead JE. A Nonlinear Controller for Flutter Suppression: from Simulation to Wind Tunnel Testing. 2014.

[96] Sastry S, Isidori A. Adaptive control of linearizable systems. IEEE Transactions on Automatic Control. 1989;34(11).

[97] Ko J, Strganac TW, Kurdila AJ. Adaptive Feedback Linearization for the Control of a Typical Wing Section with Structural Nonlinearity. Nonlinear Dynamics. 1999;18:289-301.

[98] Strganac TW, Ko J, Thompson DE, Kurdila AJ. Identification and Control of Limit Cycle Oscillations in Aeroelastic Systems. JOURNAL OF GUIDANCE, CONTROL, AND DYNAMICS. 2000;23(6).

[99] Ko J, Strganac TW, Junkins JL, Akella MR, Kurdila AJ. Structured model reference adaptive control for a wing section with structural nonlinearity. JVC/Journal of Vibration and Control. 2002;8(5):553-73.

[100] Platanitis G, Strganac TW. Control of a Nonlinear Wing Section Using Leading- and Trailing-Edge Surfaces. Journal of Guidance, Control, and Dynamics. 2004;27(1):52-8.

[101] Jiffri S, Cooper JE. Active Control of a Nonlinear Flexible Aircraft Wing; 2013. .

[102] Jiffri S, Mottershead JE, Cooper JE. Adaptive Feedback Linearisation and Control of a flexible Aircraft Wing; 2014.

[103] Jiffri S, Mottershead E J. Nonlinear control of systems with non-smooth nonlinearities. In: ICCM; 2014. p. 1-11.

[104] Jiffri S, Fichera S, Mottershead JE, Da Ronch A. Experimental nonlinear control for flutter suppression in a nonlinear aeroelastic system. Journal of Guidance, Control, and Dynamics. 2017;40(8):1925-38.

[105] Li D, Xiang J, Guo S. Adaptive control of a nonlinear aeroelastic system. Aerospace Science and Technology. 2011 7;15(5):343-52.

[106] Mannarino A, Dowell EH, Mantegazza P. An adaptive controller for nonlinear flutter suppression and free-play compensation. JVC/Journal of Vibration and Control. 2017 8;23(14):2269-90.

[107] Li D, Guo S, Xiang J. Aeroelastic dynamic response and control of an airfoil section with control surface nonlinearities. Journal of Sound and Vibration. 2010 10;329(22):4756-71.

[108] Nickol C, Guynn M, Kohout L, Ozoroski T. High Altitude Long Endurance Air Vehicle Analysis of Alternatives and Technology Requirements Development. In: 45th AIAA Aerospace Sciences Meeting and Exhibit. Reston, Virigina: American Institute of Aeronautics and Astronautics; 2007. Available from: https://arc.aiaa.org/doi/10.2514/6.2007-1050.

[109] Barbarino S, Bilgen O, Ajaj RM, Friswell MI, Inman DJ. A review of morphing aircraft. Journal of Intelligent Material Systems and Structures. 2011;22(9):823-77.

[110] Wilson T, Castrichini A, Azabal A, Cooper JE, Ajaj R, Herring M. Aeroelastic behaviour of hinged wing tips. 17th International Forum on Aeroelasticity and Structural Dynamics, IFASD 2017. 2017;2017-June:1-15.

[111] Balatti D, Haddad Khodaparast H, Friswell MI, Manolesos M, Amoozgar M. The effect of folding wingtips on the worst-case gust loads of a simplified aircraft model. Journal of Aerospace Engineering. 2019;236(2):219-37.

[112] Castrichini A, Siddaramaiah VH, Calderon DE, Cooper JE, Wilson T, Lemmens Y. Preliminary investigation of use of flexible folding wing tips for static and dynamic load alleviation. The Aeronautical Journal. 2017;121(73):73-94. Available from: https://doi.org/10.1017/aer.2016.108.

[113] Castrichini A, Hodigere Siddaramaiah V, Calderon DE, Cooper JE, Wilson T, Lemmens Y. Nonlinear folding wing tips for gust loads alleviation. Journal of Aircraft. 2016;53(5):1391-9. Available from: https://doi.org/10.2514/1.C033474.

[114] Castrichini A, Cooper JE, Wilson T, Carrella A, Lemmens Y. Nonlinear negative stiffness wingtip spring device for gust loads alleviation. Journal of Aircraft. 2017;54(2):627-41. Available from: https://doi.org/10.2514/1.C033887.

[115] Healy F, Courcy JD, Gu H, Rezgui D, Cooper J, Wilson T, et al. On the Dynamic Behavior of Wings Incorporating Floating Wingtip Fuel Tanks. Journal of Aircraft. 2023 11;(November):1-16. Available from: https://arc.aiaa.org/doi/10.2514/1.C037519.

[116] Carrillo X, Mertens C, Sciacchitano A, van Oudheusden B, De Breuker R, Sodja J. Wing Stiffness and Hinge Release Threshold Effects on Folding Wingtip Gust Load Alleviation. In: AIAA SCITECH 2022 Forum. Reston, Virginia: American Institute of Aeronautics and Astronautics; 2022. Available from: https://arc.aiaa.org/doi/10.2514/6.2022-1559.

[117] Sanghi D, Riso C, Cesnik CES, Vetrano F. Conventional and Unconventional Control Effectors for Load Alleviation in High-Aspect-Ratio-Wing Aircraft. In: AIAA Science and Technology Forum and Exposition, AIAA SciTech Forum 2022. American Institute of Aeronautics and Astronautics Inc, AIAA; 2022. .

[118] Gu H, Healy F, Rezgui D, Cooper J. Sizing of High Aspect Ratio Wings with Folding Wingtips. In: AIAA Science and Technology Forum and Exposition, AIAA SciTech Forum 2022. American Institute of Aeronautics and Astronautics Inc, AIAA; 2022. .

[119] Mastracci P, Saltari F, Mastroddi F, Wilson T, Castrichini A. Unsteady Aeroelastic Analysis of the Semi Aeroelastic Hinge Including Local Geometric Nonlinearities. AIAA Journal. 2022;60(5):3147-65.

[120] Gu H, Cheung RC, Healy F, Rezgui D, Lowenberg MH, Cooper JE. Transient Release and Lateral Gust Behavior of Aircraft Incorporating Flared Folding Wingtips. In: Proceedings of AIAA SciTech 2023. June; 2023. .

[121] Cheung RCM, Rezgui D, Cooper JE, Wilson T. Testing of a hinged wingtip device for gust loads alleviation. Journal of Aircraft. 2018;55(5):2050-67. Available from: https://doi.org/10.2514/1.C034811.

[122] Cheung RCM, Rezgui D, Cooper JE, Wilson T. Testing of folding wingtip for gust load alleviation of flexible high-aspect-ratio wing. Journal of Aircraft. 2020;57(5):876-88.

[123] Sanghi D, Cesnik CES, Riso C. Roll Maneuverability of Transonic High-Aspect-Ratio-Wing Aircraft with Flared Folding Wingtips. Journal of Aircraft. 2024 2;61(3).

[124] Delavenne M, Barriety B, Vetrano F, Ferrand V, Salaün M, Salaün Parametric M. Parametric Analysis of an Active Winglet Concept for High Aspect Ratio Wing Using CFD/CSM Computations. In: AIAA Aviation Forum; 2020. p. 10. Available from: https://doi.org/10.2514/6.2020-2662.

[125] Sanghi D, Cesnik CES. Active vs. Passive Flared Folding Wingtips in Very Flexible High-Aspect-Ratio-Wing Aircraft. In: RAeS Aircraft Structural Design Conference; 2023. .

[126] Clean Aviation. Hydrogen-Powered Aviation;. Available from: https://www.clean-aviation.eu/media/publications/hydrogen-powered-aviation.

[127] Ellis JD, Jiffri S, Friswell MI, Fichera S. Active Control of a Flexible Wing in the Presence of Gusts and Nonlinearity. In: Proceedings of IFASD 2022 - International Forum on Aeroelasticity and Structural Dynamics. July; 2022. .

[128] Ellis JD, Balatti D, Haddad Khodaparast H, Jiffri S, Friswell MI, Fichera S. Multiple-Input, Multiple-Output Linear and Nonlinear Active Control of a Flexible Wing. In: AIAA SCITECH 2023 Forum. Reston, Virginia: American Institute of Aeronautics and Astronautics; 2023. p. 1-20. Available from: https://arc.aiaa.org/doi/10.2514/6.2023-0375.

[129] Balatti D, Ellis JD, Jiffri S, Haddad Khodaparast H, Friswell MI. Active hinged wingtip for gust load alleviation and manoeuvres. In: AIAA SCITECH 2023 Forum. January. Reston, Virginia: American Institute of Aeronautics and Astronautics; 2023. Available from: https://arc.aiaa.org/doi/10.2514/6.2023-2567.

[130] Ellis JD, Balatti D, Haddad Khodaparast H, Jiffri S, Friswell MI. Reduction of Root Loads due to Gusts via Active Hinged Wing Tip Control. In: International Conference on Noise and Vibration Engineering (ISMA); 2024. .

[131] Ellis JD, Balatti D, Khodaparast HH, Jiffri S, Friswell MI. Active Hinged Wingtip Control for Reducing Wing Root Bending Moment. Journal of Aircraft. 2025 3:1-10. Available from: https://arc.aiaa.org/doi/10.2514/1.C038141.

[132] Ahmadi Tehrani M, Ellis J, Farsadi T, Jiffri S, Haddad Khodaparast H, Friswell M. Experimental Active Gust Load Alleviation via an Actuated Wingtip. In: AIAA SCITECH 2025 Forum. Reston, Virginia: American Institute of Aeronautics and Astronautics; 2025. Available from: https://arc.aiaa.org/doi/10.2514/6.2025-0715.

[133] Balatti D, Haddad Khodaparast H, Friswell MI, Manolesos M. Improving Wind Tunnel "1-cos" Gust Profiles. Journal of Aircraft. 2022;59(6):1-15.

[134] European Union Aviation Safety Agency. Flight Manoeuvre and Gust Conditions; 2023. Available from: EuropeanUnionAviationSafetyAgency.

[135] Rational Fraction Polynomial Method - File Exchange - MATLAB Central;. Available from: https://uk.mathworks.com/matlabcentral/fileexchange/3805-rational-fraction-polynomial-method.

[136] Adamson LJ, Fichera S, Mottershead JE. Receptance-based robust eigenstructure assignment. Mechanical Systems and Signal Processing. 2020 6;140.

[137] Isidori A. Nonlinear Control Systems. Springer; 1995.